Molecular Mechanics Simulations of Instabilities in 3D Deformations of Gold Nanospecimens

Alejandro Andres Pacheco Sanjuan

Dissertation submitted to the faculty of the
Virginia Polytechnic Institute and State University
in partial fulfillment of the requirements for the degree of

Doctor of Philosophy
In
Engineering Mechanics

Romesh C. Batra, Chair
Michael W. Hyer
Diana Farkas
Scott L. Hendricks
Layne T. Watson
Mark S. Cramer

January 27, 2009
Blacksburg, VA

Keywords: local instability criteria; global instability criteria; molecular mechanics; average and local stress and strain tensors.

Molecular Mechanics Simulations of Instabilities in 3D Deformations of Gold Nanospecimens

Alejandro Andres Pacheco Sanjuan

ABSTRACT

We use molecular mechanics (MM) simulations with the tight-binding (TB) potential to study local and global instabilities in initially defect-free finite specimens of gold crystals deformed in shear, simple shear, tension/compression, simple tension/compression, and triaxial tension/compression. The criteria used to delineate local instabilities in a system include the following: (*i*) a second order spatial derivative of the displacement field having large values relative to its average value in the body, (*ii*) the minimum eigenvalue of the Hessian of the potential energy of an atom becoming nonpositive, (*iii*) and structural changes represented by a high value of the common neighborhood parameter. A specimen becomes globally unstable when its potential energy decreases significantly with a small increase in its deformations. It is found that the three criteria for local instability are satisfied essentially simultaneously at the same atomic position. Deformations of a specimen are quite different when it is deformed with some bounding surfaces free from external forces as opposed to essential boundary conditions prescribed on all bounding surfaces. It is found that the initial unloaded configuration (or the reference configuration) of the minimum potential energy has significant in-plane stresses on the bounding surfaces and nonzero normal stresses at interior points. In tensile/compressive deformations of a rectangular prismatic nanobar the yield stress defined as the average axial stress when the average axial stress vs. the average axial strain curve exhibits a sharp discontinuity depends upon the specimen size; a similar result holds for simulations of shear deformations. Specimens deformed with essential boundary conditions on all bounding surfaces experience instabilities at a higher value of the average strain than identical specimens deformed similarly but with one or more pairs of opposite bounding surfaces traction free. For the former set of deformations, the response of a specimen prior to the onset of instability is the same as that

of a hyperelastic body with the strain energy derived from the TB potential and deformations obeying the Cauchy-Born rule. Specimens with some traction free bounding surfaces experience local instabilities prior to the onset of a global instability but the two instabilities occur simultaneously in specimens with essential boundary conditions prescribed on all bounding surfaces. It is believed that because of residual stresses in the reference configuration, the average axial stress at yield in compression is nearly one-half of that in tension.

Acknowledgments

I would like to take this opportunity to express my gratitude and appreciation to my advisor Dr. Romesh Batra for his unconditional support and guidance during this period of my career. His invaluable advice, not only in academic matters, but in personal issues, helped me to navigate through this small portion of the immense ocean of science that I present to you, always guided by the compass of his experience and passion for research.

I express my immense gratitude to my wife Erika whose unconditional support and infinite patience were fundamental to continuing with my doctoral studies. Her endless happiness and love gave me the fortitude to go forward in moments when problems seemed not to have solutions.

I would like to express my deep gratitude to my parents, my sisters and all my family in Colombia for their encouragement and support. Thanks to all of you for allowing me to devote a part of my life to science.

I would like to thank my aunt Maria, her husband Gilberto, my cousins Lineth and Wesley, Francisco and his wife Olga and his sister Diris, my cousins Medardo and Jairo and their families, Luis and his wife Jovanna, for making us feel again at home regardless of the distance to our country. Those were very gratifying moments that we all shared and will remain in our minds forever.

I would like to thank our friends in the Hispanic community, the Brazilian community and the Indian community resident in Blacksburg. Those moments that we spent together were enjoyable and I hope that we could repeat them in the near future. Special thanks to Francisco, Viviani, Sandra, Alejandro, Noreen, Jorge, Gabriela, Jose, Celia, Salvador, Ponkash, Ismita, Phanindra and Manju, for sharing with us the beauty of their culture.

I express my gratitude to the other committee members, Dr. Michael Hyer, Dr. Scott Hendricks, Dr. Diana Farkas, Dr. Mark Cramer, Dr. Gary Seidel and Dr. Layne Watson for their valuable comments, suggestions and fruitful discussions. Also I would like to thank the entire faculty and staff of the Engineering Science and Mechanics department (ESM) for giving me the opportunity to be an active part of this excellent academic community. To all the professors in the ESM department, I thank you for your commitment with higher standards in engineering education. Errors in this dissertation are to be attributed to the author.

I also would like to thank my colleagues in the computational mechanics group led by Dr. Batra for their important suggestions regarding my research work and their company during my stay in Blacksburg. Thank you for the interesting and entertaining discussions during the afternoon coffee times. To Mr. Kaushik Das, for giving me valuable ideas full of practicality. To Dr. Anoop Varghese who gave me useful tips in programming. To Mr. Shakti Gupta, for his company and fruitful discussions about life, science and the world. To Mr. Gautam Gopinath, for being the helping friend always there to give his support.

This work was partially supported by the ONR grant N00014-99-06-1-0567 to Virginia Polytechnic Institute and State University with Dr. Y.D.S. Rajapakse as the program manager, Virginia Tech's Institute of Critical Technologies and Sciences, the COLCIENCIAS – LASPAU scholarship, and the Universidad del Norte in Barranquilla, Colombia. Views expressed herein are those of the author, and neither of the funding agencies nor of their institutions.

Table of Contents

List of figures

List of tables

Chapter 1

Introduction

1.1 Mechanical properties of materials at nanoscale

The mechanical properties of materials with one or more dimensions of the order of nanometers are of great interest due to their potential use as reinforcements in fabricating composites for structural applications and also in the development of electrical, thermal and optical systems. Materials at the nanoscale have special features related mostly with the prominent influence of stresses induced in free surfaces and the residual stresses developed in the interior of the body.

The environment around atoms located near free surfaces differs considerably from that around atoms located in the interior. If a perfect crystal is divided by an imaginary plane and atoms from one side are removed, the atoms sitting on the dividing plane will not have counterparts on the opposite side; this will lead to a reorganization of the interatomic forces. To counteract the attraction force of atoms in the interior, the interatomic distance between atoms near the outer layers will change to generate forces for the system to be in equilibrium. The components of these forces projected on the dividing plane will generate in-plane stresses on the free surface (surface tension), and the free surface may not stay plane. These in-plane stresses induce stresses in the interior of the body.

The influence of surface and residual stresses can be important on the mechanical properties of a nanoscale structure. For instance, as the cross section of a nanowire decreases the interatomic space also decreases as compared to the interatomic space in a perfect crystal. The influence of this change increases with a decrease in dimensions of the structure up to the point of causing local yielding in the material due to high compressive stresses developed at interior atoms (Diao et al., 2006). This variation in the interatomic forces leads to a spatial variation in the mechanical properties of the material such as its elastic constants. It has been observed in molecular mechanics/molecular dynamics (MM/MD) simulations that in-plane tensile stresses on

the bounding surfaces generate compressive normal stresses in the interior of a nanowire (Diao et al., 2004; Zhang et al., 2008).

Diao et al. (2004) have performed MM simulations of tensile deformations of gold nanowires to study the effect of free surfaces on their mechanical properties. They used the modified embedded atom method potential (MEAM) (Baskes, 1992). The gold specimens of square cross section were oriented in the [1,0,0] and [1,1,1] crystallographic directions. The effective Young's modulus E and Poisson's ratio for different cross sectional areas were computed. For nanowires oriented in the [1,0,0] direction with a thickness more than 3 nm values of E equaled 42.3 GPa which equals E for the bulk material. However, for nanowires less than 1.83 nm thick E increased to 127 GPa. The local virial stress tensor was computed in the initial unloaded relaxed configuration. It was found that in-plane tensile stresses are generated in nanowire's bounding surfaces and compressive stresses in the interior. For 2 nm thick wires, values of E at the four corners of the cross section were 3.5 times of those at interior points. For nanowires in the [1,0,0] direction, the magnitude of the compressive stress at interior points exceeded 1.6 GPa which is the yield stress in compression for a bulk material. The variation of only the axial stress was shown at different stages of the deformation.

Gall et al. (2004) have studied the effect of free surfaces in rhombic nanowires and multishell wires. The rhombic nanowires had [1,1,0] axes orientation and {1,1,1} side surfaces while the multishell wires were composed of a single atomic chain surrounded by a helix of six atoms. MD simulations of tensile loading using the EAM potential were performed until yield signified by a sharp discontinuity in the average axial stress-average axial strain curve. Young's modulus of a multishell wire was found to be greater than that of a rhombic nanowire. For a 0.7 nm diameter multishell wire the computed average axial yield stress and the average axial yield strain were 13 GPa and 14% respectively. For a 2.2 nm diameter rhombic nanowire the average axial yield stress and the average axial yield strain were 3 GPa and 7% respectively. The authors explained that the {1,1,1} surfaces contract without the application of an external load generating compressive stresses in the interior of the wire. The effect of surface stresses is negligible for macroscopic bodies but is significant for specimens having diameter 10 nm or less. Gall et al. (2004) pointed out that the initially compressive stresses are responsible for the experimentally observed asymmetry in the yield stress for small diameter specimens undergoing tensile and compressive loading. In a tension test the external loads overcome the internal compressive

stress and finally the wire fails under tension. Although free surfaces contribute to the generation of internal compressive stresses that increase the strength of the structure under tension, points with high compressive stresses and other geometric irregularities are potential sites for the nucleation of instabilities.

Diao et al. (2006) studied the effect of free surfaces on the yielding of gold nanowires and proposed that unstable points are those where the resolved shear stress (RSS) reaches a critical value, and dislocations will nucleate there. Isothermal MD simulations of tension and compression tests for gold specimens of square cross section with [1,0,0] and [1,1,1] axial orientation were performed. The temperature of the specimens was set to 2 K and periodic boundary conditions were used in the length direction. The length of the representative volume element was approximately three times the thickness of the nanowires. Due to in-plane tensile surface stresses the nanowires created from a perfect crystalline structure are not in equilibrium. Under no external loads the nanowire changes its configuration and its overall dimensions are modified until the minimum potential energy configuration is reached. This process is called relaxation. For [1,0,0] nanowires less than 2.45 nm thick local yielding was observed upon relaxation. An increasing value of the axial strain imposed after relaxation caused the cross sectional area to decrease. Asymmetry in the yield stress for tension and compression was obtained for nanowires oriented in the [1,0,0] direction: ~-4.8% and ~-0.7 GPa for the average axial yield strain and the average axial yield stress, respectively, under compression, and ~10% and 4 GPa for the average axial yield strain and the average axial yield stress, respectively, under tension for a sample 4 nm thick. For 4 nm thick nanowires oriented in the [1,1,1] direction the average axial yield stress in tension and compression was ~5 GPa. The yielding was attributed to the nucleation and propagation of {1,1,1} [1,1,2] partial dislocations from the edges of the nanowires. The Schmidt factor for a bulk material at the onset of yield for the most favorable slip system in the [1,0,0] nanowires is larger in compression than that in tension causing the [1,0,0] nanowire to yield at a lower value of the axial stress in compression than that in tension. On the other hand the Schmidt factor for the most favorable slip system in the [1,1,1] nanowires is larger in tension than that in compression but the residual compressive stresses counteract this effect producing an equal value of the yield stress in tension and compression. Even though Diao et al. (2006) found that the critical RSS does not change appreciably with the cross sectional area of the nanowire and that it can be used as a criterion for the nucleation of defects Liu et al. (2007)

and Miller and Rodney (2008) have stated that in MM and MD simulations of mechanical deformations the slip system with the highest RSS is not always activated at the yield point.

Zhang et al. (2008) proposed a theoretical model to explain the influence of surface stresses upon elastic properties and the asymmetry in the yield strength in tension and compression observed experimentally in nanowires. Using the linear elasticity theory, they found analytical expressions for the effective Young's modulus, strains, stresses, and the yield stress in tension/compression for an isotropic nanowire with a circular cross section and unit length. Effects of surface stresses and initial stresses were considered. They found that the effective Young's modulus and in general the elastic constants of the nanowire do not depend upon the residual stresses. Assuming the von Mises yield criterion, they derived an expression for the yield stress in tension and compression which showed that the initial stress is responsible for the asymmetry observed in the yield stress in tension and compression. It was also found that the influence of the elastic properties of the surface and of the initial stresses on the effective elastic properties of a nanowire and the yield stress vanish as the radius of the nanowire increases. They suggested using the same methodology to study the effect of surface stresses in nanowires of different cross sections, anisotropic materials and different yield criteria. Even though the influence of residual stresses appears to be explained by this simplified model the assumptions of the material being isotropic and residual stresses being uniform are not realistic for a nanowire.

1.2 Global and local instabilities in atomic systems

In a homogeneous continuous body, a strong singularity is associated with either the deformation gradient or the displacement becoming discontinuous across a surface passing through a material point (e.g., see Truesdell and Noll, 1992). The singularity is called weak when both displacements and their first-order derivatives are continuous everywhere in the body but a second or a higher-order derivative of the displacement is discontinuous at one or more points of the body. The initiation of a weak singularity at a point is synonymous with an acceleration wave not propagating through that point (Hill, 1962). This is equivalent to the acoustic tensor evaluated at that point having a zero eigenvalue or a null determinant. Van Vliet et al. (2003) and

Steinmann et al. (2007), amongst others, have used it to characterize local instabilities in an atomic system.

The potential energy of a system of atoms is usually assumed to depend upon the current interatomic distances and the relative angles between atomic bonds. From a continuum point of view, this is tantamount to assuming that an appropriately defined strain energy density depends upon the state of deformation in the present configuration, or equivalently, the material response is elastic (Truesdell and Noll, 1992). The material objectivity is satisfied since interatomic distances and changes in angles between atomic bonds are invariant with respect to superimposed rigid body motions.

The hypothesis of the acoustic tensor becoming singular at the onset of a local instability is equivalent to assuming that the matrix of instantaneous values of elasticities, defined as the second-order derivatives of the strain energy density with respect to the Green-St. Venant strain tensor, ceases to be positive-definite. In the phonon theory the acoustic tensor is called the dynamical matrix and is a concept for discrete systems. However, in continuum mechanics the acoustic tensor is defined at every point in the continuum and is a continuous function of the deformation gradient. For discrete systems Lu and Zhang (2006) have used an atomistic counterpart of the continuum acoustic tensor, called the atomic acoustic tensor, to study the nucleation of local instabilities. It is equivalent to requiring that the energy of every atom in the system in equilibrium be convex for variations of position vectors of other atoms given by a mono-mode perturbation.

The configuration of a system in equilibrium is globally stable if its potential energy in that configuration is the minimum. Kitamura et al. (2004a) studied delamination of a nano-film from a substrate and found that the displacement at which the minimum eigenvalue of the Hessian of the potential energy of the system vanished equaled that at which the load-displacement curve became discontinuous (the displacement abruptly increased under the applied load). The same criterion has been used to analyze strengths of thin films and cracked bodies (Kitamura et al., 2004b).

Instabilities in an atomic system have also been studied by the normal mode analysis (Dmitriev et al., 2005) which exploits symmetries of the system to reduce the number of degrees of freedom (d.o.f.). For a system having no spatial symmetries, the normal mode analysis is equivalent to the method used by Kitamura et al. (2004a, b). For a system having no symmetries,

the reduction in the number of d.o.f. is not possible. The implementation of a criterion which includes all d.o.f. is prohibitive for a large system because of difficulties in finding an eigenvalue of a $N_a \; x \; N_a$ sparse matrix where N_a is the number of d.o.f. after the elimination of all prescribed displacements. Moreover, modal analysis shows not only instabilities related to the constituent material but also structural instabilities that are influenced by the magnitude of external loads and the type of constraints. Thus a local criterion helps characterize material instabilities and determine the permissible loading capacity of a system.

Regions where deformations of an atomic system first become unstable have also been identified by using geometric measures of the local atomic structure. For example, for a face-centered cubic (FCC) crystal Kelchner et al. (1998) used the centrosymmetry parameter that measures relative positions between six pairs of nearest atoms situated on opposite sides of the atom whose centrosymmetric parameter is being calculated. Other quantities used include the slip vector (Zimmerman et al., 2001), the atomic bond rotation angle (Li et al., 2006), the common neighborhood parameter (CNP) (Tsuzuki et al., 2007), and invariants of the infinitesimal strain tensor (Pasianot et al., 1993). Hartley and Mishin (2005) computed the local deformation gradient by employing the least squares method (LSM) and the Cauchy-Born rule, and used contour plots of components of the Nye tensor to identify screw and edge dislocations in a system of copper atoms. Since the integration of the Nye tensor over an area enclosed by Burger's circuit equals the Burger vector, Hartley and Mishin (2005) asserted that this technique identifies well dislocations. Zimmerman et al. (2001) used the slip vector for identifying dislocations and finding an approximation of Burger's vector.

Here we use the tight-binding (TB) potential and MM simulations of different mechanical tests to study deformations of a system of gold (Au) atoms, and use (i) second-order gradients of the displacement field, (ii) the CNP (Tsuzuki et al., 2007), (iii) and eigenvalues of the Hessian of the local potential energy to characterize the onset of local instabilities. We also investigate whether or not these three criteria are satisfied simultaneously at a point. Deformations simulated include shear, simple shear, tension/compression and simple tension/compression of specimens of different sizes and aspect ratios. A MM code to simulate these deformations and subroutines to calculate stresses and strains have been developed.

We find the local Hessian of the TB potential by considering the bond energy between an atom and other atoms included in its first shell of neighbors. The first shell of neighbors of an atom contains atoms located within one atomic distance from it.

Values of the first- and the second-order displacement gradients are found by using the modified smoothed particle hydrodynamics (MSPH) method (Zhang and Batra, 2004). Values of the average Cauchy stress tensor are computed by using four definitions of the average stress tensor. The local Cauchy stress tensor is computed following Hardy's method (Hardy, 1981). The von Mises stress and the maximum shear stress at atomic positions where instabilities were predicted by the vanishing of eigenvalues of the Hessian of the local energy are found to be much larger than their average values in the specimen. Unstable points (atoms) are located, in general, beneath free surfaces in zones with high stress gradients. For simple tensile/compressive deformations of nanorods the average axial yield stress is found to increase with a decrease in the specimen size but local stresses are found to be considerably high in certain zones in large samples.

Average stresses and strains for the simple shear deformations are also compared with those deduced by assuming that the Cauchy-Born rule applies and the response of the atomic system is equivalent to that of a hyperelastic body with the strain energy density deduced from the TB potential and the Cauchy-Born rule.

For deformations simulated here the global instability of the system is characterized either by a sharp discontinuity in the average stress-average strain curve or the strain energy density of the system ceasing to be a minimum.

Chapter 2

Review of basic quantities

2.1 Interatomic forces and many-body potentials

Considerable work has been devoted to the development of accurate expressions for interatomic forces in metals. Many currently used approaches to describe deformations of solids are based on first principle (ab-initio) calculations and experimental data for their mechanical and thermal properties. Besides the interaction between a pair of atoms in a two body potential, many-body potentials take into account the environment around each atom and how this affects interatomic forces. These potentials include the Finnis-Sinclair potential (Finnis and Sinclair, 1984), the embedded atom method (EAM) potential (Baskes and Daw, 1984; Voter and Chen, 1987), the effective medium theory (EMT) potential (Jacobsen et al., 1987), the glue models potential (Ercolessi et al., 1988), and the tight-binding (TB) potential (Cleri and Rosato, 1993). In this work, we use the TB potential to represent the internal energy and interatomic forces in an atomic system.

The functional form of the TB potential is:

$$V^{(i)} = -\left(\sum_{\substack{j=1 \\ j \neq i}}^{N} \zeta^2 \exp\left(-2D\left(\frac{r^{(ij)}}{r_0} - 1 \right) \right) \right)^{1/2} + \sum_{\substack{j=1 \\ j \neq i}}^{N} M \exp\left(-\tilde{P}\left(\frac{r^{(ij)}}{r_0} - 1 \right) \right). \qquad (2.1)$$

In Eq. (2.1), $V^{(i)}$ equals the potential energy of atom i, N the total number of atoms in the system, r_0 the first-neighbor distance ($a_0/\sqrt{2}$, where a_0 is the lattice parameter), $r^{(ij)}$ the magnitude of the position vector between atoms i and j, and ζ, D, $\tilde{P}$ and M are constants characterizing a material. These constants are obtained by the minimization of an error function containing differences between the experimentally obtained material properties and predictions of the TB

potential. For a FCC crystal in equilibrium at 0 K and oriented with the coordinate axes [1,0,0], [0,1,0] and [0,0,1] (see Fig. 2.1), parameters used in the fitting procedure for these constants are (Cleri and Rosato, 1993): the cohesive energy V_c, the lattice parameter a_0, the elastic constants, and the equilibrium equations.

For a linear elastic material the strain energy density W_0 is given by

$$W_0 = (1/2) C_{\alpha\beta\delta\varphi} \varepsilon_{\alpha\beta} \varepsilon_{\delta\varphi} \ , \tag{2.2}$$

where $C_{\alpha\beta\delta\phi}$ are elastic constants and $\varepsilon_{\alpha\beta}$ components of the infinitesimal strain tensor (the summation on repeated indices is implied). In Voigt's notation the three independent elastic constants for a FCC material are: $\tilde{C}_{11} \sim C_{1111}$, $\tilde{C}_{12} \sim C_{1122}$ and $\tilde{C}_{44} \sim C_{2323}$. With the coordinate axes aligned along [1,0,0], [0,1,0] and [0,0,1] the stress-strain relation is

$$\begin{Bmatrix} \sigma_{11} \\ \sigma_{22} \\ \sigma_{33} \\ \sigma_{12} \\ \sigma_{13} \\ \sigma_{23} \end{Bmatrix} = \begin{bmatrix} \tilde{C}_{11} & \tilde{C}_{12} & \tilde{C}_{12} & 0 & 0 & 0 \\ \tilde{C}_{12} & \tilde{C}_{11} & \tilde{C}_{12} & 0 & 0 & 0 \\ \tilde{C}_{12} & \tilde{C}_{12} & \tilde{C}_{11} & 0 & 0 & 0 \\ 0 & 0 & 0 & \tilde{C}_{44} & 0 & 0 \\ 0 & 0 & 0 & 0 & \tilde{C}_{44} & 0 \\ 0 & 0 & 0 & 0 & 0 & \tilde{C}_{44} \end{bmatrix} \begin{Bmatrix} \varepsilon_{11} \\ \varepsilon_{22} \\ \varepsilon_{33} \\ \varepsilon_{12} \\ \varepsilon_{13} \\ \varepsilon_{23} \end{Bmatrix} \tag{2.3}$$

Equations satisfied to find constants in the TB potential are summarized below:

(i). Cohesive energy for atom i: $V^{(i)} = V_c$.

(ii). First neighbor distance r_0 : $r_0 = a_0 / \sqrt{2}$

(iii). The equilibrium conditions:

$$f_\alpha^{(i)}\Big|_e = \sum_{\substack{j \neq i \\ j=1}}^{N} - \frac{\partial V^{(i)}}{\partial r_\alpha^{(ij)}}\Bigg|_e = 0 \ , \alpha = 1,2,3.$$

Here $f_\alpha^{(i)}$ is the component of the total force on atom i along the X_α-coordinate axis and $r_\alpha^{(ij)}$ the component along the X_α-coordinate axis of the position vector between atoms i and j. The subscript e signifies that the quantity is evaluated in the equilibrium configuration.

(iv). The elastic constants:

$\Omega_0^{(i)}$ is the volume assigned to atom *i* in the equilibrium configuration.

Values of material parameters for gold (Au) derived from the fitting procedure are (Cleri and Rosato, 1993):

M = 0.2061 eV, ζ = 1.7900 eV, $\tilde{P}$ = 10.2290, D = 4.0360, r_0 = 2.8850 Å.

Experimental values of elastic constants used in the computation of parameters in the TB potential are summarized in Table 2.1. In the last column the experimental value and the prediction from the TB of the bulk modulus ($B = \left(\tilde{C}_{11} + 2\tilde{C}_{12}\right)/3$) are also included.

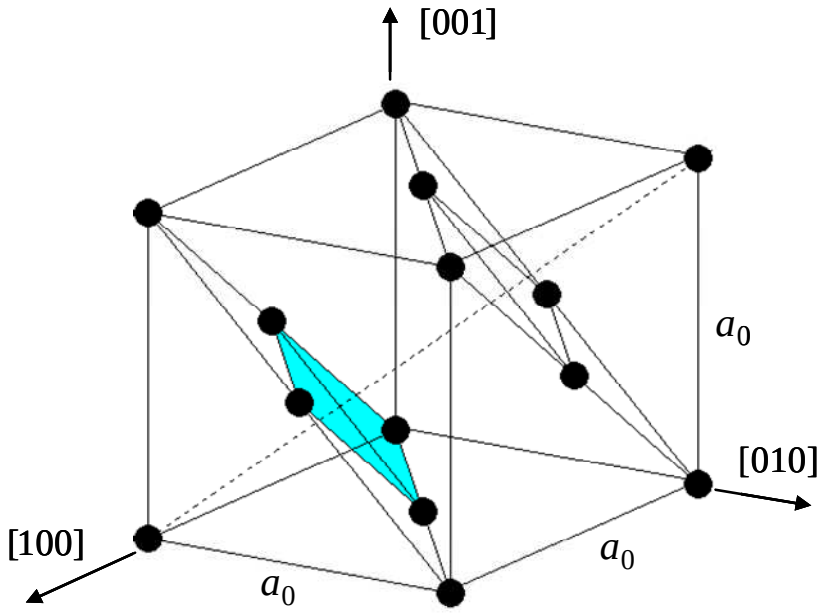

Fig. 2.1. Schematic sketch of the equilibrium configuration of a FCC unit cell.

Table 2.1: Experimental values of quantities used to determine constants for the TB potential: the cohesive energy (V_c), the lattice parameter (a_0) and the elastic constants ($\tilde{C}_{11}, \tilde{C}_{12}, \tilde{C}_{44}$). The experimental value of the bulk modulus (B) and that predicted from the TB potential are also included (Cleri and Rosato, 1993).

	$-V_c$ (eV)	a_0 (Å)	$\tilde{C}_{11}$ (GPa)	$\tilde{C}_{12}$ (GPa)	$\tilde{C}_{44}$ (GPa)	B (GPa)
Experiments	3.779	4.079	187	155	45	165
TB potential	-	-	187	154	45	166

The TB potential has been successfully used to characterize the mechanical behavior of Au nanowires (Ju et al., 2004; Lee et al., 2006, Lin et al., 2005). Pu et al. (2007) used three semiempirical potentials, namely, Vorter and Chen's (1987) EAM potential, the glue model potential of Ercolessi et al. (1988), and the TB potential. They compared results of MD simulations for a tension test on an Au cluster composed of 256 atoms using the glue model potential, the TB potential, and the EAM potential. The accuracy of a potential was determined by comparing predictions of the potential energy in the relaxed configuration and of the ultimate force at the breaking point with results obtained by using the density functional theory (DFT), which were taken as the reference values. The force at the breaking point for an atomic chain of Au atoms was found experimentally by Rubio-Bollinger et al. (2001) to be 1.5 ± 0.3 nN. Predictions from the TB potential were found to agree well with the DFT results and the experimental data. The EAM and the glue model potentials overestimated the value of the potential energy of the systems in the initial configuration (no external load applied) and also showed an initial shape of the specimen not in agreement with the DFT calculations. It was concluded that these two potentials are not adequate to describe the energetics of systems with a large number of under-coordinated atoms.

Since $V^{(i)}$ given by Eq. (2.1) is essentially zero for $r^{(ij)} > 5.5$Å , the summation in Eq. (2.1) is carried out for those values of j for which $r^{(ij)} < 6$Å to reduce the computational cost. Thus, only

atoms lying within a distance of 6Å from atom *i* contribute to the potential energy of atom *i*. We note that the TB potential and its first derivatives are continuous at the cut off radius of 6Å within the accuracy of the computing machine.

An often used interatomic potential in the MM/MD literature is the EAM. The functional form of the EAM potential (Baskes and Daw, 1984; Voter and Chen, 1987) is

$$V^{(i)} = \sum_{\substack{j=1 \\ j\neq i}}^{N} \left[\tilde{F}\left(\tilde{\rho}\left(r^{(ij)}\right)\right) + \frac{1}{2}\tilde{\Phi}\left(r^{(ij)}\right) \right] \tag{2.4}$$

In Eq. (2.4) $\tilde{F}$ is the embedding energy of atom *i*, $\tilde{\rho}$ describes contributions to the electron density of atom *i* due to atom *j*, and $\tilde{\Phi}$ is a pairwise potential describing interactions among neighboring atoms.

The potential energy *V* of a system of atoms equals the sum of the energy $V^{(i)}$ of all atoms in the system. That is

$$V = \sum_{i=1}^{N} V^{(i)} \tag{2.5}$$

The interaction force vector $\boldsymbol{f}^{(ij)}$ between atoms *i* and *j* equals the negative of the gradient of the potential energy with respect to components of the relative position vector $\boldsymbol{r}^{(ij)}$, or

$$f_{\alpha}^{(ij)} = -\left(\frac{\partial V^{(i)}}{\partial r^{(ij)}} + \frac{\partial V^{(j)}}{\partial r^{(ji)}} \right) \frac{r_{\alpha}^{(ij)}}{r^{(ij)}}. \tag{2.6}$$

Here and below, the index α ranges from 1 to 3, and $f_{\alpha}^{(ij)}$ equals the component of $\boldsymbol{f}^{(ij)}$ along the x_{α}-coordinate direction of a rectangular Cartesian coordinate system.

2.2 The atomic stress tensor

There have been several efforts to identify continuum quantities such as stresses and strains in atomistic simulations (Tsai, 1979; Hardy, 1981; Lusko, 1988; Zhou, 2003; Ogata et al., 2004; Shen and Atluri, 2004; Delph, 2005; Heinz, 2007; Gullet et al., 2008; Zimmerman et al., 2009). Starting from statistical mechanics principles, quantities such as temperature, velocity,

displacement, pressure, interatomic forces and internal energy have been used to describe a system of particles (atoms). Concepts like temperature, kinetic energy, interatomic force, moment of inertia, pressure and linear momentum were integrated by Clausius (1870) into a quantity known as the virial (from the Latin word *vis* meaning energy, force). The virial is a starting point for defining the virial stress tensor which will be related in the following paragraphs with the volume average of the Cauchy stress tensor.

For a system comprised of *N* atoms at 0 K, the average values $\bar{\sigma}_{\alpha\beta}$ of components of the Cauchy stress tensor can be computed by using the relation

$$\bar{\sigma}_{\alpha\beta} = \frac{1}{2\Omega^T} \sum_{i=1}^{N} \sum_{\substack{j=1 \\ j \neq i}}^{N} f_{\alpha}^{(ij)} r_{\beta}^{(ij)} \quad , \tag{2.7}$$

where Ω^T equals the volume occupied by the system.

The virial stress tensor was adopted as an extension of the concept of pressure tensor given in statistical mechanics. The general expression for the absolute pressure *p* for a group of *N* particles interacting with each other under a potential *V*, having average kinetic energy $\langle E_k \rangle_\tau$ and contained in a vessel of volume Ω^T is given by (Heinz, 2007)

$$p = -\frac{1}{3\Omega^T} \left\langle \sum_{k=1}^{N} \sum_{\substack{j=1 \\ j<k}}^{N} \frac{\partial V}{\partial r^{(kj)}} r^{(kj)} \right\rangle_\tau + \frac{2}{3\Omega^T} \langle E_k \rangle_\tau \quad , \tag{2.8}$$

where $\langle\ \rangle_\tau$ indicates the average value of a quantity over a period of time τ. For an ideal gas in which there is no interaction among particles except for perfect elastic collisions, the term corresponding to the internal energy *V* vanishes and the final result is the relation between the pressure in the system and the average kinetic energy $\langle E_k \rangle_\tau$ over a time period τ.

The first term on the right hand side of Eq. (2.8), containing the derivative of the internal energy with respect to the relative distance between particles, is known as the internal virial. Eq. (2.8) can be rearranged as the averaged value of the internal virial and twice the kinetic energy:

$$p = \frac{1}{3\Omega^T}\left\langle -\sum_{k=1}^{N}\sum_{\substack{j=1 \\ j<k}}^{N}\frac{\partial V}{\partial r^{(kj)}}r^{(kj)} + \sum_{k=1}^{N} m^{(k)}\boldsymbol{v}^{(k)}\cdot\boldsymbol{v}^{(k)}\right\rangle_{\tau} , \tag{2.9}$$

where $m^{(k)}$ and $\boldsymbol{v}^{(k)}$ are the mass and the velocity vector of atom k respectively. The negative of this quantity, $-p$, is the pressure that the system exerts on walls of the container. The pressure of the system of particles is also defined as one-third of the trace of the average pressure tensor $\boldsymbol{\Pi}$:

$$p = \frac{1}{3}\text{trace}(\Pi), \tag{2.10}$$

where

$$\Pi_{\alpha\beta} = \frac{1}{\Omega^T}\left\langle \sum_{k=1}^{N} f_{\alpha}^{(k)} r_{\beta}^{(k)} + \sum_{k=1}^{N} m^{(k)} v_{\alpha}^{(k)} v_{\beta}^{(k)} \right\rangle_{\tau} . \tag{2.11}$$

In Eq. (2.11) the internal virial is expressed in terms of internal forces to emphasize the dependence of the pressure tensor on the interatomic interactions. The virial stress tensor $\boldsymbol{\sigma}^*$ is defined as the negative of the average pressure tensor, i.e., $\sigma^*_{\alpha\beta} = -\Pi_{\alpha\beta}$ (Heinz, 2007). Values of components $\bar{\sigma}_{\alpha\beta}$ of the average virial stress tensor are given by

$$\begin{aligned}\sigma^*_{\alpha\beta} &= \frac{1}{\Omega^T}\left\langle -\sum_{k=1}^{N} f_{\alpha}^{(k)} r_{\beta}^{(k)} - \sum_{k=1}^{N} m^{(k)} v_{\alpha}^{(k)} v_{\beta}^{(k)} \right\rangle_{\tau} \\ &= \frac{1}{\Omega^T}\left\langle \frac{1}{2}\sum_{k=1}^{N}\sum_{\substack{j=1 \\ j\neq k}}^{N}\frac{\partial V}{\partial r^{(kj)}}\frac{r_{\alpha}^{(kj)} r_{\beta}^{(kj)}}{r^{(kj)}} - \sum_{k=1}^{N} m^{(k)} v_{\alpha}^{(k)} v_{\beta}^{(k)} \right\rangle_{\tau} .\end{aligned} \tag{2.12}$$

Equation (2.12) gives components of the average virial stress tensor. The local virial stress tensor $\sigma^{*(i)}_{\alpha\beta}$ is given by (Cormier et al., 2001)

$$\sigma^{*(i)}_{\alpha\beta} = \frac{1}{\Omega^{(i)}}\left\langle -m^{(i)} v_{\alpha}^{(i)} v_{\beta}^{(i)} + \frac{1}{2}\sum_{\substack{j=1 \\ j\neq i}}^{N}\frac{\partial V}{\partial r^{(ij)}}\frac{r_{\alpha}^{(ij)} r_{\beta}^{(ij)}}{r^{(ij)}} \right\rangle_{\tau} , \tag{2.13}$$

where $\Omega^{(i)}$ equals the volume of the region associated with atom *i*. It is important to note that the pressure and the stress tensor have two parts, a part which takes into account the internal forces and the other part that contains the linear momentum of the system of particles. The second term on the right hand-side of Eq. (2.12) involving the tensor product between the linear momentum of a particle and its velocity has been questioned by many authors (e.g., Zhou, 2003; Shen and Atluri, 2004). They argue that the linear momentum of particles crossing the surface of a control volume is not related to the Cauchy stress tensor defined in continuum mechanics. This controversy does not affect our results since we study static problems.

Using the local virial stress tensor, and either the hydrodynamic equivalence based on localization functions (Irving and Kirkwood, 1950; Hardy, 1981; Lutsko, 1988; Shen and Atluri, 2004), or the hyperelastic assumption for the material behavior at the atomic scale (Szefer, 2004; Delph, 2005), or the direct computation of the traction vector (Tsai, 1979; Sun et al., 2006), or the principle of virtual work (Zhou, 2003), one can find an approximation of the local Cauchy stress tensor defined at each atomic position. However, these techniques give different values of the local Cauchy stress tensor.

In an attempt to describe continuum quantities in terms of properties of a discrete group of particles, Irving and Kirkwood (1950) introduced the concept of a point function stress. As for the virial stress, this stress tensor has two contributions: a kinetic contribution that comes from the linear momentum transferred per unit time due to the microscopic (atomic) velocities as viewed from a coordinate system moving with the macroscopic (continuum) velocity at a given point $\boldsymbol{R}$ in space; the other term is the contribution of the internal forces to the stress tensor (internal virial). In this process they introduced a localization function $\Psi(\boldsymbol{r})$ to compute continuum quantities at a given point $\boldsymbol{R}$ in the domain as the summation of contributions of each particle to that property. The localization function chosen by Irving and Kirkwood is Dirac's delta function $\delta(\boldsymbol{r})$ with $\boldsymbol{r} = \boldsymbol{r}^{(i)} - \boldsymbol{R}$.

Hardy (1981) has pointed out following difficulties in implementing the expression for the local stress tensor proposed by Irving and Kirkwood (1950): (*i*) the validity of the conservation laws for the equivalent continuum appears to depend on a particular ensemble average, (*ii*) the obtained formula for the configurational part of the stress tensor contains an infinite series that needs to be truncated, and (*iii*) the difficulty in evaluating an expression that contains Dirac's

delta function. Hardy (1981) proposed to replace Dirac's delta function by a localization function Ψ (the units of this function are $1/L^3$) that satisfies following conditions (Root et al., 2003):

(i). $\Psi\left(\boldsymbol{r}^{(i)}-\boldsymbol{R}\right)$ has a global maximum at $\boldsymbol{r}^{(i)}=\boldsymbol{R}$.

(ii). $\Psi\left(\boldsymbol{r}^{(i)}-\boldsymbol{R}\right)\to 0$ as $\left|\boldsymbol{r}^{(i)}-\boldsymbol{R}\right|\to\infty$.

(iii). $\Psi\left(\boldsymbol{r}^{(i)}-\boldsymbol{R}\right)$ is smooth and non-negative.

(iv). $\int_{\Omega}\Psi\left(\boldsymbol{r}^{(i)}-\boldsymbol{R}\right)\mathrm{d}\Omega=1.$

Following Hardy's approach, the linear momentum density $\boldsymbol{p}$ at the position $\boldsymbol{R}$ in a given continuum domain at time t has the form

$$\boldsymbol{p}(\boldsymbol{R},t)=\sum_{i=1}^{N}m^{(i)}\boldsymbol{v}^{(i)}\Psi\left(\boldsymbol{r}^{(i)}-\boldsymbol{R}\right). \tag{2.14}$$

The partial differentiation of both sides of Eq. (2.14) with respect to time gives an equation similar to the balance of linear momentum in continuum mechanics. For quasi-static problems the contribution of inertia forces to the linear momentum equation is neglected. Thus, in the absence of body forces, the equilibrium equation at each material point requires the divergence of the Cauchy stress tensor to be zero. The divergence of the Cauchy stress tensor represents the internal force per unit volume (force density) acting at a material point. Taking into account the total force $\boldsymbol{f}^{(i)}$ on each particle (atom), the following equivalence between the force density in the continuum and the atomic system holds:

$$div\boldsymbol{\sigma}=\frac{\partial}{\partial\boldsymbol{R}}\cdot\boldsymbol{\sigma}=\sum_{i=1}^{N}\boldsymbol{f}^{(i)}\Psi\left(\boldsymbol{r}^{(i)}-\boldsymbol{R}\right). \tag{2.15}$$

Since the internal force on a particle comes from its interaction with other particles, i.e., $\boldsymbol{f}^{(i)}=\sum_{\substack{j=1\\ j\neq i}}^{N}\boldsymbol{f}^{(ij)}$ ($\boldsymbol{f}^{(ij)}$ is the force between particles i and j), and by Newton's third law, $\boldsymbol{f}^{(ij)}=-\boldsymbol{f}^{(ji)}$, Eq. (2.15) can be written as

$$div\boldsymbol{\sigma} = \frac{1}{2}\sum_{i=1}^{N}\sum_{\substack{j=1\\ j\neq i}}^{N} \boldsymbol{f}^{(ij)}\left(\Psi\left(\boldsymbol{r}^{(i)} - \boldsymbol{R}\right) - \Psi\left(\boldsymbol{r}^{(j)} - \boldsymbol{R}\right)\right) . \tag{2.16}$$

The bond function $B^{(ij)}(\boldsymbol{R})$ between two atoms *i* and *j* is defined as (Hardy, 1981)

$$B^{(ij)}(\boldsymbol{R}) \equiv \int_0^1 \Psi\left(\lambda \boldsymbol{r}^{(ij)} + \boldsymbol{r}^{(j)} - \boldsymbol{R}\right) d\lambda \ , \tag{2.17}$$

and represents the fraction of the atomic bond between atoms *i* and *j* that is contained in a representative volume defined around each material point $\boldsymbol{R}$; only properties of particles (atoms) inside this representative volume are utilized to define continuum quantities at $\boldsymbol{R}$. Taking the derivative of $\Psi\left(\lambda \boldsymbol{r}^{(ij)} + \boldsymbol{r}^{(j)} - \boldsymbol{R}\right)$ with respect to λ we get

$$\frac{\partial \Psi\left(\lambda \boldsymbol{r}^{(ij)} + \boldsymbol{r}^{(j)} - \boldsymbol{R}\right)}{\partial \lambda} = -\boldsymbol{r}^{(ij)} . \frac{\partial \Psi\left(\lambda \boldsymbol{r}^{(ij)} + \boldsymbol{r}^{(j)} - \boldsymbol{R}\right)}{\partial \boldsymbol{R}} \ . \tag{2.18}$$

Integrating both sides of Eq. (2.18) with respect to λ from λ = 0 to λ = 1, we get

$$\Psi\left(\boldsymbol{r}^{(i)} - \boldsymbol{R}\right) - \Psi\left(\boldsymbol{r}^{(j)} - \boldsymbol{R}\right) = -\boldsymbol{r}^{(ij)} . \frac{\partial B^{(ij)}(\boldsymbol{R})}{\partial \boldsymbol{R}} \ . \tag{2.19}$$

Substitution from Eq. (2.19) into Eq. (2.16) gives

$$\frac{\partial}{\partial \boldsymbol{R}} \cdot \boldsymbol{\sigma} = -\frac{1}{2}\sum_{i=1}^{N}\sum_{\substack{j=1\\ j\neq i}}^{N} \boldsymbol{f}^{(ij)} \boldsymbol{r}^{(ij)} . \frac{\partial B^{(ij)}(\boldsymbol{R})}{\partial \boldsymbol{R}} . \tag{2.20}$$

The solution of Eq. (2.20) has the general form $\boldsymbol{\sigma} = \boldsymbol{\sigma}^{(p)} + \boldsymbol{\sigma}^{(c)}$, where $\boldsymbol{\sigma}^{(p)}$ is a particular solution and $\boldsymbol{\sigma}^{(c)}$ is a solution of the homogeneous equation $div(\boldsymbol{\sigma}^{(c)}) = 0$. A particular solution of Eq. (2.20) can be derived as follows:

$$\frac{\partial}{\partial \boldsymbol{R}} \cdot \boldsymbol{\sigma}^{(p)} = -\frac{1}{2}\sum_{i=1}^{N}\sum_{\substack{j=1\\ j\neq i}}^{N} \boldsymbol{f}^{(ij)} \boldsymbol{r}^{(ij)} . \frac{\partial B^{(ij)}(\boldsymbol{R})}{\partial \boldsymbol{R}},$$

$$\frac{\partial}{\partial \boldsymbol{R}} \cdot \left(\boldsymbol{\sigma}^{(p)} + \frac{1}{2}\sum_{i=1}^{N}\sum_{\substack{j=1\\ j\neq i}}^{N} \boldsymbol{r}^{(ij)} \otimes \boldsymbol{f}^{(ij)} B^{(ij)}(\boldsymbol{R}) \right) = 0 \ , \tag{2.21}$$

$$\boldsymbol{\sigma}^{(p)} = -\frac{1}{2}\sum_{i=1}^{N}\sum_{\substack{j=1 \\ j\neq i}}^{N} \boldsymbol{r}^{(ij)} \otimes \boldsymbol{f}^{(ij)} B^{(ij)}(\boldsymbol{R}) \tag{2.22}$$

Wajnryb et al. (1995) established the uniqueness of the configurational part of the local stress tensor and concluded that it must satisfy following conditions:

(i). The divergence of the stress tensor must be equal to the internal force per unit volume at every point in the domain (in the dynamic case the internal force includes the inertia force).

(ii). The stress tensor must produce the correct contribution to the equilibrium pressure of the system (see Eq. (2.9)).

(iii). The configurational part of the stress tensor must be symmetric.

(iv). The stress tensor must be a translationally and rotationally invariant function of the position vector $\boldsymbol{R}$ and the atomic position vector $\boldsymbol{r}^{(i)}$.

(v). The stress tensor must be invariant under all permutations of particle indices.

(vi). The stress tensor must be independent of particle interactions such that when particles are linearly arrayed, the direction of the traction vector $\boldsymbol{t}$ shall be parallel to the linear array.

Wajnryb et al. (1995) have proved that for $\boldsymbol{\sigma}^{(c)}$ to satisfy these conditions it must be identically zero, and therefore $\boldsymbol{\sigma} = \boldsymbol{\sigma}^{(p)}$. Thus the Cauchy stress tensor for quasi-static problems is given by

$$\boldsymbol{\sigma} = -\frac{1}{2}\sum_{i=1}^{N}\sum_{\substack{j=1 \\ j\neq i}}^{N} \boldsymbol{r}^{(ij)} \otimes \boldsymbol{f}^{(ij)} B^{(ij)}(\boldsymbol{R}) \ . \tag{2.23}$$

Using Hardy's method Zimmerman et al. (2004) compared the local Cauchy stress tensor with the local virial stress tensor and analyzed the influence of two different localization functions. A system of 3072 copper (Cu) atoms with energetics described by the EAM potential was analyzed under zero external loads and simple tensile deformations. Periodic boundary conditions were applied on all bounding surfaces. The size of the specimen was 8 x 8 x 12 unit cells. Two localization functions were used: a radial step function and a cubic function. The averaging volume $\Omega^{(i)}$ in Eq. (2.13) for each atomic position was taken to be a sphere of radius R_C; different values of R_C were also utilized. It was shown that values of the Cauchy stress computed with the step function decreased to zero as the radius of the averaging volume increased and fluctuations

in the normal stress components were significant for R_C equal to the lattice parameter. However, the amplitude of the fluctuations was effectively suppressed to zero by using the cubic spline function as the localization function. The authors also obtained the oscillatory behavior while computing normal stresses near free surfaces with the local expression of the virial stress (Eq. (2.13)). Even though oscillations are present while computing stresses near free surfaces Hardy's approach reduces the wave length of the oscillations and keeps the mean value of the normal stress close to zero. The authors stated that there is a lower limit for the spatial resolution when trying to validate the equivalence between a group of atoms and a continuum, and this connection cannot be made for a very small atomic system. When the representative volume increases, i.e., when more particles are used to compute properties at a given material point, components of the Cauchy stress tensor computed by Hardy's method converge to the average values given by Eq. (2.12) for every choice of the localization function.

Webb et al. (2008) have computed the stress field around an edge dislocation embedded in an elastic material. The EAM potential for aluminum was used in MM simulations of the edge dislocation in a cylindrical specimen. The radius of the cylinder was set to 40 nm and its length to 4 nm. Displacement boundary conditions consistent with this type of imperfection in an anisotropic crystal were prescribed on the lateral surface of the cylinder while periodic boundary conditions were enforced along the cylinder axis. The specimen was oriented with the {0,0,1} family of crystalline planes parallel to the coordinate planes such that the Y-axis was parallel to the cylinder axis and the X-axis parallel to Burger's vector. The stress tensor at each atom was computed by defining a representative cylindrical volume. The σ_{xx} distribution was obtained by using Eq. (2.23) with radial step functions and results compared with analytical solutions from the linear elasticity theory. The two distributions of σ_{xx} agreed well with each other at points far from the core of the imperfection. Close to the core, the solution from the linear elasticity theory diverges while stress components computed from the MM simulation results converged to zero.

2.3 The atomic deformation gradient

We recall that the interaction among atoms is defined by the interatomic potential that depends on interatomic distances. By assuming continuity of the displacement field, one can estimate a

mapping of the initial relative position vector $\boldsymbol{R}^{(ij)}$ between atoms *i* and *j* to the final relative position vector $\boldsymbol{r}^{(ij)}$ by using the atomic deformation gradient $\boldsymbol{F}^{(i)}$ as

$$r_\alpha^{(ij)} \approx F_{\alpha\beta}^{(i)} R_\beta^{(ij)} \ . \tag{2.24}$$

Eq. (2.24) states the Cauchy-Born rule. The continuity assumption implies that the displacement and other properties can be described by continuous functions. Here and below a repeated Greek index implies summation over the range (1, 2, 3) of the index. One can find an approximate value of $\boldsymbol{F}^{(i)}$ by using the Least Squares Method (LSM), i.e., by minimizing the residual *ER* defined by

$$ER = \sum_{j=1}^{Nc} \left| F_{\alpha\beta}^{(i)} R_\beta^{(ij)} - r_\alpha^{(ij)} \right|^2 \ , \tag{2.25}$$

where *Nc* is the number of atoms whose distance from atom *i* is less than or equal to the cut-off radius of 6 Å. Equations for components of the deformation gradient $\boldsymbol{F}^{(i)}$ are obtained by equating the partial derivatives of *ER* with respect of $\boldsymbol{F}^{(i)}$ to zero. That is

$$\frac{\delta ER}{\delta F_{\alpha\beta}^{(i)}} = 2 \left(F_{\alpha\phi}^{(i)} \sum_{\substack{j=1 \\ j\neq i}}^{Nc} \left(R_\beta^{(ij)} R_\phi^{(ij)} \right) - \sum_{\substack{j=1 \\ j\neq i}}^{Nc} \left(r_\alpha^{(ij)} R_\beta^{(ij)} \right) \right) = 0. \tag{2.26}$$

Thus

$$F_{\alpha\phi}^{(i)} = \left(\sum_{\substack{j=1 \\ j\neq i}}^{Nc} \left(R_\beta^{(ij)} R_\phi^{(ij)} \right) \right)^{-1} \left(\sum_{\substack{j=1 \\ j\neq 1}}^{Nc} \left(r_\alpha^{(ij)} R_\beta^{(ij)} \right) \right). \tag{2.27}$$

Zimmerman et al. (2009) have used Eq. (2.27) to analyze deformations of a one dimensional (1D) atom chain, a biaxially stretched film, and the nanoindentation of a layer of a FCC metal. They also computed *curl*($\boldsymbol{F}^{(i)}$). For a continuously differentiable displacement field, the *curl*($\boldsymbol{F}^{(i)}$) should vanish everywhere. For the three problems studied, the *curl*($\boldsymbol{F}^{(i)}$) vanished everywhere except in zones of highly inhomogeneous deformations.

The second order partial derivatives $\boldsymbol{G}^{(i)}$ estimated by

$$r_{\alpha}^{(ij)} \approx F_{\alpha\beta}^{(i)} R_{\beta}^{(ij)} + \frac{1}{2} G_{\alpha\beta\phi}^{(i)} R_{\beta}^{(ij)} R_{\phi}^{(ij)} \tag{2.28}$$

have also been considered for the description of the deformation field. These can be computed by minimizing the residual defined by the difference between the left and the right hand sides of Eq. (2.28).

Hartley and Mishin (2005) computed the local deformation gradient by employing the LSM and the Cauchy-Born rule, and used contour plots of components of the Nye tensor (or *curl*($\boldsymbol{F}^{(i)}$)) to identify screw and edge dislocations in a system of copper atoms. Since the integration of the Nye tensor over an area enclosed by a closed circuit equals Burger's vector, Hartley and Mishin (2005) asserted that this technique identifies well dislocations.

In the next chapter the MSPH method will be introduced to compute first and higher order gradients of the displacement field. It will also be explained how approximations of the deformation gradient can be used to find local and averaged strain measures.

Chapter 3

MM simulations and determination of macroscopic variables

3.1 Molecular mechanics simulations

The MM simulations address homothermal static deformations at 0 K of an atomic system. We start the numerical simulation by assigning the initial position vector $\boldsymbol{X_I^{(i)}}$ of each atom in the system in a perfect lattice configuration (cf. Fig. 3.1). Without applying any external force, each atom is allowed to move freely till the potential energy of the system has reached a local minimum by using the conjugate gradient (CG) with warranted descent technique of Hager and Zhang (2005). The minimization procedure is stopped when the magnitude of each component of the gradient of the internal energy at every atom in the system equals at most $1x10^{-8}$ eV/Å (this value is very small as compared to the interatomic force between an atom and its nearest neighbor). The position vector of an atom in this relaxed configuration is denoted by $\boldsymbol{X_R^{(i)}}$, and this configuration is taken as the reference configuration. This is similar to annealing a specimen before conducting a mechanical test. However, for a nanosize structure, this relaxation process may induce residual stresses whereas the annealing process is designed to eliminate them. Moreover the annealing process involves raising the system's temperature to the re-crystalization temperature which is not intended in the present work.

For three cubic specimens of gold oriented with crystallographic planes of the {1,0,0} family and different number of atoms, Fig. 3.2 shows the variation with the number of iterations in the CG method of the total energy fraction for the relaxation process. The energy fraction equals the ratio of the total potential energy V_{ls} in the current iteration to that (V_I) in the initial configuration. The general trend is that as the size of the sample increases the total potential energy fraction decreases. For the specimen with 3480 atoms the total potential energy in the relaxed configuration differs by ~ 0.37% from that in the initial configuration. Fig. 3.3 shows the variation with the number of iterations of the max-norm of the gradient of the total potential energy during the relaxation process. A vanishing norm of the gradient of the total potential

energy is an indication that all particles (atoms) in the specimen have reached a local equilibrium position. The rate at which the norm of the gradient of the potential energy decreases depends on the number of particles in the system; the larger the size of the specimen the greater the number of iterations needed to reach a local equilibrium.

Subsequently, after each increment in the prescribed displacements of atoms on the bounding surfaces of the body, the total potential energy is locally minimized, i.e., the system is allowed to locally equilibrate after every load step. The change in the potential energy of the system from that in the reference configuration equals the strain energy required to deform the body or the system of atoms. The process is continued till atoms on the bounding surface have been displaced by the prescribed amount. The procedure is summarized in Fig. 3.4.

In problems studied here, either an atom on a bounding surface has a displacement component prescribed or the corresponding traction component is null in the sense that the corresponding component of the external force applied at that atom is zero.

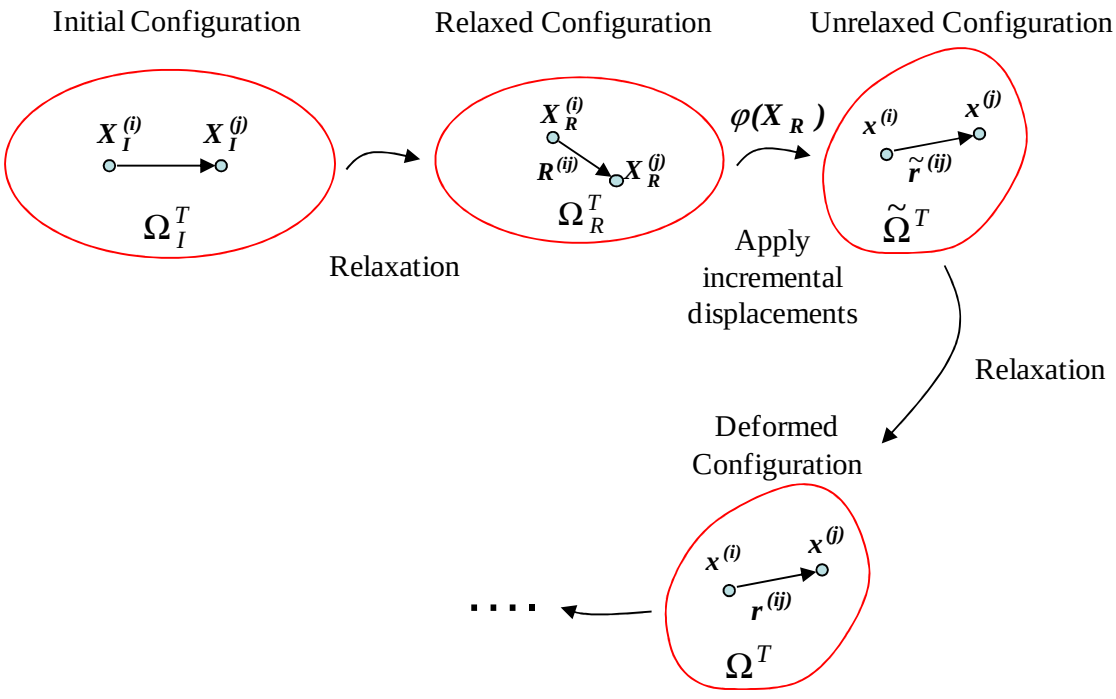

Fig. 3.1. Schematics of the initial, the relaxed (reference), the unrelaxed deformed, and the current (deformed) configurations of an atomic system.

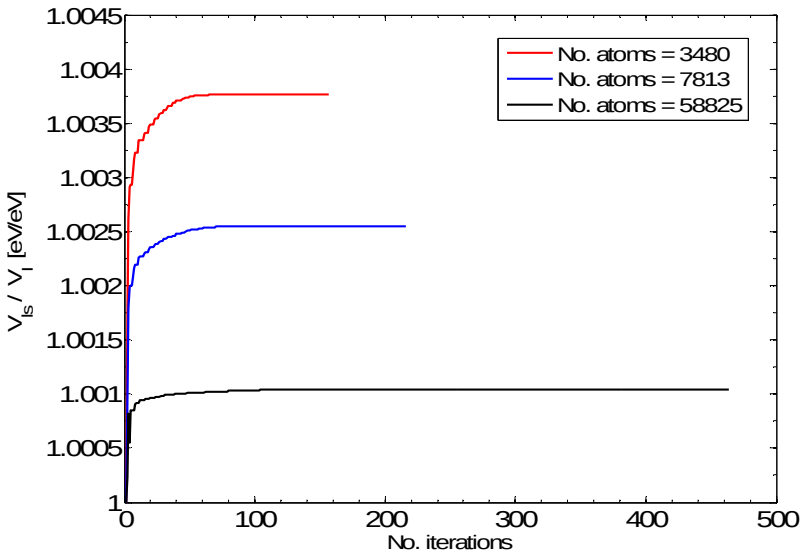

Fig. 3.2. For the minimization of the total potential energy with the CG method and for three cubic samples of different sizes, variation with the number of iterations of the ratio of the total potential energy V_{ls} in the current iteration to the total potential energy V_I in the initial configuration.

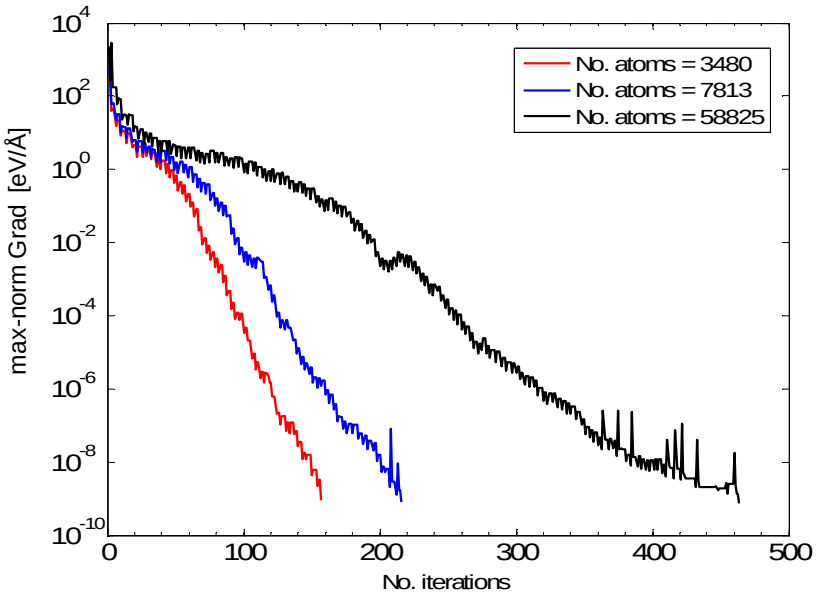

Fig. 3.3. For the minimization of the total potential energy with the CG method, variation with the number of iterations of the max-norm of the gradient of the total potential energy of three cubic samples of different sizes.

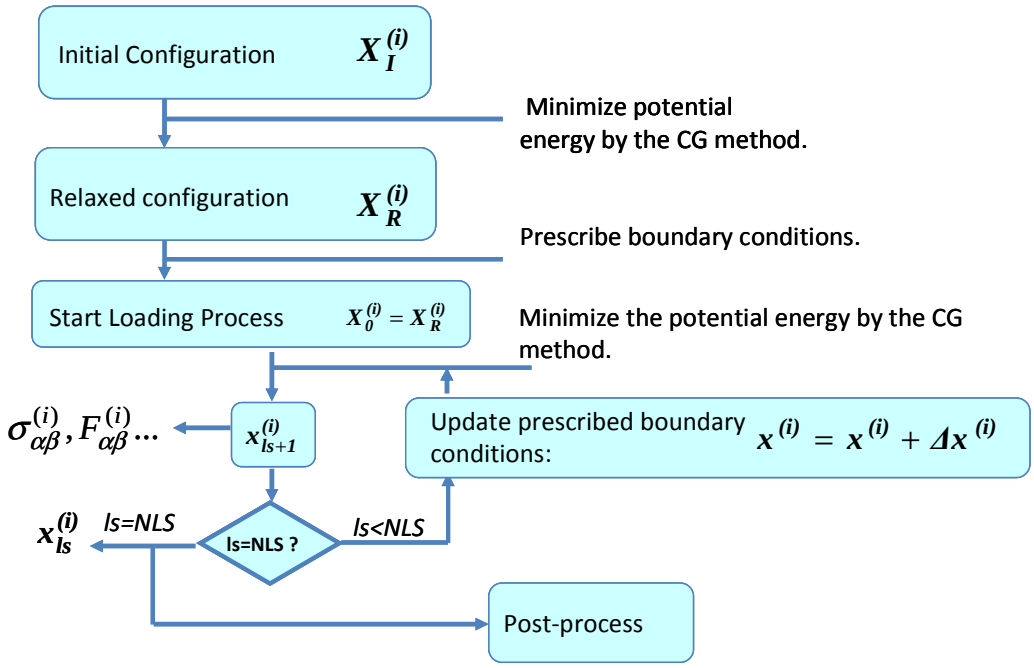

Fig. 3.4. Schematics of the numerical procedure in MM simulations. NLS and ls stand for the predefined total number of load steps and the current load step number, respectively.

3.2 Determination of Macroscopic Variables

3.2.1 Strains

Mott et al. (1992) studied 3D deformations of an atomic system, and interpolated displacements using continuous piecewise-linear basis functions defined on a Delaunay tessellation of the atomic positions. Falk (1999) used the finite-difference method to compute infinitesimal strains using relative displacements between two neighboring atoms. Zimmerman et al. (2009) used Eq. (2.27) to find displacement gradients from positions of atoms in the current and the reference configurations.

We employ the modified smoothed particle hydrodynamics (MSPH) method (Zhang and Batra, 2004) to compute the spatial distribution of the deformation gradient $\boldsymbol{F}$ and the second-order partial derivatives $\boldsymbol{G}$ of displacements from positions of atoms in the current and the reference configurations. The MSPH method offers the advantage of giving a good approximation of a

function and its derivatives without relying on a mesh or any other geometrical construction. As will be explained below, the accuracy of the approximation can also be improved.

The Cauchy-Born rule (Stakgold, 1950; Born and Huang, 1954; Ericksen, 2008, and references cited therein) states that for a crystal with a simple Bravais lattice, relative position vectors $\boldsymbol{r}^{(ij)}$ and $\boldsymbol{R}^{(ij)}$ between atoms i and j in the current and the reference configurations are related by $\boldsymbol{r}^{(ij)} \approx \boldsymbol{F}^{(i)} \boldsymbol{R}^{(ij)}$, where $\boldsymbol{F}^{(i)}$ is the deformation gradient at the position of atom i in the reference configuration. To partially account for nonlocal interactions in continuum mechanics, Kouznetsova et al. (2002) also considered $\boldsymbol{G}$ in the kinematic description of the deformation. We propose to use components of the tensor $\boldsymbol{G}$ to characterize local instabilities in an atomic system.

In the MSPH method a continuously differentiable function $\varphi(\boldsymbol{X})$ (e.g., the position vector component $r_\alpha^{(i)}$) is first expanded in terms of the Taylor series. The three-term Taylor series approximation of $\varphi(\boldsymbol{X})$ at the point $\boldsymbol{\xi}=(\xi_1,\xi_2,\xi_3)$ in the neighborhood of the point $\boldsymbol{X}=\boldsymbol{X}^{(i)}=(X_1^{(i)},X_2^{(i)},X_3^{(i)})$ is

$$\varphi(\boldsymbol{\xi}) \approx \varphi\left(\boldsymbol{X}^{(i)}\right) + \frac{\partial \varphi(X^{(i)})}{\partial X_\alpha^{(i)}}\left(\xi_\alpha - X_\alpha^{(i)}\right) + \frac{1}{2}\frac{\partial^2 \varphi(X^{(i)})}{\partial X_\alpha^{(i)} \partial X_\beta^{(i)}}\left(\xi_\alpha - X_\alpha^{(i)}\right)\left(\xi_\beta - X_\beta^{(i)}\right) \tag{3.1}$$

To evaluate the function $\varphi(\boldsymbol{X})$ and its first- and second-order derivatives at the point $\boldsymbol{X}^{(i)}$, we multiply both sides of Eq. (3.1) by a non-negative kernel function $W(|\boldsymbol{X}-\boldsymbol{\xi}|,h)$ with compact support, and by its first- and second-order derivatives, $W_{,\alpha}(|\boldsymbol{X}-\boldsymbol{\xi}|,h)$ and $W_{,\alpha\beta}(|\boldsymbol{X}-\boldsymbol{\xi}|,h)$; here $W_{,\alpha} = \partial W / \partial \xi_\alpha$ and $W_{,\alpha\beta} = \partial^2 W / \partial \xi_\alpha \partial \xi_\beta$, and h is the smoothing length that determines the size of the compact support of the kernel function W. The magnitude of h usually equals three times the atomic spacing. For a 3D problem one needs at least ten atoms within the compact support of $W(|\boldsymbol{X}-\boldsymbol{\xi}|,h)$. We integrate the resulting equations with respect to $\boldsymbol{\xi}$ over the volume Ω_R^T occupied by the system in the reference configuration, employ atomic positions as integration points, and volumes associated with them as the corresponding weights to obtain a set of ten algebraic equations for $\varphi(\boldsymbol{X})$, $\varphi_{,\alpha}(\boldsymbol{X})$ and $\varphi_{,\alpha\beta}(\boldsymbol{X})$. Setting $\varphi(\boldsymbol{X}) = r_\alpha^{(i)}$ gives values of $\boldsymbol{F}$ and $\boldsymbol{G}$ at the point $\boldsymbol{X}^{(i)}$. Unless the function $W(|\boldsymbol{X}-\boldsymbol{\xi}|,h)$ is a constant over its compact support, the influence of displacements of atom j on values of $\boldsymbol{F}$ and $\boldsymbol{G}$ at the point $\boldsymbol{X}^{(i)}$ occupied by atom i depends upon the relative values of $W(|\boldsymbol{X}-\boldsymbol{\xi}|,h)$ at locations of atoms i and j. For a 3D problem, one needs to

solve three systems of ten simultaneous linear algebraic equations to find displacements, $\boldsymbol{F}$ and $\boldsymbol{G}$ at a point.

We use the following cubic spline kernel function

$$W(s)=\frac{1}{\pi h^3}\begin{cases}\left(1-\frac{3}{2}s^2+\frac{3}{4}s^3\right), s\le 1\\ \frac{1}{4}(2-s)^3, 1<s\le 2\\ 0, \text{otherwise}\end{cases}, \tag{3.2}$$

$$s=\frac{|\boldsymbol{X}-\boldsymbol{\xi}|}{h}=\frac{r}{h}\ . \tag{3.3}$$

Other techniques like the LSM or the LSM in conjunction with smoothing functions (Gullett et al., 2008) can also be used to find values of $\boldsymbol{F}^{(i)}$ at the location of atom *i*.

From $\boldsymbol{F}^{(i)}$ at the point $\boldsymbol{x}^{(i)}$, we evaluate there the Almansi-Hamel strain tensor $\boldsymbol{\varepsilon}^{(i)}$ from

$$\varepsilon_{\alpha\beta}^{(i)}=(1/2)\left(\delta_{\alpha\beta}-\left(F^{-1}\right)_{\phi\alpha}^{(i)}\left(F^{-1}\right)_{\phi\beta}^{(i)}\right), \tag{3.4}$$

where $\delta_{\alpha\beta}$ is the Kronecker delta. The volume averaged value, $\bar{\varepsilon}$, of this tensor for the system is defined by

$$\bar{\varepsilon}_{\alpha\beta}=\frac{1}{\Omega^T}\int_{\Omega}\varepsilon_{\alpha\beta}(\boldsymbol{x})d\Omega=\sum_{i=1}^{N}\frac{\Omega^{(i)}}{\Omega^T}\varepsilon_{\alpha\beta}^{(i)}\ , \tag{3.5}$$

where $\Omega^{(i)}$ and Ω^T equal, respectively, the volume assigned to atom *i* and the total volume of the system in the deformed configuration. We set $\Omega^{(i)}$ equal to the Voronoi volume associated with atom *i*. An approximation of the Voronoi volume is given by (e.g., see Lin et al., 2005)

$$\Omega^{(i)}=\frac{4\pi}{3}a_i^3,\quad a_i=k_v\frac{\sum_{\substack{j=1\\ j\neq i}}^{Ne}\left(r^{(ij)}\right)^{-1}}{\sum_{\substack{j=1\\ j\neq i}}^{Ne}\left(r^{(ij)}\right)^{-2}}\ . \tag{3.6}$$

Here N_e equals the number of atoms in the neighborhood of atom *i* for which $r^{(ij)}\le(\sqrt{3}/2)a_0$, a_0 the lattice parameter, and we set the constant k_v = 0.55. This value of k_v was found by computing

the Voronoi volume of an atom at the centroid of the specimen, and equating it to the volume given by Eq. (3.6).

3.2.2 Average stresses

For a continuous body, the average value over volume Ω of the Cauchy stress tensor defined by

$$\bar{\sigma}_{\alpha\beta} = \frac{1}{\Omega}\int_{\Omega} \sigma_{\alpha\beta} d\Omega \ , \tag{3.7}$$

can be written as

$$\begin{aligned} \bar{\sigma}_{\alpha\beta} &= \frac{1}{\Omega}\int_{\Omega} \sigma_{\alpha\varphi}\delta_{\varphi\beta} d\Omega = \frac{1}{\Omega}\int_{\Omega} \sigma_{\alpha\varphi} x_{\beta,\varphi} d\Omega \, , \\ &= \frac{1}{\Omega}\int_{\Omega} \left(\sigma_{\alpha\varphi} x_{\beta}\right)_{,\varphi} d\Omega \ - \frac{1}{\Omega}\int_{\Omega} \sigma_{\alpha\varphi,\varphi} x_{\beta} d\Omega \, , \end{aligned} \tag{3.8}$$

where $x_{\beta,\varphi} = \partial x_{\beta} \big/ \partial x_{\varphi} = \delta_{\beta\varphi}$. Using the divergence theorem on the first term on the right hand side of Eq. (3.8), and the balance of linear momentum with null body forces, we get

$$\begin{aligned} \bar{\sigma}_{\alpha\beta} &= \frac{1}{\Omega}\int_{\partial\Omega} \sigma_{\alpha\varphi} x_{\beta} \hat{n}_{\varphi} dS \, , \\ &= \frac{1}{\Omega}\int_{\partial\Omega} t_{\alpha} x_{\beta} dS \, , \end{aligned} \tag{3.9}$$

where $\hat{\boldsymbol{n}}$ is a unit outward normal to the boundary $\partial\Omega$ of Ω, and $\boldsymbol{t} = \hat{\boldsymbol{n}} \cdot \boldsymbol{\sigma}$ is the surface traction. Thus the average Cauchy stress tensor multiplied by the volume of the region occupied by the body equals the first moment of tractions acting on the bounding surfaces of the body.

For a discrete system, Eq. (3.9) can be written as

$$\bar{\sigma}_{\alpha\beta} = \frac{1}{\Omega^{T}} \sum_{i=1}^{Nb} x_{\beta}^{(i)} f_{\alpha}^{(i)} \, , \tag{3.10}$$

where N_b equals the number of atoms on the bounding surface of the region whose deformations are being studied.

Assuming that the volume assigned to each atom is the same, Eq. (2.7) becomes

$$\bar{\sigma}_{\alpha\beta} = \frac{1}{N}\sum_{i=1}^{N}\frac{1}{2\Omega^{(i)}}\sum_{\substack{j=1\\ j\neq i}}^{N} f_\alpha^{(ij)} r_\beta^{(ij)} = \frac{1}{N}\sum_{i=1}^{N}\omega_{\alpha\beta}^{(i)}, \tag{3.11}$$

where

$$\omega_{\alpha\beta}^{(i)} = \frac{1}{2\Omega^{(i)}}\sum_{\substack{j=1\\ j\neq i}}^{N} f_\alpha^{(ij)} r_\beta^{(ij)}$$

is the dipole force tensor (Potirniche et al., 2006). However, for a finite size specimen, Eq. (3.11) is approximately valid since the volume assigned to an atom on the bounding surface equals ½ of that assigned to an atom in the interior of the body. Also, the volume of an atom at a vertex of the region is taken to equal 1/8 of that for an interior atom.

3.2.3 Local stresses

Eq. (2.23) derived by Hardy for the local Cauchy stress is used here. A spherical averaging volume with radius = $2a_0$ is defined at each atomic position. The cubic spline function defined by Eq. (3.2) is used as the localization function. It was found that for the evaluation of the 1D integral in the bond function a 5-point Gauss quadrature rule was sufficient. Results computed with eight integration points differed from those with five integration points by less than 0.1%.

Chapter 4

Instabilities in shear and simple shear deformations of gold crystals

4.1 Introduction

An important problem in structural analysis is the investigation of the stability and the failure of the structure under external loads. From the macroscopic point of view, a structural element can be considered to have failed when stresses or strains at a material point have just reached the level to make its deformation inelastic and the material point cannot return to its original state upon complete unloading of the structure. For a general stress or strain distribution, the concept of a yield surface is frequently used to establish the failure condition. The yielding of a material is a process closely related to deformations at the atomic level.

In an atomic system, the onset of an irreversible deformation is termed material instability (Wang et al., 1995; Van Vliet et al., 2003). A stability criterion determines the critical level of strains at which a lattice becomes structurally unstable.

Born (1940) proposed that a perfect crystal is structurally stable under applied mechanical loads if the quadratic form $C_{\alpha\beta}\delta q_\alpha \delta q_\beta$ is always non-negative (convexity condition). Here q_α are generalized strains (e.g., components of the Green-St.Venant strain tensor), $C_{\alpha\beta}$ are strain-dependent elastic moduli ($C_{\alpha\beta} = \partial^2 V / \partial q_\alpha \partial q_\beta$), V is crystal's internal energy, δq_α represents a virtual increment in q_α, and indices α and β range over the number of linearly independent generalized strains. The necessary and sufficient conditions for the convexity of the internal energy V are (Milstein et al., 2005) that all eigenvalues λ_C of the matrix C be positive, i.e.,

$$C_{\alpha\beta}\delta q_\alpha \delta q_\beta > 0 \leftrightarrow \lambda_C > 0. \tag{4.1}$$

Born's criterion has been used extensively to analyze the stability of a perfect crystal. For example, Milstein et al. (2005) used this criterion to analyze the stability of a perfect FCC crystal deformed in uniaxial tension in the [1,1,1] direction. Djohari et al. (2006) have used Born's criterion to analyze the stability of FCC crystals oriented in the [1,1,0] direction and subjected to tensile loading. They found that the ideal crystal remained stable up to the maximum average axial stress on the linear part of the theoretical axial stress-axial strain curve.

Wang et al. (1995) postulated a criterion based on the positive definiteness of an elastic stiffness $\boldsymbol{B}$ that is the sum of the elastic constants tensor $\boldsymbol{C}$ and a fourth rank tensor that depends only on external loads. They assumed that the stability of a homogeneous crystal does not only depend on material properties but also on the applied external loads. They also explained that the stability of a lattice under a given load may be determined by imagining that the lattice undergoes a virtual displacement with internal stresses and applied tractions held constant. If the work done by the applied loads exceeds the increase in the internal energy, then there will be an excess of work done available to cause displacements to grow, and the lattice shall be considered unstable.

Using different approaches, Hill (1962) and Rice (1976) introduced the concept of the acoustic tensor to characterize material stability. Hill (1962) used the acoustic tensor $\Lambda(\boldsymbol{w},\boldsymbol{k}) = \left(C_{\alpha\beta\phi\gamma} w_\alpha w_\phi + \sigma_{\beta\gamma}\right) k_\beta k_\gamma$ to define the stability of a homogeneous medium. Here $\boldsymbol{C}$ is the isothermal elastic moduli, $\boldsymbol{w}$ the polarization vector and $\boldsymbol{k}$ the wave vector. If there is a pair of vectors $\boldsymbol{w}$ and $\boldsymbol{k}$ such that $\Lambda(\boldsymbol{w},\boldsymbol{k})$ is negative, then the medium is unstable since it implies the existence of a negative frequency, i.e., the existence of an elastic wave with continuously increasing amplitude. The stability criterion is summarized as

$$\Lambda_{\min} = \min_{|\boldsymbol{k}|=1,|\boldsymbol{w}|=1} \left(C_{\alpha\beta\phi\gamma} w_\alpha w_\phi + \sigma_{\beta\gamma}\right) k_\beta k_\gamma > 0. \tag{4.2}$$

Following a different reasoning, Rice (1976) stated that when $\Lambda(\boldsymbol{w},\boldsymbol{k})$ is negative then the velocity field is discontinuous across the plane normal to the wave vector $\boldsymbol{k}$. For $\boldsymbol{w}$ parallel to $\boldsymbol{k}$, there will be an instability in the form of a shear band.

The concept of the acoustic tensor has been extended to atomic systems as a criterion for dislocation nucleation. Following Hill (1962), Van Vlient et al. (2003) used the criterion (4.2) for studying the stability of a representative volume composed of a number of discrete particles and termed it the Λ criterion. They postulated that a local instability initiates at the spatial position where Λ vanishes. They performed MD simulations for the cylindrical and the spherical indentation of defect free copper and aluminum films, predicted locations of instabilities and compared them with changes in the coordination number of unstable regions. For the 2D indentation problems with a circular cylindrical indenter and the 3D indentation problems with a spherical indenter, the instability first occurred at locations beneath the contact surface that were not on the axis of the indenter.

Lu and Zhang (2006) have proposed that the atomic acoustic tensor $\boldsymbol{Q}^{(i)}$ defined by

$$Q_{\alpha\beta}^{(i)}(\hat{\boldsymbol{n}}) = \sum_{\substack{j=1 \\ j\neq i}}^{Ne} \sum_{\substack{k=1 \\ k\neq l}}^{Ne} \left(\boldsymbol{r}^{(ij)} \cdot \hat{\boldsymbol{n}}\right) \frac{\partial^2 V^{(i)}}{\partial r_\alpha^{(ij)} \partial r_\beta^{(kl)}} \left(\boldsymbol{r}^{(kl)} \cdot \hat{\boldsymbol{n}}\right) \tag{4.3}$$

be used instead of the Λ criterion to characterize local instabilities. In Eq. (4.3), $\hat{\boldsymbol{n}}$ is an arbitrary unit vector. Thus, an atom is stable in the present position if and only if all eigenvalues of $\boldsymbol{Q}^{(i)}$ there are positive. Equivalently, the position of an atom is unstable if $\det[\boldsymbol{Q}^{(i)}] = 0$. All eigenvalues of $\boldsymbol{Q}^{(i)}$ will be positive if and only if the potential energy $V^{(i)}$ of atom i is a convex function of the relative position vectors between atom i and all other atoms. Lu and Zhang (2006) used this criterion to predict instabilities in carbon nanotubes using MM simulations to analyze their deformations. The authors emphasized that the atomic acoustic tensor is a quantity that does not rely on any continuum concept such us the stress or the tensor of elastic constants making it suitable for the analysis of instabilities in discrete systems.

Steinmann et al. (2007) have used MD simulations to study simple shearing and uniaxial tensile deformations of an FCC crystal oriented with the {1,1,1} plane. They related the local instability with the loss of the ellipticity expressed by the Legendre–Hadamard condition (Truesdell and Noll, 1992). The acoustic tensor $\boldsymbol{Q}$ at a material point of a continuous system is given by

$$Q(\hat{N})_{ik} = L_{iMkK}\hat{N}_M\hat{N}_K, \tag{4.4}$$

where

$$L_{iMkK} = \frac{\partial \overline{P}_{iM}}{\partial F_{kK}}, \tag{4.5}$$

is the elasticity matrix evaluated at the present value of $\boldsymbol{F}$, $\overline{\boldsymbol{P}}$ is the first Piola-Kirchhoff stress tensor, and the unit vector $\hat{\boldsymbol{N}}$ gives the direction of propagation of the disturbance in the reference configuration. An eigenvector of $\boldsymbol{Q}$ is parallel to the disturbance vector. Steinmann et al. (2007) found that the strain at which the determinant of $\boldsymbol{Q}$ vanished coincided with that at which deformations departed from those dictated by the prescribed boundary conditions. The effect of boundary conditions on the bounding surfaces was suppressed by prescribing displacements of atoms near the boundaries so that other atoms in the interior did not interact with under-coordinated atoms (the coordination number is the total number of nearest neighbors of a central atom, and equals 12 for an FCC crystal). For the Au crystal this can be generally satisfied by prescribing displacements of atoms within 6Å of the bounding planes.

Based on the first law of thermodynamics and field equations of dislocation dynamics derived by Acharya (2003), Miller and Acharya (2004) have presented a criterion for homogeneous dislocation nucleation. They deduced an expression for the quantity that is the work conjugate of the dislocation motion and identified – $curl(\boldsymbol{\sigma})$ as the work conjugate of the dislocation nucleation rate. They postulated that the driving force for the nucleation of dislocations with density ρ_d equals $-\boldsymbol{m}\cdot curl(\boldsymbol{\sigma})\cdot\boldsymbol{l}$ where the unit vector $\boldsymbol{m}$ points in the direction of Burger's vector and the unit vector $\boldsymbol{l}$ is perpendicular to the plane containing dislocations. Thus dislocations nucleate if

$$N_{m,l} = \left| m_i e_{rjk} \sigma_{ik,j} l_r \right| \geq N_{crit}, \tag{4.6}$$

where e_{rjk} is the permutation symbol and N_{crit} is a material property. The criterion was tested by performing MM simulations for the 2D indentation of defect-free hexagonal aluminum and nickel lattices, and uniaxial stretching of an aluminum hexagonal lattice containing an initial void. This criterion predicted accurately defects formed in these numerical simulations.

Liu et al. (2007) performed MD simulations of the bending of aluminum strips and analyzed conditions for instabilities to occur with the following three criteria: the critical RSS, Hill's

elastic stability criterion (the Λ criterion), and a stress-gradient based criterion (Miller and Acharya, 2004). Predictions from these criteria were compared with the structure of the nucleated dislocations given by a geometric factor computed using the difference between the relative position vectors in the reference and the current configurations of each atom and its nearest neighbors. In all simulations, slip systems with the largest RSS were not activated. The authors found that the Λ criterion predicted instabilities even in the undeformed configuration. The principal reason for this behavior is that the stress and the elastic moduli C_{ijkl} are defined for a bulk material. For an atomic system, the energy redistribution observed on a free surface is not taken into account. The authors showed the stress-gradient based criterion was able to predict dislocations where the RSS criterion failed. However, the evaluation of gradients of the Cauchy stress tensor near free surfaces may not be accurate. The authors have pointed out that currently there is no accurate criterion for dislocation nucleation from free surfaces.

Recently Miller and Rodney (2008) performed simulations of 2D and 3D indentation problems for FCC crystals. They proposed that the initiation of instability at an atomic position is not necessarily due to deformations in the neighborhood of that point but is the result of deformations at several atoms surrounding the one whose stability is being studied. Furthermore, they showed that a vanishing eigenvalue of the Hessian of the d.o.f. of atoms within a region surrounding an atom implied the nucleation of local instability at the atom.

In the remainder of this chapter we use the TB potential and MM simulations to study shear and simple shear deformations of a system of Au atoms, and use (i) second-order gradients of the displacement field, (ii) the CNP (Tsuzuki et al., 2007), and (iii) eigenvalues of the Hessian of the local potential energy to characterize the onset of local instabilities. We also investigate whether or not these three criteria are met simultaneously at a point. We find the local Hessian of the TB potential by considering the bond energy between an atom and other atoms included in the first shell of neighbors. The first shell of neighbors contains atoms located within one atomic spacing of the atom whose stability is being investigated.

Values of the first- and the second-order displacement gradients are found by using the MSPH method (Zhang and Batra, 2004). Values of the average Cauchy stress tensor are computed by using four definitions of the average stress tensor. Hardy's Eq. (2.23) is used to compute components of the Cauchy stress tensor at each atomic position. The von Mises stress, the maximum shear stress and eigenvalues of the local Cauchy stress tensor are also computed

and their values at unstable atoms compared to their values for atoms in the rest of the specimen. Average stresses and strains for the simple shear deformations are also compared with those deduced by assuming that the Cauchy-Born rule applies till the onset of a global instability and the response of the atomic system is equivalent to that of a hyperelastic body with the strain energy density equal to that given by the TB potential.

4.2 Stress and strain tensors for simple shearing deformations

Consider a system of atoms with a simple Bravais lattice deformed homogeneously by the deformation gradient

$$[F(k_s)]=\begin{bmatrix}1 & k_s & 0\\ 0 & 1 & 0\\ 0 & 0 & 1\end{bmatrix}, \tag{4.7}$$

for which

$$[\varepsilon(k_s)]=\begin{bmatrix}0 & k_s/2 & 0\\ k_s/2 & {k_s}^2/2 & 0\\ 0 & 0 & 0\end{bmatrix}, \tag{4.8}$$

where k_s is a positive constant. Assuming that the overall response of the system of atoms is equivalent to that of a simple hyperelastic material with the strain energy density W_0 defined by

$$W_0(\boldsymbol{F})=\sum_{i=1}^{N}\frac{V^{(i)}}{\Omega_R^{(i)}}, \tag{4.9}$$

where $\Omega_R^{(i)}$ is the volume associated with atom i in the reference configuration and $\sum_{i=1}^{N}\Omega_R^{(i)}=\Omega_R^T$ is the volume occupied by the body in the reference configuration. The first Piola-Kirchhoff stress tensor $\bar{\boldsymbol{P}}$ is given by

$$\bar{\boldsymbol{P}}=\frac{\partial W_0}{\partial \boldsymbol{F}}=\frac{\partial}{\partial \boldsymbol{F}}\left(\sum_{i=1}^{N}\frac{V^{(i)}}{\Omega_R^{(i)}}\right), \tag{4.10}$$

or equivalently by

$$\bar{P}_{\alpha\beta}=\sum_{i=1}^{N}\sum_{\substack{k=1\\k\neq i}}^{N}\frac{1}{\Omega_R^{(i)}}\frac{\partial V^{(i)}}{\partial r^{(ik)}}\frac{\partial r^{(ik)}}{\partial r_\gamma^{(ik)}}\frac{\partial r_\gamma^{(ik)}}{\partial F_{\alpha\beta}}=\sum_{\substack{i,k=1\\i\neq k}}^{N}\frac{1}{\Omega_R^{(i)}}\frac{1}{r^{(ik)}}\frac{\partial V^{(i)}}{\partial r^{(ik)}}r_\alpha^{(ik)}R_\beta^{(ik)}. \tag{4.11}$$

For simple shear deformations, we get

$$\left[\overline{P}(k_s)\right]=\sum_{\substack{i,k=1\\ i\neq k}}^{N}\frac{1}{\Omega_R^{(i)}}\frac{1}{r^{(ik)}}\frac{\partial V^{(i)}}{\partial r^{(ik)}}\left[\Phi^{(ik)}(k_s)\right], \tag{4.12}$$

where

$$\left[\Phi^{(ik)}(k_s)\right]=\begin{bmatrix} R_{xx}^{(ik)}+k_sR_{xy}^{(ik)} & R_{xy}^{(ik)}+k_sR_{yy}^{(ik)} & R_{xz}^{(ik)}+k_sR_{yz}^{(ik)} \\ R_{yx}^{(ik)} & R_{yy}^{(ik)} & R_{yz}^{(ik)} \\ R_{zx}^{(ik)} & R_{zy}^{(ik)} & R_{zz}^{(ik)} \end{bmatrix},$$

$$\left(r^{(ik)}\right)^2=R_\xi^{(ik)}R_\xi^{(ik)}+2k_sR_{xy}^{(ik)}+3k_s{}^2\left(R_y^{(ik)}\right)^2,$$

$R_{xy}^{(ik)}=R_x^{(ik)}R_y^{(ik)}, R_{yy}^{(ik)}=R_y^{(ik)}R_y^{(ik)},\ldots.$ From expression (4.12) of the first Piola-Kirchhoff stress tensor, we obtain the following expression for the Cauchy stress tensor:

$$\left[\overline{\sigma}(k_s)\right]=\sum_{\substack{i,k=1\\ i\neq k}}^{N}\frac{1}{\Omega^{(i)}}\frac{1}{r^{(ik)}}\frac{\partial V^{(i)}}{\partial r^{(ik)}}\left[\Theta^{(ik)}(k_s)\right], \tag{4.13}$$

where

$$\left[\Theta^{(ik)}(k_s)\right]=\begin{bmatrix} R_{xx}^{(ik)}+k_sR_{xy}^{(ik)}+k_s\left(R_{xy}^{(ik)}+k_sR_{yy}^{(ik)}\right) & R_{xy}^{(ik)}+k_sR_{yy}^{(ik)} & R_{xz}^{(ik)}+k_sR_{yz}^{(ik)} \\ R_{yx}^{(ik)}+k_sR_{yy}^{(ik)} & R_{yy}^{(ik)} & R_{yz}^{(ik)} \\ R_{zx}^{(ik)}+k_sR_{zy}^{(ik)} & R_{zy}^{(ik)} & R_{zz}^{(ik)} \end{bmatrix}.$$

Here we have set $\Omega^{(i)}=J\Omega_R^{(i)}=\Omega_R^{(i)}$ since $J=\det[\boldsymbol{F}]=1$. We note that $\boldsymbol{r^{(ij)}}$ and $\partial V^{(i)}/\partial r^{(ik)}$ also depend upon k_s. Thus, one can not characterize the dependence of $\overline{\boldsymbol{\sigma}}$ upon k_s simply from the expression for $\left[\Theta^{(ik)}(k_s)\right]$.

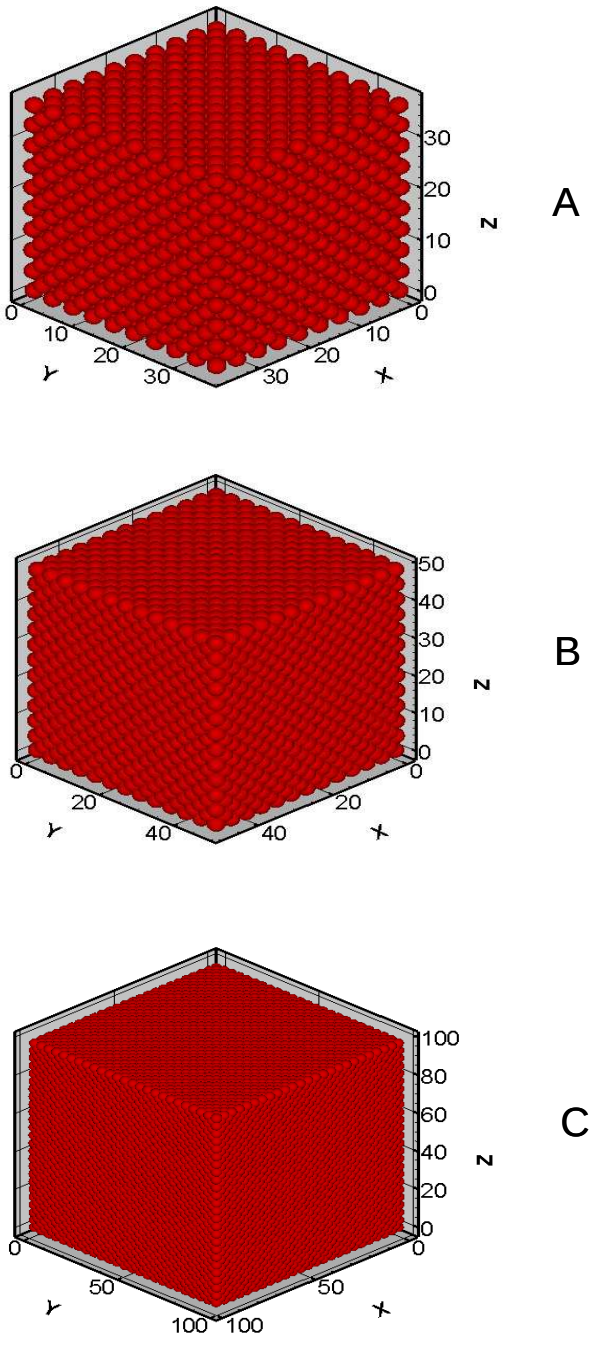

Fig. 4.1. Atomic systems A, B, and C in reference configurations having 3480, 7813 and 58825 atoms, respectively, used to study shear and simple shear deformations (all distances in Å).

4.3 Simulation of deformations

4.3.1 Shear test

We simulate the shear test on cubic Au crystal specimens of three different sizes. The system A with side ~32 Å contains 3480 atoms, the system B with side ~50 Å has 7813 atoms, and the system C with side ~100 Å has 58825 atoms. In each case, atoms are located in planes parallel to the coordinate planes {1,0,0}, {0,1,0} and {0,0,1} as shown in Fig. 4.1. After finding the initial relaxed configuration, atoms on the bottom surface $Y = Y_{min}$ are constrained from moving in all directions. For atoms on the top surface, $Y = Y_{max}$, the Y- and the Z- displacements are prescribed to be zero and the X-displacement is prescribed in increments of 0.0025 Å. The magnitude of the incremental X-displacement was halved if the potential energy of the deformed configuration could not be minimized in a preassigned number of iterations. There are no external surface tractions applied on the remaining four bounding faces. A schematic of the problem being studied is exhibited in Fig. 4.2a in which atoms enclosed in red boxes have prescribed displacements.

4.3.2 Simple shear test

The simulation of the simple shear test (cf. Fig. 4.2b) differs from that of the shear test described above only in boundary conditions prescribed on the bounding surfaces. In this case, the three components of displacement are prescribed on all bounding surfaces so that $x = X + k_s Y, y = Y, z = Z$, where (x, y, z) are coordinates of the atom in the deformed configuration that in the reference configuration was located at (X, Y, Z). Only interior atoms are allowed to move during the minimization of the potential energy of the system. The nondimensional constant $k_s = \tan(\gamma)$ is increased in increments of 0.0025 to induce additional deformations of the body.

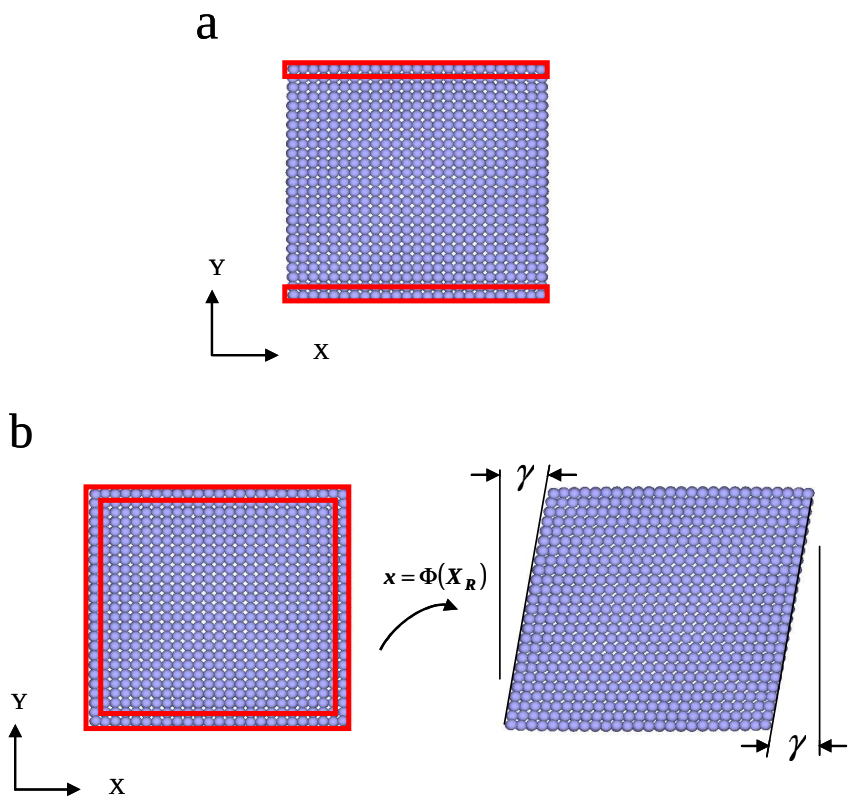

Fig. 4.2. (a) Reference configuration of a gold specimen for the shear test. (b) Reference and deformed configurations of a gold specimen for the simple shear test. Displacements of atoms enclosed in red boxes are prescribed.

4.4 Average stresses and strains from results of numerical simulations.

4.4.1 Shear test

Fig. 4.3 shows the variation with the shear angle γ of the average components of the Cauchy stress tensor defined by Eqs. (2.7) and (3.10). Ideally, the two equations should give the same values of stress components. Results plotted in Fig. 4.3 for the three systems reveal that, in each case, the shear stress σ_{xy} and the normal stress σ_{yy} are dominant, and their values computed from Eqs. (2.7) and (3.10) are nearly equal to each other. Furthermore, the evolution of σ_{yy} with the shear angle γ is qualitatively similar for the three specimens. Recall that the average stress defined by Eq. (3.10) is computed from forces and positions of atoms at the boundaries. In Table

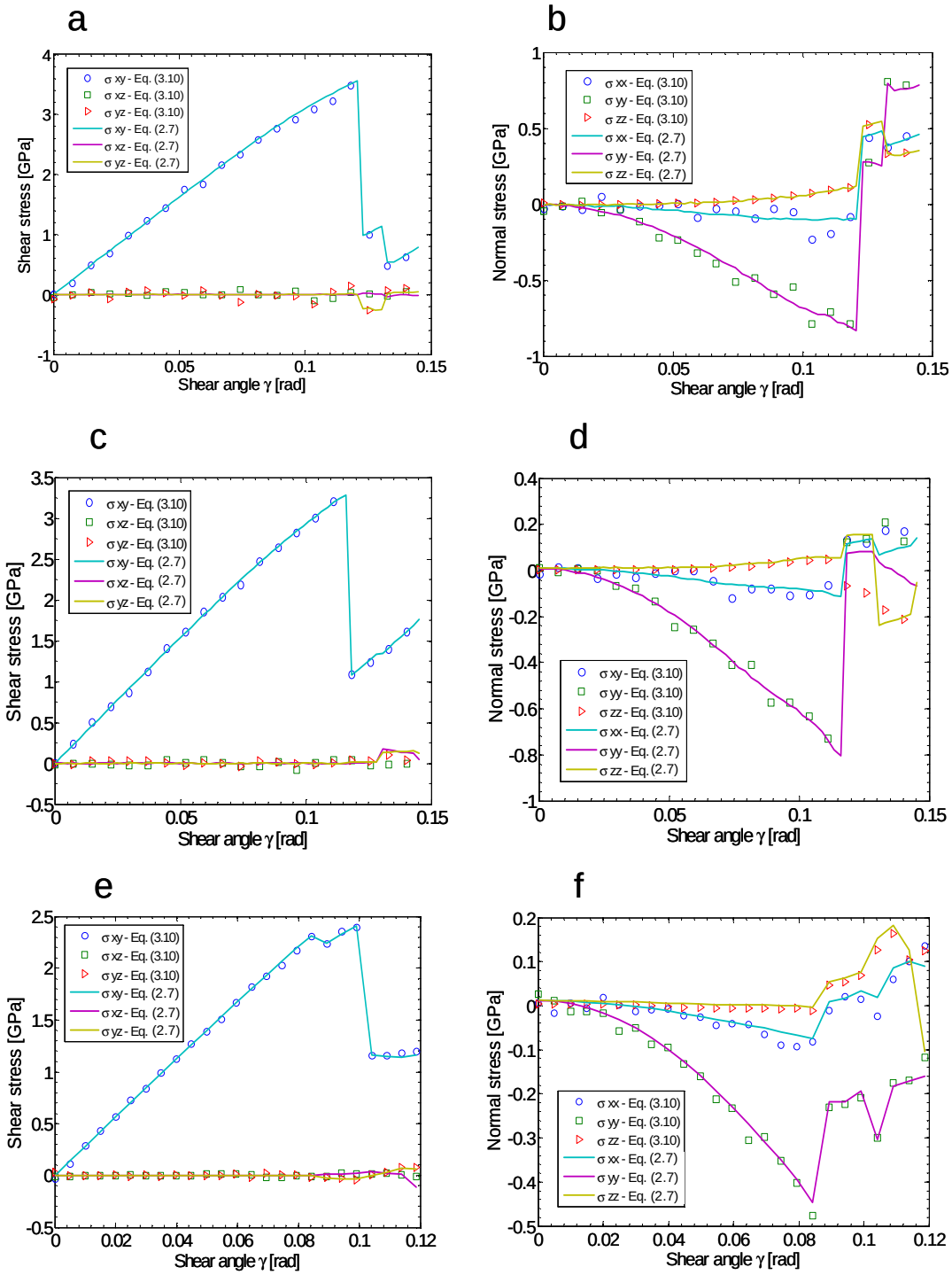

Fig. 4.3. Evolution with the shear angle γ of the average components of the Cauchy stress tensor for the shear test computed from Eqs. (2.7) and (3.10); (a), (c), (e) σ_{xy}, σ_{xz} and σ_{yz} for systems A, B, and C, respectively; (b), (d), (f) σ_{xx}, σ_{yy} and σ_{zz} for systems A, B, and C, respectively.

4.1 we have listed, for the three specimens, values of the maximum shear stress σ_{xy}, the maximum von Mises stress σ_{VM}, σ_{xy} and σ_{VM} at yield, and values of the angle γ at the proportionality limit and at the yield point. We note that the von Mises stress defined as

$$\sigma_{VM} = \frac{1}{\sqrt{2}}\sqrt{(\sigma_{11}-\sigma_{22})^2+(\sigma_{22}-\sigma_{33})^2+(\sigma_{33}-\sigma_{11})^2+6(\sigma_{12}{}^2+\sigma_{13}{}^2+\sigma_{23}{}^2)},$$

is proportional to the second invariant of the Cauchy stress tensor. The yielding of the material is identified by a drop in the shear stress σ_{xy} with an increase in the shear angle γ.The variation of σ_{xy} with γ is linear for $\gamma \leq \gamma_{\text{linear}}$ while values of σ_{xz} and σ_{yz} are negligible as compared to those of σ_{xy} up to $\gamma = \gamma_{\text{yield}}$ where the first discontinuity in the shear stress vs. the shear angle curve appears. The number of atoms in the system being studied affects significantly values of the yield stress and the yield strain. Because of the scale used to plot results it is not easy to delineate γ_{linear} in the stress vs. γ curves. Whereas, values of γ_{linear} for specimens B and C differ by ~ 6%, γ_{yield} for specimen C is nearly 72% of that for specimen B. Similarly, the shear stress at yield and the maximum shear stress for specimen C equal nearly 70% of those for specimen B. The simulation of the shear and the simple shear deformations in larger specimens should give converged values of the yield stress and the maximum shear stress.

We hypothesize that at $\gamma = \gamma_{\text{yield}}$ there is a critical density of unstable atoms so that the local atomic structure changes noticeably, dislocations originate, and the body subsequently deforms plastically. If we adopt Considère's (1888) criterion according to which a system becomes globally unstable at the peak in the load (or equivalently the shear stress for the problem being studied), then the global and the local instabilities initiate at different values of the shear strain as should be evident from results of specimen C summarized in Table 4.1 and depicted in Fig. 4.3e. For this specimen $\gamma_{\text{yield}} = 0.084$, and $\sigma_{xy}^{\max} = 2.408$ GPa occurs at $\gamma = 0.102$. For specimen C there are two discontinuities in the shear stress σ_{xy} vs. γ curve, the first corresponding to the yielding of the material and the second corresponding to the global instability. However, for specimens A and B only one sharp discontinuity in the σ_{xy} vs. γ curve is observed. Thus whether yielding is followed by the global instability or the two occur simultaneously depends upon the number of atoms in the system studied.

Table 4.1: Values of the **s**hear modulus, the maximum shear stress, the shear stress at yield, the von Mises stress, the shear strain at the proportional limit, and the shear strain at yield computed from results of the shear test.

Specimen	γ_{linear} (rad)	γ_{yield} (rad)	σ_{xy}^{yield} (GPa)	σ_{xy}^{max} (GPa)	σ_{VM}^{yield} (GPa)	σ_{VM}^{max} (GPa)	$\tilde{C}_{44}$ (GPa)
A	0.044	0.121	3.562	3.562	6.230	6.230	32.229
B	0.037	0.116	3.285	3.285	5.750	5.740	31.077
C	0.035	0.084	2.315	2.408	4.030	4.180	28.264

Values of the shear modulus $\tilde{C}_{44}$, based on the average shear stress, and obtained by linear regression of the shear stress – the shear angle curve for points up to γ_{linear}, equal 32.23 GPa, 31.08 GPa and 28.26 GPa for systems A, B, and C, respectively. Since $\gamma_{linear} \leq 0.044$, $k_s \approx \gamma$. We note that elastic constants for Au were used to find values of parameters in the TB potential given by Eq. (2.1). Accordingly, we should have obtained $\tilde{C}_{44}$ equal to 45 GPa. The difference in the computed and the ideal value of $\tilde{C}_{44}$ is partly due to changes in lattice parameter at points near bounding surfaces that occur during the relaxation of the initial configuration; cf. Fig. 4.4a. Also in-plane stresses in bounding planes induce stresses in the interior of the specimen.

Only at points close to the centroid of the specimen the lattice parameter *a* equals 4.079 Å, that is, the value for a pristine Au crystal. To eliminate the effect of inhomogeneous deformations of atoms near free surfaces, we compute the value of $\tilde{C}_{44}$ based on the shear stress averaged over a spherical representative volume (SRV) of radius R around specimen's centroid. From results plotted in Fig. 4.4b, it can be observed that for small SRVs computed values of $\tilde{C}_{44}$ are close to that for a pristine crystal. However, with an increase in the value of R, the value of the shear modulus saturates to a value of 28.26 GPa.

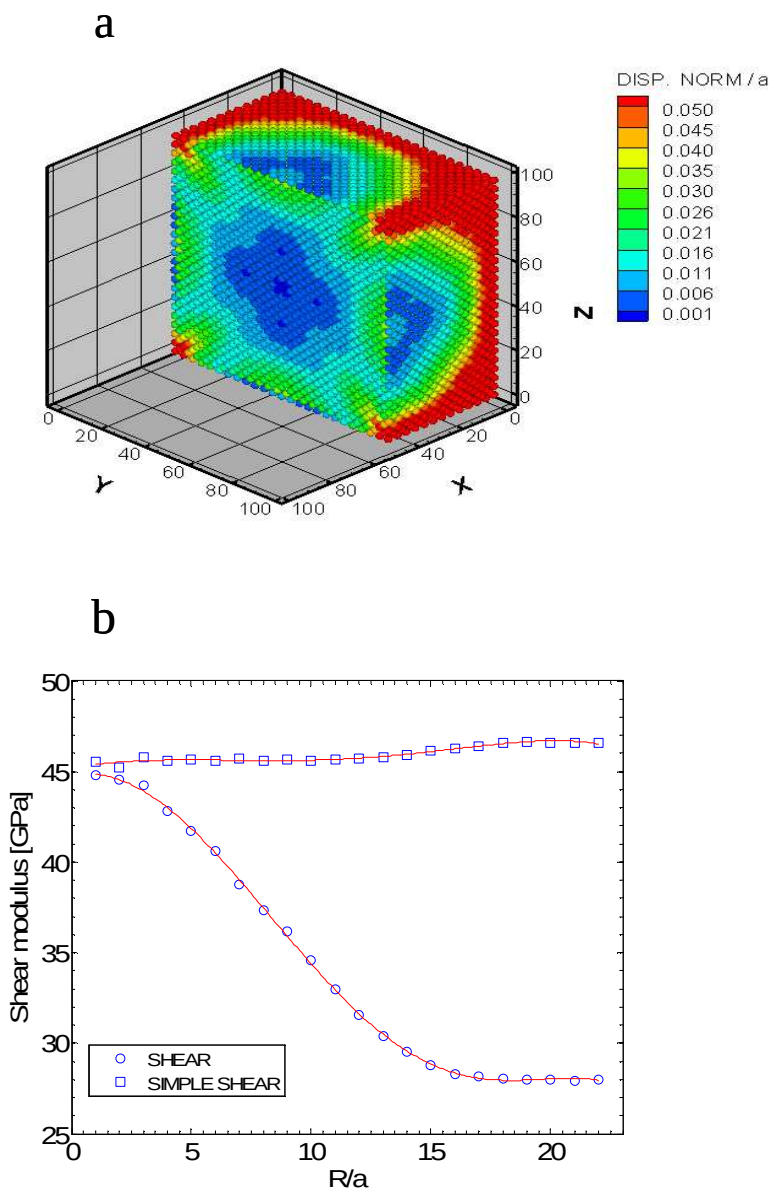

Fig. 4.4. (a) Reference configuration of system C; fringe plots give the magnitude of the normalized displacement vector in going from the perfect lattice configuration to the relaxed configuration. (b) Variation of the shear modulus $\tilde{C}_{44}$ with the radius of the sphere used to define the representative volume around the specimen centroid.

The evolution of the average values of components of the Almansi-Hamel strain tensor with the shear angle γ is plotted in Fig. 4.5. For each one of the three systems, and for $\gamma < \gamma_{yield}$ the variation of the average shear strain component ε_{xy} with γ is linear while values of ε_{xz} and ε_{yz} are negligibly small. The evolution of the average normal strains ε_{yy} and ε_{zz} for the three specimens are essentially similar, but their magnitudes decrease with an increase in the number of atoms in the system studied. The difference in the maximum values of the axial or the normal strains from system A to system C is about 40%. Prior to yielding, ε_{yy} and ε_{zz} are negative but ε_{xx} is positive. For specimen C magnitudes of normal strains are approximately an order of magnitude smaller than that of ε_{xy}. Subsequent to the system becoming globally unstable, stress components exhibit oscillations with an increase in γ; reasons for these oscillations are not obvious.

The evolution with the shear angle γ of stresses and strains plotted in Figs. 4.3 and 4.5 suggests that for a given value of γ, the shear stress σ_{xy} and the shear strain ε_{xy} have higher values than the other two shear stresses and the other two shear strains, respectively. Whereas σ_{xx} and σ_{zz} have negligible values until the discontinuity in the stresses at $\gamma = \gamma_{yield}$ appears, the normal stress σ_{yy} is compressive and its magnitude is about 20% of that of the shear stress σ_{xy}. Thus compressive normal tractions need to be applied to the top and the bottom surfaces. In the absence of these normal tractions, the height of the specimen will increase. It confirms the Poynting effect in nonlinear elasticity (Poynting, 1909).

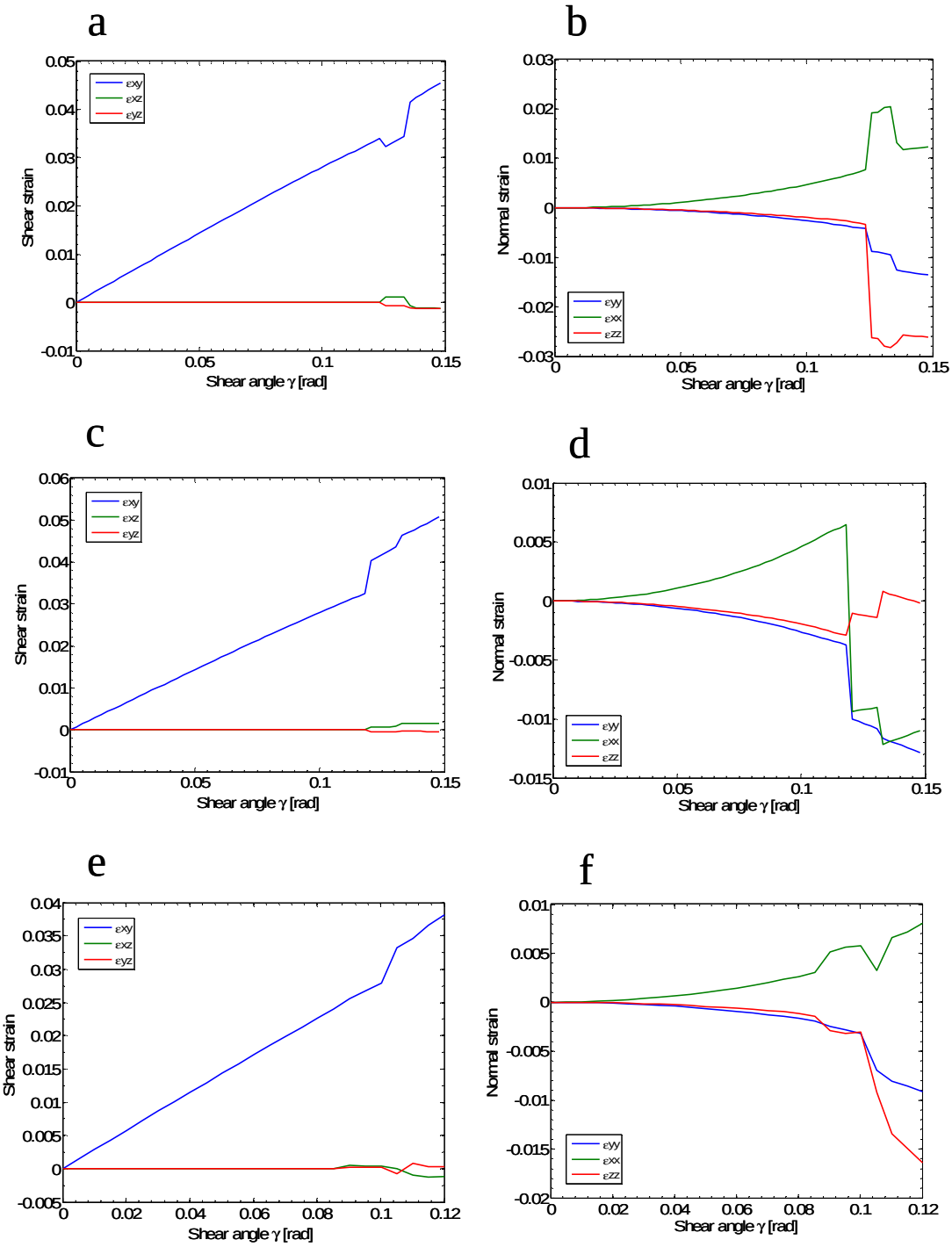

Fig. 4.5. Evolution with the shear angle γ of the average values of components of the Almansi-Hamel strain tensor for the shear test; (a), (c), (e) ε_{xy}, ε_{xz} and ε_{yz} for systems A, B, and C, respectively; (b), (d), (f) ε_{xx}, ε_{yy} and ε_{zz} for systems A, B, and C, respectively.

4.4.2 Simple shear test

Figs. 4.6 and 4.7 depict, respectively, evolutions with the shear angle γ of the average stresses and strains for the three specimens. In Table 4.2 we have summarized for the three specimens values of the shear stress, the von Mises stress, and the shear angle γ at the proportionality limit and at the yield point. Magnitudes of all three compressive normal stresses increase with an increase in γ and are comparable to the magnitude of σ_{xy}. This is because all bounding planes are restricted from moving in normal directions. Thus in the absence of normal tractions applied to the bounding planes, the cube will expand. As for the shear test, the material exhibits the Poynting (1909) effect.

Fig. 4.6 also exhibits average values of the stress components computed from Eqs. (2.7), (3.10) and (4.13); the three sets of values agree with each other until $\gamma = \gamma_{\text{yield}}$. At $\gamma = \gamma_{\text{yield}}$ stress components computed for the equivalent hyperelastic body do not show any sudden drop, and the slope of the σ_{xy} vs. γ curve continues to increase. One may say that the hyperelastic body exhibits a hardening effect in the sense that its tangent modulus continues to increase with an increase in γ. *The close agreement between stresses computed from results of MM simulations and the analytic expression verifies our code, and validates the MM results.* Evolutions of strains plotted in Fig. 4.7 reveal that Eqs. (3.5) and (4.8) give nearly the same values of strain components.

The value of σ_{xy}^{yield} derived from results of the simple shear deformations is nearly four times that from the shear test results. Even for system C with 58825 atoms, the two values of the yield stress differ noticeably. The main difference between the tests is the presence of four free surfaces in the shear deformations and no free surface in the simple shear deformations. For the simple shear test involving displacements prescribed on all bounding surfaces, the onset of local instabilities is delayed, that increases the yield stress.

The slope of the average shear stress σ_{xy} vs. the shear angle γ curve for $\gamma \leq \gamma_{\text{linear}}$ gives values for the shear modulus $\tilde{C}_{44}$ equal to 51.64 GPa, 49.88 GPa and 46.40 GPa for specimens A, B, and C respectively. These values are closer to the 45 GPa than those derived from simulations of the shear test, and converge to this value with an increase in the number of atoms in the system. As shown in Fig. 4.4b, the computed value of $\tilde{C}_{44}$ for SRVs of different radii centered at specimen's centroid is nearly constant and equals 45.5 GPa.

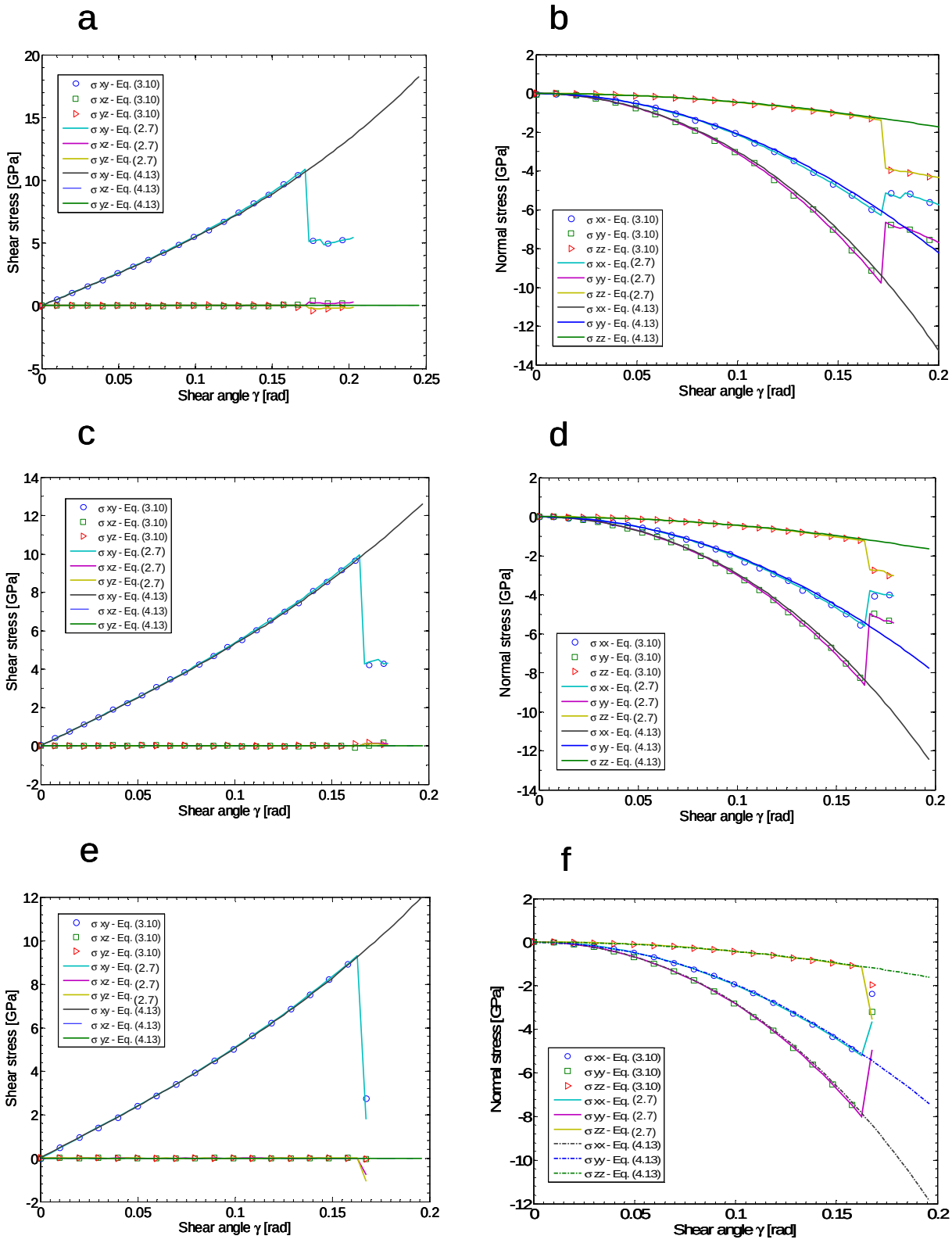

Fig. 4.6. Evolution with the shear angle γ of the average values of components of the Cauchy stress tensor for the simple shear test computed from Eqs. (2.7), (3.10) and (4.13); (a), (c) and (e) σ_{xy}, σ_{xz} and σ_{yz} for systems A, B, and C, respectively; (b), (d) and (f) σ_{xx}, σ_{yy} and σ_{zz} for systems A, B, and C, respectively.

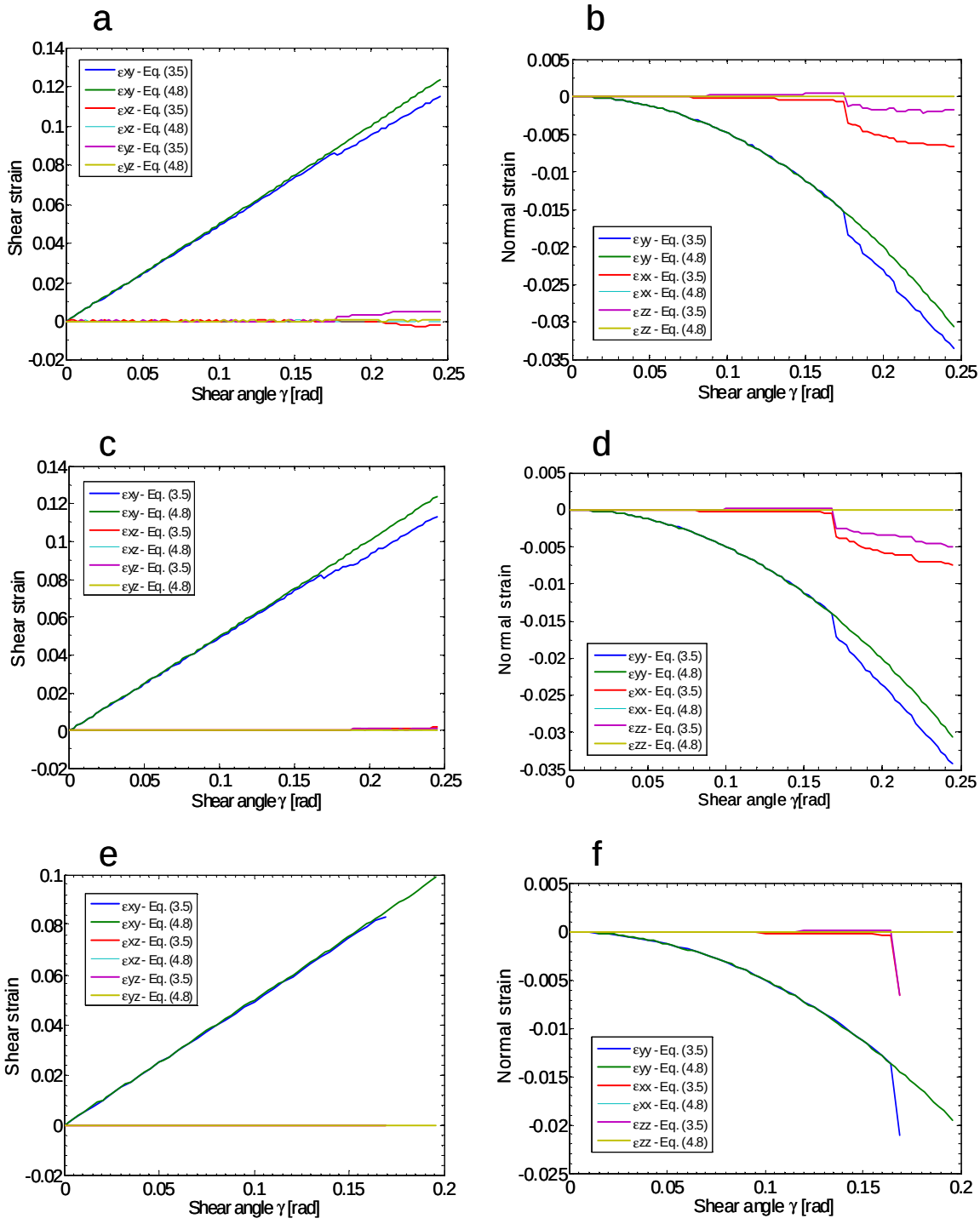

Fig. 4.7. Evolution with the shear angle γ of the average values of components of the Almansi-Hamel strain tensor for the simple shear test computed with Eqs. (3.5) and (4.8); (a), (c) and (e) ε_{xy}, ε_{xz} and ε_{yz} for systems A, B, and C, respectively; (b), (d) and (f) ε_{xx}, ε_{yy} and ε_{zz} for systems A, B, and C, respectively.

Table 4.2: Values of the **s**hear modulus, the maximum shear stress, the shear stress at yield, the von Mises stress, the shear strain at the proportional limit, and the shear strain at yield computed from results of the simple shear test.

Specimen	γ_{linear} (rad)	γ_{yield} (rad)	σ_{xy}^{yield} (GPa)	σ_{xy}^{max} (GPa)	σ_{VM}^{yield} (GPa)	σ_{VM}^{max} (GPa)	$\tilde{C}_{44}$ (GPa)
A	0.050	0.173	10.780	10.780	20.220	20.220	51.644
B	0.043	0.165	9.944	9.944	18.390	18.390	49.883
C	0.040	0.162	9.170	9.170	17.190	17.190	46.401

4.5 Comparison between different measures of the average Cauchy stress tensor

In Fig. 4.8 we have plotted the evolution of the average shear stress σ_{xy} for system B computed with the following four definitions: the configurational part of the virial stress tensor (Eq. (2.7)), the total force acting on atoms at the bounding surfaces (Eq. (3.10)), the average local stress tensor (Eq. (3.11)), and the mechanics of materials approach (the tangential force per unit surface area). It is evident that all these stresses agree with each other. During the computation of average stresses from the virial and the local stress tensors, all atoms in the system, including those with prescribed displacements, were considered. In the limit of very large number of atoms in the system, using only active or all atoms in the computation of stresses should give essentially the same results. We note that the average shear stress computed from the total tangential force acting on the top and the bottom surfaces agrees well with that obtained by using Eqs. (2.7), (3.10) and (3.11).

For both shear and simple shear tests, values of the shear modulus and the yield stress determined with different ways of finding average stresses are summarized in Table 4.3. It is clear that these methods give nearly the same values of the shear modulus and the yield stress. However, their values for the shear and the simple shear tests are different.

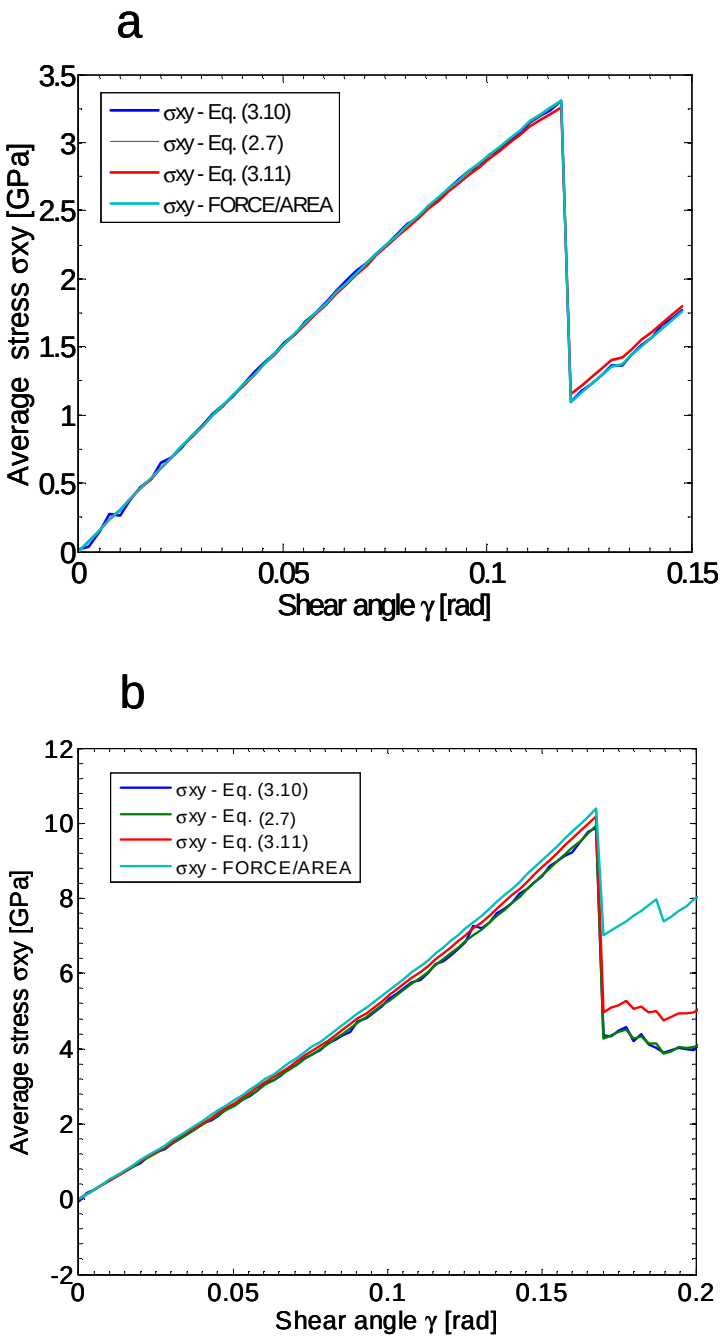

Fig. 4.8. Comparison between different stress measures of the average Cauchy stress tensor for the system B in the shear and the simple shear tests, (Eq. 2.7), (Eq. 3.10), (Eq. 3.11) and the mechanics of materials approach (force/area); (a) shear test, (b) simple shear test.

Table 4.3: Comparison of the shear modulus and the yield stress computed with different averaged stresses for system B.

	Shear		Simple shear	
Method	Shear modulus $\tilde{C}_{44}$ (GPa)	Yield stress σ_{xy}^{yield} (GPa)	Shear modulus $\tilde{C}_{44}$ (GPa)	Yield stress σ_{xy}^{yield} (GPa)
Eq. (3.10)	31.375	3.304	52.802	9.857
Eq. (2.7)	31.077	3.285	49.883	9.944
Eq. (3.11)	30.346	3.254	49.904	10.187
Force/Area	30.399	3.304	51.272	10.383

4.6 Analysis of instabilities

4.6.1 Instability criteria

4.6.1.1 Local instability

We assume that an atom is stable at the position $\boldsymbol{r}^{(i)}$ if its potential energy $V^{(i)}$ there is the minimum. Recall that while finding the relaxed configuration of a system of atoms, the sum of potential energies of all atoms is minimized. Thus, it is possible that the overall system is in stable equilibrium, but one or more atoms are either in neutral or unstable equilibrium positions.

An alternative criterion for local stability is the following. An atom in its present position is stable provided that an acceleration wave can propagate through that point. Since the wave speed is proportional to an eigenvalue of the acoustic tensor, one can ascertain the local stability of an atom by finding eigenvalues of the acoustic tensor evaluated in the deformed configuration of the atomic system.

For simulations of the shear and the simple shear deformations described above, we compute $\boldsymbol{Q}^{(i)}$ after every increment in the prescribed displacements, and find the unit vector $\hat{\boldsymbol{n}}$ that minimizes eigenvalues of $\boldsymbol{Q}^{(i)}$. If the lowest eigenvalue of $\boldsymbol{Q}^{(i)}$ is nonpositive then the atom is unstable in the present position. Note that the unit vector $\hat{\boldsymbol{n}}$ can be expressed in terms of the longitude and the latitude angles as $\hat{\boldsymbol{n}} = [\cos\varphi\cos\theta, \cos\varphi\sin\theta, \sin\varphi]$. Thus we need to find angles φ and θ in the range $0 \le \theta \le 2\pi$ and $-\pi/2 \le \varphi \le \pi/2$ that minimize eigenvalues of $\boldsymbol{Q}^{(i)}$. We accomplish this by evaluating the determinant of $\boldsymbol{Q}^{(i)}$ on a grid of 1800 points obtained by dividing the ranges for φ and θ into equal segments of length $\pi/30$.

In an attempt to correlate the onset of local instabilities with highly inhomogeneous deformations near the specimen boundaries, we propose that an atom *i* becomes unstable when the energy $V^{(i)}$ due to atoms in the SRV with $R = \left(\sqrt{3}/2\right)a_0$ ceases to be positive definite; atoms in the SRV of $R = \left(\sqrt{3}/2\right)a_0$ are usually referred to as those within the first shell of atom *i*. For a pristine FCC crystal the number of atoms in the first shell of an atom equals 12. This criterion is motivated by the form of the interatomic TB potential and the observation that the contribution to the local energy from these atoms is more than 97% of that due to all atoms in the system, and this is so even when an atom is close to a free surface; e.g., see Fig. 4.9 in which the energy of atom *i* due to contributions from atoms in shells 1, 2, 3 and 4 are plotted. Shells 2, 3 and 4 are SRVs with *R* approximately equal to $(3/2)\left(\sqrt{3}/2\right)a_0$, $\sqrt{3}\,a_0$, and $(5/2)\left(\sqrt{3}/2\right)a_0$ Å respectively. Thus an atom becomes unstable when the local Hessian matrix

$$H_{jk}^{(i)} = \frac{\partial^2 V^{(i)}}{\partial r^{(ij)} \partial r^{(ik)}} \tag{4.14}$$

has a nonpositive eigenvalue. In Eq. (4.14) atoms in the first shell of atom *i* are considered. The condition for local stability is therefore $\min\left\{\lambda^{(i)}\right\} > 0$, where $\lambda^{(i)}$ is an eigenvalue of $\boldsymbol{H}^{(i)}$.

In order to find a correlation, if any, between atoms that become locally unstable and also have a relatively large value of the CNP we compute the CNP for atom *i* from

$$CNP^{(i)} = \frac{1}{N_f} \sum_{j=1}^{N_f} \left| \sum_{k=1}^{N_{ij}} \left(\boldsymbol{r}^{(ik)} + \boldsymbol{r}^{(jk)} \right) \right|^2 , \tag{4.15}$$

where N_{ij} is the number of common neighbors between atoms i and j, and N_f equals the number of atoms in the first shell of atom i. For a perfect crystal the value of the CNP for every interior atom is essentially zero; it exceeds 20 for atoms on bounding surfaces, and is greater than 2 at atoms located at positions of crystallographic defects.

We also explore a correlation between regions of local instabilities and relatively large values of one or more components of ***G***.

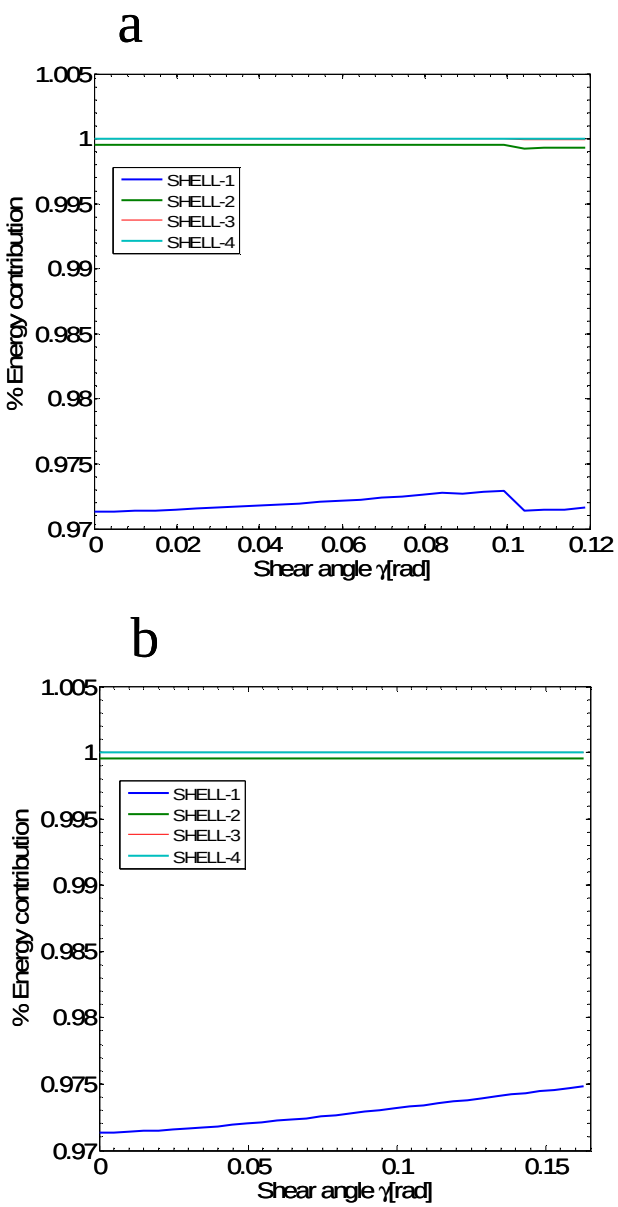

Fig. 4.9. Variation of the local energy at the centroid of system C due to contributions of different number of neighboring atoms. The blue line is the % of the total energy due only to atoms in shell 1; other curves are for atoms in shells 2, 3 and 4; (a) shear test, (b) simple shear test.

4.6.1.2 Global instability

As in continuum mechanics, the configuration of a system comprised of a collection of atoms is globally stable if the potential energy of the system in that configuration is the minimum. The potential energy equals the strain energy of deformation less the work done by external forces. For boundary conditions considered here (i.e., either displacements or null surface tractions prescribed), the potential energy of the system equals its strain energy which for the discrete system being studied equals the sum of the strain energy of all atoms in it.

For the potential energy of the system to be the minimum, the Hessian matrix with elements equaling second derivatives of the potential energy with respect to relative position vectors between atoms in the current configuration and evaluated at their current positions must be positive definite. Equivalently, all eigenvalues of this Hessian matrix must be positive. When computing eigenvalues of the Hessian matrix, rows and columns corresponding to atoms with prescribed displacements are eliminated to get the reduced Hessian matrix. With each atom having three d.o.f., the size of the reduced Hessian matrix equals *3Na x 3Na* where *Na* equals the number of active atoms in the system being studied. Thus the system of atoms will become globally unstable when at least one eigenvalue of the reduced Hessian matrix equals zero.

In terms of the Considère criterion (1888) the system will become globally unstable when the load (which for the shear and the simple shear deformations implies the shear stress in the plane of deformation) becomes the maximum.

4.7 Results of numerical simulations

4.7.1 Local instabilities

4.7.1.1 Shear test

The local instability criterion in terms of the minimum eigenvalue of the local acoustic tensor $\boldsymbol{Q}^{(i)}$ becoming nonpositive predicted instabilities for small values of the shear angle when no discontinuity in a stress-strain curve or a change in the curvature of the local energy vs. the shear angle curve was observed. Fig. 4.10a shows variation with the shear angle of the minimum value

of the determinant of $\boldsymbol{Q}^{(i)}$ for any atom in system B. Atoms where instabilities first occurred are located close to the free surfaces X = X_{min} and X = X_{max} of the system.

We note that the strain energy density versus the shear angle curve in Fig. 4.10a exhibits a discontinuity at the value of the shear angle that is much larger than the one where det[$\boldsymbol{Q}^{(i)}$] = 0.

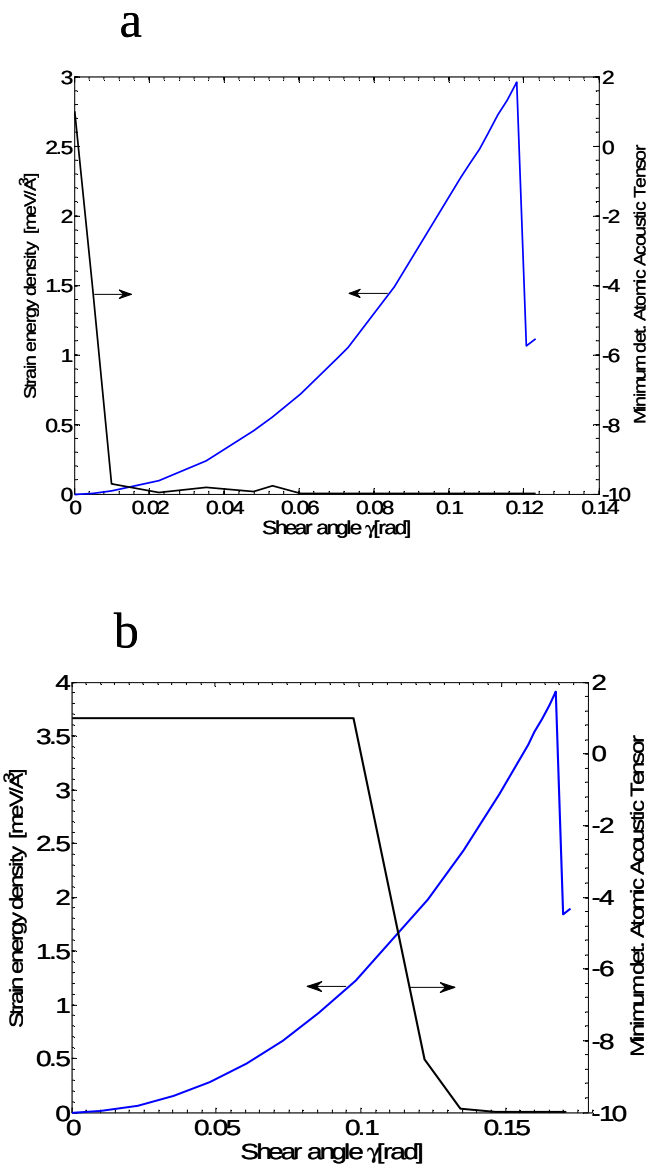

Fig. 4.10. Variations with the shear angle γ of the total strain energy density (blue curve) and the minimum value of the determinant of the atomic acoustic tensor $\boldsymbol{Q}^{(i)}$ for system B; (a) shear test, and (b) simple shear test.

Fig. 4.11a exhibits the evolution of the minimum eigenvalue of the local Hessian $\boldsymbol{H}^{(i)}$ among all atoms in the system where displacements are not prescribed. This value remains positive until $\gamma = 0.066$, 0.053 and 0.042, respectively, for systems A, B, and C, when the minimum eigenvalue of $\boldsymbol{H}^{(i)}$ becomes negative and stays negative during subsequent deformations for at least one atom in the specimen. Fig. 4.11b shows evolution of the fraction of atoms that have become unstable. This percentage increases rapidly for system C. The increase in the number of unstable atoms is similar for specimens A and B. The dashed vertical lines correspond to the shear angle values at which the global instability ensues. It is clear that for each one of the three specimens only about 8% of atoms have become unstable just prior to the onset of the global instability, and this number has increased to nearly 30% for systems B and C, and ~50% for system A at the end of the sharp discontinuity in the strain energy density vs. γ curve.

Fig. 4.12 shows, for system C, distributions of the minimum eigenvalue of $\boldsymbol{H}^{(i)}$ and the CNP. Figs. 4.12a and b correspond to the strain level when local instabilities were detected first at $\gamma = 0.042$. Only atomic positions where the local instability condition has been satisfied are depicted in Figs. 4.12a, c, e, g and t. Similarly, only atoms with high values of the CNP are exhibited in Figs. 4.12b, d, f, h and u. The eight blue points in Fig. 4.12a are diametrically opposite to each other and are in regions where the atomic volume $\Omega^{(i)}$ is greater than its value in the reference configuration; i.e., $\det[\boldsymbol{F}^{(i)}] > 1$. In Fig. 4.12b only atoms at the bounding surfaces have large values of the CNP.

Figures 4.12c and d correspond to the shear angle of 0.0872 that is just prior to the occurrence of the first discontinuity in the σ_{xy} - γ curve; at this point the number of unstable atoms has increased mainly in the four corners and in the top and the bottom surfaces (planes parallel to the xz-plane). It can be observed that unstable atoms are in 10 sub-volumes symmetrically distributed with respect to planes passing through the diagonals of the xy-plane. If one excludes atoms on the bounding surfaces, then there is a reasonable correlation between atoms having large values of the CNP and those where the minimum eigenvalue of the local Hessian matrix is nonpositive. Figs. 4.12e and f correspond to the shear angle of 0.0921 that is just after the first steep drop in the σ_{xy} - γ curve; it can be observed that on the corners $Y = Y_{max}$, $X = 0$ and $Y = 0$, $X = X_{max}$ groups of new unstable atoms have appeared. These new atoms are located on crystallographic planes {1,1,1} of high density where the shear deformation is

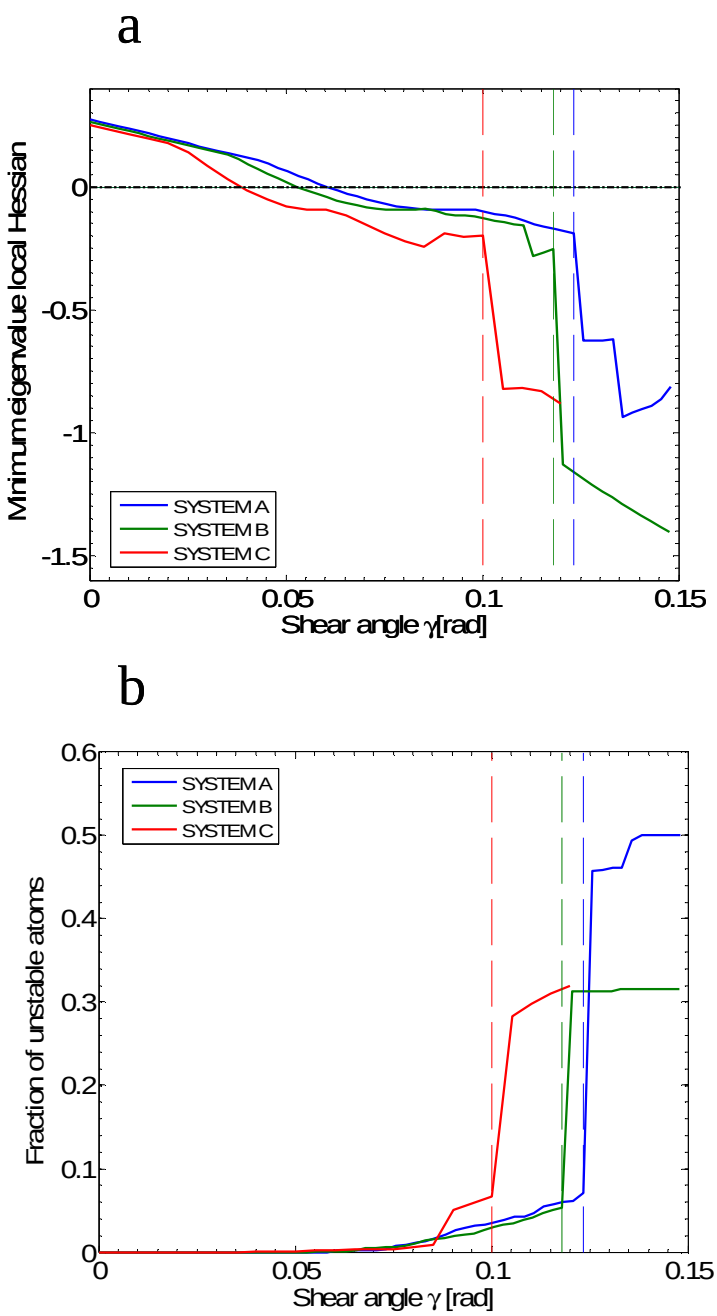

Fig. 4.11. For the shear test, variation with the shear angle γ of (a) the minimum eigenvalue of the Hessian of the local energy, and (b) the fraction of unstable atoms.

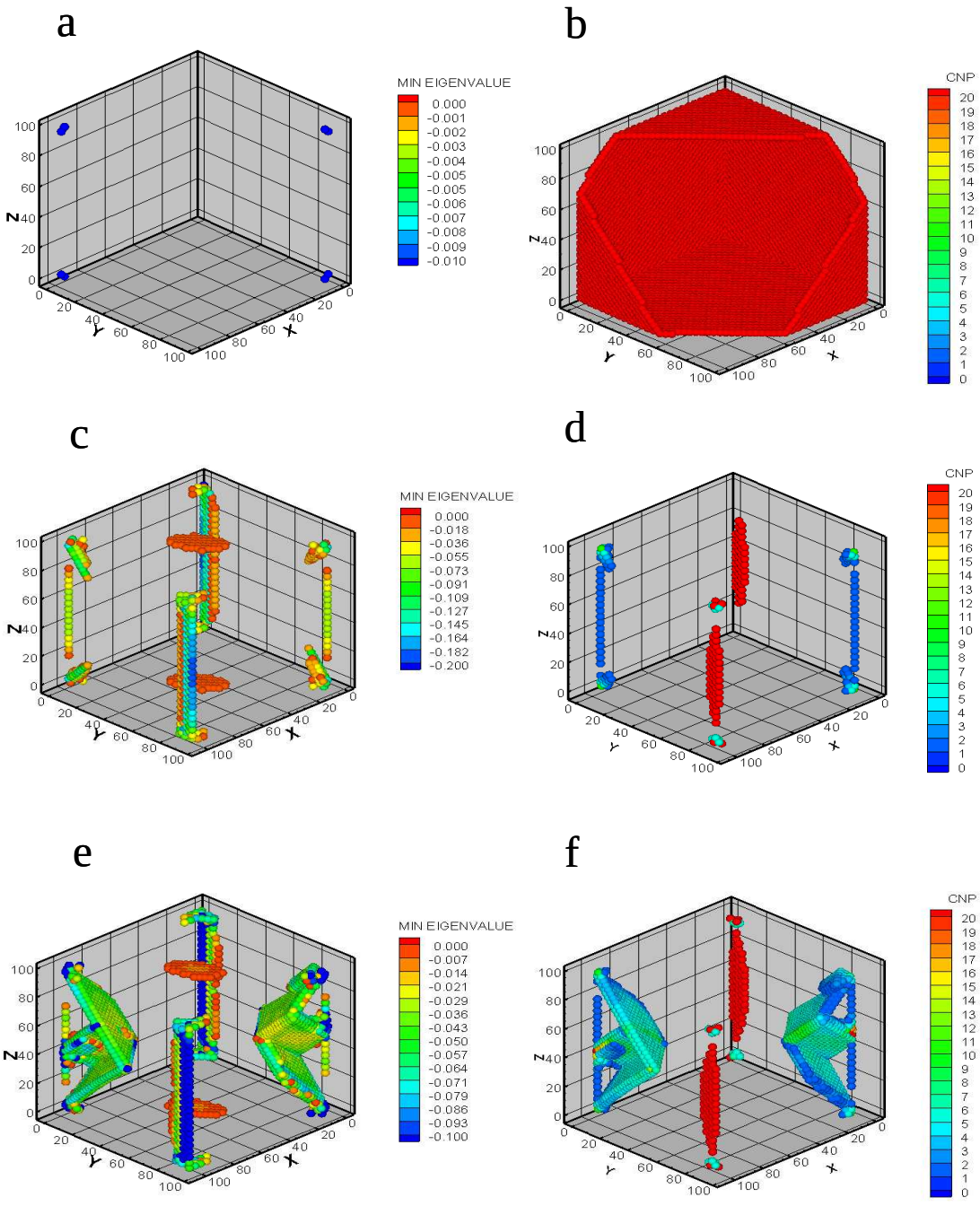

Fig. 4.12. Contd.

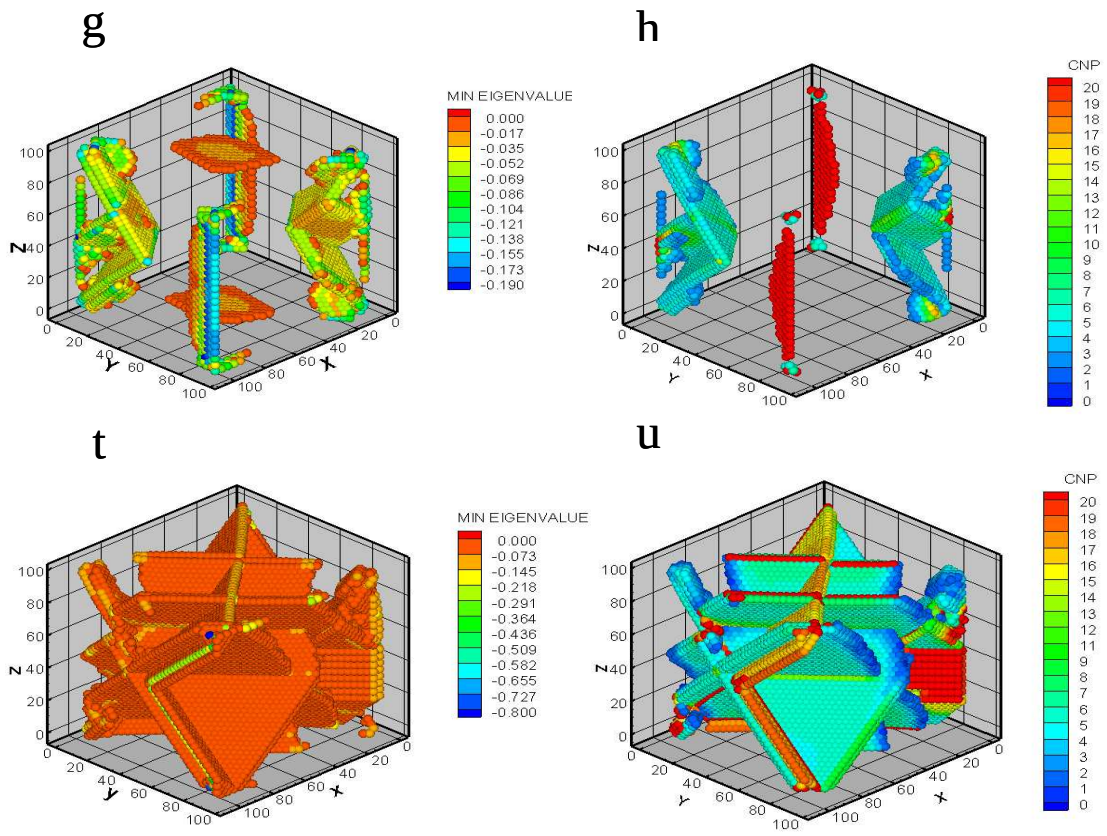

Fig. 4.12. Distribution of the minimum eigenvalue of the local Hessian and the CNP for the shear test in system C; (a) and (b) $\gamma = 0.0426$, (c) and (d) $\gamma = 0.0872$, (e) and (f) $\gamma = 0.0921$, (g) and (h) $\gamma = 0.102$, (t) and (u) $\gamma = 0.1069$

accommodated by changing the stacking sequence in the crystal. As for the previous case these atomic positions correlate well with the interior atoms exhibited in Fig. 4.12f where the CNP has relatively high values. Figs. 4.12g and h correspond to the shear angle of 0.102 just prior to the system becoming globally unstable when the most pronounced drop in the σ_{xy} - γ curve occurs. Between the instants of $\gamma = 0.0921$ and $\gamma = 0.102$ considerably more atoms have become unstable. Figs. 4.12t and u are for the shear angle of 0.1069 that is just after the sharp drop in the σ_{xy} - γ curve when nearly 30% of atoms in the system have become unstable. Atoms with nonpositive values of the minimum eigenvalue of the local Hessian matrix $\boldsymbol{H}^{(i)}$ and those with large values of the CNP are similarly situated, and their numbers are essentially equal. We have not investigated if a large value of the CNP corresponds to a higher magnitude of the negative eigenvalue of $\boldsymbol{H}^{(i)}$. However, results presented in Fig. 4.12 imply that there is a good correlation between locations of unstable atoms and those having a large value of the CNP.

For the system C, Fig. 4.13 exhibits atoms with a large value of $\|\mathbf{G}\|$ defined by

$$\|\mathbf{G}\| = (a \max(|G_{\alpha\beta\gamma}|)).$$

Here $\max(|G_{\alpha\beta\gamma}|)$ equals the maximum value of any one of the 27 components of $\boldsymbol{G}$ at any point in the system, and it is multiplied by the lattice parameter a to get a nondimensional number. Results plotted in Figs. 4.13a and b correspond to $\gamma = 0.0872$ and $\gamma = 0.0921$ respectively; that is instants immediately preceding and following the first drop in the shear stress-shear angle curves. Results plotted in Figs. 4.12c-f also correspond to these strain levels. Figs. 4.13c and d are for $\gamma = 0.102$ and $\gamma = 0.1069$ respectively, the same values of the shear angle for which results are depicted in Figs. 4.12g,h and t,u. We note that regions with a large value of $\|\mathbf{G}\|$ have high inhomogeneous deformations.

Atoms evinced in Figs. 4.13c and d having a large value of $\|\mathbf{G}\|$ when compared with those included in Figs. 4.12g, h and t,u suggest that shapes and locations of geometric regions of high values of $\|\mathbf{G}\|$, large values of the CNP, and nonpositive values of the minimum eigenvalue of $\boldsymbol{H}^{(i)}$ are essentially identical. Thus any one of these three criteria can be used to characterize a local instability. Each one of these three methods predicts that atoms on a bounding plane become unstable first. However, the local instability does not seem to propagate from atoms on the boundaries to those in the interior of the cube since the interior unstable atoms are not necessarily bonded to those on the bounding surfaces.

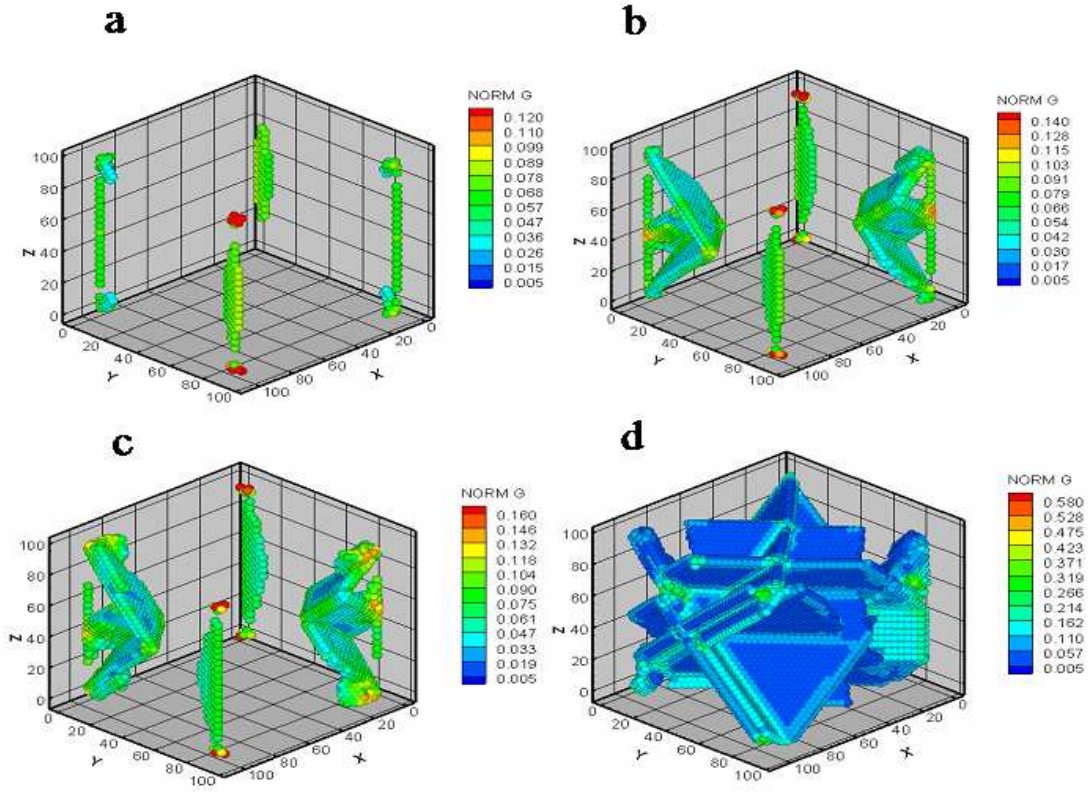

Fig. 4.13. Distribution of $\|\mathbf{G}\|$ for the shear test in system C; (a) $\gamma = 0.0872$, (b) $\gamma = 0.0921$, (c) $\gamma = 0.102$, and (d) $\gamma = 0.1069$.

Fig. 4.14 shows the variation of the derivative with respect to γ of the expected value $<\|\mathbf{G}\|>$ of $\|\mathbf{G}\|$ computed from a kernel approximation of the probability density function of its distribution at each load step. From the probability density functions (not shown) for $\gamma = 0.0227$ and $\gamma = 0.0426$, the distributions of $\|\mathbf{G}\|$ in the specimen are essentially zero and the expected values are 0.0104 and 0.0138 respectively. Between these two configurations the change in the expected value with respect to γ, $d<\|\mathbf{G}\|>/d\gamma$, is only 0.171. From the probability densities for $\gamma = 0.0872$ and $\gamma = 0.0921$ which correspond to distributions shown in Figs. 4.12c and f, $d<\|\mathbf{G}\|$

>/dγ = 0.755 which is substantially higher than 0.171. Similarly, between γ = 0.102 and γ = 0.1069, d<‖ **G** ‖ >/dγ = 6.26. Thus a large value of d<‖ **G** ‖ >/dγ also signifies that a major part of the system has undergone severe inhomogeneous deformations, and has become locally unstable.

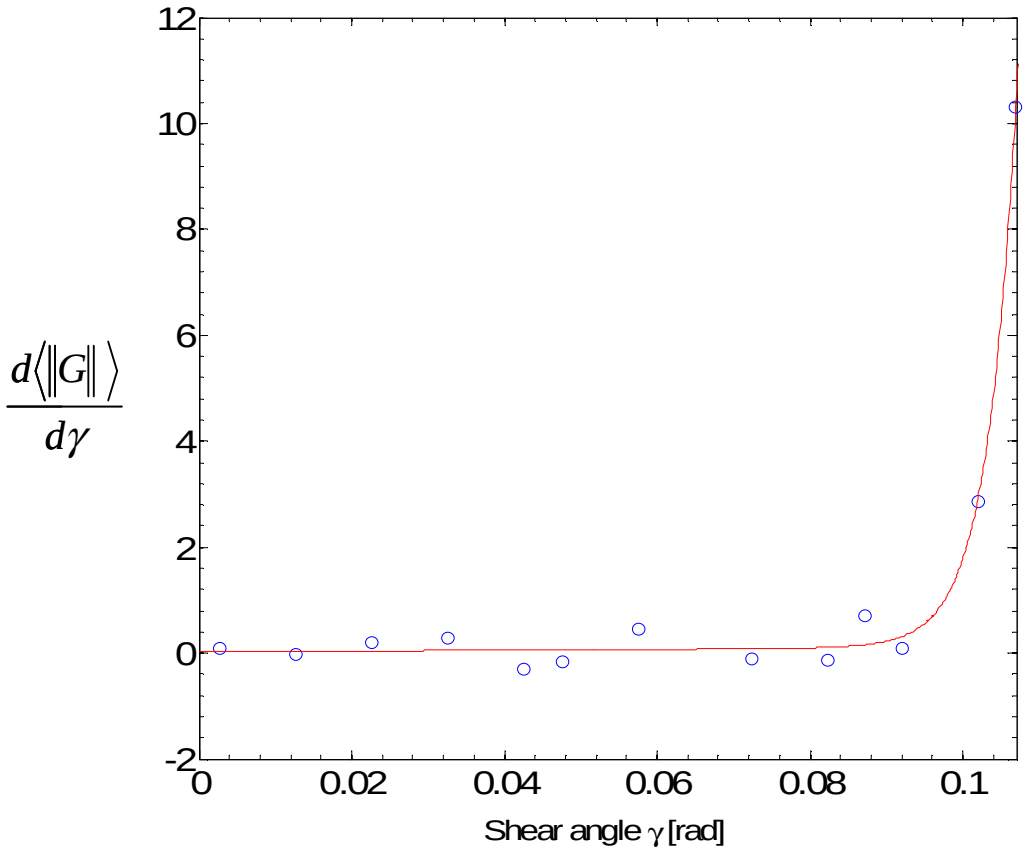

Fig. 4.14. Variation with the shear angle γ of $d\langle\|\boldsymbol{G}\|\rangle/d\gamma$ for the shear test on system C.

In Fig. 4.15a,c,e we have plotted incremental displacements in going from the configuration just prior to the system yielding to the configuration at yield, and in Fig. 4.15b,d,f incremental displacements in going from the yielded state to the immediately next configuration. In order to clearly show results incremental displacements of only unstable atoms are shown in Fig. 4.15b,d,f. Prior to the initiation of yielding, displacements of all atoms except a few near the corners are approximately of the order of the incremental displacements imposed on the surface

$Y = Y_{max}$. No slip system is activated prior to yielding of the material. However, in going from the state just before yielding to the one just after yielding, several atoms that have become unstable undergo displacements in all three directions whose magnitude is an order of magnitude higher than that of the imposed incremental displacement. Because of the enormous number of atoms becoming unstable it is almost impossible to find Burger's vectors and classify dislocations into different categories. By closely looking at the direction and the magnitude of displacements, e.g. see red and light blue fringes in Fig. 4.15d, one can identify planes across which slip has occurred. There are many such planes across which atoms have slid in opposite directions.

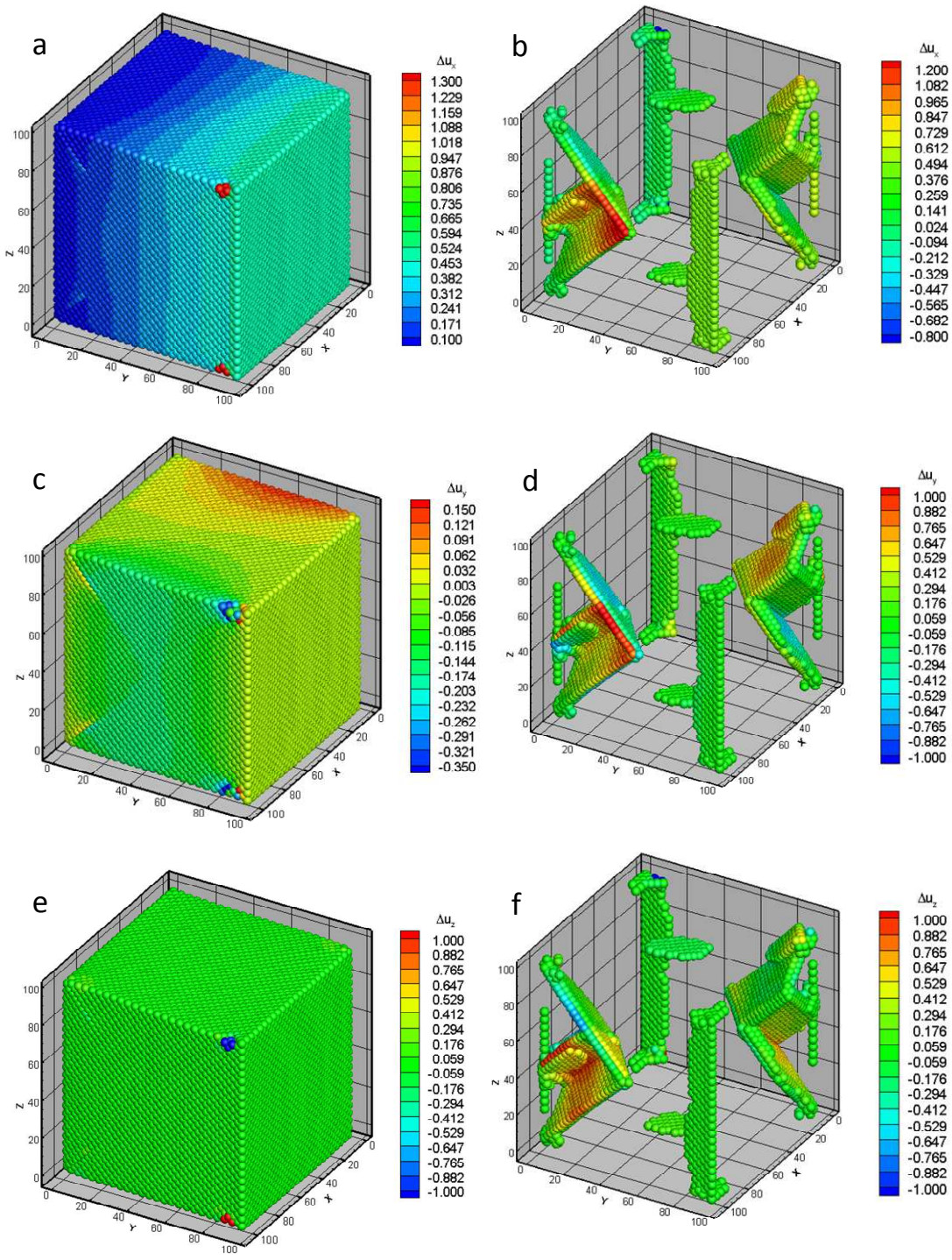

Fig. 4.15. For the shear test on system C, distributions of the change Δu_x, Δu_y and Δu_z in the displacement components on (a, c, e) the bounding surfaces in going from the configuration just before yielding to that corresponding to yielding at $\gamma = 0.084$ and (b, d, f) at in going from the yielded configuration to that at $\gamma = 0.0921$ (incremental displacements in Å).

4.7.1.2 Simple shear test

For the simple shear test, nonpositive values of the minimum eigenvalue of $\boldsymbol{Q}^{(i)}$ were found at atoms close to the bounding surfaces just prior to the system becoming globally unstable. None of the local instability criteria is satisfied for values of the shear angle γ that are noticeably less than the one where the system becomes globally unstable.

Fig. 4.16a exhibits the evolution of the minimum eigenvalue of the local Hessian $\boldsymbol{H}^{(i)}$. Unlike in the shear test, no pronounced local inhomogeneities occur before the onset of the global instability. It could be due to the fact that displacements prescribed on all bounding surfaces constrain deformations of all interior atoms. The first local instability at four atoms occurs simultaneously just prior to the onset of the global instability at $\gamma = 0.155$, and the relative positions of the four atoms and the shear strain at the onset of the instability are essentially independent of the specimen size. Nearly 40% of atoms become unstable at $\gamma = 0.1752$, 0.1675 and 0.1644 for specimens A, B, and C respectively. Fig. 4.16a also shows the evolution of the minimum eigenvalue of the local Hessian for the hyperelastic material. Although the minimum eigenvalue of the Hessian decreases with an increase in the shear strain, it does not become negative. Since the shear stress vs. the shear strain curve for the hyperelastic material basically coincides with that derived from the MM simulations till the onset of instabilities, it is reasonable to conclude that the Cauchy-Born rule used to derive the strain energy density from the atomic potential holds for averaged quantities till the initiation of instabilities.

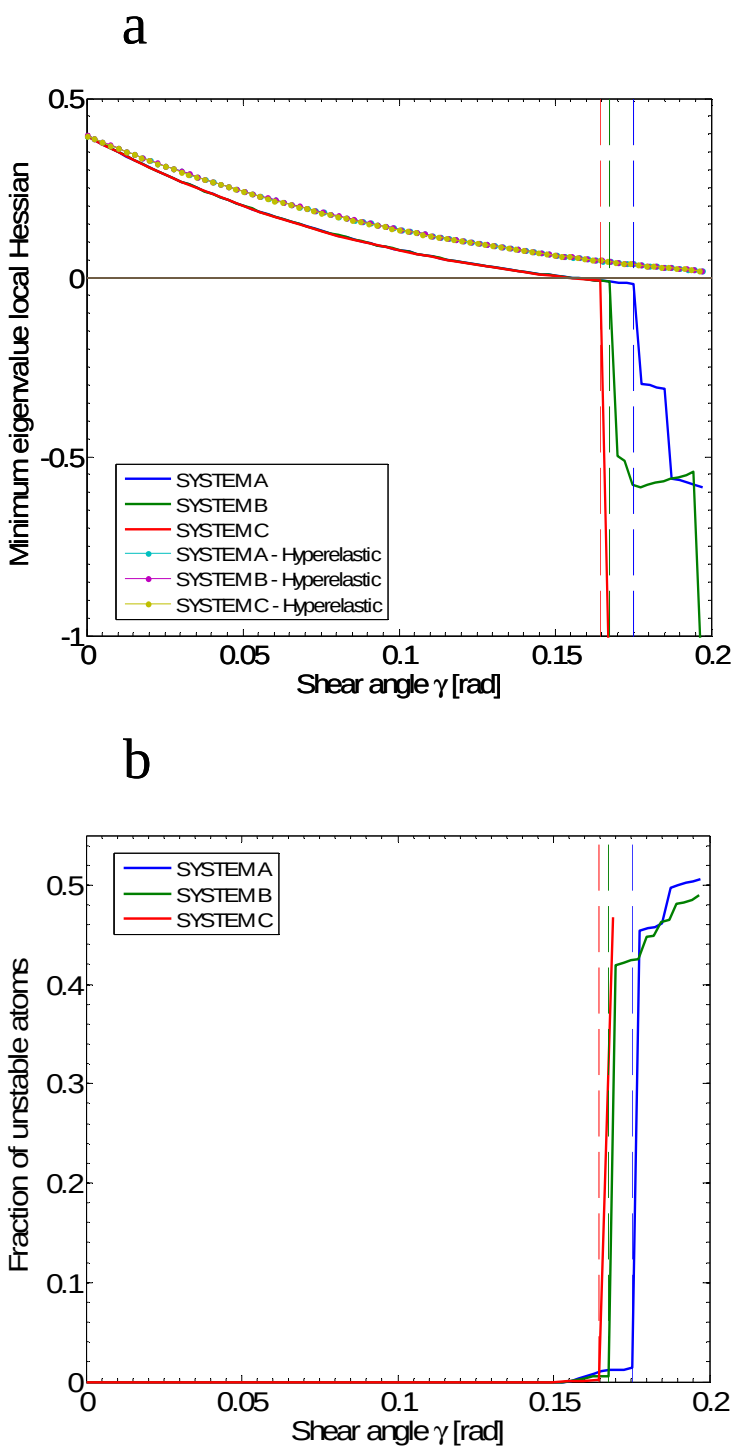

Fig. 4.16. For the simple shear test, variation with the shear angle γ of (a) the minimum eigenvalue of the Hessian of the local energy, and (b) the fraction of unstable atoms.

Fig. 4.17a shows locations of the four atoms where local instabilities ensue for the system C at $\gamma = 0.155$. In Figs. 4.17a, c and e positions of only unstable atoms are exhibited. At $\gamma = 0.1655$ two geometrically opposite columns of unstable atoms have formed (cf. Fig. 4.17c). After the next load step, $\gamma = 0.1703$, a considerable number of atoms distributed over atomic planes in the interior of the system have become unstable. Thus both local and global instabilities occur almost simultaneously in the simple shear test but the initiation of local instabilities precedes that of the global instability by a large value of the shear strain in the shear test having four out of six bounding surfaces free of external forces.

Figs. 4.17b, d and f show distributions of the CNP for specimen C at $\gamma = 0.155$, 0.1655 and 0.1703 respectively. For shear angles of 0.155 and 0.1655 atoms that become unstable are located close to the bounding surfaces (CNP ~ 20) at two diametrically opposite corners where $\det[\boldsymbol{F}^{(i)}] > 1$ locally. The CNP parameter also has the same high value for those atoms on bounding surfaces where no instability was detected. After the occurrence of the global instability the distribution of unstable atoms correlates well with the distribution of values of the CNP. No major change in the structure of the system was predicted by the CNP prior to the onset of the global instability. The presence of planes of unstable atoms before the occurrence of the global instability is not observed in the simple shear deformation.

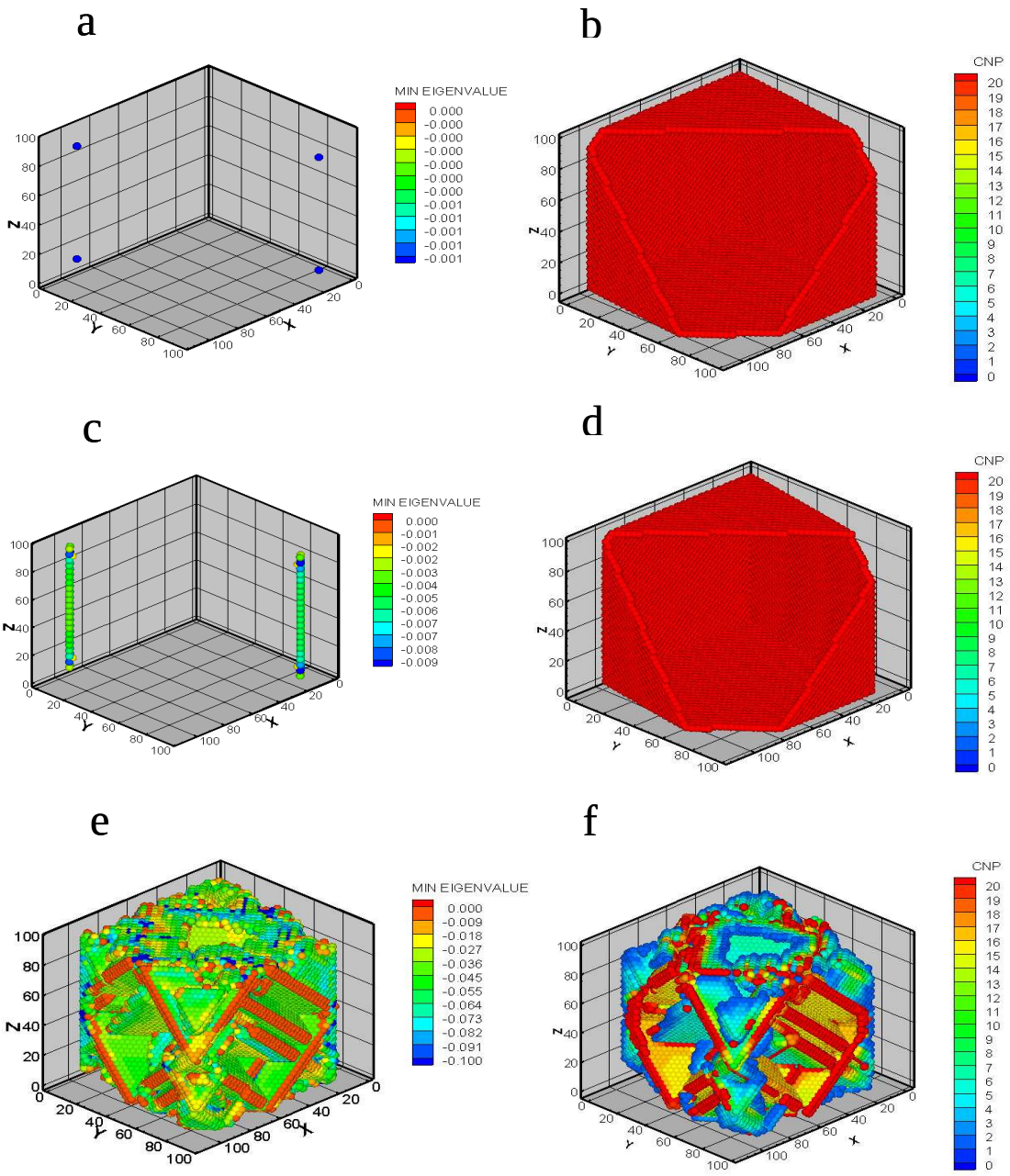

Fig. 4.17. For the simple shear test, distribution of the minimum eigenvalue of the local Hessian and the CNP in system C; (a) and (b) $\gamma = 0.1555$, (c) and (d) $\gamma = 0.1655$, (e) and (f) $\gamma = 0.1703$.

Figs. 4.18a and b show the distribution of $\|\mathbf{G}\|$ for specimen C at γ = 0.1655 and 0.1703 respectively. As for the shear deformations the maximum value of $\|\mathbf{G}\|$ occurs at points located mainly near the bounding surfaces. From the probability density functions of $\|\mathbf{G}\|$ for strain levels just before and just after the occurrence of the global instability, the expected values are 0.0120 and 0.0948 respectively. Thus $d<\|\mathbf{G}\|>/d\gamma$ has a very large value of 17.25 when the global instability occurs. Fig. 4.19 shows the evolion with the shear angle of $d<\|\mathbf{G}\|>/d\gamma$ and confirms that it is essentially zero till the onset of a global instability when it increases rapidly.

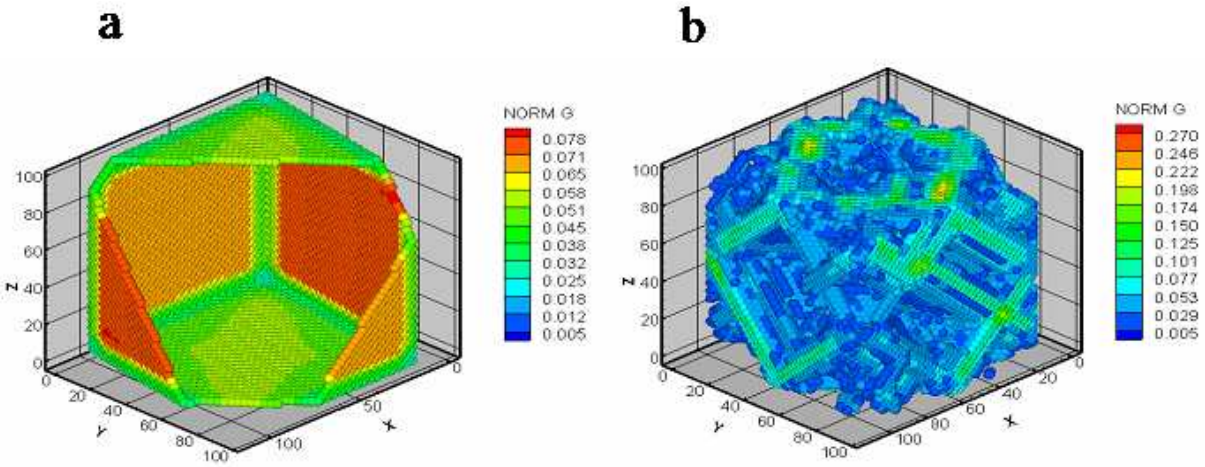

Fig. 4.18. Distribution of $\|G\|$ for the simple shear test in system C; (a) γ = 0.1655, and (b) γ = 0.1703.

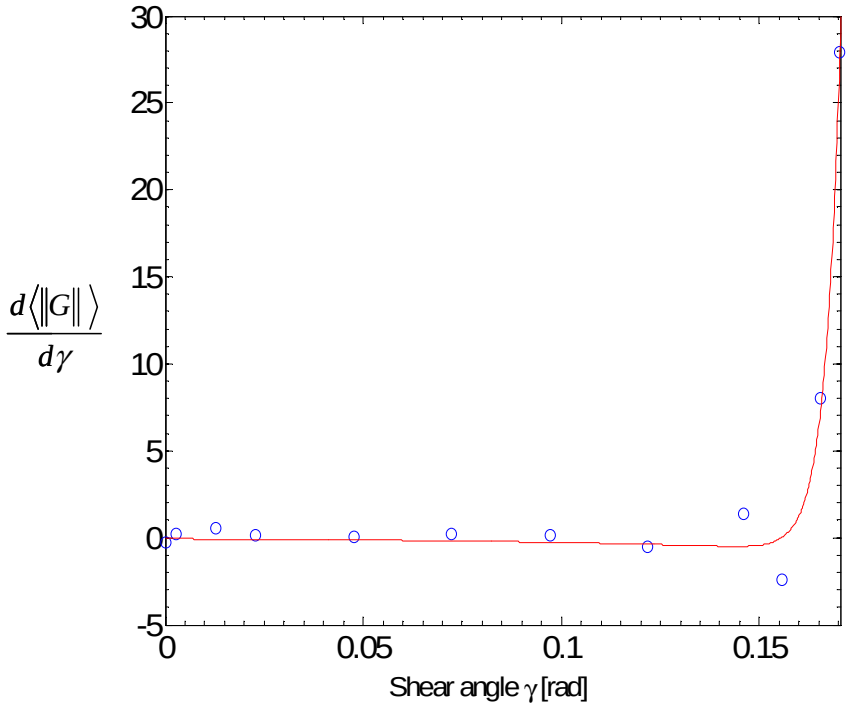

Fig. 4.19. Variation with the shear angle γ of $d\langle\|\boldsymbol{G}\|\rangle/d\gamma$ for the simple shear test on system C

4.8 Global instabilities

The variations with the shear angle γ of system's strain energy density for the shear and the simple shear deformations are shown in Fig. 4.20. In the simple shear deformations the energy continuously increases up to a point where the global instability occurs. For the shear deformations, slight changes in the curvature of the energy vs. the shear angle γ curve are observed due to the presence of unstable atoms.

For specimens A and B deformed in shear the energy continuously increases with no major changes in the curvature of the energy vs. γ curve. For specimen C at γ = 0.0921 the presence of two diametrically opposite columns of unstable atoms (cf. Figs. 4.12e, f) is reflected in a small change of curvature in the energy vs. γ curve. Subsequently, the energy continuously increases till γ = 0.102 where a sudden drop in the energy occurs and the system becomes unstable.

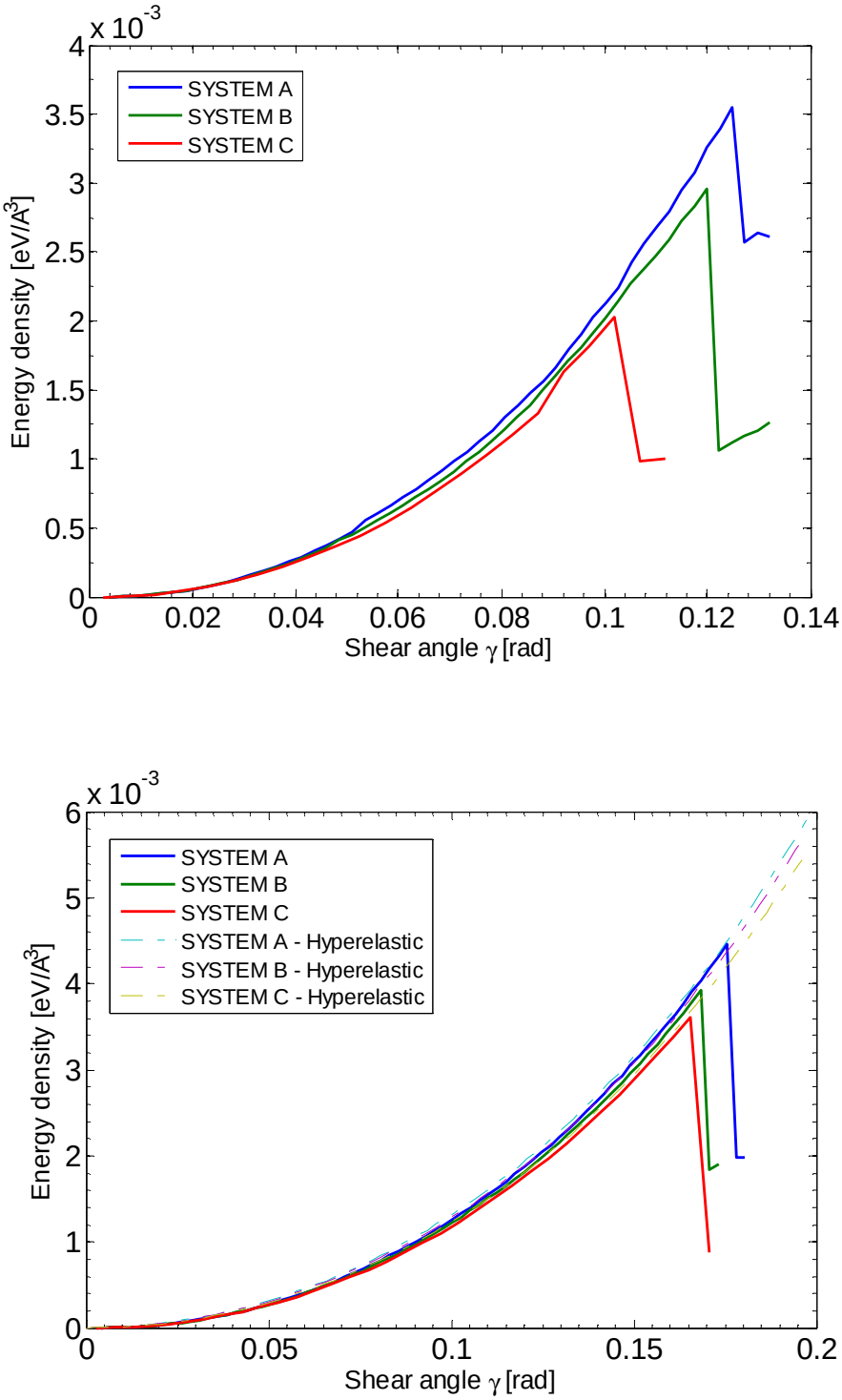

Fig. 4.20. Variation with the shear angle γ of the strain energy density; (a) shear test, (b) simple shear test.

Recalling results depicted in Figs. 4.11 and 4.16, we conclude that the shear strain at the onset of the global instability equals that at which the percentage of atoms becoming unstable increases the most, and the energy of the system drops noticeably.

For the system of Au atoms deformed in simple shear (Fig. 4.20b) the strain energy density increases monotonically till $\gamma = 0.1675$ when it suddenly drops by a large amount. For the three specimens differences among the strain levels at the onset of the global instability are not as pronounced as it is for the shear deformations.

In an attempt to see if the minimum eigenvalue $\lambda^H_{\min}$ of the Hessian matrix $\boldsymbol{H}$ suddenly jumps at the onset of a global instability, we have plotted in Figs. 4.21a and b the evolution of the change in $\lambda^H_{\min}$ with respect to γ for the two types of deformation of specimen B. These two plots reveal that indeed $d\lambda^H_{\min}/d\gamma$ increases noticeably with γ when the system becomes globally unstable. Whereas the evolution with the shear angle of $d\lambda^H_{\min}/d\gamma$ is oscillatory for shear deformations, it is smooth for the simple shear deformations.

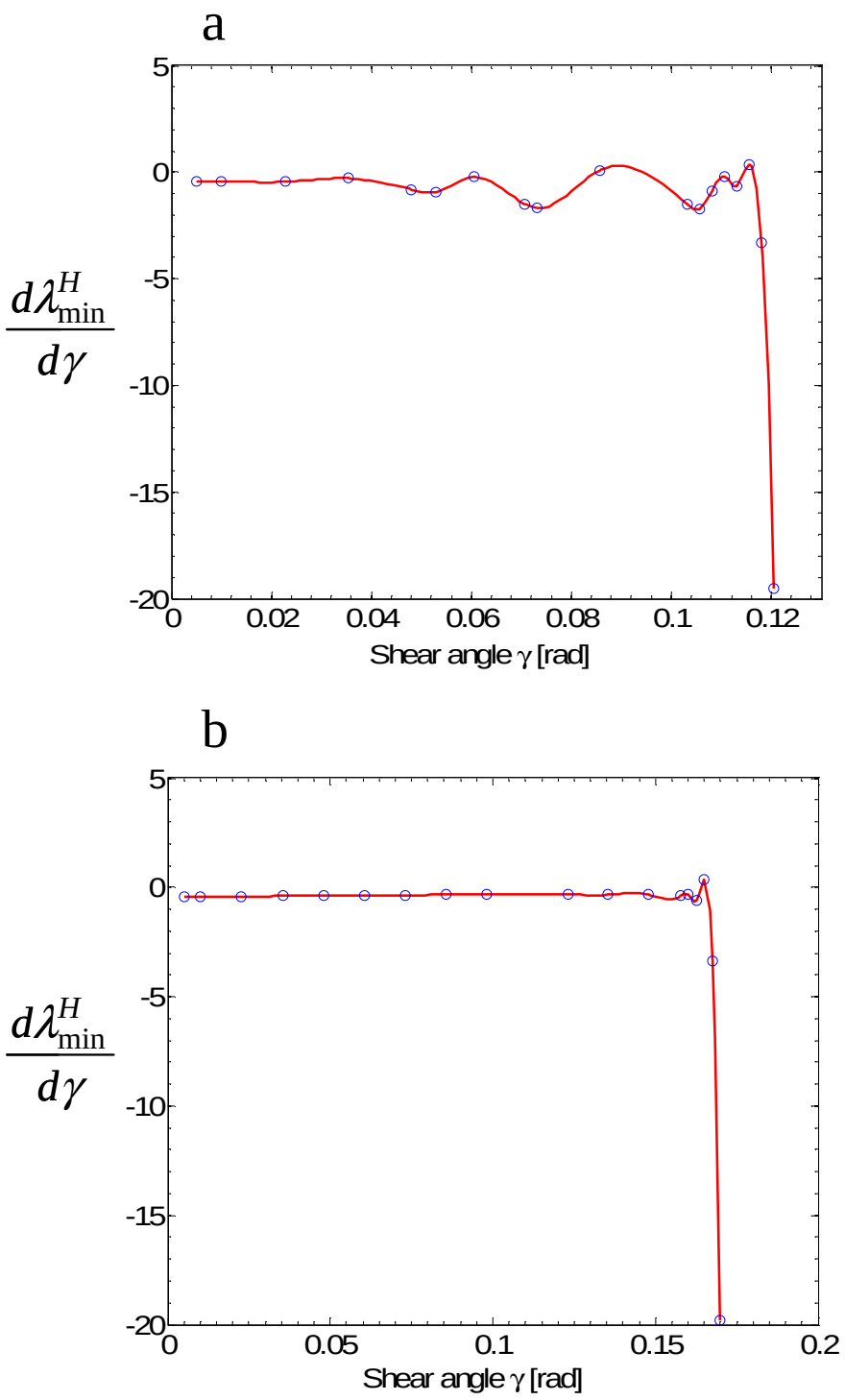

Fig. 4.21. For system B, variation with the shear angle γ of $d\lambda_{\min}^{H}/d\gamma$; (a) shear test, (b) simple shear test.

4.9 Distributions of local stresses for the shear tests

Values of the Cauchy stress tensor at each atomic position were computed following the method proposed by Hardy (Eq. 2.23). For specimen C, Fig. 4.22 shows distributions of σ_{xx}, σ_{xy} and σ_{VM} in the reference configuration. The effect of the surface tension in bounding surfaces of the specimen is reflected in nonvanishing values of the initial local stresses. The distribution of σ_{xx} in Fig. 4.22a shows a compressive stress of ~ 0.5 GPa at the centroid of the specimen; σ_{xx} equals zero on free surfaces perpendicular to the X-axis and has a maximum tensile value of ~1.8 GPa on the remaining four surfaces. Similar distributions were obtained for σ_{yy} and σ_{zz} components. The shear stress σ_{xy} is zero everywhere in the specimen except at edges parallel to the Z-axis where it has a magnitude of ~ 0.9 GPa. The distribution of the von Mises stress depicted in Fig. 4.22c shows that the highest values of ~ 2 GPa are present on free surfaces and σ_{VM} = 0.2 GPa at the specimen centroid. Even though the distribution of stresses in the reference configuration is qualitatively the same for all three cubic specimens their magnitudes differ. For the three specimens, Table 4.4 summarizes relative change in the total volume, the relative change in the total potential energy, the average axial strain (change in length per unit initial length) in the X-direction, and σ_{xx} induced at the specimen centroid, in going from the initial perfect lattice configuration to the unloaded relaxed (reference) configuration. The total volume of a specimen was computed by adding the atomic volumes given by Eq. 3.6. In the reference configuration the initially plane bounding surfaces of a cubic specimen become curved.

Table 4.4: During the relaxation of the initial unloaded perfect cubic specimen, relative change in the total potential energy (V), relative change in the total volume (Ω^T), the average axial strain ($\varepsilon_{xx} = \varepsilon_{yy} = \varepsilon_{zz}$) and the axial stress σ_{xx} at the centroid of the cubic specimens.

Specimen	$\frac{\Delta V}{V_I}$ (eV/eV)	$\frac{\Delta\Omega^T}{\Omega_I^T}$ (Å^3/Å^3)	ε (Å/Å)	σ_{xx} (GPa)
A	3.763e-3	-2.021E-2	-2.081E-2	-1.6
B	2.549e-3	-1.486E-2	-1.713E-2	-1.5
C	1.044e-3	-6.923E-3	-1.036E-2	-0.5

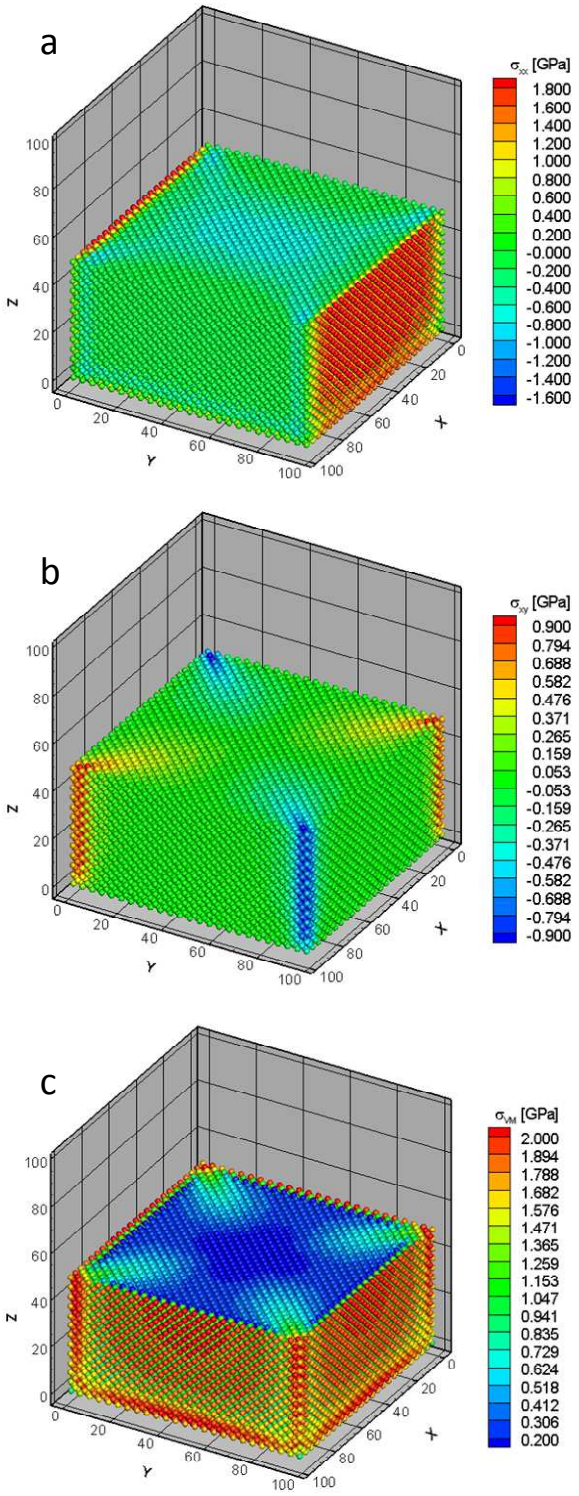

Fig. 4.22. For specimen C, distribution in the reference configuration of stresses on the mid-section; (a) σ_{xx}; (b) σ_{xy}; (c) σ_{VM}.

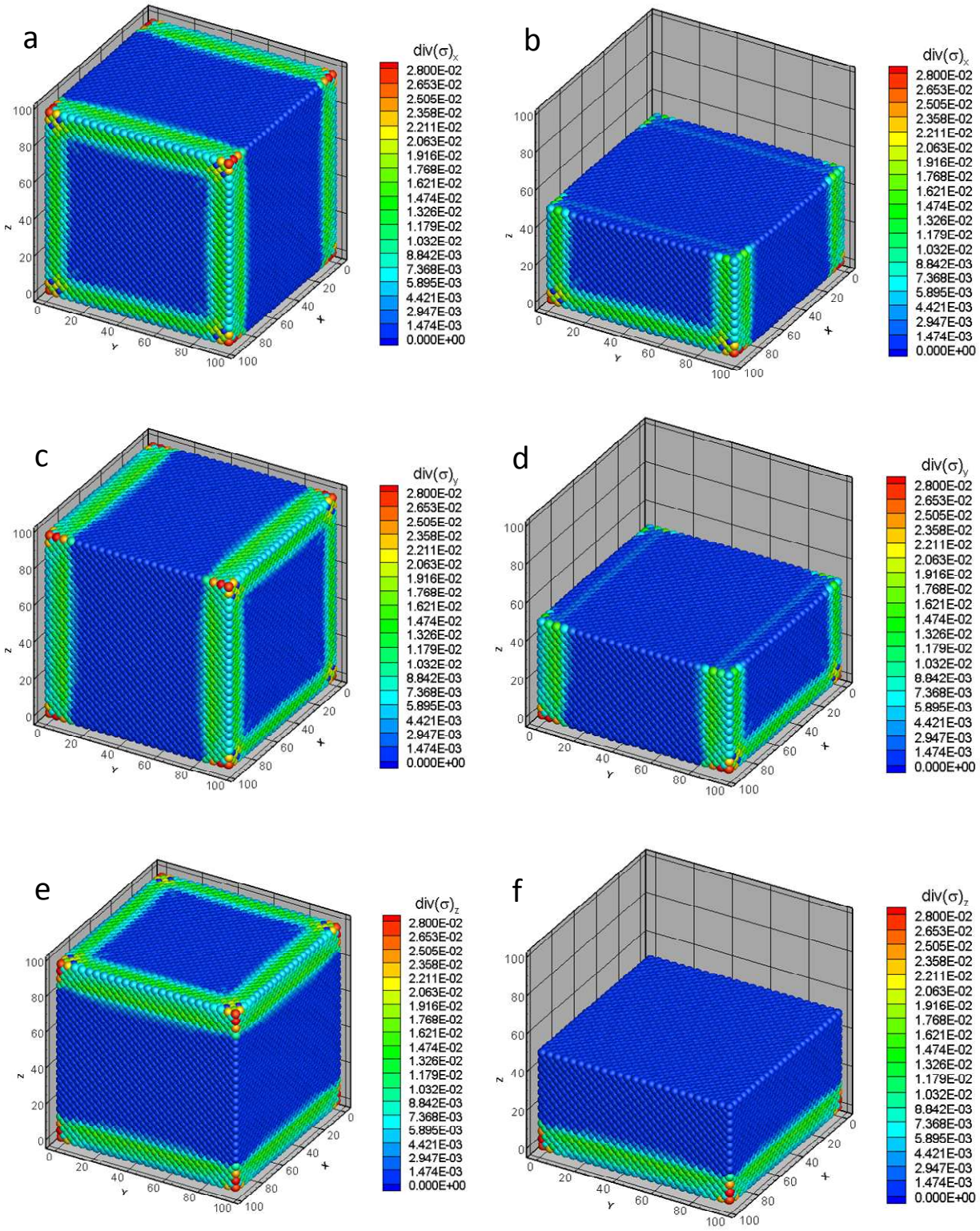

Fig. 4.23. For specimen C, distributions of components of $div(\boldsymbol{\sigma})$ on the bounding surfaces and on the mid-section Z = 50 Å in the reference configuration; (a) and (b) $(div(\boldsymbol{\sigma}))_x$; (c) and (d) $(div(\boldsymbol{\sigma}))_y$; (e) and (f) $(div(\boldsymbol{\sigma}))_z$.

The change in the total potential energy of a specimen during the minimization of its potential energy is not significant for any one of the three specimens; it is ~ 0.37% for the specimen with 3480 atoms and only ~ 0.1% for the specimen with 58825 atoms. The reduction, ~ 2%, in the total volume is noticeable for the smallest sample as compared to ~ 0.7% for the largest sample. The axial strain along each centroidal line of a specimen is more than ~1%; the largest specimen C has the minimum values of the volumetric and the axial strains. These geometrical changes are accompanied by the development of residual stresses. For the smallest sample A, σ_{xx} = ~ -1.6 GPa at the centroid, and σ_{xx} = ~ -0.5 GPa at the centroid of the largest specimen C. We have plotted the x-, the y- and the z-components of div($\boldsymbol{\sigma}$) in Figs. 4.23a,b, 4.23c,d and 4.23e,f respectively. It is clear that except for points near the bounding surfaces, div($\boldsymbol{\sigma}$) is nearly zero everywhere attesting to the equilibrium of the reference configuration. The gradients of stresses from their values at atomic positions were computed by the MSPH method.

Figs. 4.24a and b show distributions of σ_{xy} on bounding surfaces for γ = 0.0872 and γ = 0.0921 respectively. At γ = 0.0872, the shear stress varies from ~ -0.5 GPa to ~3.6 GPa; on free surfaces initially parallel to the YZ-coordinate plane the shear stress is almost uniform and equals ~ 0.25 GPa. Towards the edge Y = 0 the shear stress increases to ~2.6 GPa along atomic positions parallel to the Z-axis. At the four corners on these planes the shear stress is negative and equals ~ -0.5 GPa. The locations of these negative values of σ_{xy} also coincide with the locations of four columns of unstable atoms shown in Fig. 4.12c. The maximum values of the shear stress occur at points on the edges where unstable atoms are located (see green fringes along the Z-axis). Values of the shear stress = ~2.6 GPa also occur on the two planes parallel to the shear XY-plane. In this case high values of the stress occur along the diagonal of the specimen; these decrease towards the edges to ~0.25 GPa.

The shear stress on planes (Y = Y_{min} and Y = Y_{max} in Fig. 4.24a) with prescribed displacements is high at edges parallel to the Z-axis. On these planes the shear stress decreases for atoms with increasing X-coordinate. The stress distribution at $\gamma = \gamma^{yield}$ is symmetric with respect to the diagonal of the YZ-plane. During the drop in the average $\sigma_{xy} - \gamma$ curve the stress levels on bounding surfaces remain essentially unchanged but the symmetry in the stress distribution observed in the previous load step is lost (cf. Fig. 4.24b). New regions around the center of the two XZ-planes with negative values of the shear stress have formed. The

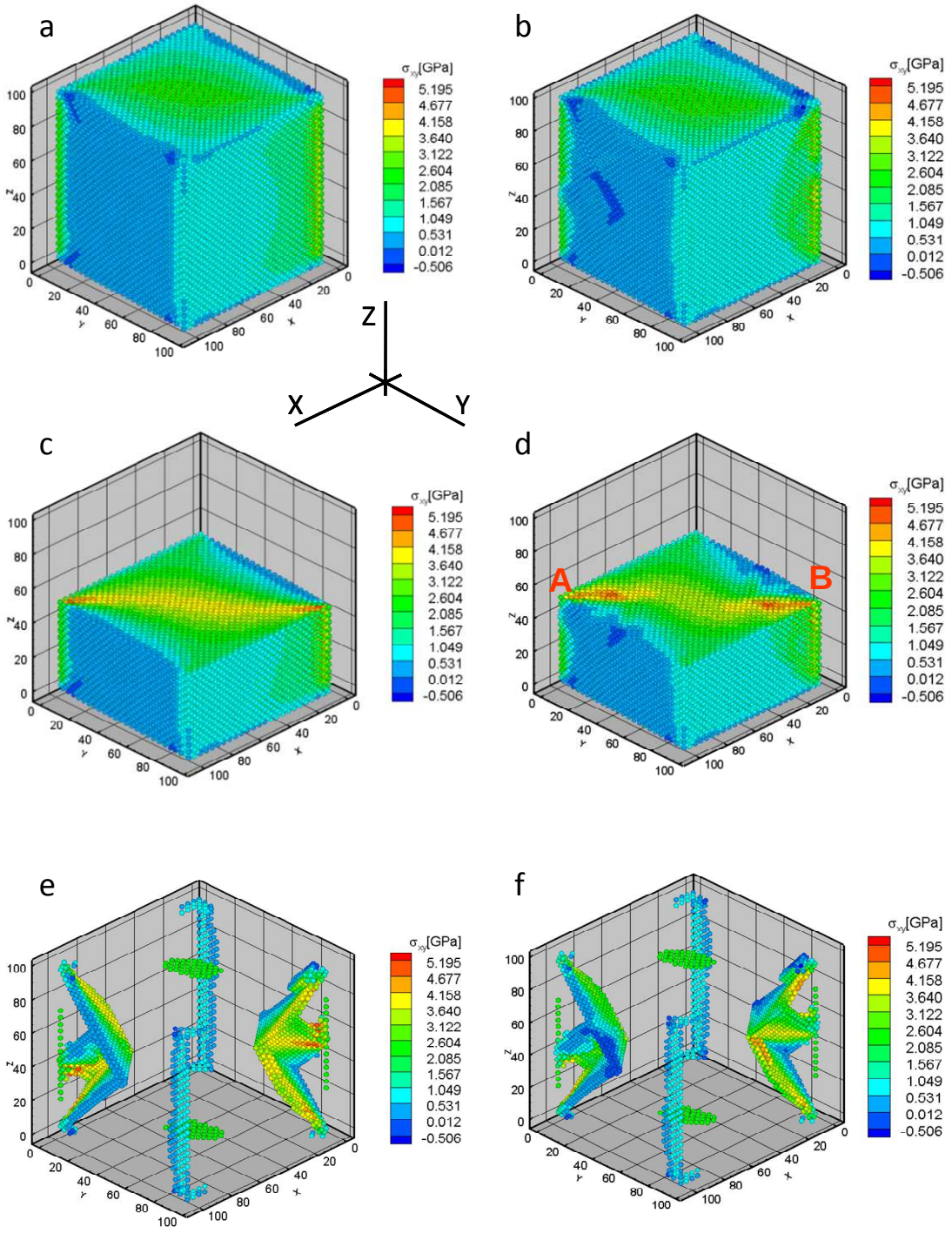

Fig. 4.24. For the shear test, distribution of the σ_{xy} component of the local Cauchy stress tensor on the bounding surfaces, the mid-section and at unstable points in specimen C; (a), (c) and (e) $\gamma = 0.0872$; (b), (d) and (f) $\gamma = 0.0921$.

distribution of σ_{xy} on the XY-plane remains essentially unaffected by the nucleation of instabilities.

Figs. 4.24c and d show, respectively, the distribution of σ_{xy} on the plane Z = 50Å for γ = 0.0872 and γ = 0.0921. The details of the distribution of the shear stress in the interior of the specimen before the occurrence of instabilities are depicted in Fig. 4.24c. A diagonal (yellow color) band of high shear stress between ~3.6 and ~ 4.2 GPa is apparent. The value of σ_{xy} near the corners equals ~5.2 GPa. We note that instabilities nucleated at atomic positions in these regions of high values of the shear stress. Subsequently, at γ = 0.0921, there are two regions near the opposite corners where $\sigma_{xy} \approx 5$ GPa. However, at the center of the specimen, σ_{xy} varies between ~3.1 and ~3.6 GPa. The stress distribution is not symmetric about the diagonal AB in Fig. 4.24d.

Figs. 4.24e and f show the distribution of σ_{xy} at unstable points when γ = 0.0872 and γ = 0.0921 respectively. For the atoms shown $\boldsymbol{H}^{(i)}$ has at least one negative eigenvalue in the configuration after the drop in the average $\sigma_{xy} - \gamma$ curve (γ = 0.0921). Stresses are also computed for the same group of atoms in the configuration corresponding to γ = 0.0872. Fig. 4.24e depicts that σ_{xy} has very high values of ~5.2 GPa at points prior to their becoming unstable. After the nucleation of instabilities, σ_{xy} there decreases to ~3.6 GPa. On planes of high atomic density depicted in this figure the stress drops from ~3.8 GPa (yellow fringes) to ~2.6 GPa (green fringes). Thus the shear stress at atoms decreases during the nucleation of instabilities there. However, the shear stress in other regions may increase due to the redistribution of the interatomic forces. Resuls plotted in Fig. 4.3e imply that the specimen can still support tangential tractions after the nucleation of instabilities in some regions. After the first discontinuity in the average $\sigma_{xy} - \gamma$ curve in Fig. 4.3e at γ = 0.0872, the average shear stress increases until the point where both the average $\sigma_{xy} - \gamma$ curve and the W - γ curve exhibit sharp discontinuities at γ = 0.102 and several more atoms have become unstable (cf. Figs. 4.12t and 4.12u).

For γ = 0.0872, Fig. 4.25a depicts the distribution of σ_{yy} on the bounding surfaces. Four regions can be distinguished; they are symmetrically distributed by pairs and located parallel to the Z-axis. There are two diametrically opposite regions where σ_{yy} is tensile and in the other two diametrically opposite regions σ_{yy} is compressive. On planes parallel to the YZ and the XZ-planes σ_{yy} changes gradually from tensile (~6 GPa) along one edge parallel to the Z-axis to compressive (~ -6 GPa) on the opposite edge. On the shear XY-plane σ_{yy} at the center varies

between ~0.42 and ~1.80 GPa. Fig. 4.25b shows that after the nucleation of instabilities the symmetry in the distribution of σ_{yy} is lost but its values remain essentially unchanged.

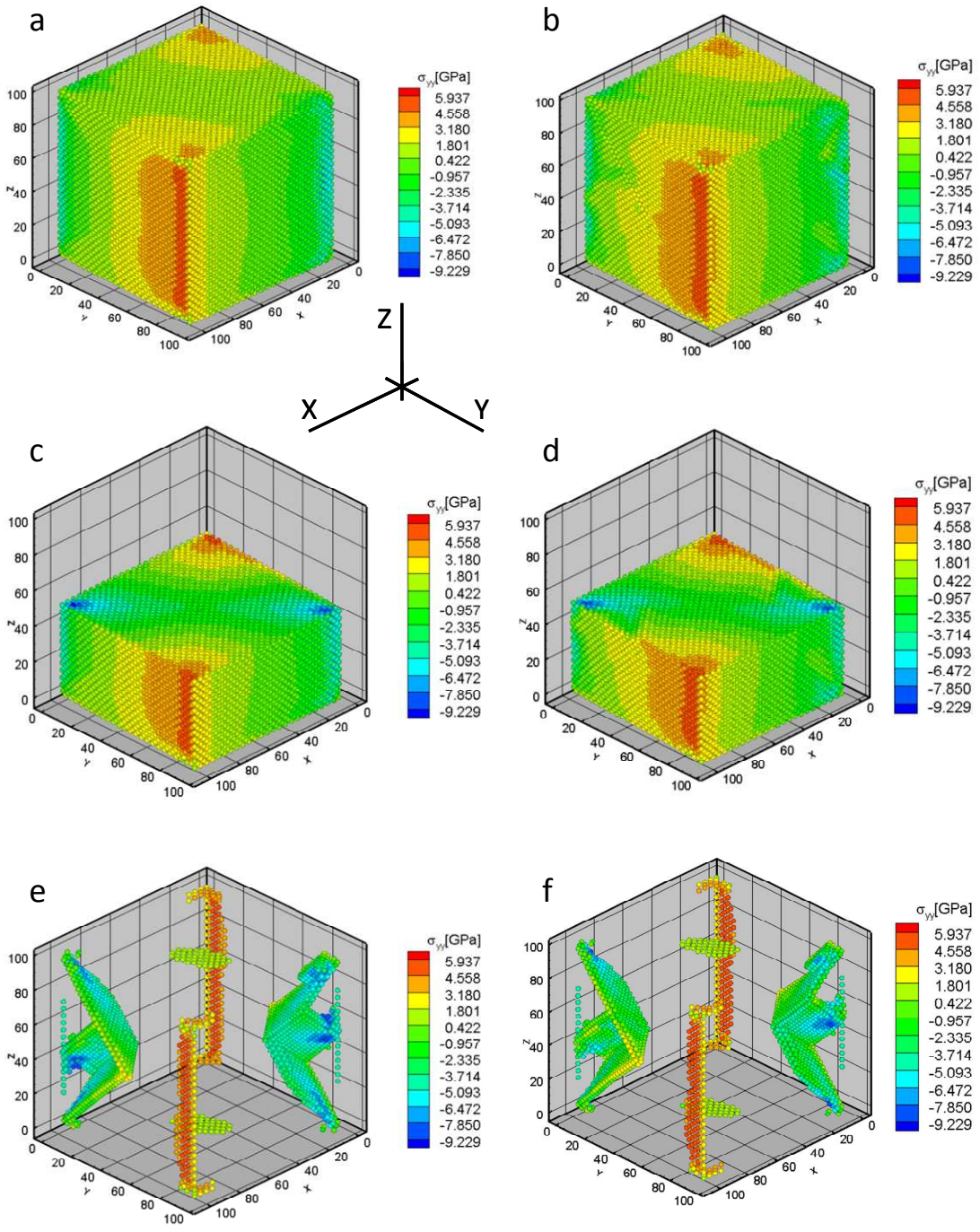

Fig. 4.25. For the shear test, distribution of the σ_{yy} component of the local Cauchy stress tensor on the bounding surfaces, the mid-section and at unstable points in specimen C; (a), (c) and (e) $\gamma = 0.0872$; (b), (d) and (f) $\gamma = 0.0921$.

Fig. 4.25c shows the distribution of σ_{yy} on the section Z = 50Å when $\gamma = 0.0872$. It is clear that high compressive values (~ -9 GPa) of σ_{yy} do not occur at points on planes with the prescribed boundary conditions as we might expect but in two diametrically opposite regions at the corners of the mid-section. The magnitude of compressive σ_{yy} decreases as one goes towards the center. High tensile stresses are located at points on the two free surfaces parallel to the YZ-plane. The distribution and values of σ_{yy} at $\gamma = 0.0921$, shown in Fig. 4.26d, do not change noticeably from those at $\gamma = 0.0872$ except in regions where defects nucleate.

The distributions of σ_{yy} at unstable points for $\gamma = 0.0872$ and $\gamma = 0.0921$ are depicted in Figs. 4.25e and f respectively. Compressive stresses, ~ -9 GPa, at the unstable points decrease after the nucleation of instabilities to -2 GPa; however, the magnitude of the σ_{yy} compressive stress does not decrease at all unstable points. Groups of atoms with tensile σ_{yy} remain unchanged, and the value of σ_{yy} does not decrease during the nucleation of instabilities.

Figs. 4.26a and c show that, at interior points, the value of σ_{xz} is close to zero prior to the drop in the average $\sigma_{xy} - \gamma$ curve but that at points on the four edges parallel to the Y-axis equals ~1 GPa. These atoms are located on opposite edges in the specimen. Atoms on two edges have negative σ_{xz} (light blue ~ -0.9 GPa), and those on the other two edges have positive values of the same magnitude. Figs. 4.26c and e show that at the mid-section and at the atomic positions where instabilities nucleate $\sigma_{xz} \sim 0$ at $\gamma = \gamma^{yield}$. After the nucleation of instabilities other regions with nonzero values of σ_{xz} appear in the specimen. For instance, regions with $\sigma_{xz} \sim 1.5$ GPa and ~ -1.5 GPa can be seen in Fig. 4.26f.

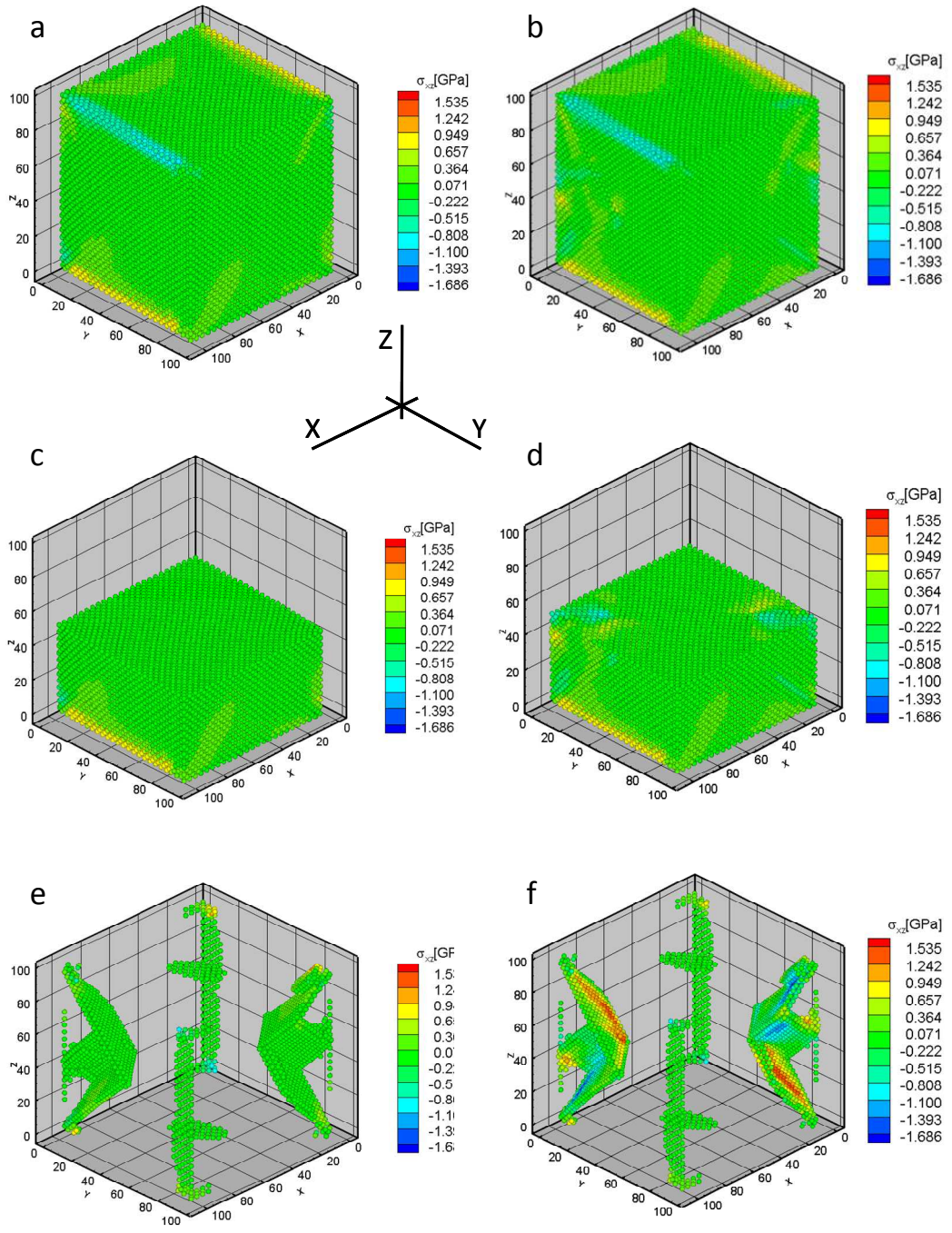

Fig. 4.26. For the shear test, distribution of the σ_{xz} component of the local Cauchy stress tensor on the bounding surfaces, the mid-section and at unstable points in specimen C; (a), (c) and (e) $\gamma = 0.0872$; (b), (d) and (f) $\gamma = 0.0921$.

The distributions of σ_{VM} and $2\tau_{max}$ are depicted in Figs. 4.27 and 4.28 respectively. Twice the maximum shear stress equals the absolute value of the difference between the minimum and the maximum eigenvalues of the Cauchy stress tensor, denoted by P_1 and P_3 respectively. The distributions of σ_{VM} and $2\tau_{max}$ are very similar to each other just before and immediately after the nucleation of instabilities. The highest values of the two stresses are located at points near corners of the mid-section (Z = 50 Å) parallel to the shear XY-plane. After the instabilities have nucleated two new regions of atoms with high values of σ_{VM} and $2\tau_{max}$ appear on the mid-section. From the distributions of σ_{VM} and $2\tau_{max}$ on unstable points depicted in Figs. 4.27e,f and Figs. 4.28e,f it is not clear if the nucleation of instabilities is accompanied by the reduction in the magnitudes in these two stresses. A close look at points with high values of σ_{VM} and $2\tau_{max}$ reveals that, during the nucleation of instabilities, σ_{VM} drops from ~9.5 GPa to 8 GPa, and $2\tau_{max}$ from ~10.5 GPa to ~9 GPa. However, higher values (σ_{VM} = ~9.95 GPa and $2\tau_{max}$ = ~11.45 GPa) of these stresses occur at other points after the nucleation of instabilities.

Figures 4.29a and b show in more detail the distribution of σ_{VM} on planes of unstable points for γ = 0.0872 and γ = 0.0921 respectively. At points with high values of σ_{VM}, such as point 3 in Fig. 4.29, the value of σ_{VM} drops from ~9 to ~8 GPa during the nucleation of instabilities; for point 2 the value of σ_{VM} drops from 8.74 to 7.59 GPa. These two points also have very high compressive principal stresses; -11.42 GPa and -10.07 GPa for points 3 and 2 respectively. New unstable points in the interior of the specimen on planes of high density were not observed. On planes of unstable atoms, points with moderate values of σ_{VM} experience a decrease in σ_{VM} during the nucleation of instabilities. For example, at point 1 in Fig. 4.29 σ_{VM} drops from 6.67 GPa to 3.36 GPa; point 1 also has a high value of compressive stresses ~ -8 GPa at the yield point. Values of stresses at points 1, 2 and 3 before and after the drop in the average $\sigma_{xy} - \gamma$ curve are summarized in Table 4.5

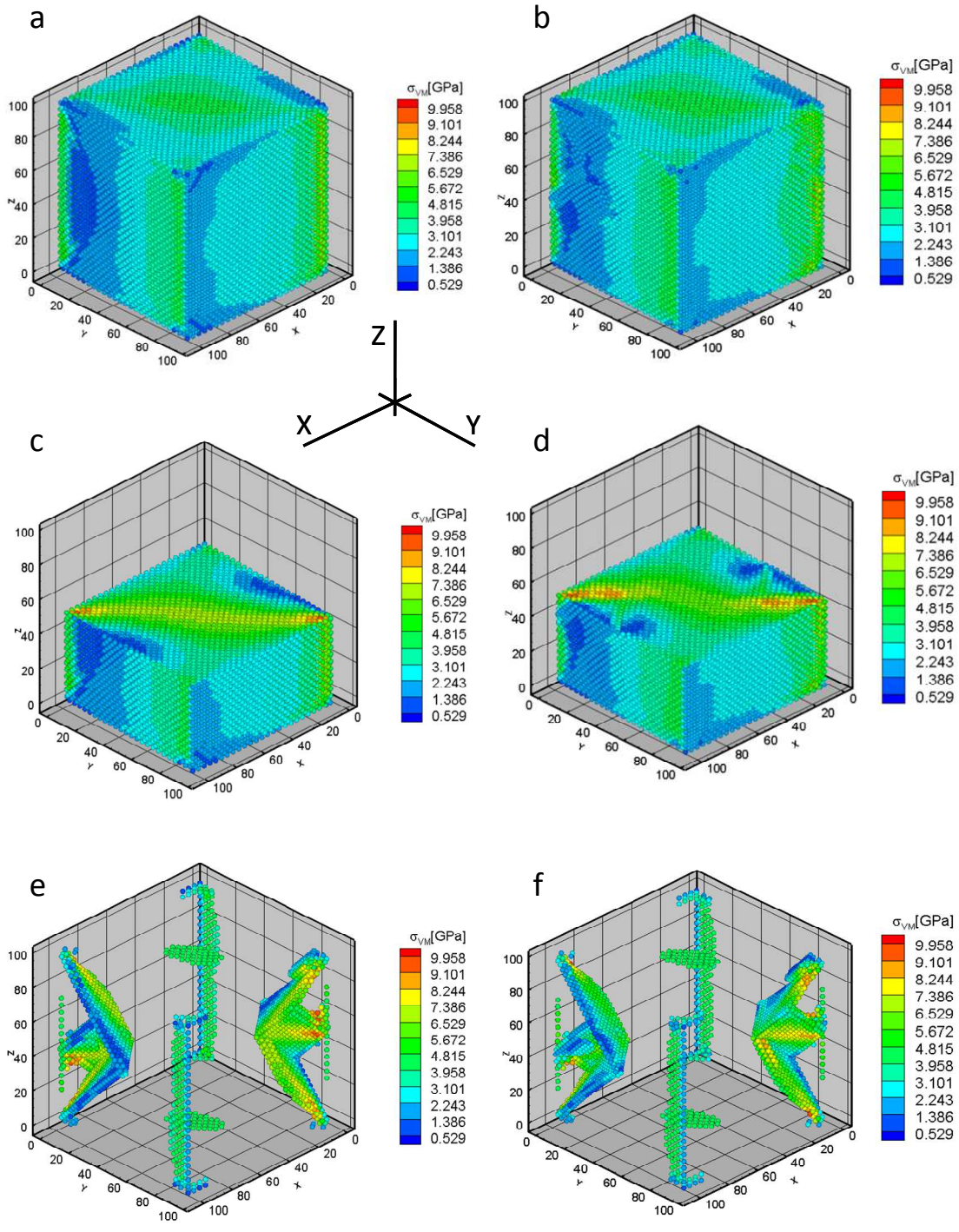

Fig. 4.27. For the shear test, distribution of the σ_{VM} on the bounding surfaces, the mid-section and at unstable points in specimen C; (a), (c) and (e) $\gamma = 0.0872$; (b), (d) and (f) $\gamma = 0.0921$.

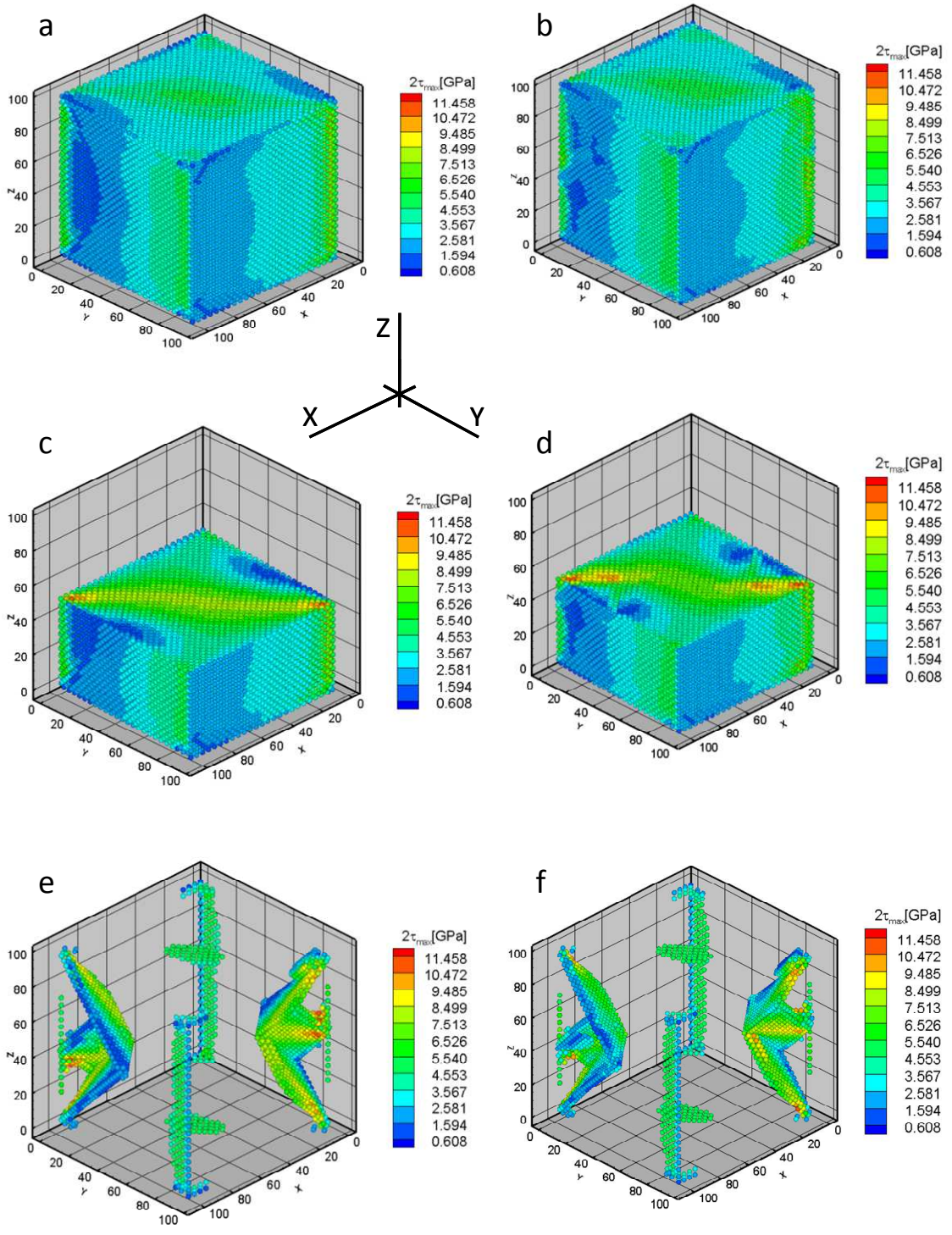

Fig. 4.28. For the shear test, distribution of the $2\tau_{max}$ on the bounding surfaces, the mid-section and at unstable points in specimen C; (a), (c) and (e) $\gamma = 0.0872$; (b), (d) and (f) $\gamma = 0.0921$.

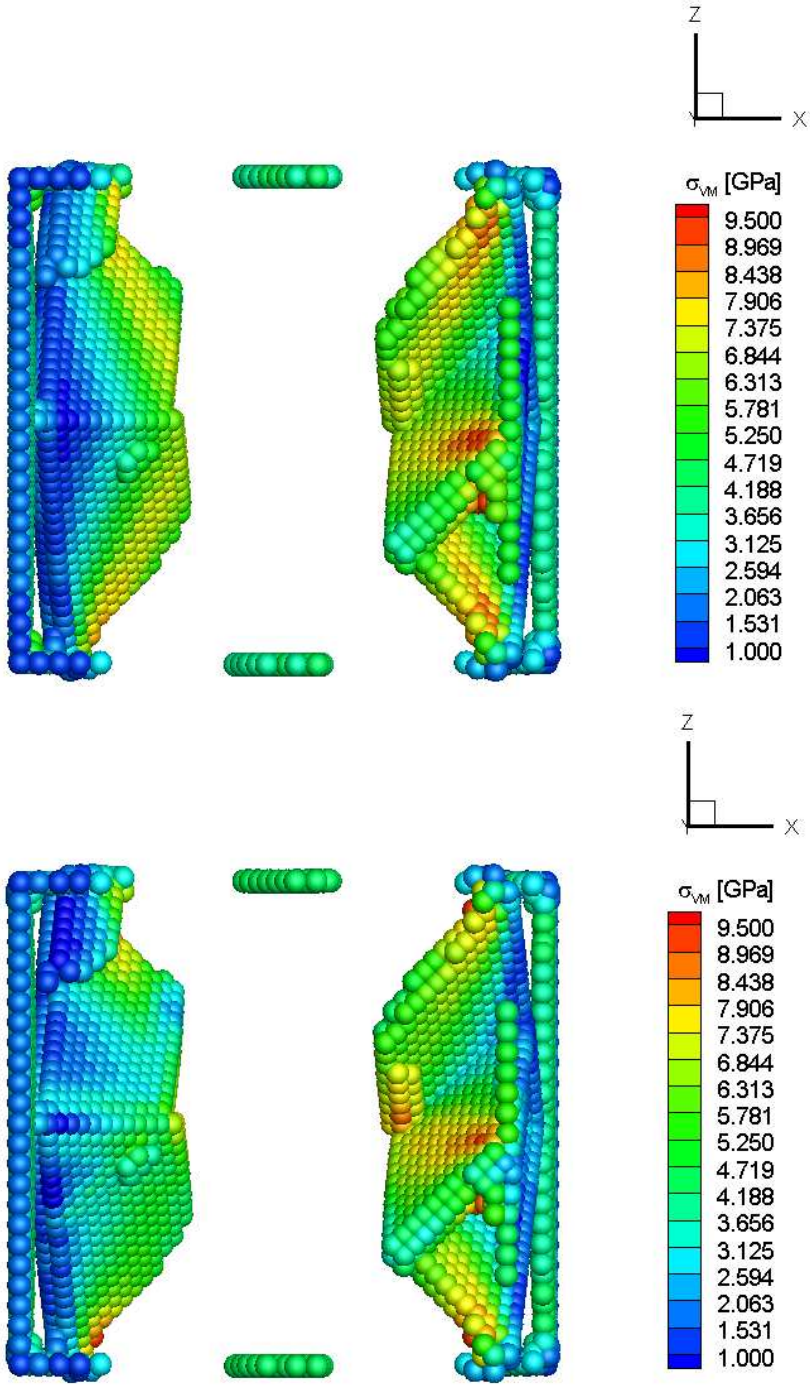

Fig. 4.29. For the shear test, distribution of the σ_{VM} at unstable points in specimen C; (a) $\gamma = 0.0872$; (b) $\gamma = 0.0921$.

Table 4.5: From results of the shear test on specimen C, values of σ_{xy}, σ_{VM}, $2\tau_{max}$, and principal stresses P_1, P_2 and P_3 at points 1, 2, and 3 depicted in Fig. 4.29.

Stress (GPa)	Pre-instability Point 1	Post-instability Point 1	Pre-instability Point 2	Post-instability Point 2	Pre-instability Point 3	Post-instability Point 3
σ_{VM}	6.672	3.364	8.741	7.594	9.038	7.968
σ_{xy}	3.747	1.186	4.043	3.864	4.646	3.512
P_1	-8.004	-3.641	-10.075	-8.386	-11.424	-9.900
P_2	-3.079	-1.701	-4.733	-3.884	-5.691	-4.105
P_3	-0.411	0.243	-0.215	0.381	-1.004	-0.813
$2\tau_{max}$	7.593	3.884	10.075	8.767	10.419	9.087

4.10 Distributions of local stresses for the simple shear tests

Fig. 4.30 depicts, for specimen C, the distribution on the mid-section of different stresses for configurations corresponding to $\gamma = \gamma^{yield}$ and $\gamma = 0.1703$. Fig. 4.30a shows the distribution of σ_{xy} at $\gamma = \gamma^{yield}$. In this configuration a band of high shear stress crosses the XY-shear plane along the diagonal. Values of σ_{xy} range from ~10 GPa at the center of the band to ~8 GPa at points near the extremities of the band. At points on the bounding surfaces the shear stress varies between ~1.5 and 6 GPa. The average value of σ_{xy} obtained in section 4.4.2 is 9.170 GPa (cf. Table 4.2) which agrees with the average of the distribution of the local values of σ_{xy} presented in Fig. 4.30a. After the nucleation of instabilities spatial symmetries in the stress distribution are lost and values of the shear stress at most places drop to ~1.5 GPa (cf. Fig. 4.30b). Negative values of σ_{xy} at some points are also observed after the nucleation of instabilities.

Fig. 4.30c depicts the distribution of the normal stress σ_{yy} at $\gamma = \gamma^{yield}$. Values of σ_{yy} are uniformly distributed on the mid-section and equal ~8 GPa. Smaller values between ~-0.7 and ~0.9 GPa occur on the bounding surfaces initially parallel to the YZ-plane. Values of $\sigma_{yy} < -10$

GPa occur at the specimen corners that are close to surfaces parallel to the XZ-coordinate planes. We recall that the average value of σ_{yy} in Fig. 4.6f at the yield point is ~ -8 GPa. After the nucleation of instabilities (cf. Fig. 4.30d) the initially high compressive stress at the center of the section drop to values between ~1 GPa and ~ -3 GPa, and high tensile stresses (~ 4 GPa) are generated at points on bounding surfaces initially parallel to the YZ-plane.

Fig. 4.30e exhibits the distribution of the shear stress σ_{xz} at $\gamma = \gamma^{yield}$. This component of the Cauchy stress tensor has negligible values for strains up to the yield point; a similar distribution was observed for the component σ_{yz}. After the nucleation of instabilities magnitudes of these shear stresses increase at some points to 4 GPa. Average values of σ_{xz} and σ_{yz} are also close to zero for $\gamma \leq 0.1655$ (cf. Fig. 4.6e).

The distributions of σ_{VM} and $2\tau_{max}$ in the specimen at the yield point are depicted in Figs. 4.30g and 4.30i respectively. These two distributions are identical but $2\tau_{max}$ is slightly greater than σ_{VM}. High values, ~17 GPa, of σ_{VM} are observed along the diagonal of the shear plane. Outside the band, σ_{VM} varies between ~14 GPa and ~16 GPa. Smaller values occur at points on bounding surfaces with a minimum value of ~5 GPa at edges parallel to the Z-axis. The rather high values of σ_{VM} and $2\tau_{max}$ are observed in two regions close to the corners where $|\sigma_{yy}|$ is also large.

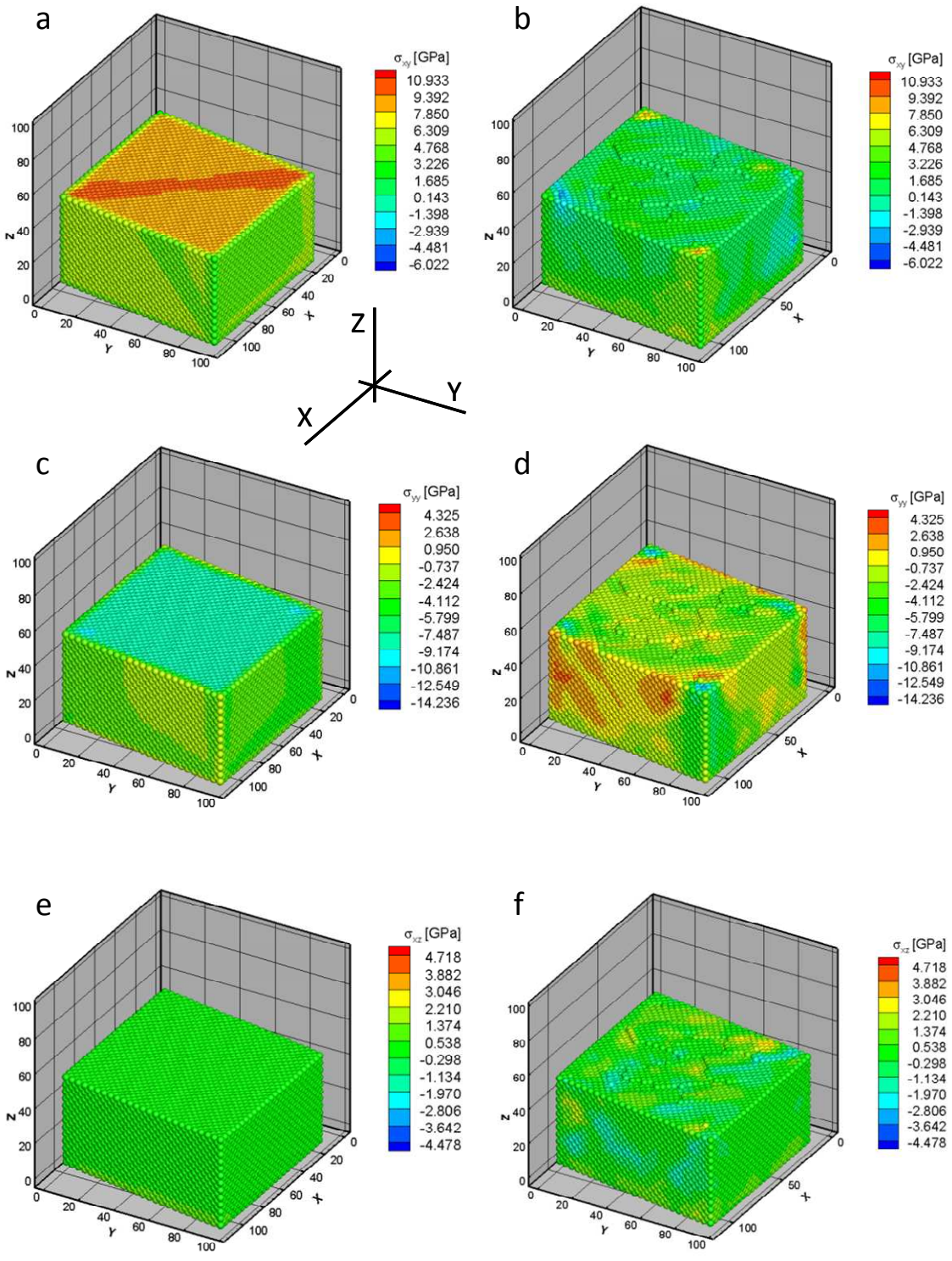

Fig. 4.30. Contd.

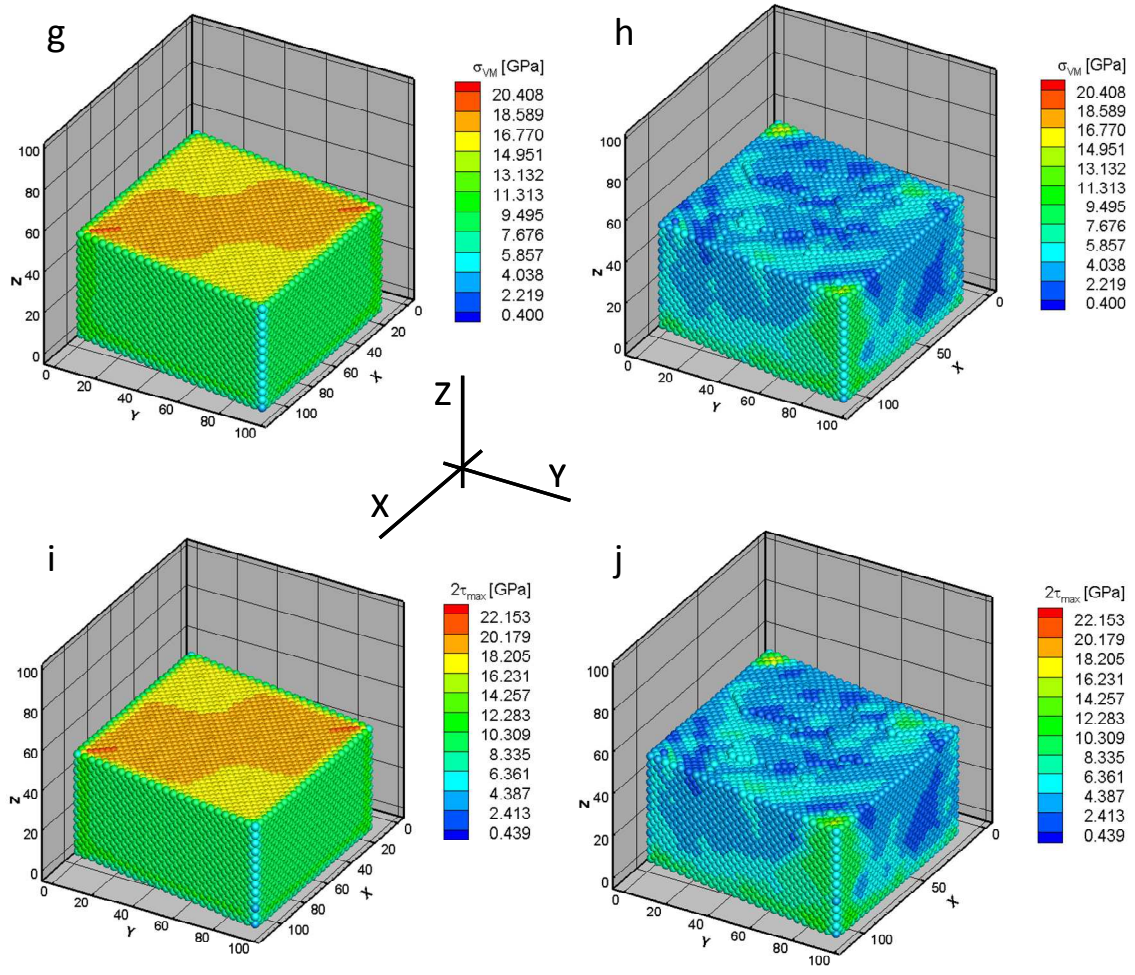

Fig. 4.30. For the simple shear test, distributions of σ_{xy}, $\sigma_{yy,}$ $\sigma_{xz,}$ σ_{VM} and $2\tau_{max}$ on the mid-section of specimen C; (a), (c) , (e), (g) and (i) $\gamma = 0.1655$; (b), (d), (f), (h) and (j) $\gamma = 0.1703$.

Chapter 5

Instabilities in tensile and compressive deformations

5.1 Introduction

In this chapter we study instabilities in tensile and compressive deformations of square gold specimens. Two types of boundary conditions are considered: one in which all atoms on the end faces are constrained to move axially only, and the other in which only their axial motion is prescribed but they are free to move in transverse directions. The former set of deformations are called tensile/compressive and the latter simple tensile/compressive. The average stresses and strains are computed and the influence of the length/width (L/H) ratio on the average axial yield stress is delineated. The correlations, if any, between distributions of internal stresses and material instabilities are investigated. Local stresses are computed by using Hardy's Eq. (2.23).

5.2 Simulation of deformations

We simulate tensile and compressive deformations of Au crystals having a fixed square cross section but different lengths. The width H of specimens is ~37 Å and their lengths range from ~37 Å for L/H = 1 to ~742 Å for L/H = 20; the number of atoms in a specimen is listed in Table 5.1. In each case the specimen is oriented with the coordinate planes {1,0,0}, {0,1,0} and {0,0,1}. For the tension/compression tests, atoms in the reference configuration located on planes $Y = Y_{min}$ and $Y = Y_{max}$ are constrained from moving in the X- and the Z-directions while the Y-displacement is prescribed in increments of 0.25 Å. For the simple tension/compression tests, atoms on planes $Y = Y_{min}$ and $Y = Y_{max}$ and located along the centroidal line parallel to the X-axis are constrained from moving in the Z-direction; atoms located along the centroidal line parallel to the Z-axis are constrained from moving in the X-direction. Thus all cross sections of a specimen are allowed to expand or contract. The Y-displacement is prescribed in increments of 0.25 Å. Once a discontinuity in the strain energy density vs. the axial strain curve is observed the

simulations are restarted from the immediately preceding displacement increment with the prescribed Y-displacement increment reduced to 0.1 Å. There are no external forces applied on the four lateral surfaces.

Table 5.1: Aspect ratios, number of atoms, and lengths of specimens tested in tension and compression.

L/H	No. of atoms	Length (Å)
1	3430	~37
3	9928	~110
5	16787	~188
10	32671	~367
20	65883	~742

5.3 Average stresses and strains from numerical simulations

5.3.1 Tension/compression

For different L/H ratios Fig. 5.1a,b shows the variation with the average axial strain ε (change in length per unit initial length) of the average values of σ_{xx} and σ_{yy} components of the Cauchy stress tensor computed using Eq. (2.7). It is observed that the variation with ε of the average σ_{yy} stress is the same for L/H ≥ 3. For L/H = 1 all normal stresses are of the same order of magnitude showing a very different behavior as compared to that for samples having L/H ≥ 3. For a square cross section σ_{zz} equals σ_{xx}. Note that atoms on the end faces are constrained to move axially only; thus these cross sections do not change. With an increase in L/H, the average values of σ_{xx} and σ_{zz} decrease and are nearly $1/10^{th}$ of the average value of σ_{yy}. The average values of all shear stresses are negligible till discontinuities in the σ_{yy} vs. ε curve occur. Subsequent to the occurrence of these discontinuities, values of local shear stresses may not be very small and are comparable to the values of the local normal stresses in regions close to edges and vertices of the specimen. In Table 5.2 we have listed, for different L/H ratios, average values of σ_{yy} and ε at yield identified by a sharp drop in the average axial stress for an infinitesimal increase in the average axial strain. Values of the axial yield stress and the corresponding axial strain for L/H ≥ 3 for tension are ~ 6.2 GPa and ~ 9.8%, respectively. However, values of the axial stress and the axial strain at the yield point in compression for L/H=1 and 20 differ noticeably from those for L/H = 3, 5 and 10.

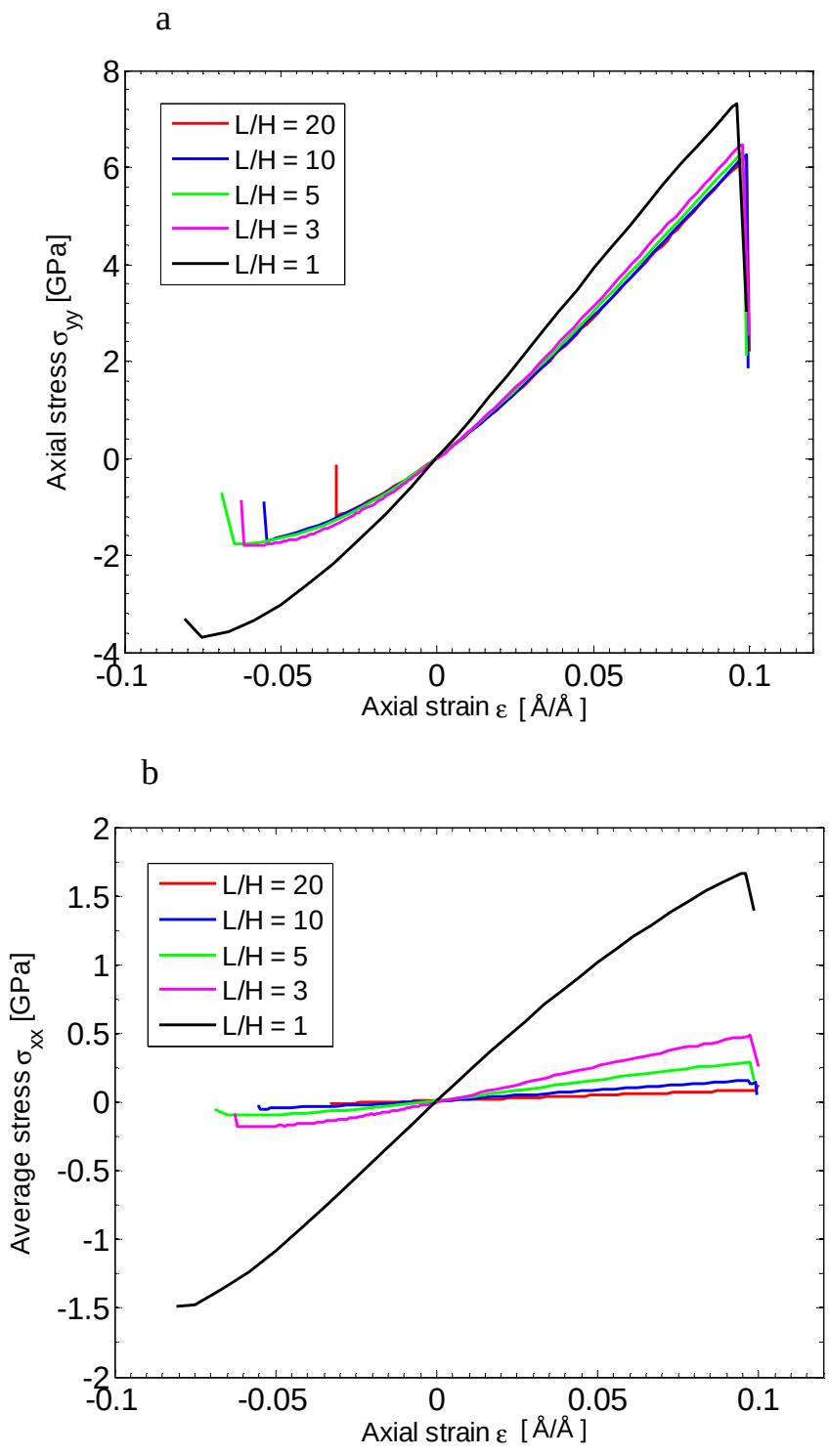

Fig. 5.1. Evolution with the average axial strain ε of the average values of components of the Cauchy stress tensor for the tension/compression tests for different L/H ratios. (a) σ_{yy}; (b) σ_{xx}.

For the same L/H ratio asymmetry in the yield stress in tension and compression is apparent from values listed in Table 5.2 as was also found by Diao et al. (2004, 2006), and Zhang et al. (2008). This asymmetry is attributed to initial stresses in the reference configurations of specimens. The internal compressive stresses induced by the surface tension cause a local critical stress in compression to be reached at a smaller strain level than that in an initially stress free specimen. Whereas the average axial stress vs. the average axial strain curve is essentially linear in tension that in compression is nonlinear. For the specimen with L/H=20, we have not examined closely details of deformation fields to ascertain if any other instability (e.g., buckling) initiated up to an average axial strain of 3.245%.

Fig. 5.2 depicts σ_{yy} vs. ε curves by computing average values of stresses with definition (2.7) of the virial stress, Eq. (3.10) for the first moment of forces on bounding surfaces, and the mechanics of materials approach (force/area) in which forces along the Y- direction of atoms on an end face of the specimen have been considered. The three values are in good agreement with each other. The average values of stresses do not give any information about their local values.

Fig. 5.4 shows the variation with the average axial strain of the strain energy density. The σ_{yy} versus ε curves show a discontinuity at the strain level where the energy density for the entire system decreases noticeably. The variation of the strain energy density for L/H = 1 is different from that for specimens with $L/H \geq 3$.

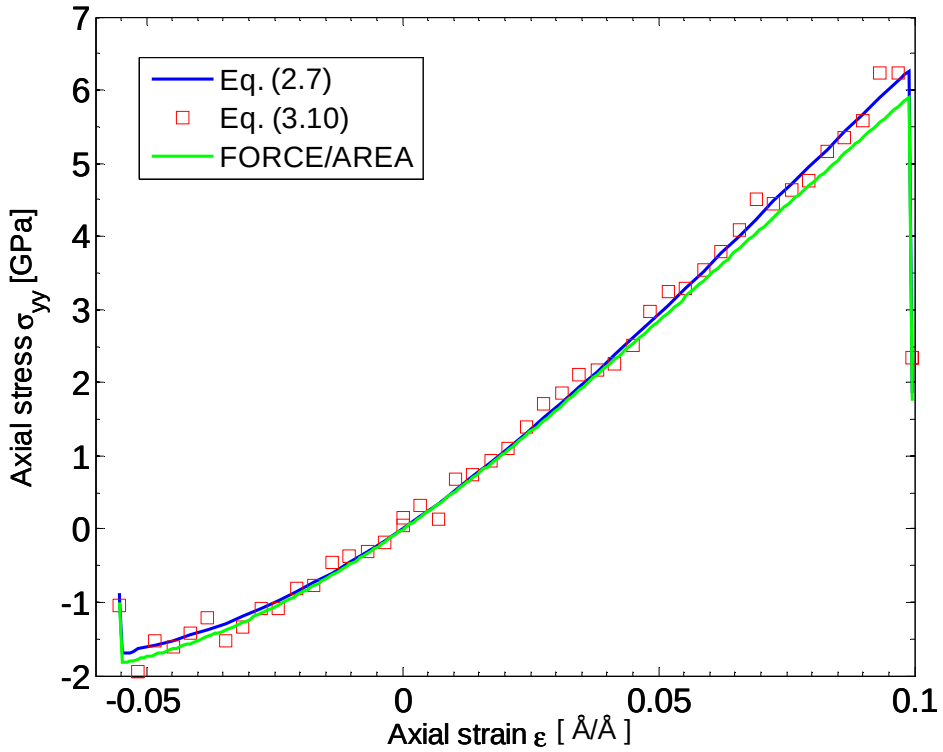

Fig. 5.2. Comparison of three measures of the Cauchy stress tensor for L/H=10 in tension/compression tests; Eq. (2.7), Eq. (3.10) and the mechanics of materials approach (force/area).

Table 5.2: Values of the average axial stress and the average axial strain at the yield point for specimens with different L/H ratios deformed in tension and compression.

	Tension		Compression	
L/H	σ_{yy}^{yield} (GPa)	ε_{yy}^{yield} (%)	σ_{yy}^{yield} (GPa)	ε_{yy}^{yield} (%)
1	7.317	9.597	-3.698	-7.789
3	6.481	9.745	-1.783	-6.182
5	6.344	9.809	-1.788	-6.764
10	6.256	9.883	-1.704	-5.460
20	6.242	9.942	-1.209	-3.245

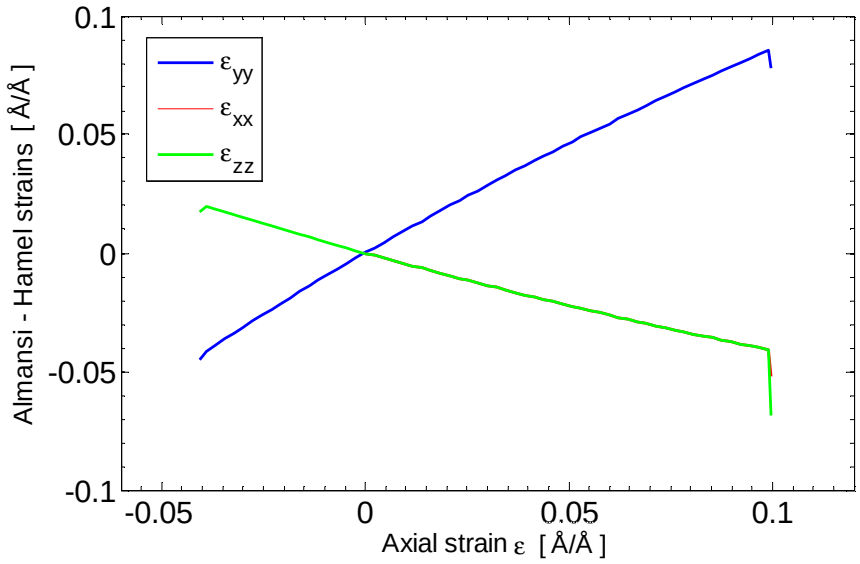

Fig. 5.3. For L/H=10, evolution with the average axial strain ε of the average values of the normal components of the Almansi-Hamel strain tensor for the tension/compression tests. Curves for ε_{xx} vs. ε and ε_{zz} vs. ε overlap each other.

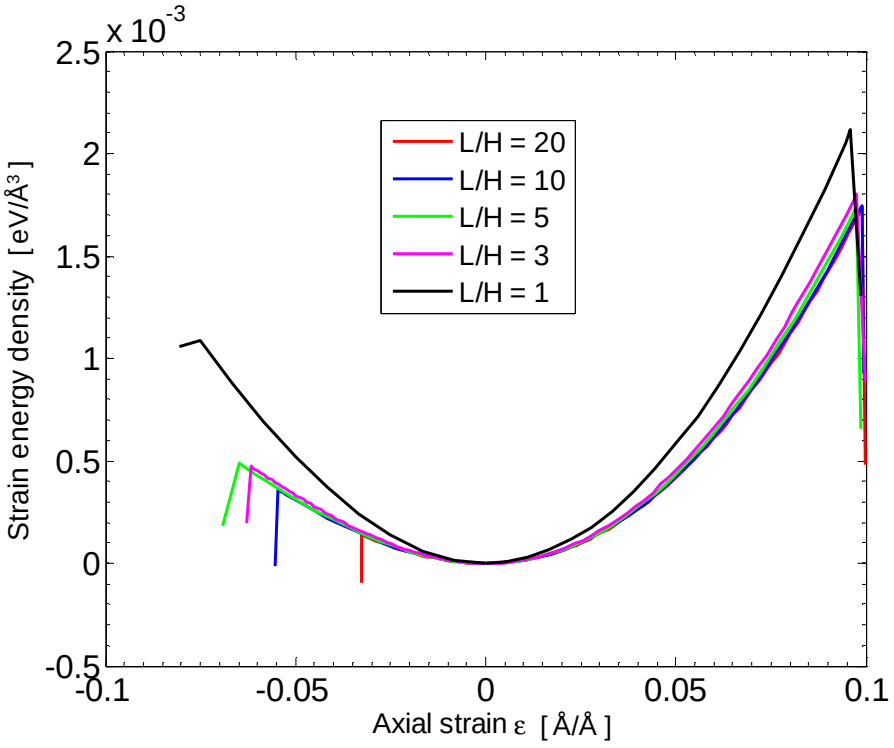

Fig. 5.4. Variation with the average axial strain ε of the strain energy density in tension/compression tests.

The evolution of the average values of normal components of the Almansi-Hamel strain tensor with the average axial strain for a specimen with L/H=10 is plotted in Fig. 5.3; curves for ε_{xx} vs. ε and ε_{zz} vs. ε overlap each other. The equality of ε and ε_{yy} suggests that, on the average, effects of geometric nonlinearities can be neglected up to the yield point. Normal strains in the transverse direction have opposite sign to that in the axial direction showing Poisson's effect. The averaged components of the shear strains are negligible. A similar behavior is observed for other values of $L/H \geq 3$.

5.3.2 Simple tension/compression

For different L/H ratios, Fig. 5.5 shows the variation with ε of the average value of σ_{yy} component of the Cauchy stress tensor found by using Eq. (2.7). In agreement with results for the tension/compression simulations reported in subsection 5.3.1, it is observed that the variation with ε of the average value of σ_{yy} is the same for specimens with $L/H \geq 3$. However, for the simple tension/compression simulations, the average values of σ_{zz} and σ_{xx} are negligible as compared to the average values of σ_{yy}. The applied boundary conditions allow atoms on the end faces to move freely in the X- and the Z-directions; consequently, edge effects are negligible and averaged values of σ_{zz} and σ_{xx} are very small.

As in the tension/compression tests the average values of all shear stresses are negligible up to the discontinuity in the σ_{yy} vs. ε curves. In Table 5.3 we have listed, for different L/H ratios, values of the average σ_{yy} stress and the average axial strain at the yield point. Values of the axial yield stress and the average axial strain at yield for $10 \geq L/H \geq 3$ for the simple tension case are ~ 5 GPa and ~ 8% respectively; the corresponding values for the tension test are ~ 6.2 GPa and ~ 9.8%. In simple compression, a dependence of the axial yield stress and the average axial strain at yield on the L/H ratio is also observed. For a given value of L/H, the yield stress in simple tension is higher than that in simple compression. Because of residual stresses in the reference configuration, the difference in the yield stress in simple tension and simple compression cannot be attributed to the Bauschinger effect.

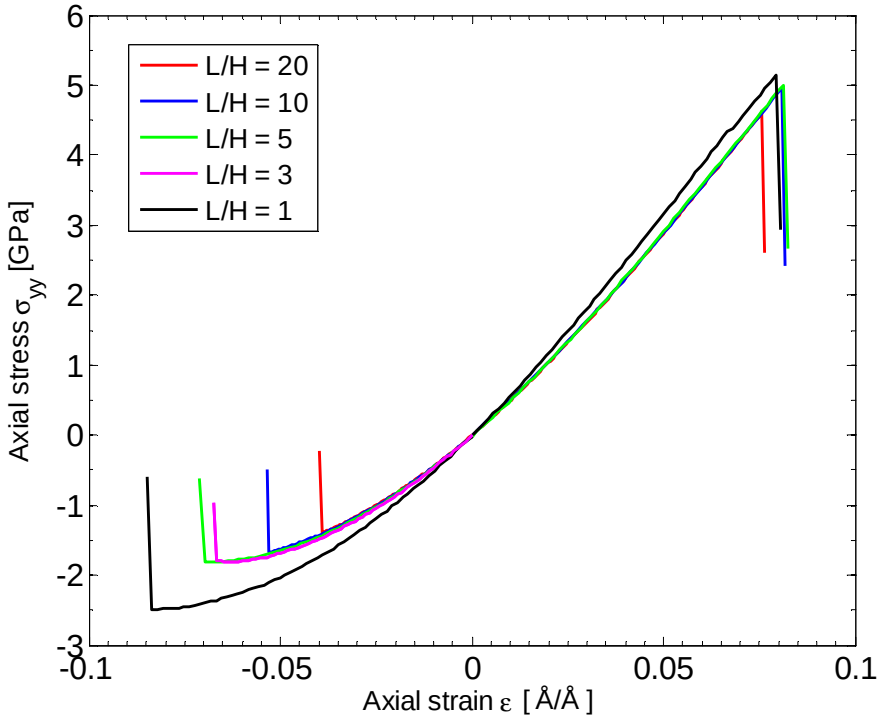

Fig. 5.5. For different values of L/H, evolution with the average axial strain ε of the average value of σ_{yy} component of the Cauchy stress tensor for the simple tension/compression tests.

For simulations of the simple tension and the simple compression deformations of the sample with L/H = 10, we have plotted in Figs. 5.6 through 5.9, incremental displacements in going from the configuration just prior to the system yielding to the configuration in which it yields, and incremental displacements in going from the yielded state to the immediately next configuration. In order to clearly show results incremental displacements of only unstable atoms are displayed in Figs. 5.7 and 5.9. Prior to the initiation of yielding, displacements of all atoms in the transverse directions equal nearly one-tenth of that in the axial direction. However, in going from the yielded state to the next configuration, several atoms that have become unstable undergo displacements in all three directions whose magnitude is of the order of the lattice parameter. Since several atoms have become unstable, it is an arduous task to find Burger's vectors and classify dislocations into different categories.

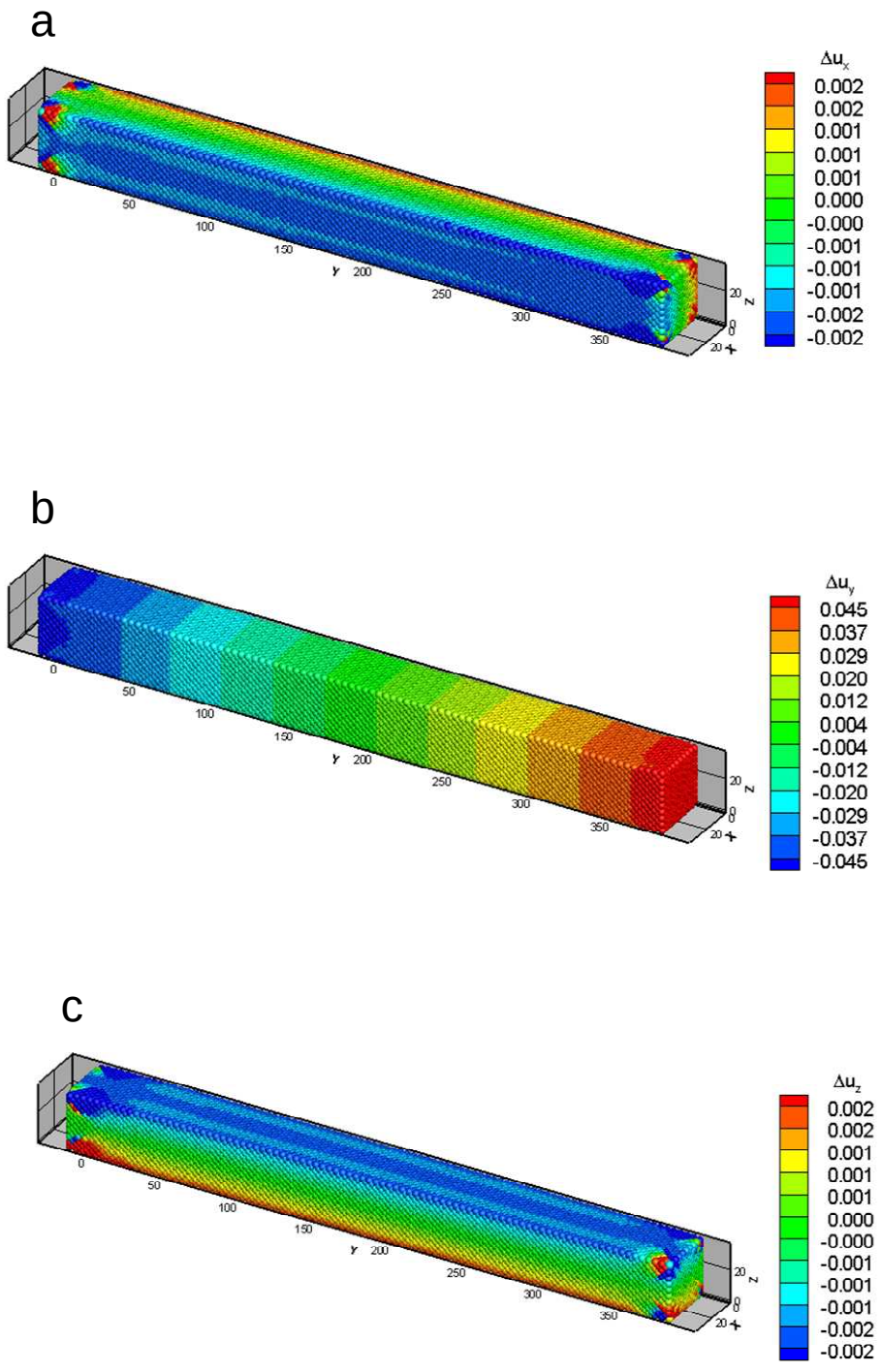

Fig. 5.6. For the simple tension test, distributions of the changes in the components of the displacement field on the bounding surfaces at ε = 8.08% in the specimen with L/H=10; (a) Δu_x; (b) Δu_y; (c) Δu_z. (Displacements in Å)

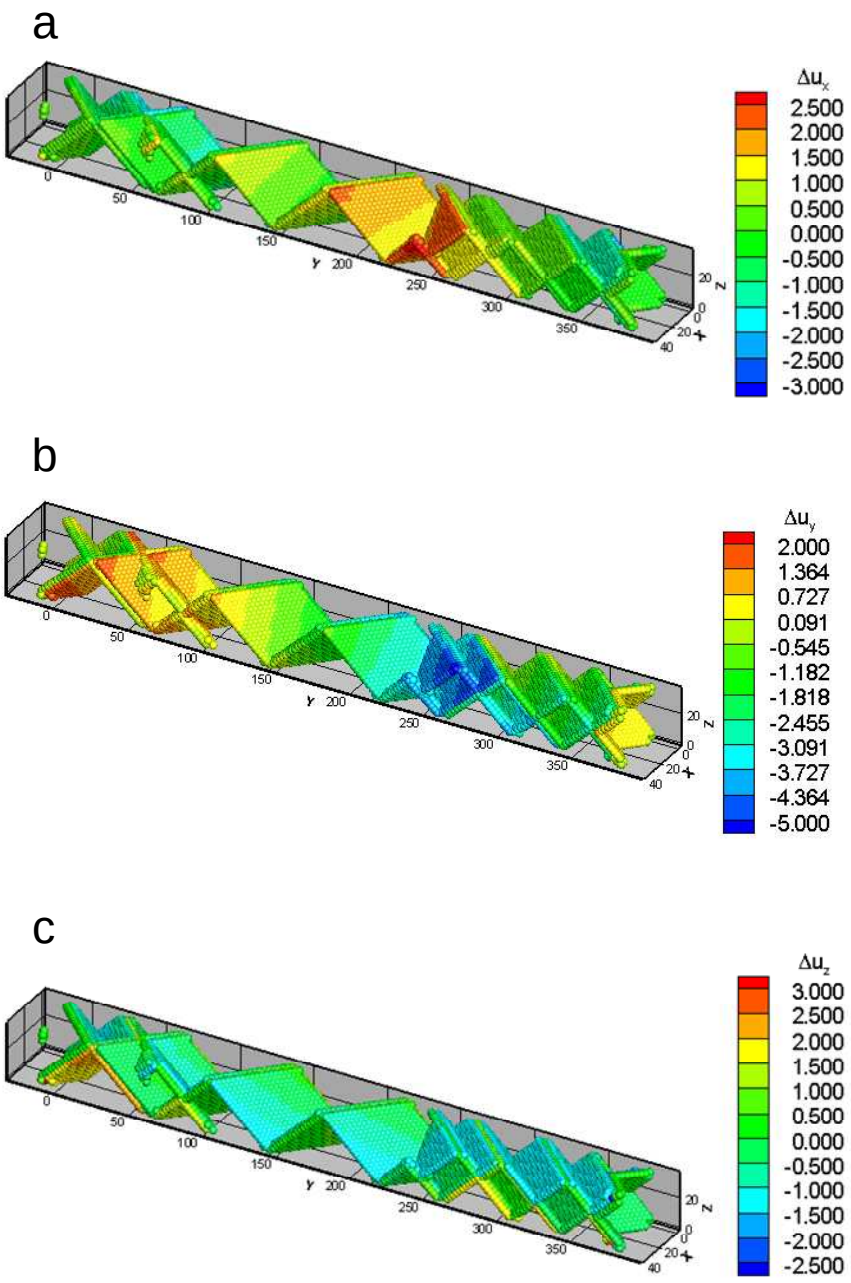

Fig. 5.7. For the simple tension test, distributions of the changes in the components of the displacement field at points where instabilities have initiated at ε = 8.15% in the specimen with L/H=10; (a) Δu_x; (b) Δu_y; (c) Δu_z. (Displacements in Å)

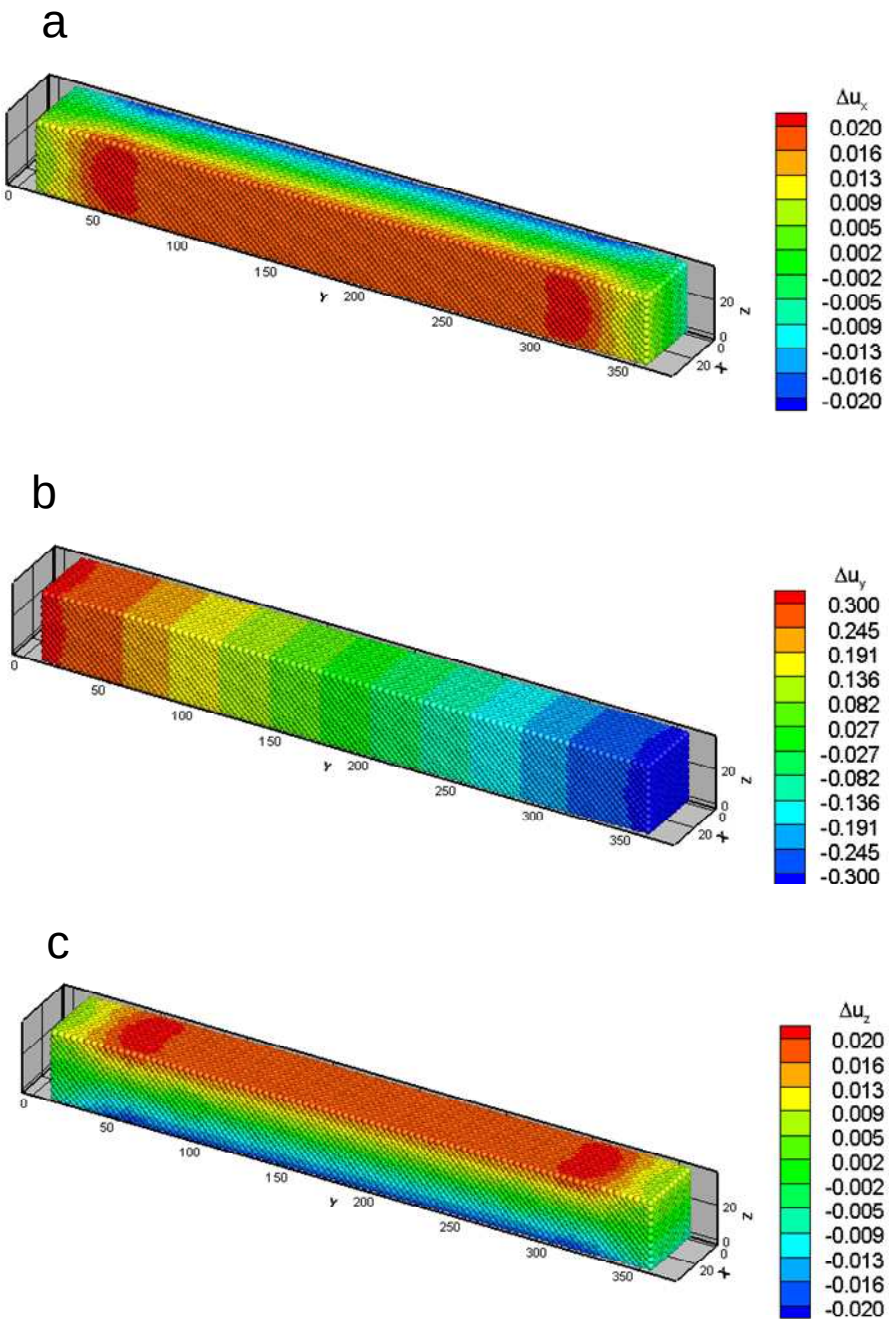

Fig. 5.8. For the simple compression test, distributions of the changes in the components of the displacement field on the bounding surfaces at ε = -5.15%; (a) Δu_x; (b) Δu_y; (c) Δu_z. (Displacements in Å)

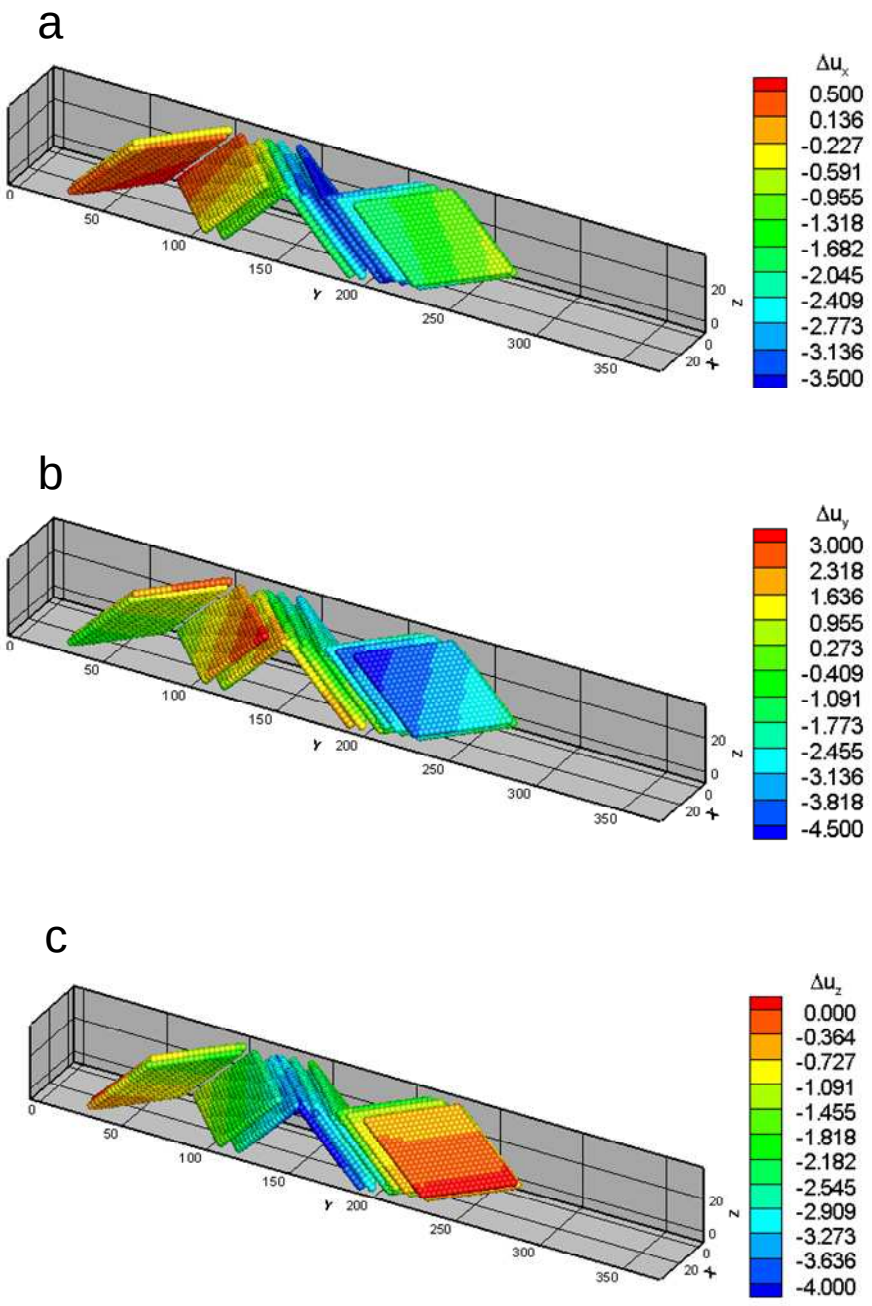

Fig. 5.9. For the simple compression test, distributions of the changes in the components of the displacement field at points where instabilities have initiated at ε = -5.16%; (a) Δu_x; (b) Δu_y; (c) Δu_z. (Displacements in Å)

As evidenced from results exhibited in Fig. 5.10, a good agreement between three measures of average stresses is found but in this case there is more scatter in data from the first moment of forces on bounding surfaces than that from the other two methods. The number of atoms on bounding surfaces with nonvanishing forces is less as compared to that in the tension/compression simulations. With more of such atoms the scatter in the data will decrease, e.g. see results of the shear test for specimen C plotted in Fig. 4.3.

For L/H = 10, the evolution of the average normal components of the Almansi-Hamel strain tensor with the average axial strain is plotted in Fig. 5.11. Curves for ε_{xx} vs. ε and ε_{zz} vs. ε overlap each other, and ε_{yy} is almost equal to ε till the specimen yields. Thus the effect of geometric nonlinearities can be ignored until the yield point.

For an FCC material the effective Young's modulus in the loading direction [0,1,0] is given by

$$E = \frac{\tilde{C}_{11}^2 + \tilde{C}_{12}\tilde{C}_{11} - 2\tilde{C}_{12}^2}{\tilde{C}_{11} + \tilde{C}_{12}}.$$

From the elastic constants of gold at 0 K listed in Table 2.1, Young's modulus in the Y-direction is found to equal 46.5 GPa. For the computation of *E* from results of the MM simulations a representative length L_g was defined around the mid-section of each specimen. The average axial stress - the average axial strain curves obtained by taking contributions of atoms inside the length L_g were used to find *E*. The simple tension/compression tests were performed up to $\varepsilon = 1\%$ and the slopes of the stress-strain curves were computed by linear regression. For the specimen having L/H = 10, Fig. 5.12a shows the variation with L_g/a (recall that *a* is the lattice parameter) of *E* in simple tension and compression. For $L_g/a < 10$ the value of *E* varies between 46.8 GPa and 47.9 GPa; the difference between the maximum and the minimum values of *E* is only 2.3%. For $10 < L_g/a < 40$ the value of *E* equals ~ 47.1 GPa. For $L_g/a > 40$ a small increase in the values of *E* is found. Boundary effects are reflected in changes of the distribution of interatomic forces but their influence along the axial direction goes up to 1 or 1.5 times the value of specimen's width in agreement with Saint-Venant's principle. The computed value 47.1 GPa of *E* in the Y-direction is only 1.3% higher than the 46.5 GPa obtained from elastic constants of the material.

Recalling Eq. (2.3) and the result that the average values of σ_{xx} and σ_{zz} equal zero, we get

$$\nu = -\frac{\varepsilon_{xx}}{\varepsilon_{yy}} = \frac{\tilde{C}_{12}}{\tilde{C}_{11} + \tilde{C}_{12}}$$

For the specimen with L/H = 10, Fig. 5.12b exhibits the variation of ν with L_g/a. For $10 < L_g/a < 30$, the computed value 0.478 of ν agrees well with 0.453 obtained from values of $\tilde{C}_{11}$ and $\tilde{C}_{12}$ listed in Table 2.1.

We note that *E* and ν can be computed from the average values of stresses and strains, and not from the plots of local values of σ_{yy}, ε_{yy} and ε_{xx} since the stress state locally is not that of uniaxial tension/compression.

Results exhibited in Fig. 5.13 reveal that the variation with the average axial strain of the strain energy density for $3 \leq L/H \leq 20$ is essentially independent of the aspect ratio L/H. However, the yield stress in simple compression depends noticeably upon the value of L/H.

In Fig. 5.14 we have plotted the averagae axial stress vs. the average axial strain during unloading from two configurations – one just before the drop in the average axial stress vs. the average axial strain curve and the other just after this drop. When the specimen is unloaded from the configuration just before the average axial stress drops noticeably, the average axial stress vs. the average axial strain curve during unloading overlaps that during loading suggesting that the specimen deformed elastically. However, when the specimen is unloaded by reversing the direction of prescribed axial incremental displacements from the configuration just after the severe drop in the axial stress or the strain energy density, there is a residual average axial strain at zero average axial stress. It confirms that the specimen deformed plastically during the instant the average stress dropped.

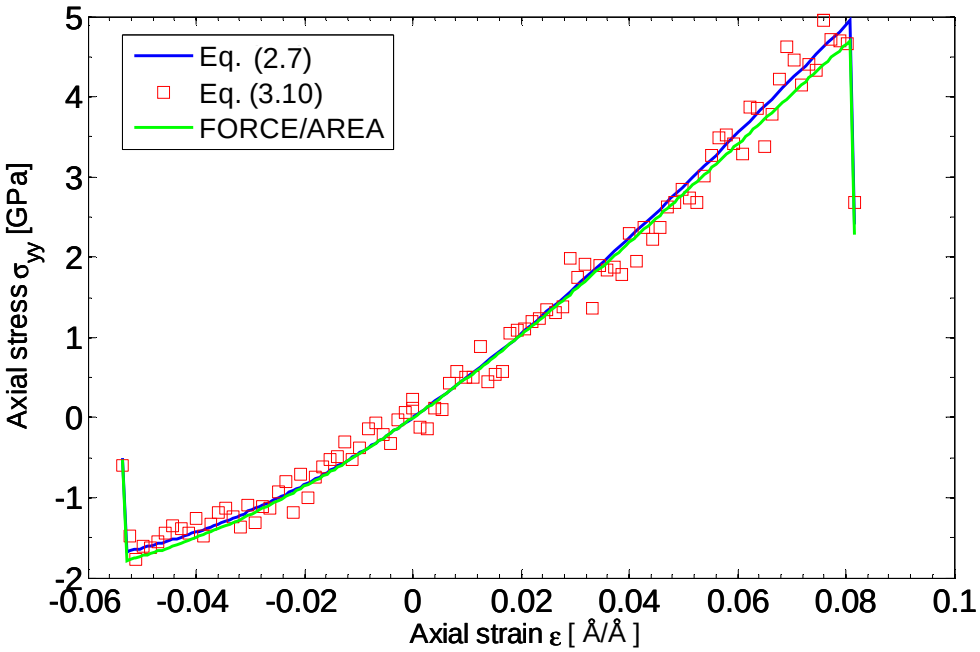

Fig. 5.10. For L/H=10, comparison between different measures of the average Cauchy stress tensor in the simple tension/compression tests, (Eq. 2.7), (Eq. 3.10) and the mechanics of materials approach (force/area).

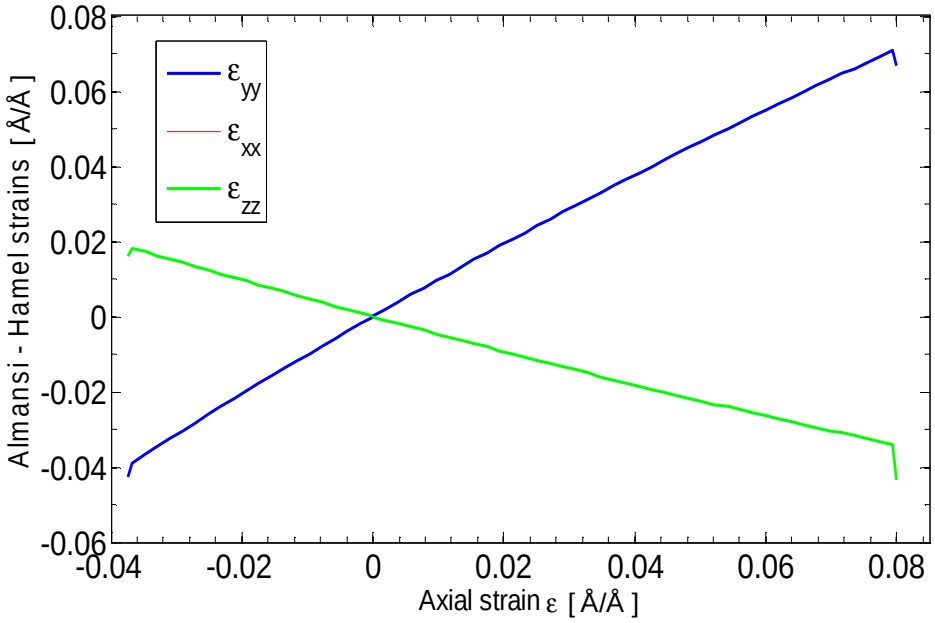

Fig. 5.11. For L/H=10, evolution with the average axial strain ε of the average values of normal components of the Almansi-Hamel strain tensor for the simple tension/compression tests. Curves for ε_{xx} vs. ε and ε_{zz} vs. ε overlap each other.

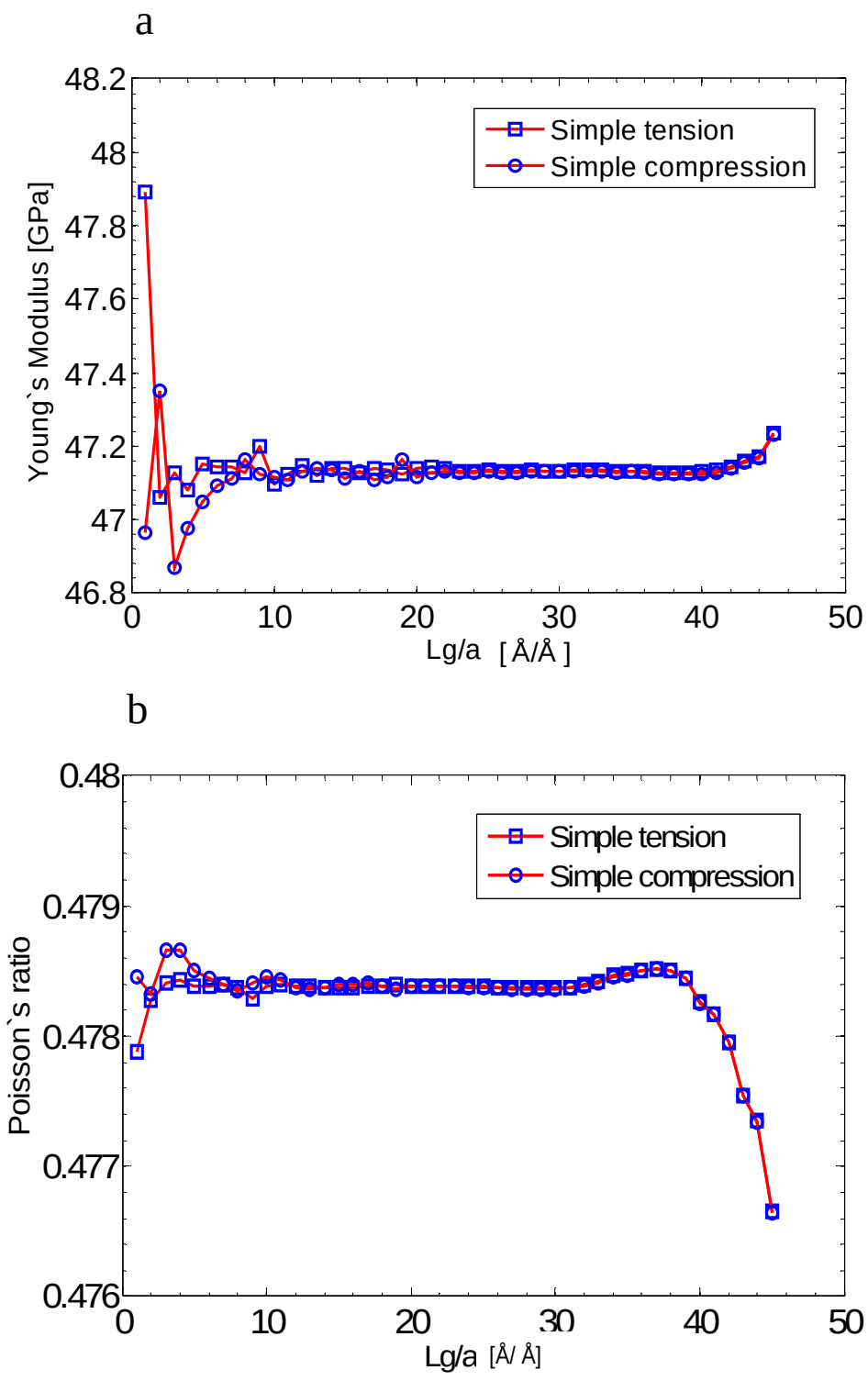

Fig. 5.12. For L/H=10, variation with the averaging length (L_g) in simple tension and compression of (a) the effective Young's modulus E, and (b) Poisson's ratio.

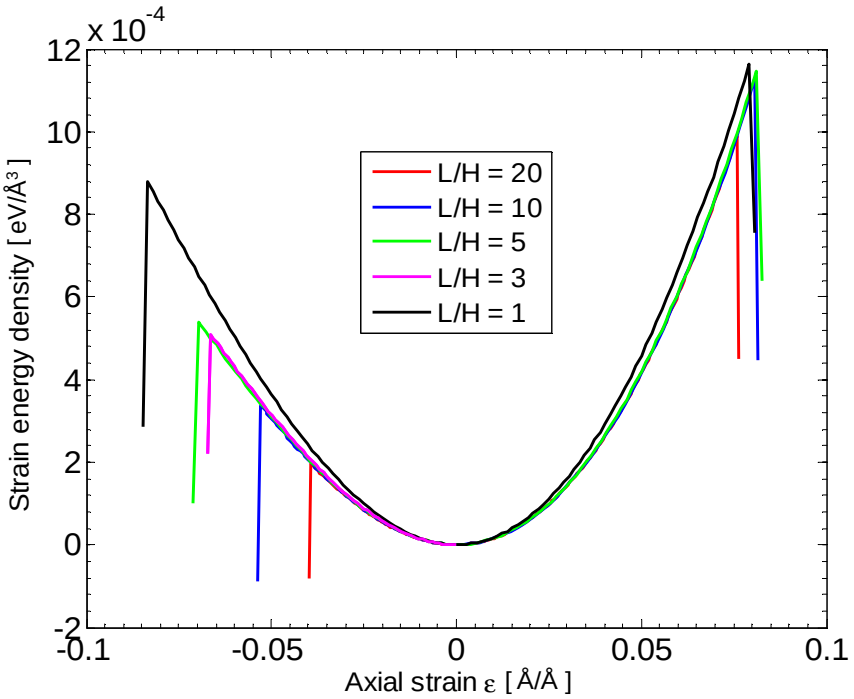

Fig. 5.13. Variation with the average axial strain ε of the strain energy density in simple tension/compression tests.

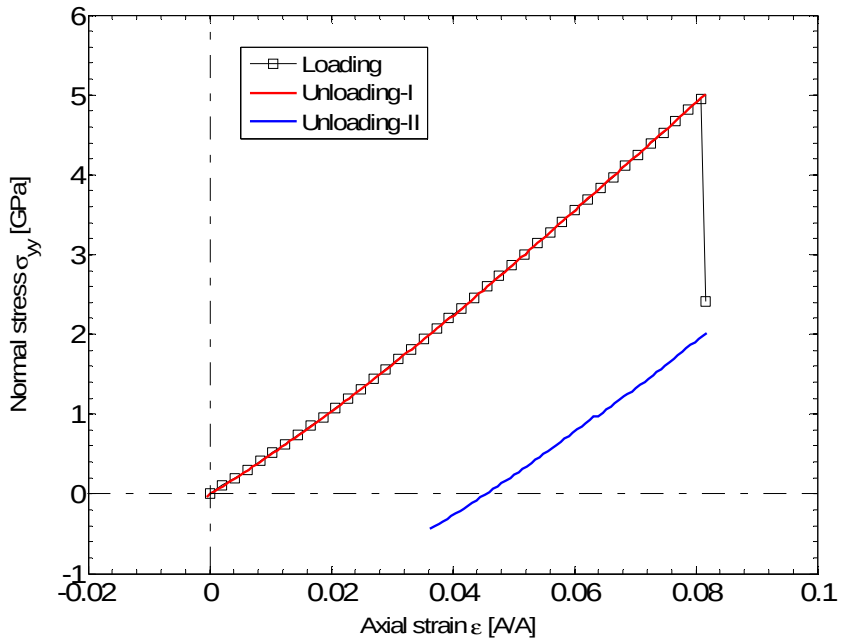

Fig. 5.14. For L/H=10, variation with the average axial strain ε of the average axial stress for loading and unloading paths in simple tension.

5.4 Analysis of local instabilities

5.4.1 Simple tension/compression

For different values of L/H, Fig. 5.15 exhibits the evolution of the minimum eigenvalue of the local Hessian $\boldsymbol{H^{(i)}}$ among all atoms in the system for simple tensile/compressive deformations. For simple compression, the minimum eigenvalue continuously decreases and remains positive until the strain level where the sharp drop in the average stress - average strain curve occurs. The strain levels at which local instabilities, signified by the minimum eigenvalue of $\boldsymbol{H^{(i)}}$ becoming negative, appear correspond to ε_{yy}^{yield}(see Table 5.3). No local instability occurred prior to this strain level. However, for simple tensile deformations, and for all values of L/H considered here, a group of atoms in each of the eight corners of the sample become unstable at an average axial strain of ~ 6% when curves in Fig. 5.15 exhibit the first discontinuity. The minimum eigenvalue remains negative and continuously decreases up to ~ 8% average axial strain; at this strain level the discontinuities in the average axial stress vs. the average axial strain curves also occur (cf. Fig. 5.5).

Values of $\boldsymbol{\varepsilon_{yy}^{yield}}$ listed in Table 5.3 correspond to the initiation of the second sharp drop in the magnitude of the minimum eigenvalue of $\boldsymbol{H^{(i)}}$. For both simple tensile and simple compressive deformations, $\left|\boldsymbol{\varepsilon_{yy}^{inst}}\right| \leq \left|\boldsymbol{\varepsilon_{yy}^{yield}}\right|$ for the five values of L/H considered here. The $\boldsymbol{\varepsilon_{yy}^{inst}}$ equals the average axial strain when the first discontinuity in the average axial vs. the average axial strain curve appears.

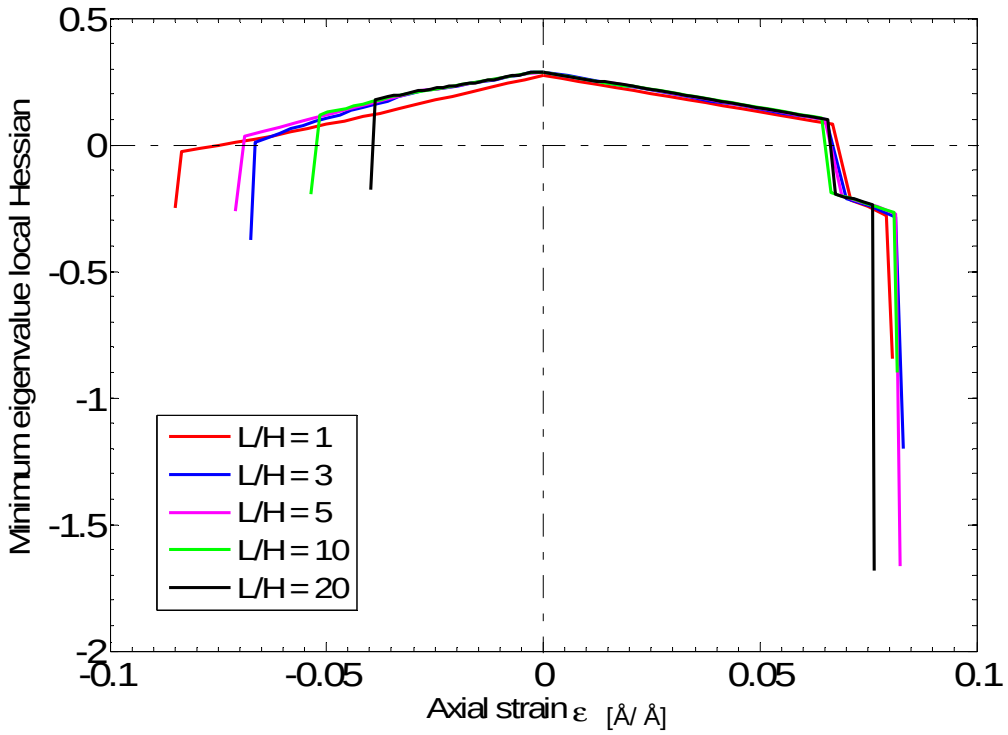

Fig. 5.15. For simulations with different values of L/H, variation with the average axial strain ε of the minimum eigenvalue of the local Hessian $\boldsymbol{H}^{(i)}$ in simple tensile/compressive deformations.

Table 5.3: Values of the average axial stress and the average axial strain at the yield point for specimens with different L/H ratios deformed in simple tension and compression.

	Simple tension		Simple compression	
L/H	σ_{yy}^{yield} (GPa)	ε_{yy}^{yield} (%)	σ_{yy}^{yield} (GPa)	ε_{yy}^{yield} (%)
1	5.134	7.928	-2.498	-8.345
3	5.050	8.119	-1.784	-6.643
5	4.996	8.117	-1.810	-6.897
10	4.990	8.086	-1.671	-5.157
20	4.618	7.584	-1.387	-3.874

For L/H = 10, Fig. 5.16 shows distributions of the minimum eigenvalue of $\boldsymbol{H^{(i)}}$, the CNP parameter and $\|\mathbf{G}\|$ for simple compression at ε slightly less than ε_{yy}^{yield} and at ε slightly greater than ε_{yy}^{yield}. Negative eigenvalues of $\boldsymbol{H^{(i)}}$ occur at points located in planes {1,1,1} of high atomic density. The unstable atoms are not distributed symmetrically about the mid-section, Y = L/2, of the specimen (see Fig. 5.16b). Fig. 5.16d displays the distribution of the CNP at ε a little greater than ε_{yy}^{yield}. The CNP equals either zero or has very small values at stable points but has large values at generally the same atomic positions where the local instability was predicted by the negative eigenvalues of $\boldsymbol{H^{(i)}}$. At ε a little less than ε_{yy}^{yield} values of the CNP parameter are negligible everywhere except at some points located on the bounding surfaces.

Fig. 5.16e exhibits the distribution of $\|\mathbf{G}\|$ at ε slightly less than ε_{yy}^{yield}. High values of $\|\mathbf{G}\|$ occur at points close to the lateral surfaces and at points located near the end faces where displacements are prescribed. Values of $\|\mathbf{G}\|$ vanish at points in the interior of the specimen whose distance from the end faces exceeds ~37 Å, i.e., the width of the sample. For ε a little greater than ε_{yy}^{yield} high values of $\|\mathbf{G}\|$ occur at the same atomic positions where the minimum eigenvalue of $\boldsymbol{H^{(i)}}$ is negative (cf. Fig. 5.16f).

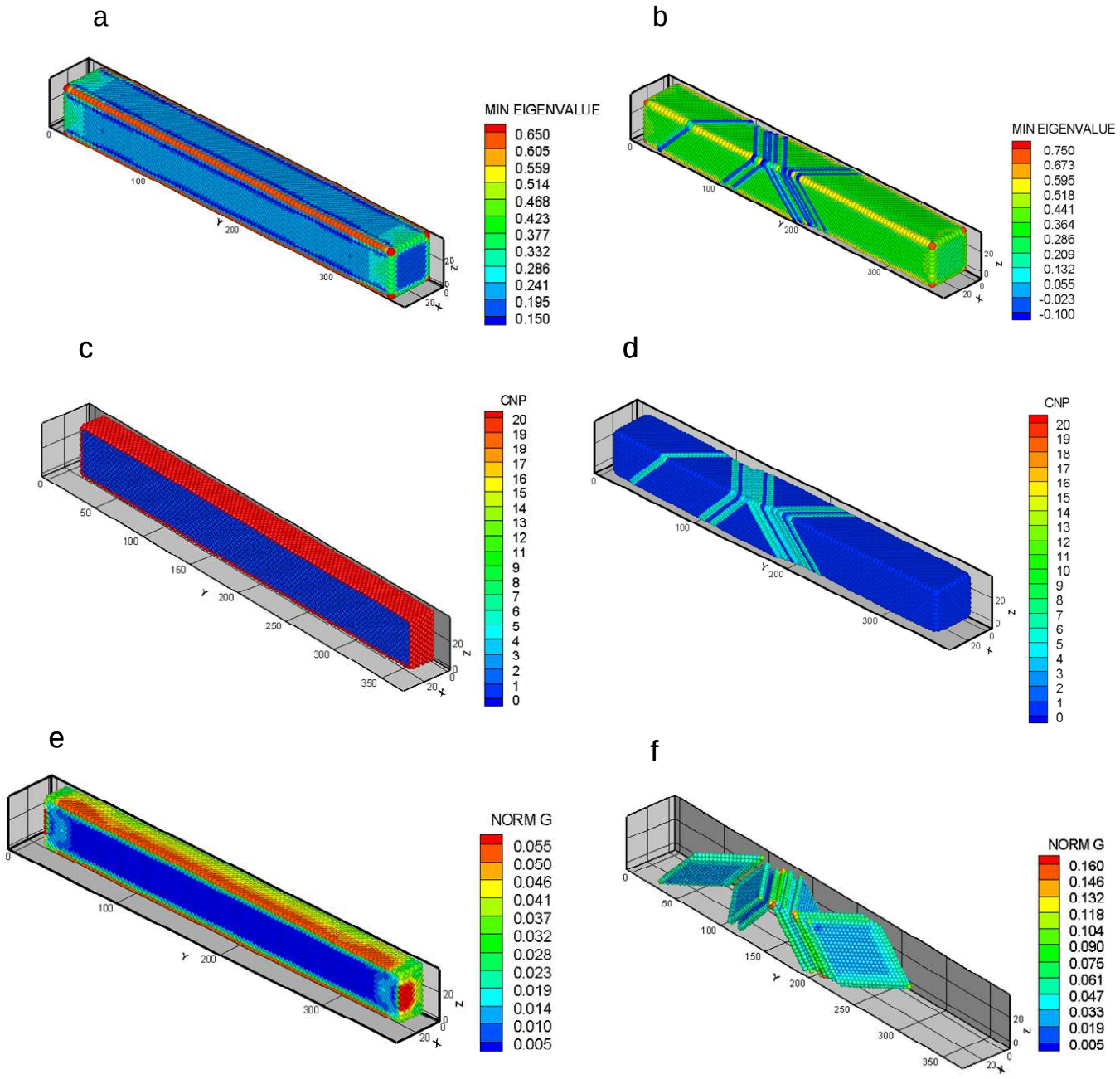

Fig. 5.16. For the simple compression test, distribution of the minimum eigenvalue of the local Hessian, the CNP and $\|G\|$ in the specimen with L/H=10; (a) minimum eigenvalue, ε = -5.15%; (b) minimum eigenvalue, ε = -5.16%; (c) CNP on the mid-section X = 18 Å, ε = -5.15%; (d) CNP, ε = -5.16%; (e) $\|G\|$ on the mid-section X = 18 Å, ε = -5.15%; and (f) $\|G\|$ at unstable points, ε = -5.16%; In Fig. (d) atoms on the bounding surface have been removed to clearly depict values of the CNP at unstable points in the interior of the specimen.

5.4.2 Tension/compression

Fig. 5.17 depicts, for L/H=10, distributions of the minimum eigenvalue of $\boldsymbol{H}^{(i)}$, the CNP parameter and $\|\mathbf{G}\|$ for the compressive deformations. The distributions of unstable points predicted by the minimum eigenvalue of $\boldsymbol{H}^{(i)}$ becoming negative differ from those observed for simple compressive deformations shown in Fig. 5.16b. Similarly, the distribution of points in Figs. 5.17e and 5.16e with high values of $\|\mathbf{G}\|$ at ε slightly less than ε_{yy}^{yield} for compression and simple compression are quite different. We recall that the only difference between compressive and simple compressive simulations is in the boundary conditions at the two end faces. Park et al. (2006) performed MD simulations of tensile and compressive deformations of gold, copper and nickel nanowires with different crystallographic orientations. However, their results cannot be compared with the present ones because of inertia effects included in Park et al.'s work.

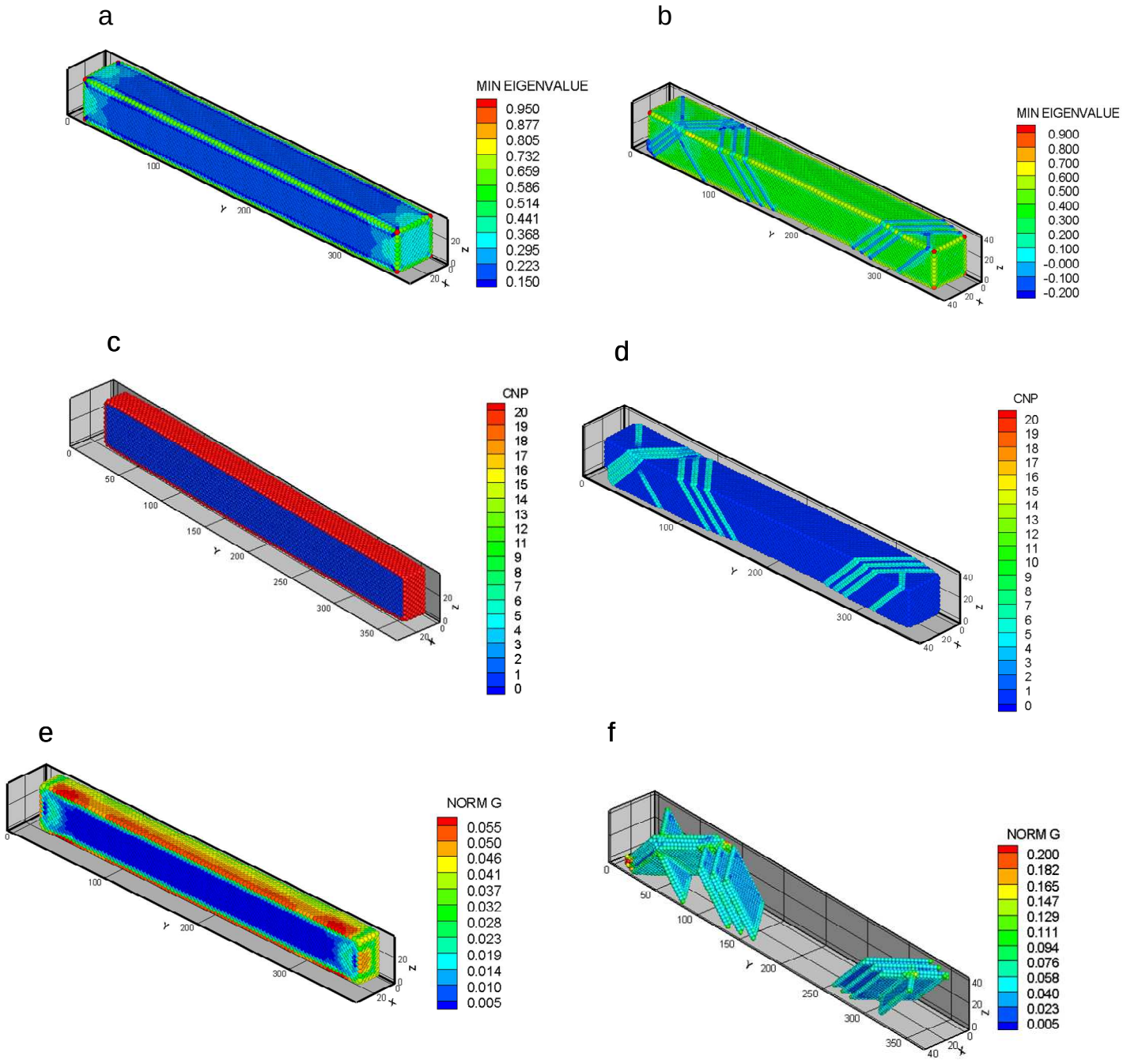

Fig. 5.17. For the compression test, distribution of the minimum eigenvalue of the local Hessian, the CNP and $\|G\|$ in the specimen with L/H=10; (a) minimum eigenvalue, ε = -5.46%; (b) minimum eigenvalue, ε = -5.52%; (c) CNP on the mid-section, X = 18 Å, ε = -5.46%; (d) CNP, ε = -5.52%; (e) $\|G\|$ on the mid-section, X = 18 Å, ε = -5.46%; and (f) $\|G\|$ at unstable points, ε = -5.52%; In Fig. (d) atoms on bounding surfaces have been removed to clearly show values of the CNP at unstable points in the interior of the specimen.

Fig. 5.18 depicts, for L/H=10, distributions of the minimum eigenvalue of $\boldsymbol{H}^{(i)}$, the CNP and $\|\mathbf{G}\|$ for simple tensile deformations. At ε slightly less than ε_{yy}^{yield} there are only very few atoms near the eight vertices of the specimen that have become unstable. However, at ε just greater than ε_{yy}^{yield} several atoms have become unstable. The distribution of unstable points has a serrated pattern along specimen's Y-centroidal line formed by atoms located on planes of high atomic density. The instabilities under compression and simple compression do not propagate through the entire length of the specimen. A similar serrated pattern was reported by Liang and Zhou (2004) who performed MD simulations of tensile deformations of copper nanowires at 300 K with specimens having the same crystallographic orientations as in the present work.

In a uniaxial stress state, the RSS on a plane equals $\sigma_0 \cos\phi \cos\lambda$ where σ_0, ϕ and λ equal the magnitude of the axial stress, the angle between the normal to the slip plane and the loading axis, and the angle between the slip direction and the loading axis, respectively. The Schmidt factor, $\cos\phi \cos\lambda$, is a geometric factor ranging from 0 to 0.5. The higher the Schmidt factor the higher the probability for a slip system to be activated. The Schmidt law states that the slip will occur on a plane in a given direction when the RSS exceeds a material-dependent critical value. We have not used this criterion to find planes on which slip may occur.

The distribution of unstable points predicted by the nonvanishing values of the CNP also coincides with the distribution predicted by the minimum eigenvalue of the local Hessian (see Figs. 5.18b and 5.18d) becoming negative. The distribution of $\|\mathbf{G}\|$ depicted in Fig. 5.18e shows patterns symmetric with respect to the Y-centroidal line of the specimen. At $\varepsilon=\varepsilon_{yy}^{yield}$ values of $\|\mathbf{G}\|$ increase from almost zero at the centroidal line of the specimen to ~0.07 at atoms located on the traction free lateral surfaces. The regions of high values of $\|\mathbf{G}\|$ located at points close to the end faces of the specimen observed in compression and simple compression are not present in specimens deformed in tension. At ε slightly greater than ε_{yy}^{yield} high values of $\|\mathbf{G}\|$ occur at numerous points where the minimum eigenvalue of $\boldsymbol{H}^{(i)}$ is negative.

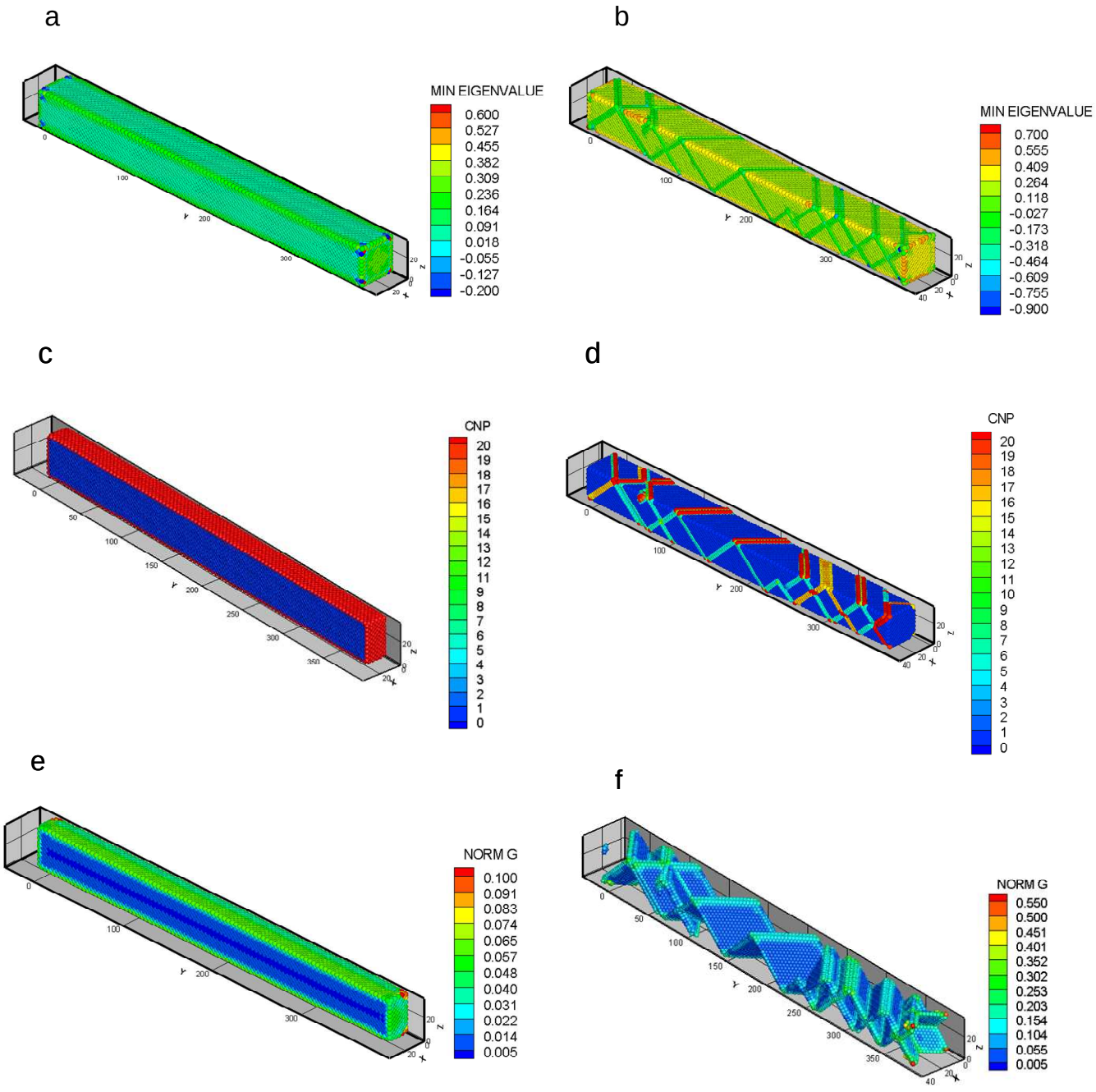

Fig. 5.18. For the simple tension test, distribution of the minimum eigenvalue of the local Hessian, the CNP and $\|G\|$ in the specimen with L/H=10; (a) minimum eigenvalues when ε = 8.08%; (b) minimum eigenvalues when ε = 8.15%; (c) CNP on the mid-section X = 18 Å, ε = 8.08%; (d) CNP, ε = 8.15%; (e) $\|G\|$ on the mid-section X = 18 Å, ε = 8.08%; and (f) $\|G\|$ at unstable points, ε = 8.15%; in Fig. (d) atoms on the bounding surface have been removed to clearly show values of the CNP at unstable points in the interior of the specimen.

5.5 Local stress distributions

5.5.1 Simple compression

For L/H=10, Figs. 5.19 through Fig. 5.23 show, respectively, distributions of σ_{yy}, σ_{xx}, σ_{xy}, σ_{VM} and τ_{max} at $\varepsilon = \varepsilon_{yy}^{yield}$ = -5.15% and ε = -5.16% that just exceeds ε_{yy}^{yield}.

The distribution of σ_{yy} on bounding surfaces in Fig. 5.19a at ε = -5.15% is tensile even though overall deformations are compressive. The maximum value, 0.896 GPa, of the tensile axial stress equals the magnitude, 0.807 GPa, of the compressive axial stress at the specimen centroid. The distribution of σ_{yy} on the bounding surfaces is symmetric about the three centroidal planes. Values of σ_{yy} at points on the edges and at points in the middle of the bounding surface are quite large. At a slightly larger value of the axial strain that just exceeds the axial strain at yield, values of σ_{yy} on the bounding surfaces are nearly uniform and equal 1.322 GPa. The axial stress σ_{yy} is still tensile on the surface; however, its values are compressive at the interior points of the specimen. Values of σ_{yy} at the eight corners and at points on the four edges are not exorbitantly high as compared to those at the interior points. For a 3D rectangular body comprised of a linear elastic material, one expects at least one component of the Cauchy stress to have very large values at the vertices and at points on the corners.

For ε = -5.15%, Fig. 5.19c shows the distribution of σ_{yy} on the mid-section; σ_{yy} is compressive and nearly uniform in the interior of the sample with values between -2.510 and -2.935 GPa. Near the free surfaces the stress changes from negative to positive values in a very short distance of ~ 4Å. Two groups of atoms having smaller compressive stress than that in atoms at the center of the specimen are symmetrically located at a distance of ~L/4 from each end of the specimen. Close to the end faces, the compressive stress in a small group of atoms forming a dark blue circle in the figure equals -3.361 GPa which is more than twice the average value of σ_{yy} in the specimen.

In Fig. 5.19d we have displayed the distribution of σ_{yy} on the mid-section when $\varepsilon = \varepsilon_{yy}^{yield}$. The tensile axial stress on the free lateral surface Z = Z_{max} increases from ~0.7 GPa at $\varepsilon = \varepsilon_{yy}^{yield}$ to ~1.3 GPa just after the nucleation of instabilities. Thus the onset of instabilities does not decrease stresses everywhere. The axial stress at points on the end faces where displacements are

prescribed remains essentially unchanged with a small increase in ε from -5.15 to -5.16%. However, at points in the interior of the specimen, the axial stress drops from -2.7 GPa to -1.7 GPa. The size of regions of high compressive stresses close to the edges present in Fig. 5.19c corresponding to $\varepsilon = \varepsilon_{yy}^{yield}$ is diminished in Fig. 5.19d but there are still two small groups of atoms with $|\sigma_{yy}|$ = ~1.5 GPa near the center of the specimen and close to the end faces.

A closer view of the stress level at unstable points after the specimen has yielded is given in Figs. 5.19e and f. These points correspond to atomic positions where the minimum eigenvalue of $\boldsymbol{H}^{(i)}$ is negative. Unstable points are located far from the two end faces and are concentrated near the center of the specimen on planes of high atomic density. At $\varepsilon = \varepsilon_{yy}^{yield}$, in every one of the rhombic forms of unstable atoms, the axial stress is nearly uniform and equals ~ -2.7 GPa at the center and changes rapidly from compressive to tensile for atoms close to the free surfaces. For atoms at the center a drop in the stress level to ~ -1.7 GPa is observed after yielding. The reduction in the magnitude of the compressive stress in the interior is accompanied by an increase in the tensile stress at atoms on the free surfaces.

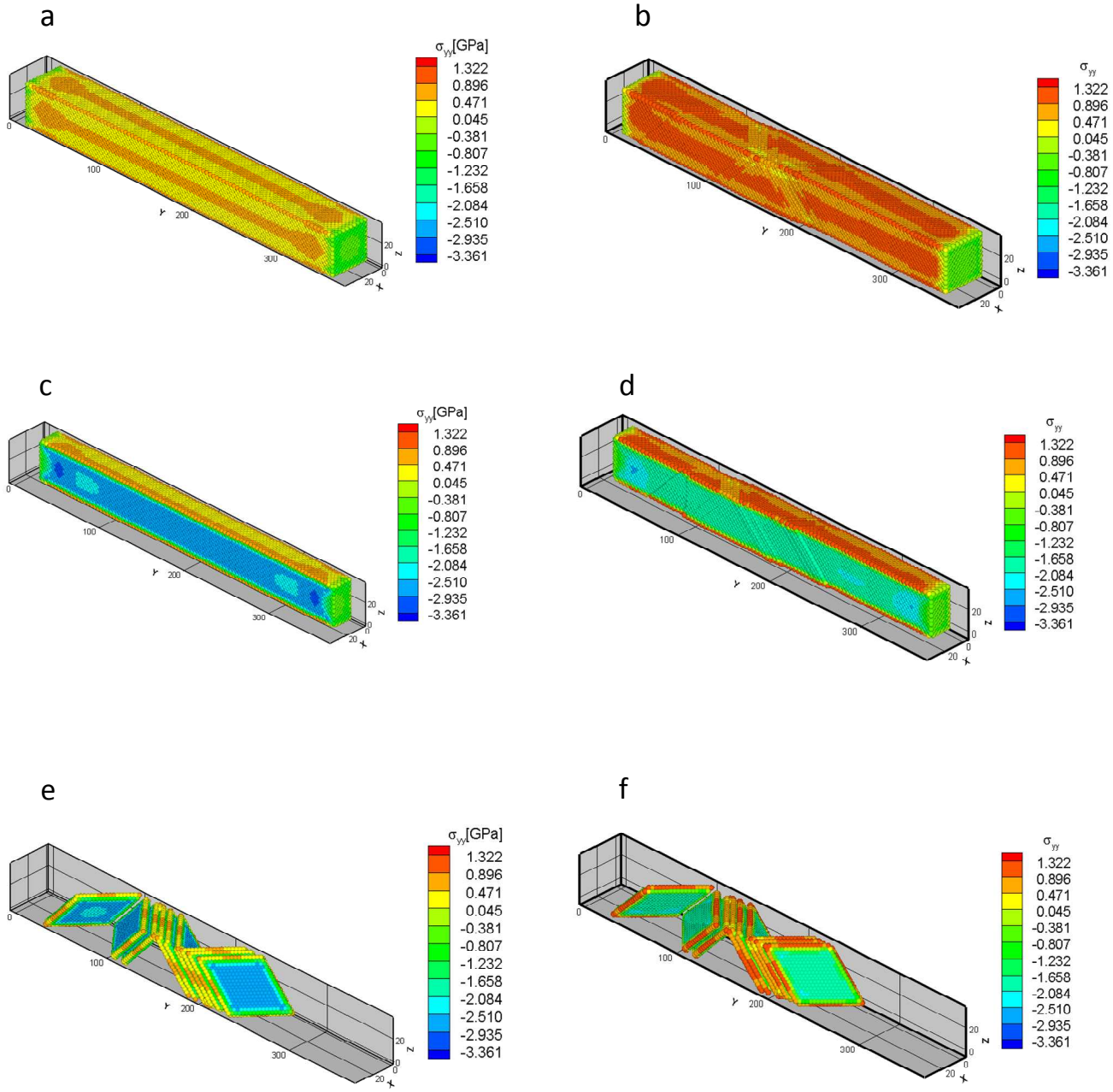

Fig. 5.19. For simulations of the simple compressive deformations of the specimen with L/H = 10, distribution of σ_{yy} component of the local Cauchy stress tensor on (a, b) the bounding surfaces, (c, d) the mid-section, X = 18 Å, and (e, f) at points where instabilities have initiated; for Figs. (a), (c) and (e) ε = -5.15%; and for (b), (d) and (f) ε = -5.16%.

Fig. 5.20 depicts distributions of σ_{xx} on different planes at ε = -5.15% and -5.16%. From results plotted in Fig. 5.20a and those in previous configurations not included here, we conclude that till $\varepsilon = \varepsilon_{yy}^{yield}$ the distribution of σ_{xx} is symmetric with respect to the three centroidal planes. From Fig. 5.20a it is also observed that σ_{xx} at points on the bounding plane, X = 36 Å, is negligible as compared to the maximum value, ~1.9 GPa, of σ_{xx} at other points. The condition of zero traction and hence zero normal stress should be satisfied on this plane. However, the computed values of σ_{xx} on this plane are not exactly zero because it is not perfectly flat in the reference configuration obtained after the minimization of the potential energy.

Fig. 5.20c shows the distribution of σ_{xx} on the mid-section, X = 18 Å. Values of σ_{xx} in the interior of the specimen range from -0.436 to -0.777 GPa; these values are one-fifth of those of σ_{yy} at the same locations. Values of σ_{xx} change along the Z-direction from compressive for atoms in the interior to tensile for atoms on the free surface. The distributions of σ_{xx} in Figs. 5.20e and f for atoms that have become unstable are very similar for configurations just before and just after the discontinuity in the stress-strain curve. The pattern on each one of the rhombic planes is not uniform but is symmetric with respect to the centroidal axes of the planes. Even though the number of unstable points in the configuration at $\varepsilon = -5.16\%$ is more than that in the configuration at $\varepsilon = -5.15\%$ the general distribution and the magnitude of σ_{xx} remain essentially unchanged.

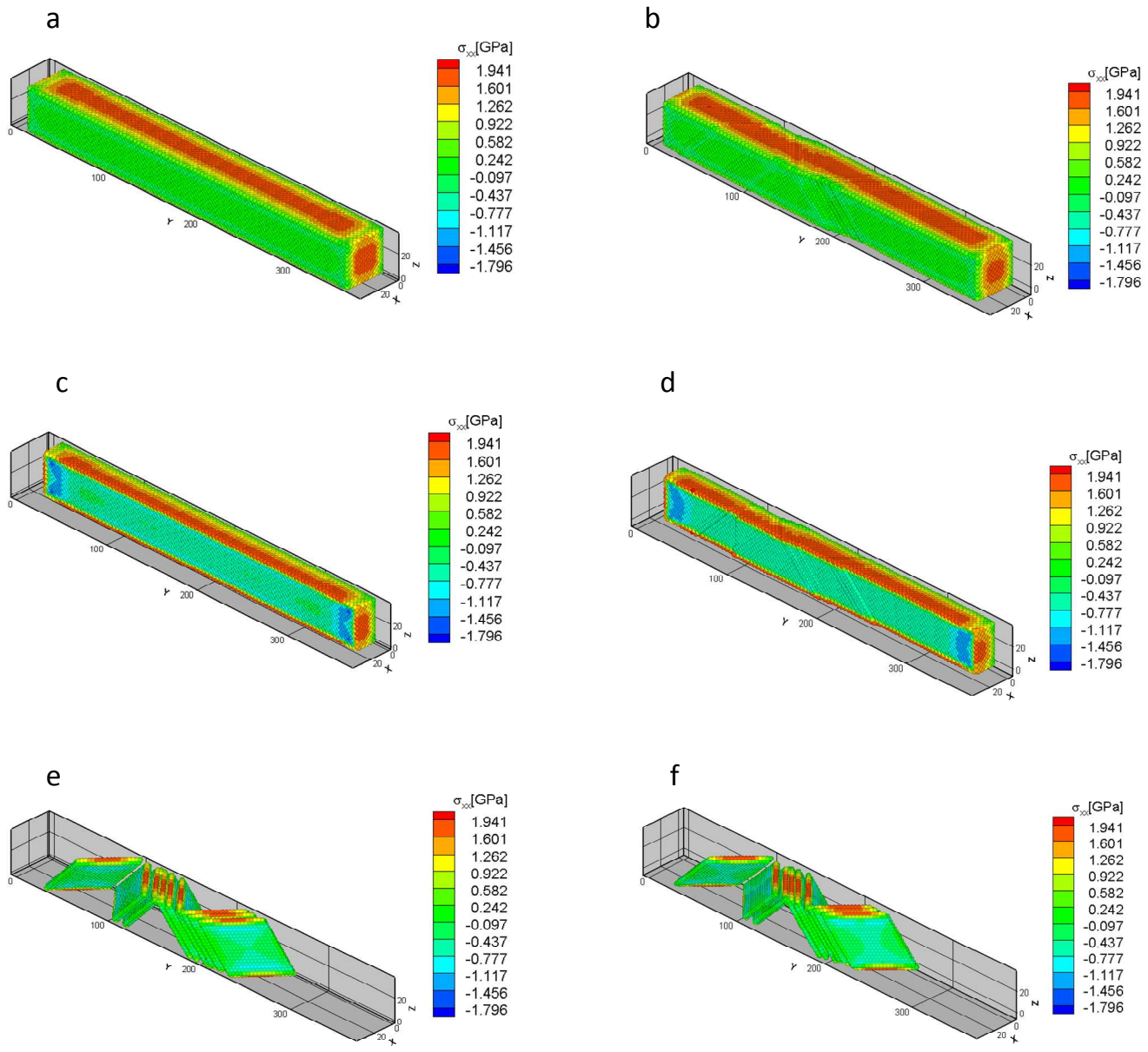

Fig. 5.20. For simulations of the simple compressive deformations of the specimen with L/H = 10, distribution of σ_{xx} component of the local Cauchy stress tensor on (a, b) the bounding surfaces, (c, d) the mid-section, X = 18 Å, and (e, f) at points where instabilities have initiated; for Figs. (a), (c) and (e) ε = -5.15%; and for (b), (d) and (f) ε = -5.16%.

For ε = - 5.15% and – 5.16% distributions of the shear stress σ_{xy} are depicted in Fig. 5.21. Values of σ_{xy} are close to zero except at points located on the two end faces of the specimen. These atomic positions with nonzero values of σ_{xy} are located along edges parallel to the Z-axis. The same behavior is observed for distributions of σ_{xz} and σ_{yz} components except that the nonzero values are along edges parallel to the Y- and the X-axis respectively. From Figs. 5.21e and f, we conclude that even at atoms that have become unstable values of shear stresses for the present choice of the coordinate planes remain negligible as compared to values of σ_{yy}.

To compare stress levels at different points in the specimen and their relation, if any, with the nucleation of instabilities, values of the von Mises stress and the maximum shear stress were computed. These two quantities are compared with the yield stress of the material in simple tension/compression to formulate a yield criterion in the continuum theory. The distributions of σ_{VM} depicted in Figs. 5.22a and b show values ranging from 1.31 to 1.76 GPa at points on the four lateral surfaces. Values around 0.5 GPa before and after the nucleation of instabilities are observed on edges along the Y-axis and at the corners of the specimen. Maximum values of σ_{VM} , ~ 2.67 GPa, occur on planes where boundary conditions are applied. After the drop in the average axial stress - the average axial strain curve values of σ_{VM} at points on the two end faces vary between 2.0 and 2.4 GPa. The value of σ_{VM} is almost constant at points in the interior of the specimen prior to the nucleation of instabilities and it ranges from 2.0 to 2.22 GPa except for atoms located close to the end faces. Near the end faces there are groups of atoms having values of σ_{VM} between 0.63 and 1.31 GPa. However, atoms with the same stress level as that in atoms at the center enclose these regions. After the drop in the average axial stress - the average axial strain curve values of σ_{VM} at most points in the interior of the specimen vary between 1.0 and 2.0 GPa. The lowest value, ~ 0.18 GPa, of σ_{VM} is found at the same group of atoms close to the two end faces as was observed for the configuration just before the nucleation of instabilities.

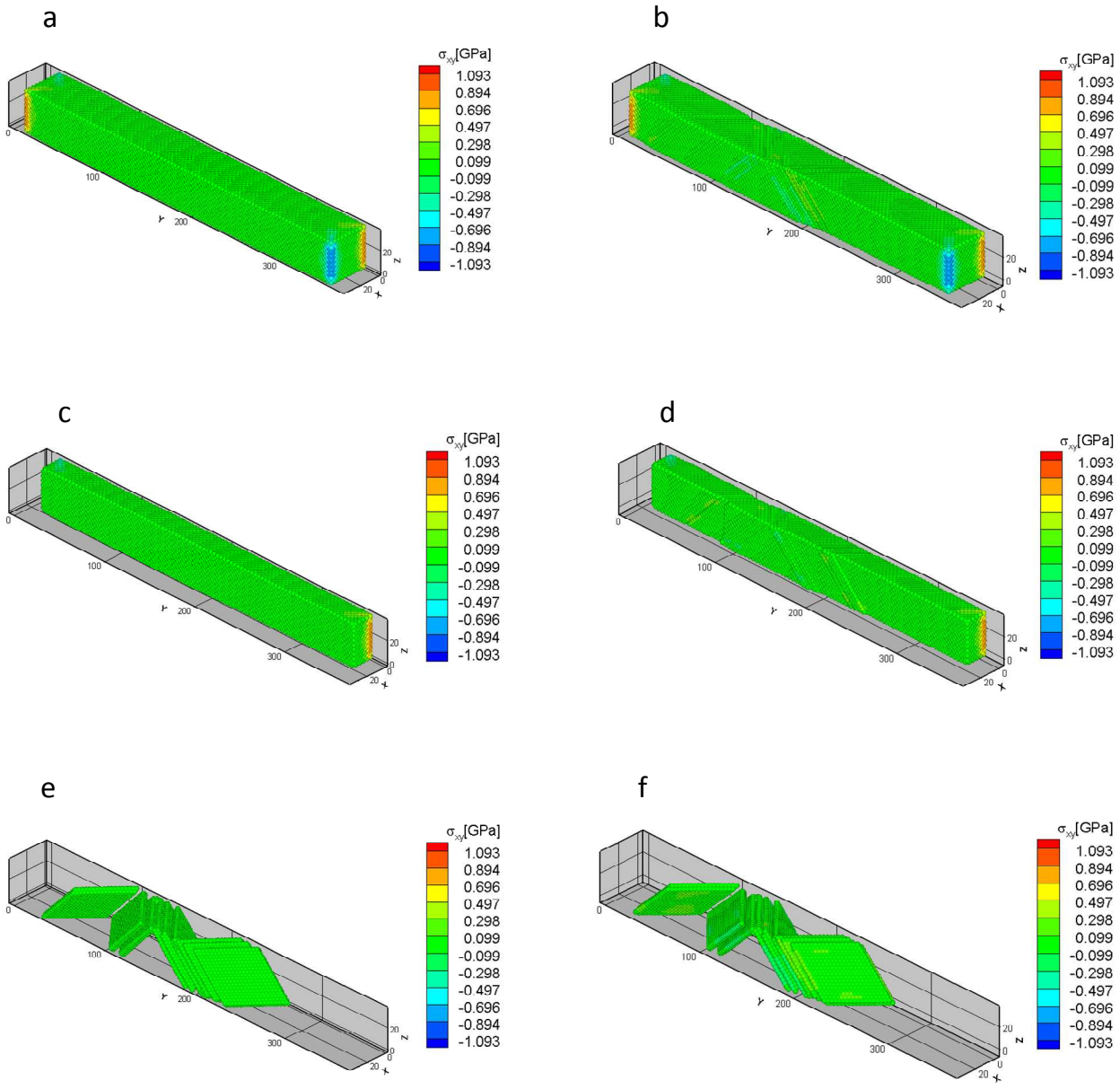

Fig. 5.21. For simulations of the simple compressive deformations of the specimen with L/H = 10, distribution of σ_{xy} component of the local Cauchy stress tensor on (a, b) the bounding surfaces, (c, d) the mid-section, X = 18 Å, and (e, f) at points where instabilities have initiated; for Figs. (a), (c) and (e) ε = -5.15%; and for (b), (d) and (f) ε = -5.16%.

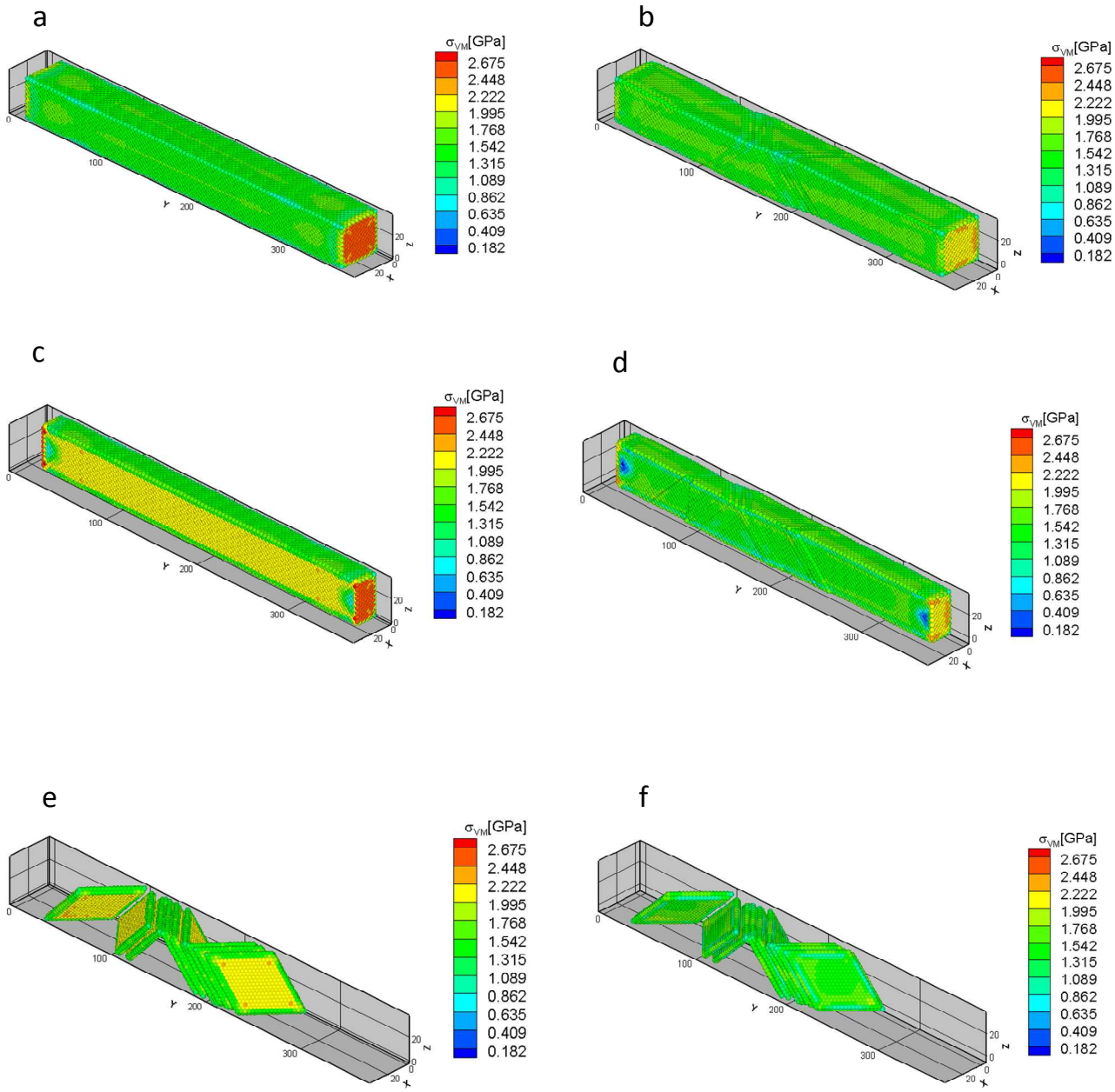

Fig. 5.22. For simulations of the simple compressive deformations of the specimen with L/H = 10, distribution of σ_{VM} stress on (a, b) the bounding surfaces, (c, d) the mid-section, X = 18 Å, and (e, f) at points where instabilities have initiated; for Figs. (a), (c) and (e) ε = -5.15%; and for (b), (d) and (f) ε = -5.16%.

Of special interest are atoms on four lines parallel to the Y-axis with a high value of σ_{VM} as compared to that at the remaining atoms in the specimen. These lines are located three atomic layers below the lateral free surfaces and atoms on them have a stress level between ~2.22 and ~2.44 GPa. From fringe plots of Figs. 5.22e and f we see that values of σ_{VM} at points on these lines (orange dots in the planar surfaces) drop from ~ 2.7 GPa to ~ 1.3 GPa when $|\varepsilon|$ is increased from 5.15% to 5.16%; after the nucleation of instabilities σ_{VM} at atoms in the interior of the specimen equals ~ 1.3 GPa. Even though the value of σ_{VM} at atoms on these four lines is higher than that at atoms in the interior of the specimen the difference between the two values is less than the difference between the values of σ_{VM} at atoms in the interior of the specimen and at atoms located on the end surfaces where boundary conditions are applied. We note that none of the atoms on surfaces with prescribed displacements where the highest values of σ_{VM} occur become unstable. Atoms that become unstable are located away from the end faces by at least $1/10^{th}$ of the length of the specimen.

Figs. 5.23a and b depict, for ε = -5.15% and ε = -5.16%, the distribution of $2\tau_{max}$ in the specimen, i.e., the absolute value of the difference between the minimum and the maximum eigenvalues of the Cauchy stress tensor at each atomic position. The distribution of $2\tau_{max}$ is uniform over the four lateral surfaces with values ranging from 1.1 to 2.0 GPa. The value of $2\tau_{max}$ peaks at ~ 2.75 GPa for atoms located on the two ends faces of the specimen. Fig. 5.23c shows, prior to the nucleation of instabilities, values of $2\tau_{max}$ between 2.0 and 2.3 GPa for atoms around the centroidal line parallel to the Y-axis. From the fringe plots on the mid-section X = 18Å reported in Fig. 5.23c we notice two lines parallel to the Y-axis on which τ_{max} is the same as that on the two end faces. These atoms of high shear stress are located on a square band that surrounds the interior of the specimen. The shear stress at atoms located $3a/2$ from the free surface (e.g., yellow regions close to the lateral surfaces) nearly equals that at atoms at the center of the specimen.

Figs. 5.23e and f depict the distribution of $2\tau_{max}$ at atoms just before and immediately after their becoming unstable. After the nucleation of instabilities $2\tau_{max}$ drops from ~2.75 to ~1.8 GPa for points that had maximum values of $2\tau_{max}$ prior to their becoming unstable and from ~2.1 to ~1.13 GPa for points at the specimen center. As was also observed in the distributions of σ_{yy} and $\sigma_{VM,}$ stresses at most atoms in the system decrease after the nucleation of instabilities.

Contrary to the distribution of the maximum values of σ_{VM} prior to the occurrence of instabilities, the distribution of $2\tau_{max}$ shows that the maximum values of shear stresses occur in regions where instabilities nucleate. Values of $2\tau_{max}$ at points on the free surfaces are nearly $1/4^{th}$ of the maximum values at atoms just below the free surfaces.

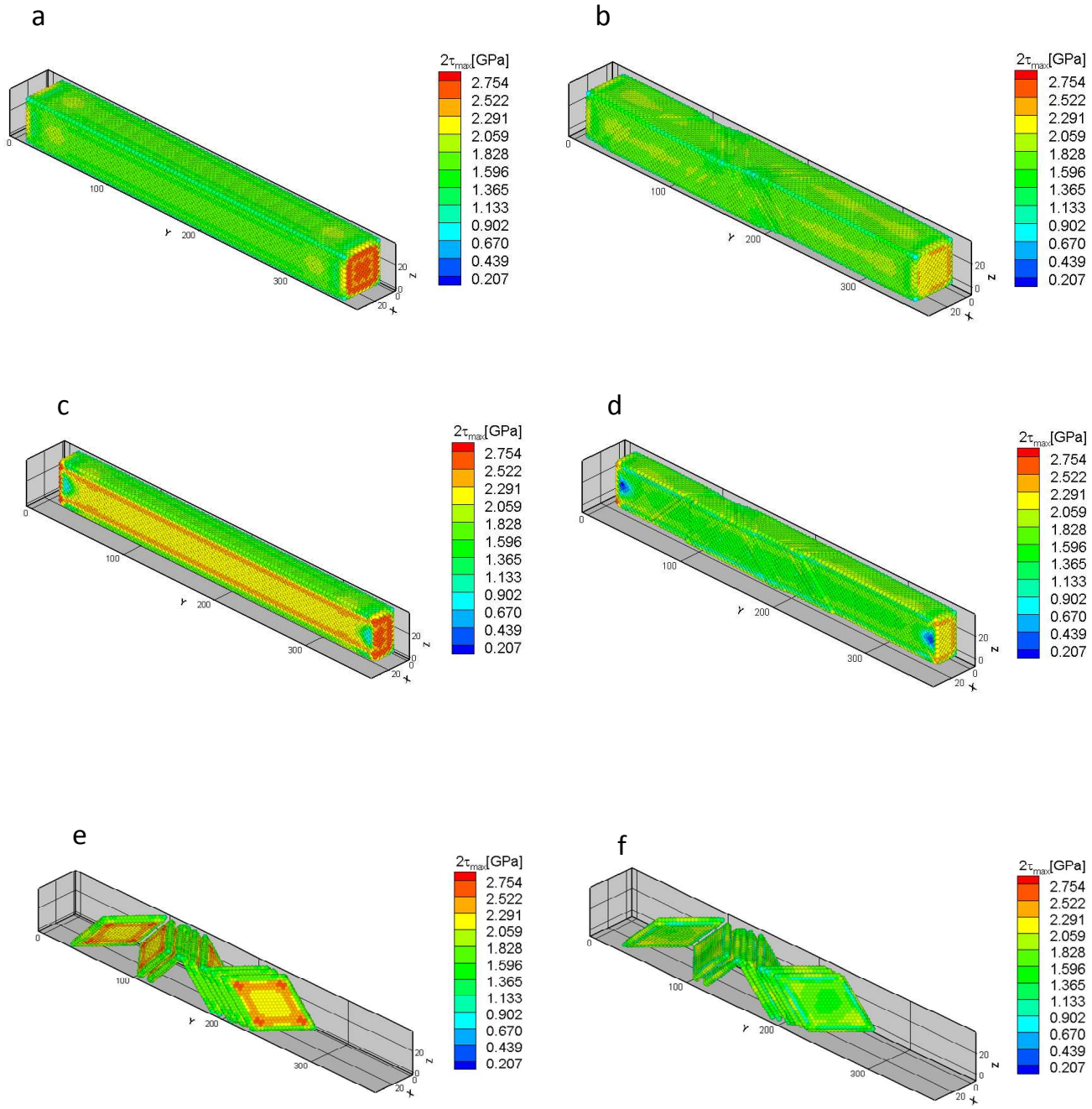

Fig. 5.23. For simulations of the simple compressive deformations of the specimen with L/H = 10, distribution of $2\tau_{max}$ stress on (a, b) the bounding surfaces, (c, d) the mid-section, X = 18 Å, and (e, f) at points where instabilities have initiated; for Figs. (a), (c) and (e) ε = -5.15%; and for (b), (d) and (f) ε = -5.16%.

5.5.2 Simple tension

For L/H = 10, Fig. 5.24 exhibits the distribution of σ_{yy} in configurations corresponding to ε = 8.08% and ε = 8.15%. In contrast to the distribution of σ_{yy} for simple compression, the distribution of σ_{yy} in Fig. 5.24a for simple tension on the lateral surfaces is uniform along the Y-direction, and σ_{yy} = ~ 4.93 GPa. Smaller values, ~3.2 GPa, of σ_{yy} occur at points near the edges. At points near the two end faces σ_{yy} equals $1/5^{th}$ of its maximum value at points on the lateral surfaces. Subsequent to the initiation of instabilities, the distribution of σ_{yy} displayed in Fig. 5.24b is nonuniform and σ_{yy} on the lateral surfaces has dropped from ~ 4.9 GPa to ~ 3 GPa.

Fig. 5.24c depicts the distribution of σ_{yy} on the mid-section, X = 18 Å, when ε = 8.08%. The magnitude of σ_{yy} increases from ~ 0.5 GPa at the centroid of the specimen to ~ 4.93 GPa at points on the free lateral surfaces. An initially compressive stress of ~ -1.5 GPa at points on the centroidal axis in the reference configuration changes to tensile stress with increasing axial deformations. The magnitude of the in-plane tensile stress at atoms on the traction free lateral surfaces increases from ~ 1.8 GPa at ε = 0% to ~ 4.5 GPa at ε = 8.08%. Fringe plots of σ_{yy} exhibited in Fig. 5.24d reveal that at points around the center of the specimen, σ_{yy} is relaxed from ~ 2.8 GPa before the nucleation of instabilities to ~ 1.4 GPa just after the nucleation of instabilities; for atoms on free surfaces this reduction in σ_{yy} is from ~ 4.5 GPa to ~ 2.6 GPa.

From the distributions of σ_{yy} on planes of atoms that become unstable during the next load step, shown in Fig. 5.24f, it is clear that the axial stress increases from ~ 2.8 GPa at the center to ~ 4.5 GPa at points on the free surfaces. This is different from that in the simple compressive deformations where a high gradient in σ_{yy} occurs at points close to the lateral free surfaces due to the difference in the signs of the axial stress (compressive at the center and tensile at points on the free surfaces). During the nucleation of instabilities at these atoms σ_{yy} drops by ~ 40%; e.g. compare fringe plots in Figs. 5.24e and f.

The distribution of σ_{xx} depicted in Fig. 5.25a is similar to the one observed in simple compressive deformations. On lateral surfaces, X = 0, 36 Å, the value of σ_{xx} is negligible, consistent with the boundary conditions of null traction on these surfaces. However, at lateral surfaces, Z = 0, 36 Å, $\sigma_{xx} \approx 2.25$ GPa. From the fringe plots of Fig. 5.25c it can be noticed that σ_{xx} at the specimen centroid is compressive and its magnitude equals that of the tensile stress at points on traction-free surfaces, Z = 0, 36 Å. After the occurrence of local instabilities the

symmetry in the distribution of σ_{xx} is lost but the magnitude of σ_{xx} remains essentially unchanged even at atoms that have become unstable (see Figs. 5.25c,d and Figs. 5.25e,f). At a point in the specimen σ_{zz} and σ_{xx} are equal till $\varepsilon = 8.05\%$; subsequently no major qualitative changes occur in σ_{zz} and σ_{xx}.

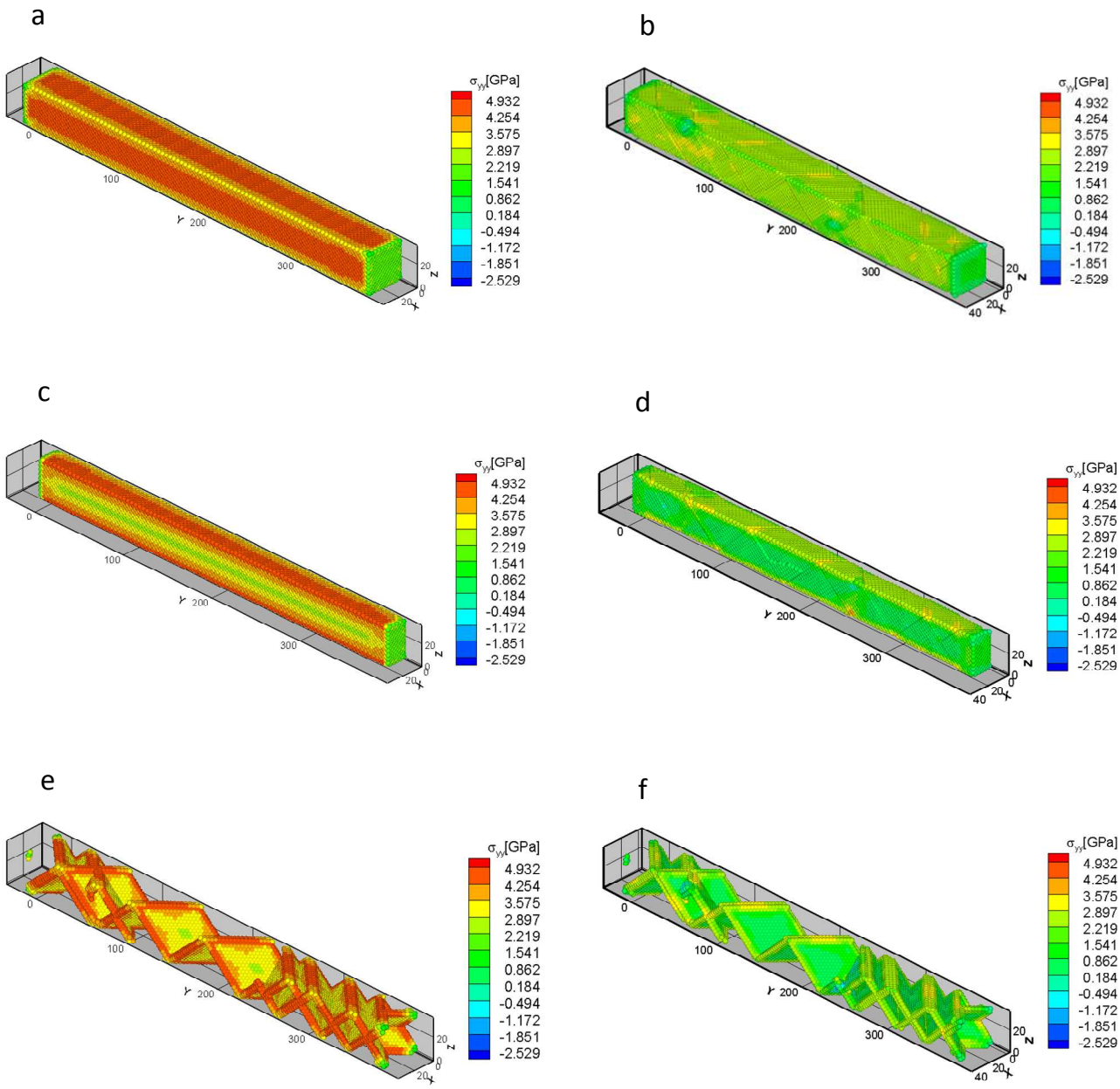

Fig. 5.24. For simulations of the simple tensile deformations of the specimen with L/H = 10, distribution of σ_{yy} component of the local Cauchy stress tensor on (a, b) the bounding surfaces, (c, d) the mid-section, X = 18 Å, and (e, f) at points where instabilities have initiated; for Figs. (a), (c) and (e) ε = 8.08%; and for (b), (d) and (f) ε = 8.15%.

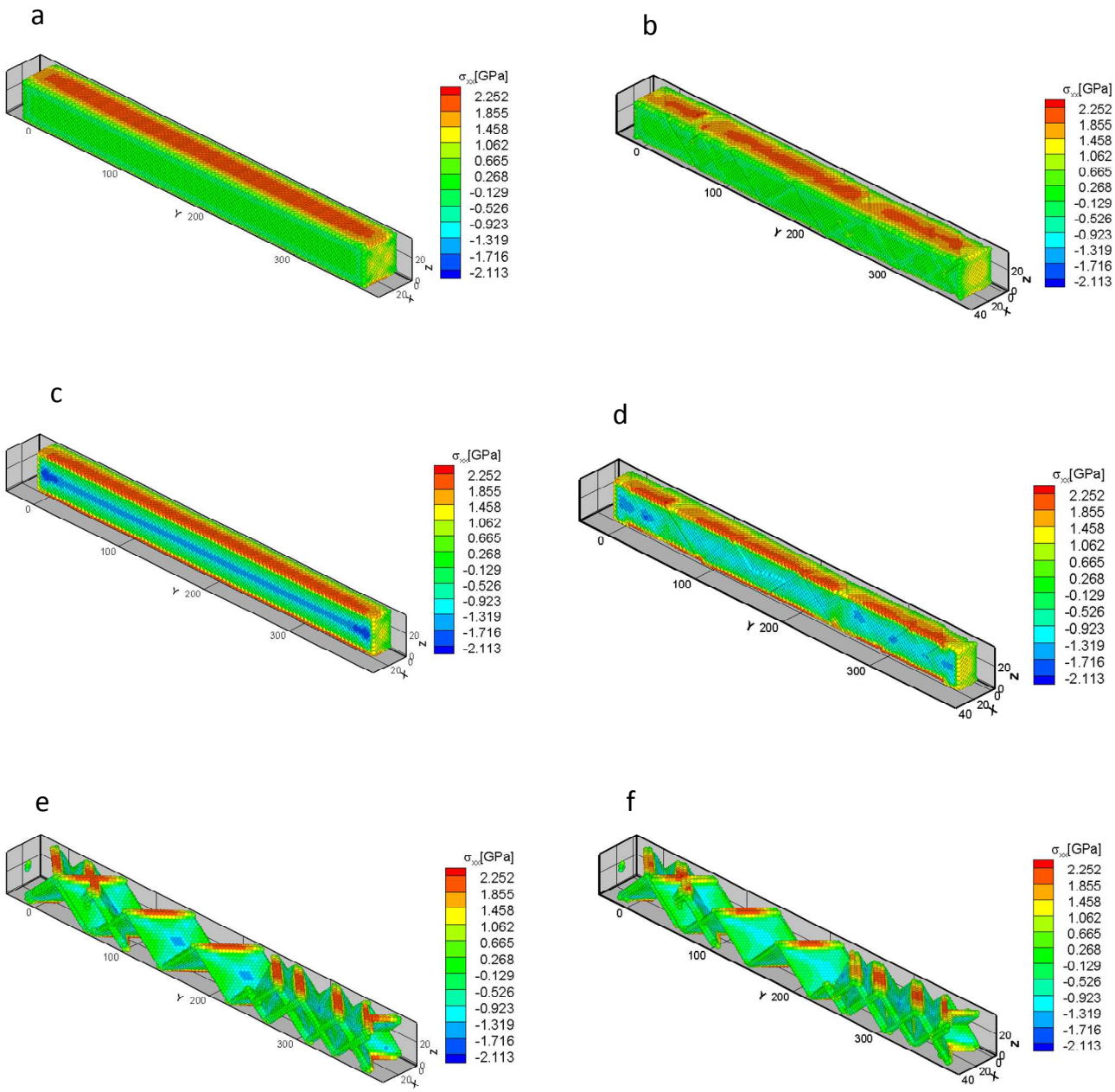

Fig. 5.25. For simulations of the simple tensile deformations of the specimen with L/H = 10, distribution of σ_{xx} component of the local Cauchy stress tensor on (a, b) the bounding surfaces, (c, d) the mid-section, X = 18 Å, and (e, f) at points where instabilities have initiated; for Figs. (a), (c) and (e) ε = 8.08%; and for (b), (d) and (f) ε = 8.15%.

As for simple compressive deformations values of σ_{xy} are negligibly small till $\varepsilon = \varepsilon_{yy}^{yield}$, i.e., 8.08%, except at atoms along the four vertical edges parallel to the Z-axis (cf. Figs. 5.26a and c). After the occurrence of local instabilities the magnitude of σ_{xy} reaches a maximum of ~ 0.76 GPa at some points located close to the bounding surfaces.

The distribution of σ_{VM} on the bounding surfaces is depicted in Figs. 5.27a and b; it is essentially uniform on these surfaces prior to the nucleation of instabilities with values ranging from ~ 2.22 to ~ 4.61 GPa. Fringe plots of Fig. 5.27c show that on the mid-section, X = 18 Å, values of σ_{VM} at points near the end faces of the specimen are higher than those at points on its lateral surfaces. Two groups of atoms, starting with the third layer from the end faces, have the maximum value ~ 5.57 GPa of σ_{VM}; it rapidly decreases to ~ 4.3 GPa, and stays at that value on atoms near the longitudinal centroidal axis of the specimen. At points near the center, values of σ_{VM} vary between ~ 4.3 GPa and ~ 3.8 GPa along the Z- and the X-axes. A high gradient in the values of σ_{VM} is found at points close to the free lateral surfaces while that at points near the center is moderate. The distribution of σ_{VM} at points where instabilities have initiated, depicted in Fig. 5.27e, shows the presence of four lines of atoms with σ_{VM} = ~ 5.57 GPa which is nearly the same as at points close to the edges of the mid-section. At these points, after the nucleation of instabilities, the σ_{VM} drops to ~2 GPa; a similar drop in the stress level occurs at all atoms in the rhombic planes of unstable atoms shown in Fig. 5.27f. We note that none of the atoms with high values of σ_{VM} located at the end faces become unstable.

The distributions of $2\tau_{max}$ in Fig. 5.28a-f are similar to those of σ_{VM} in Fig. 5.27a-f. For establishing a relation, if any, between the stress level and the nucleation of instabilities, we note that the maximum values of τ_{max} and σ_{VM} at $\varepsilon = \varepsilon_{yy}^{yield}$ at points that have become unstable are different for simple tension and simple compression. For simple compression, the maximum values of $2\tau_{max}$ and σ_{VM} are 2.75 and 2.33 GPa, respectively. For simple tension, $2\tau_{max}$ and σ_{VM} equal 5.95 and 5.57 GPa respectively. There is a difference of ~100% between these values, showing that for this specific case

$(\tau_{max})_{tension} = \sim 2(\tau_{max})_{compression}$ and $(\sigma_{VM})_{tension} = \sim 2(\sigma_{VM})_{compression}$.

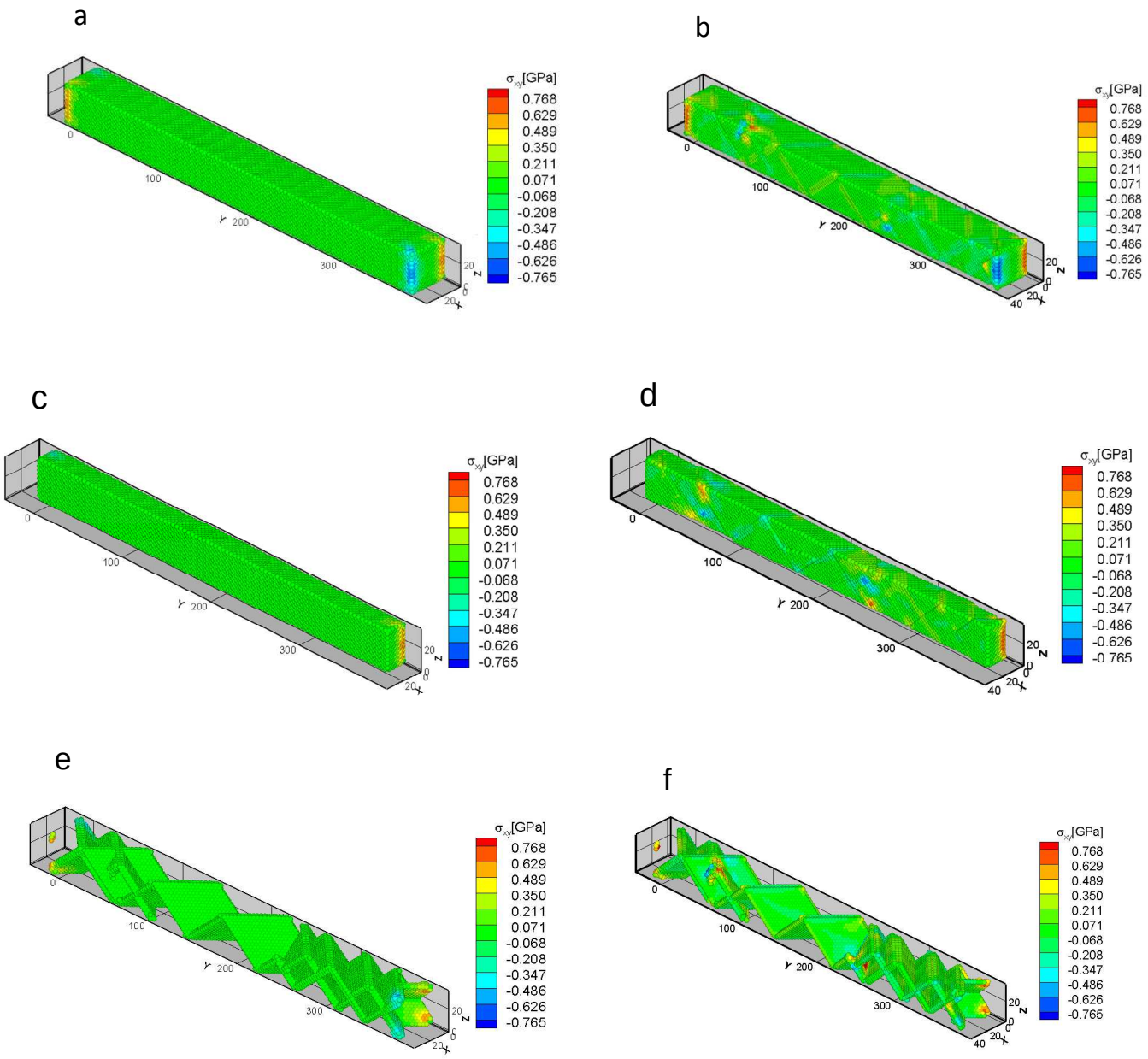

Fig. 5.26. For simulations of the simple tensile deformations of the specimen with L/H = 10, distribution of σ_{xy} component of the local Cauchy stress tensor on (a, b) the bounding surfaces, (c, d) the mid-section, X = 18 Å, and (e, f) at points where instabilities have initiated; for Figs. (a), (c) and (e) ε = 8.08%; and for (b), (d) and (f) ε = 8.15%.

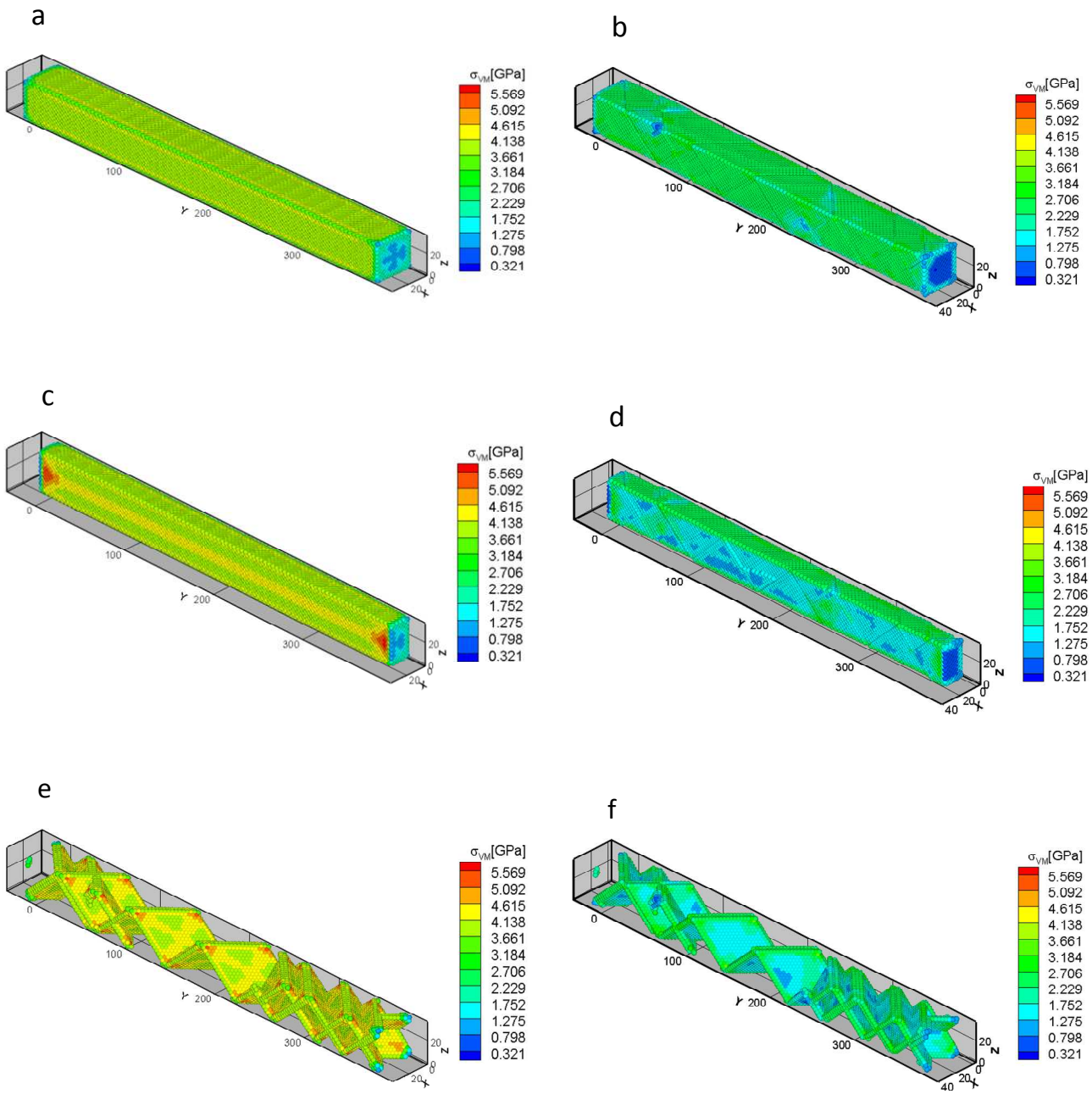

Fig. 5.27. For simulations of the simple tensile deformations of the specimen with L/H = 10, distribution of σ_{VM} on (a, b) the bounding surfaces, (c, d) the mid-section, X = 18 Å, and (e, f) at points where instabilities have initiated; for Figs. (a), (c) and (e) $\varepsilon = 8.08\%$; and for (b), (d) and (f) $\varepsilon = 8.15\%$.

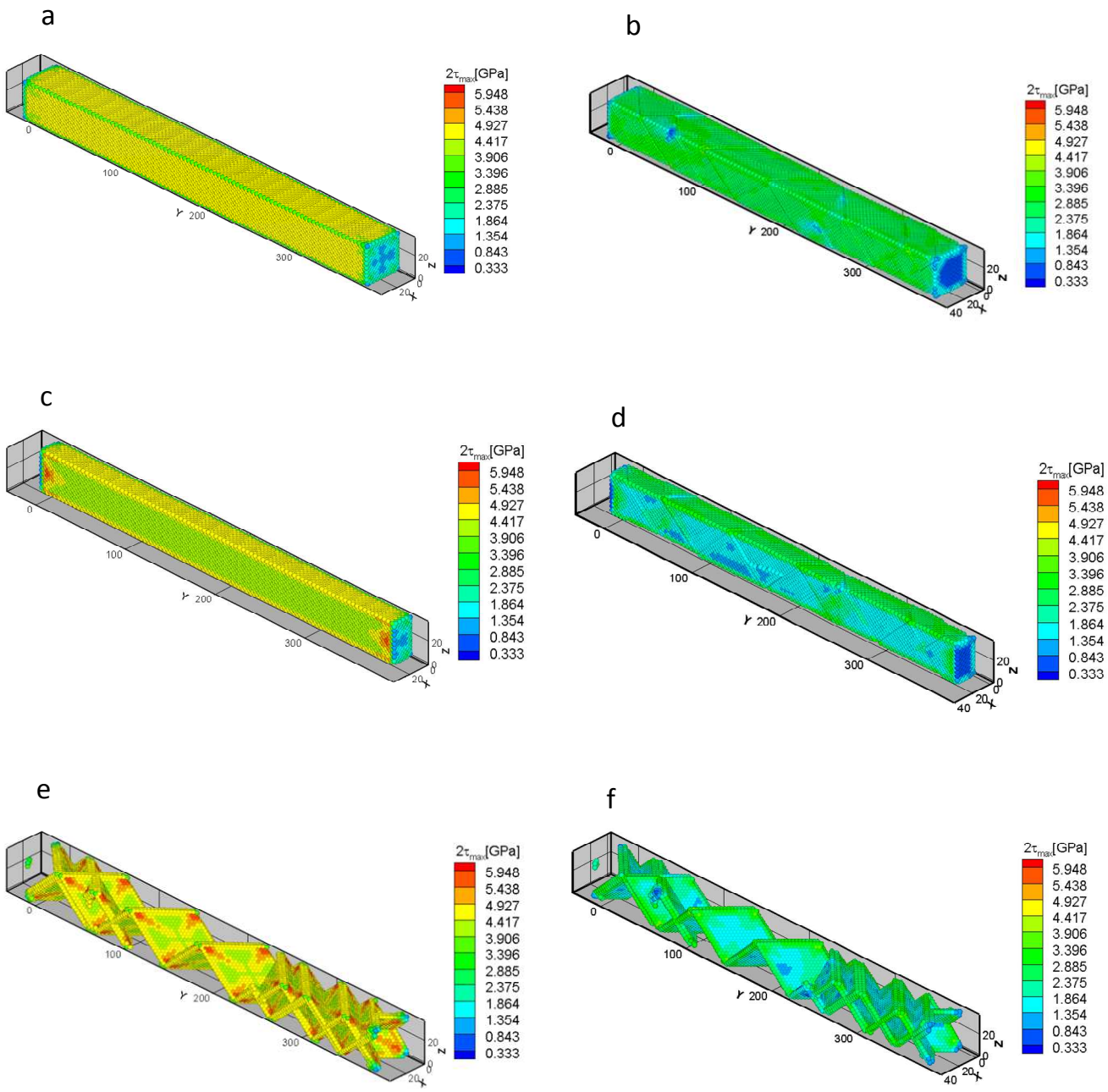

Fig. 5.28. For simulations of the simple tensile deformations on the specimen with L/H = 10, distribution of $2\tau_{max}$ on (a, b) the bounding surfaces, (c, d) the mid-section, X = 18 Å, and (e, f) at points where instabilities have initiated; for Figs. (a), (c) and (e) $\varepsilon = 8.08\%$; and for (b), (d) and (f) $\varepsilon = 8.15\%$.

5.6 Effect of the aspect ratio L/H

5.6.1 Simple tension

For simple tension and L/H = 5, 10 and 20, Figs. 5.29a, b, and c exhibit distributions of σ_{yy} on the centroidal axis at various values of the average axial strain ε. For $\varepsilon < \varepsilon_{yy}^{yield}$, σ_{yy} changes rapidly at points close to the end faces, $Y = Y_{min}$ and $Y = Y_{max}$, and saturates to a constant value at the center. At $\varepsilon = 0$, i.e., the reference configuration, σ_{yy} is close to zero at points near the two end faces but it is compressive at other points on the centroidal axis; the maximum magnitude of σ_{yy} = ~ 1.7 GPa is at points whose distance from the end faces equals 20 Å. At points near the center of the specimen σ_{yy} = ~ -1.2 GPa for the three L/H values. The σ_{yy} at a point increases with an increase in the deformation. At $\varepsilon = \sim 1\%$, the stress at points near the end faces becomes tensile. At ε= 4%, σ_{yy} is positive (tensile) at all points on the centroidal axis. Till $\varepsilon = \varepsilon_{yy}^{yield}$, the qualitative and the quantitative evolutions of σ_{yy} are the same for L/H = 5, 10 and 20. The material yields at $\varepsilon = \sim 8\%$ with a stress level of σ_{yy} = ~2.8 GPa at the center for L/H = 5 and 10 and σ_{yy} = ~2.4 GPa for L/H = 20.

The black curve in Figs. 5.29a, b, c gives the distribution of σ_{yy} on the centroidal axis for ε slightly greater than ε_{yy}^{yield}. After the nucleation of local instabilities in the specimen, the distribution of σ_{yy} becomes asymmetric about the plane Y = L/2; σ_{yy} decreases by different amounts at various points on the centroidal axis and its distribution depends upon the value of L/H. We recall that the distribution of unstable points in the specimen is not the same for all L/H ratios.

Fig. 5.30a shows, for L/H=10, the variation of σ_{yy} on the centroidal line Y = L/2, Z = H/2. At $\varepsilon = 0$, σ_{yy} is compressive at points away from the lateral free surfaces. As the axial deformation increases σ_{yy} in the cross section becomes positive. At $\varepsilon = \sim 5\%$, $\sigma_{yy} > 0$ everywhere on the centroidal line. For $\varepsilon < \varepsilon_{yy}^{yield}$, the distribution of σ_{yy} on the centroidal line is symmetric about X = H/2. The variation of σ_{yy} on the centroidal axis Y = L/2, X = H/2 is similar to that on the centroidal axis Y = L/2, Z = H/2.

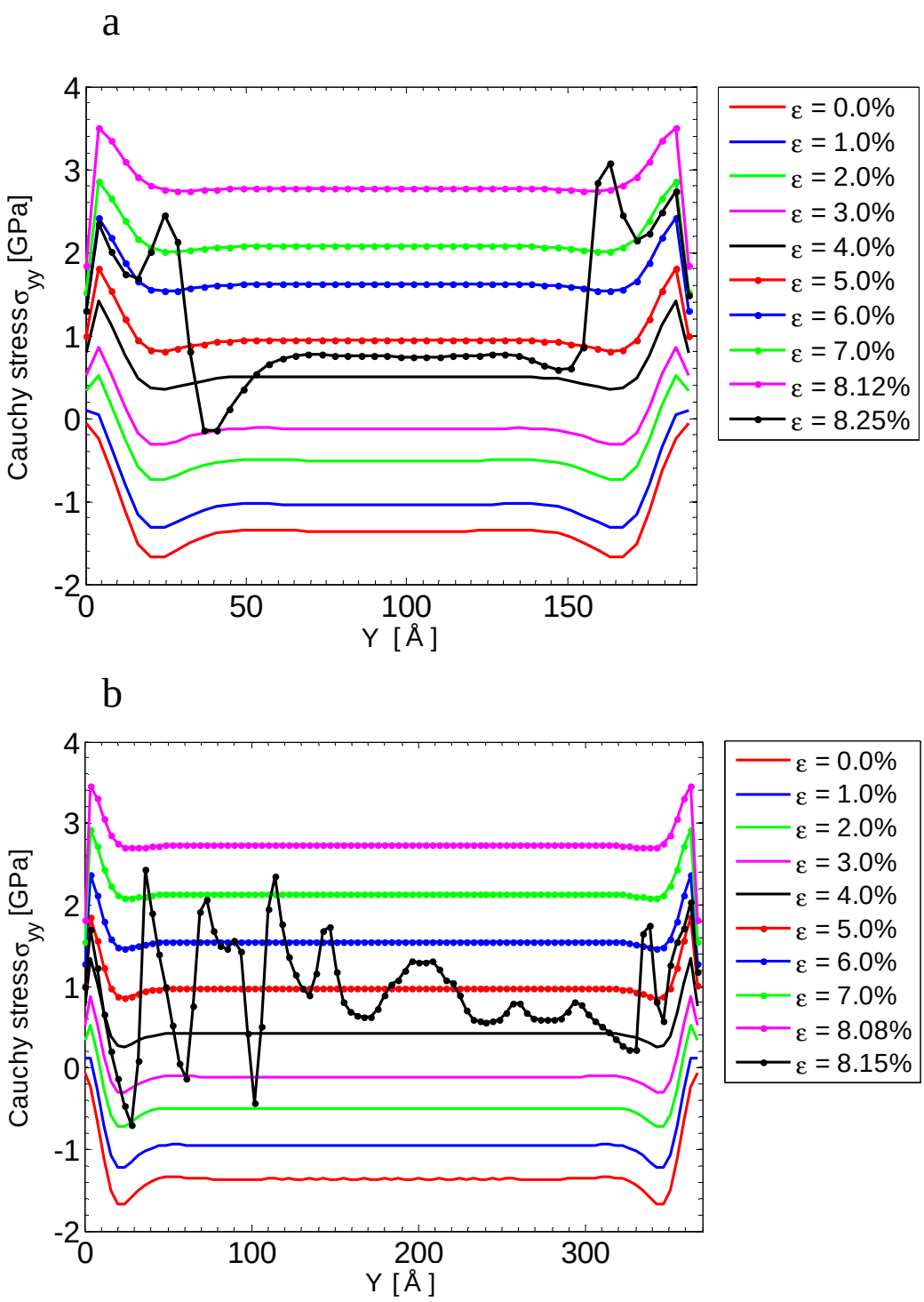

Fig. 5.29. Contd.

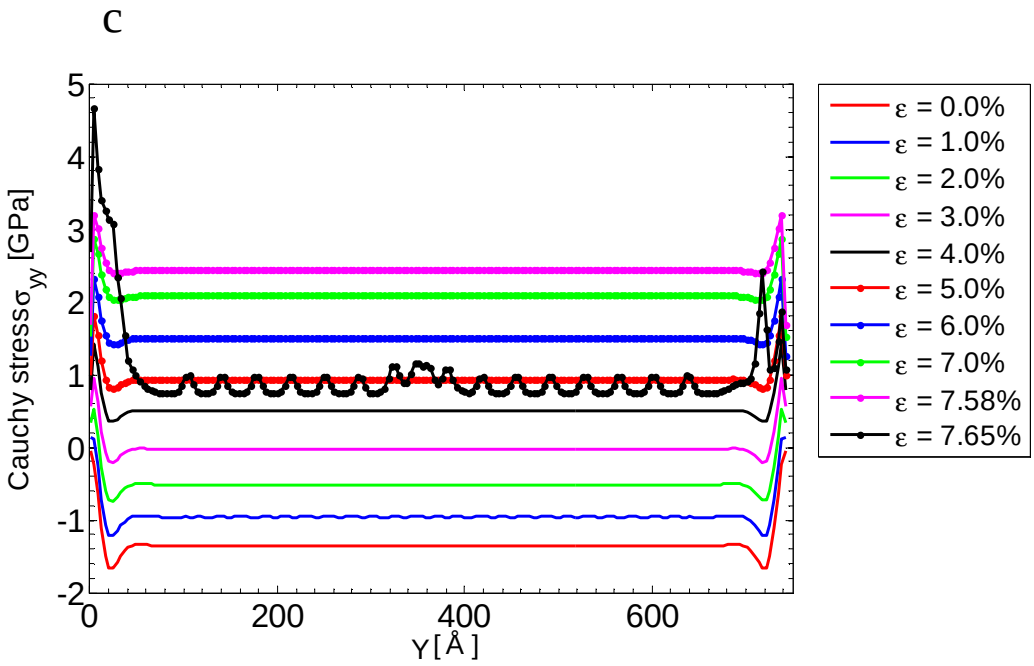

Fig. 5.29. For simulations of the simple tensile deformations, variation with the average axial strain ε of σ_{yy} component of the local Cauchy stress tensor along the centroidal axis; (a) L/H = 5, (b) L/H = 10 and (c) L/H = 20.

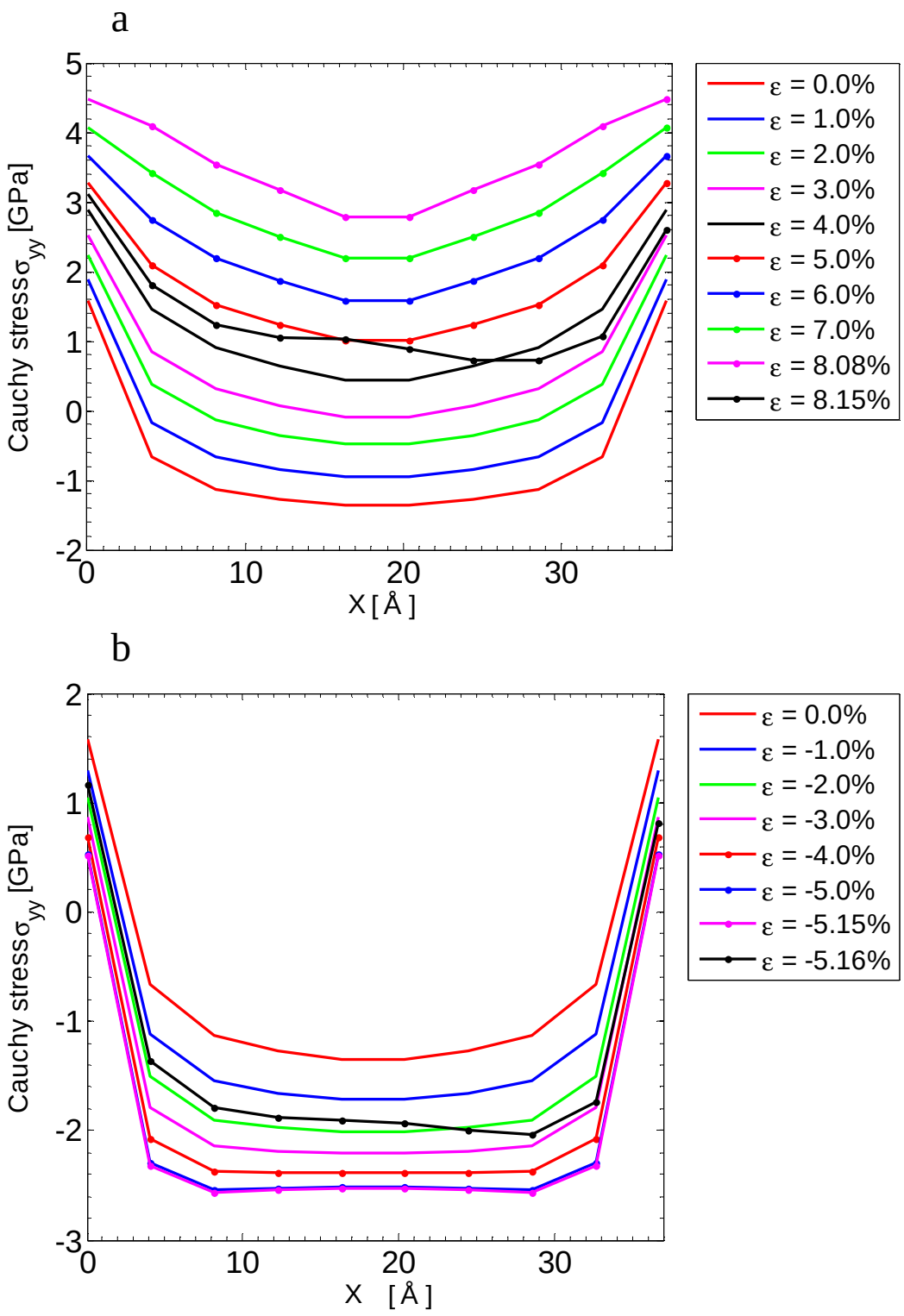

Fig. 5.30. For L/H=10, variation with the axial strain ε of the σ_{yy} component of the local Cauchy stress tensor along the X-centroidal line; (a) simple tension, and (b) simple compression.

Figures 5.31a, b, and c depict distributions on the mid-surfaces X = H/2 of σ_{yy} at $\varepsilon = \varepsilon_{yy}^{yield}$ for L/H = 5, 10 and 20 respectively. The three distributions are qualitatively similar in that the maximum tensile stress ~5 GPa occurs at points on the lateral surfaces, and the minimum tensile stress ~2.8 GPa at points on and near the centroidal axis.

Figures 5.32a and b depict, for four different values of L/H, distributions of σ_{xx} and σ_{yy} on the centroidal axis for the four specimens in configurations corresponding to $\varepsilon = 0$ and $\varepsilon = \varepsilon_{yy}^{yield}$. From Fig. 5.32a we see that the distribution of σ_{yy} on the centroidal axis is similar for the four specimens. At $\varepsilon = 0$, σ_{yy} equals zero at atoms close to the end faces and is compressive at other points.

With an increase in the axial tensile strain, σ_{yy} switches from compressive to tensile at points on the centroidal axis. However, σ_{xx} at points on the centroidal axis stays compressive with its magnitude increasing with an increase in ε. For L/H = 20, at the specimen centroid, σ_{xx} = - 0.7 GPa, σ_{yy} = - 1.35 GPa when $\varepsilon = 0$, and σ_{xx} = - 1.5 GPa, σ_{yy} = 2.5 GPa when $\varepsilon = \varepsilon_{yy}^{yield}$. Whereas, initially, $\sigma_{xx} = \sigma_{zz} \approx 0.5\ \sigma_{yy}$ at the specimen centroid, at yielding $|\sigma_{xx}| = |\sigma_{zz}| \approx 0.6\ \sigma_{yy}$. Note that in the reference configuration the three normal stresses are compressive but in the deformed configuration corresponding to $\varepsilon = \varepsilon_{yy}^{yield}$, σ_{xx} and σ_{zz} are compressive but σ_{yy} is tensile.

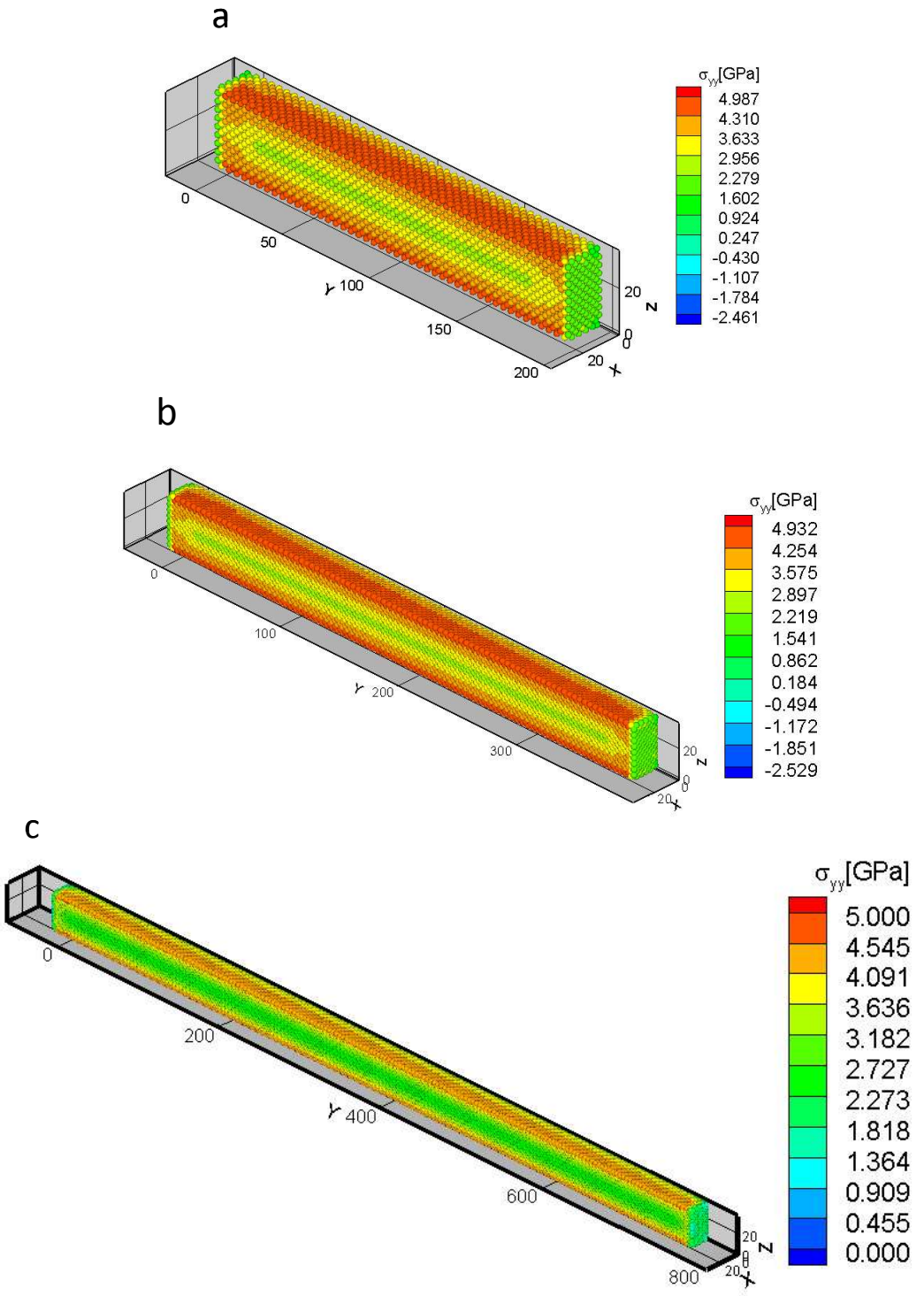

Fig. 5.31. For simulations of the simple tensile deformations, distribution of the local Cauchy stress tensor component σ_{yy} on the mid- section X = H/2 at $\mathcal{E} = \mathcal{E}_{yy}^{yield}$; (a) L/H = 5, (b) L/H = 10, and (c) L/H = 20.

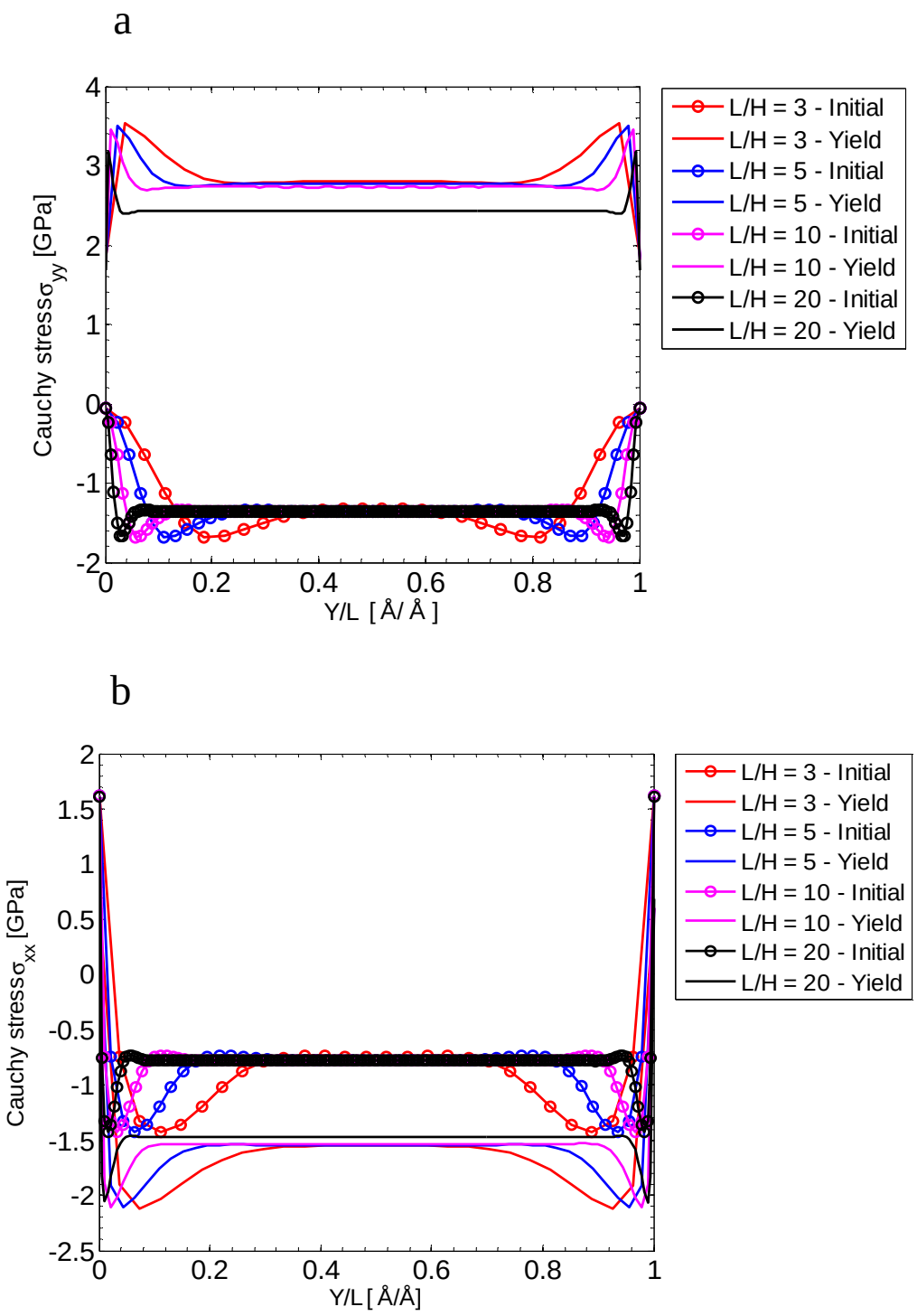

Fig. 5.32. For simple tensile deformations at $\varepsilon = 0$ and $\varepsilon = \varepsilon_{yy}^{yield}$, variation of the local Cauchy stresses σ_{yy} and σ_{xx} along the Y-centroidal line; (a) $\sigma_{yy,}$ and (b) σ_{xx}.

5.6.2 Simple compression

At different strain levels for L/H = 5, 10 and 20 Figs. 5.33a, b, and c show, respectively, distributions of σ_{yy} along the centroidal line parallel to the Y-axis. For different values of the axial strain ε, distributions of σ_{yy} on the centroidal line parallel to the Y-axis are qualitatively and quantitatively similar to each other for L/H = 5, 10 and 20. As for the case of simple tension, at $\varepsilon = 0$, $|\sigma_{yy}|$ is maximum at points situated at a distance of ~20Å from the free surfaces $Y = Y_{min}$ and $Y = Y_{max}$. The compressive stress at these points continuously increases with an increase in the axial deformation up to $\varepsilon = \varepsilon_{yy}^{yield}$. For L/H = 5, at $\varepsilon = \sim -3\%$, a concavity in the distribution of σ_{yy} at the center of the specimen is observed. This small concavity, not observed for L/H = 10 and 20, becomes more pronounced with increasing compressive deformation. After $|\varepsilon| > \sim 5\%$, $|\sigma_{yy}|$ at points on the centroidal line for the specimen with L/H = 5 does not increase appreciably; in Fig. 5.33a curves for $|\varepsilon| \geq \sim 6\%$ almost overlap each other until the yield point is reached. At $|\varepsilon|$ just greater than $\left|\varepsilon_{yy}^{yield}\right|$ the variation of σ_{yy} with Y depends upon the specimen size. We have not investigated the buckling instability in any of these specimens.

Figure 5.30b shows, for L/H = 10, the variation of σ_{yy} along the centroidal line parallel to the X- axis. The initially tensile stresses on the free surfaces $X = X_{min}$ and $X = X_{max}$ decrease and the compressive stresses in the interior increase monotonically till $\varepsilon = -5.15\%$. As σ_{yy} in the specimen approaches the yield stress the rate of change of σ_{yy} with ε decreases at the specimen centroid. However, gradients of stresses at points close to the free surfaces remain essentially unchanged. This differs substantially from that in tensile deformations (see Fig. 5.30a).

Figures 5.34a, b, and c depict the distribution at $\varepsilon = \varepsilon_{yy}^{yield}$ of σ_{yy} on the mid-section X = H/2 of specimens with L/H = 5, 10 and 20 respectively. The distribution in the specimen of the axial stress at the yield point for L/H = 5 is quite different from that in specimens with L/H = 10 and 20. At the yield point $|\sigma_{yy}|$ at points on the lateral traction free surfaces varies from ~ 0.005 to ~ 0.444 GPa; only small groups of atoms on the lateral traction free surfaces located at ~ 30 Å from the two loaded end faces have higher tensile stress σ_{yy} than that at atoms at the center of the lateral surfaces. These high values of the tensile stress on the lateral surface are observed in those cross-sections that have high values of compressive stresses at interior points. For L/H = 10 and L/H = 20 atoms on lateral surfaces with high positive values of σ_{yy} are spread along the length of

the specimen. At points far from the two loaded end faces, the distribution in the specimen of σ_{yy} is nearly uniform. On a cross section the stress σ_{yy} changes gradually from negative at the centroid to positive at the free surface.

In Fig. 5.35 at $\varepsilon = 0$ and $\varepsilon = \varepsilon_{yy}^{yield}$ the variations of σ_{xx} and σ_{yy} along the Y-centroidal line have been plotted for specimens with L/H = 3, 5, 10 and 20. The distributions of σ_{xx} and σ_{yy} in the reference configuration are similar for the four specimens. The maximum compressive stresses occur at the same relative locations and their values become uniform on the central $4/10^{th}$ of the specimen length. However, at the yield point, the stress distribution depends upon L/H. For L/H = 3 and 5 the stress distribution on the central portion of the specimen length is nonuniform but for L/H = 10 and 20 it is uniform. Values of σ_{xx} and σ_{yy} in the central $4/10^{th}$ of the specimen length depend upon L/H; their magnitudes are the maximum for L/H = 3 and the minimum for L/H = 20. At $\varepsilon = \varepsilon_{yy}^{yield}$, $\sigma_{xx} \approx 0.46\ \sigma_{yy}$, $0.6\ \sigma_{yy}$, $0.85\ \sigma_{yy}$ and $0.9\ \sigma_{yy}$ for L/H = 20, 10, 5, and 3, respectively, whereas at $\varepsilon = 0$, $\sigma_{xx} \approx 0.5\ \sigma_{yy}$ for each one of the four values of L/H.

a

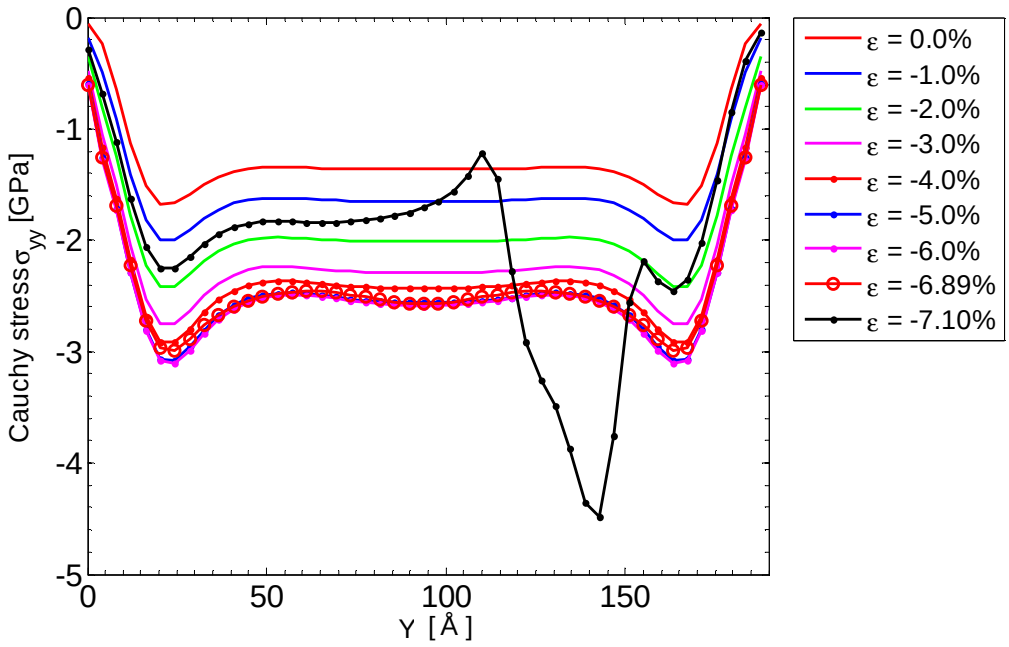

b

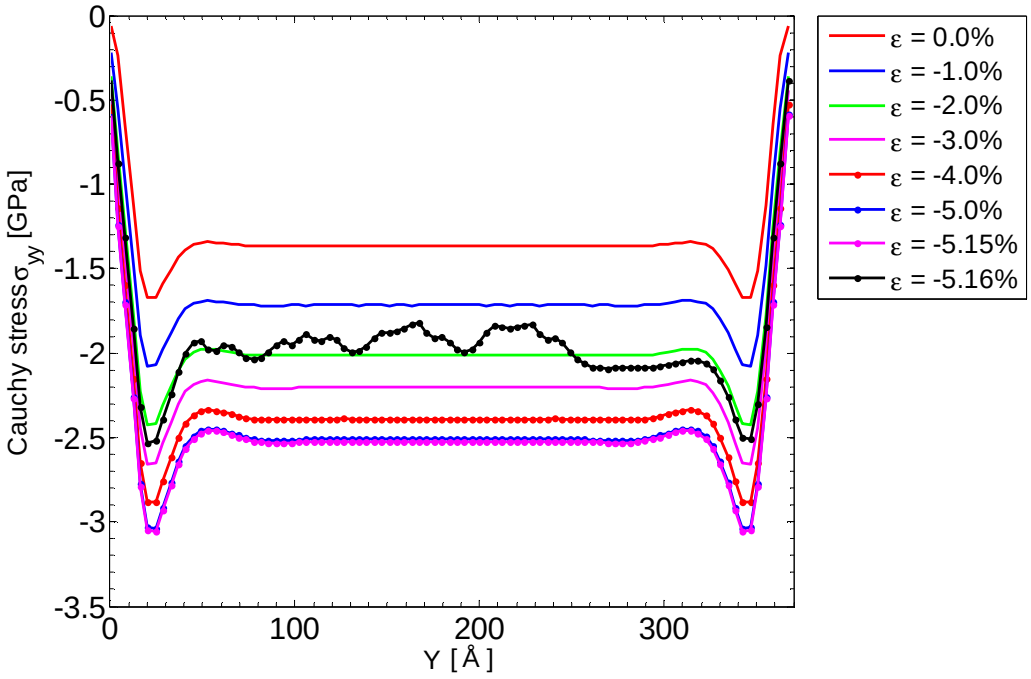

Fig. 5.33. Contd.

c

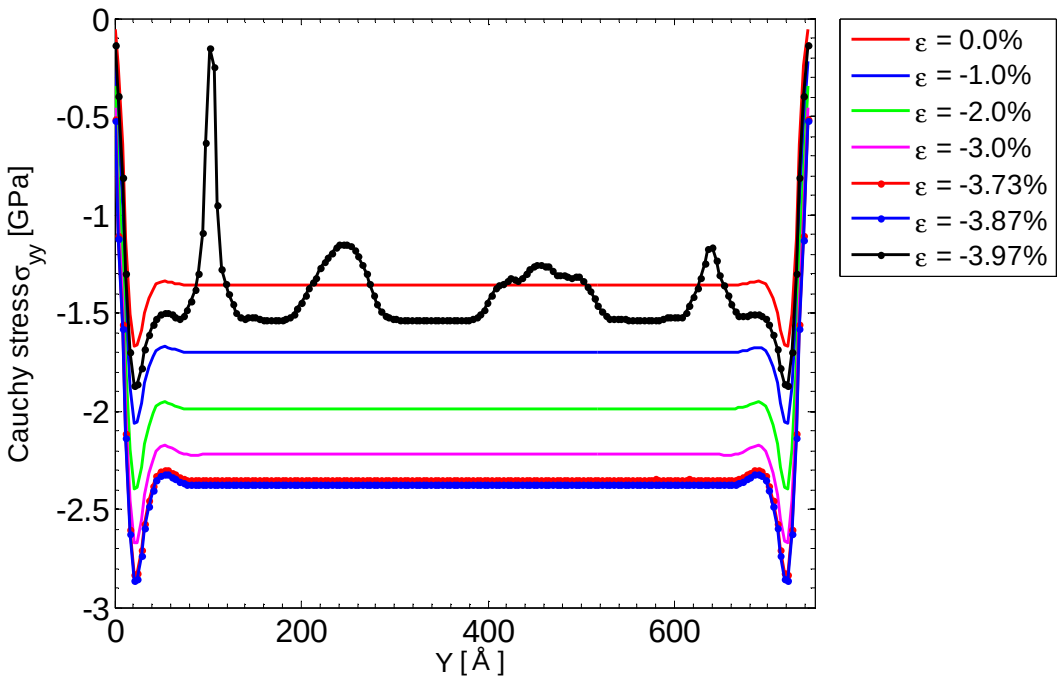

Fig. 5.33. For simulation of the simple compressive deformations, variation with the average axial strain ε of σ_{yy} component of the local Cauchy stress tensor along the centroidal axis; (a) L/H = 5, (b) L/H = 10, and (c) L/H = 20.

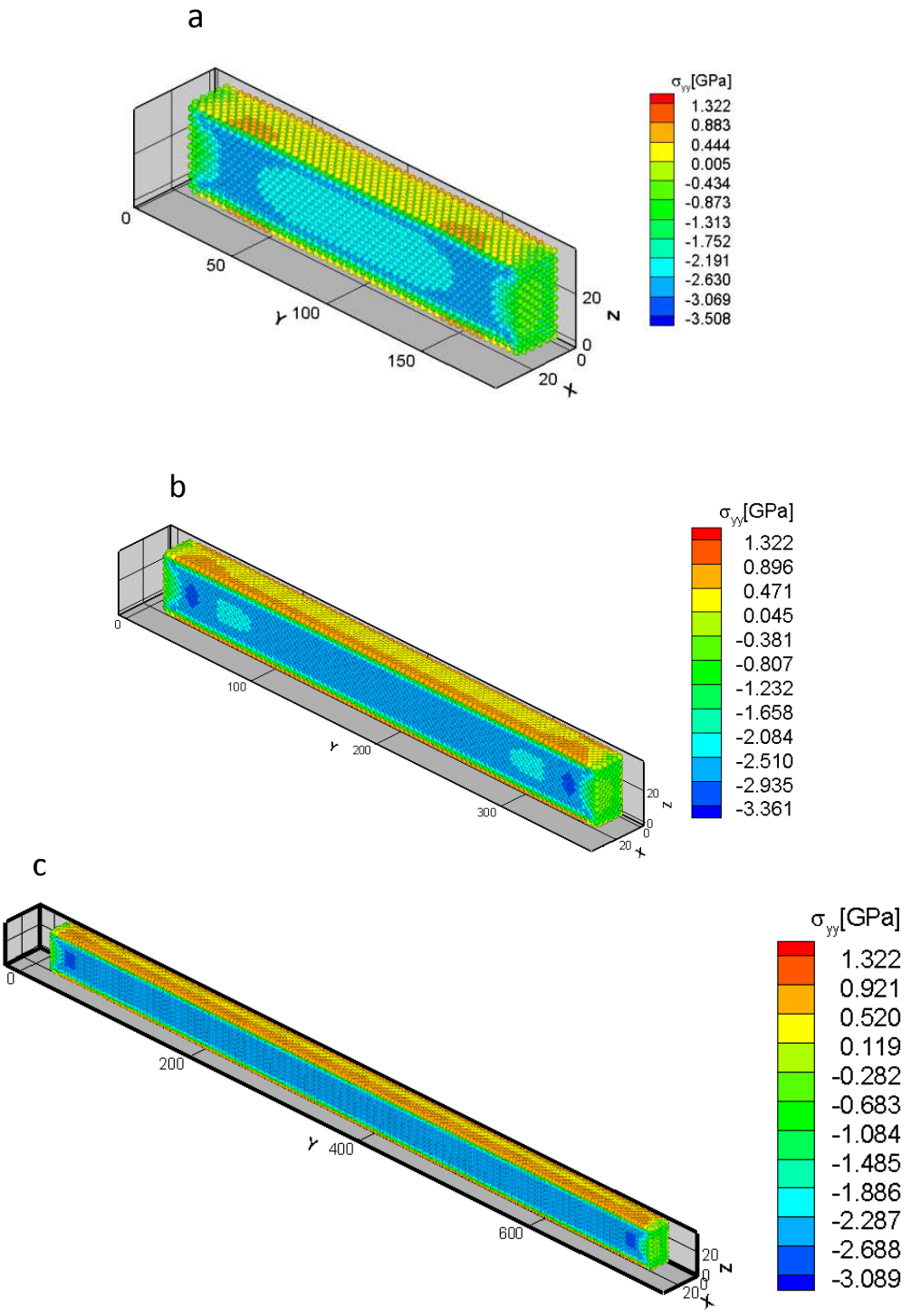

Fig. 5.34. For simulations of the simple compressive deformations, distribution of the σ_{yy} component of the local Cauchy stress tensor on the mid-section X = H/2 at $\mathcal{E} = \mathcal{E}_{yy}^{yield}$; (a) L/H = 5, (b) L/H = 10, and (c) L/H = 20.

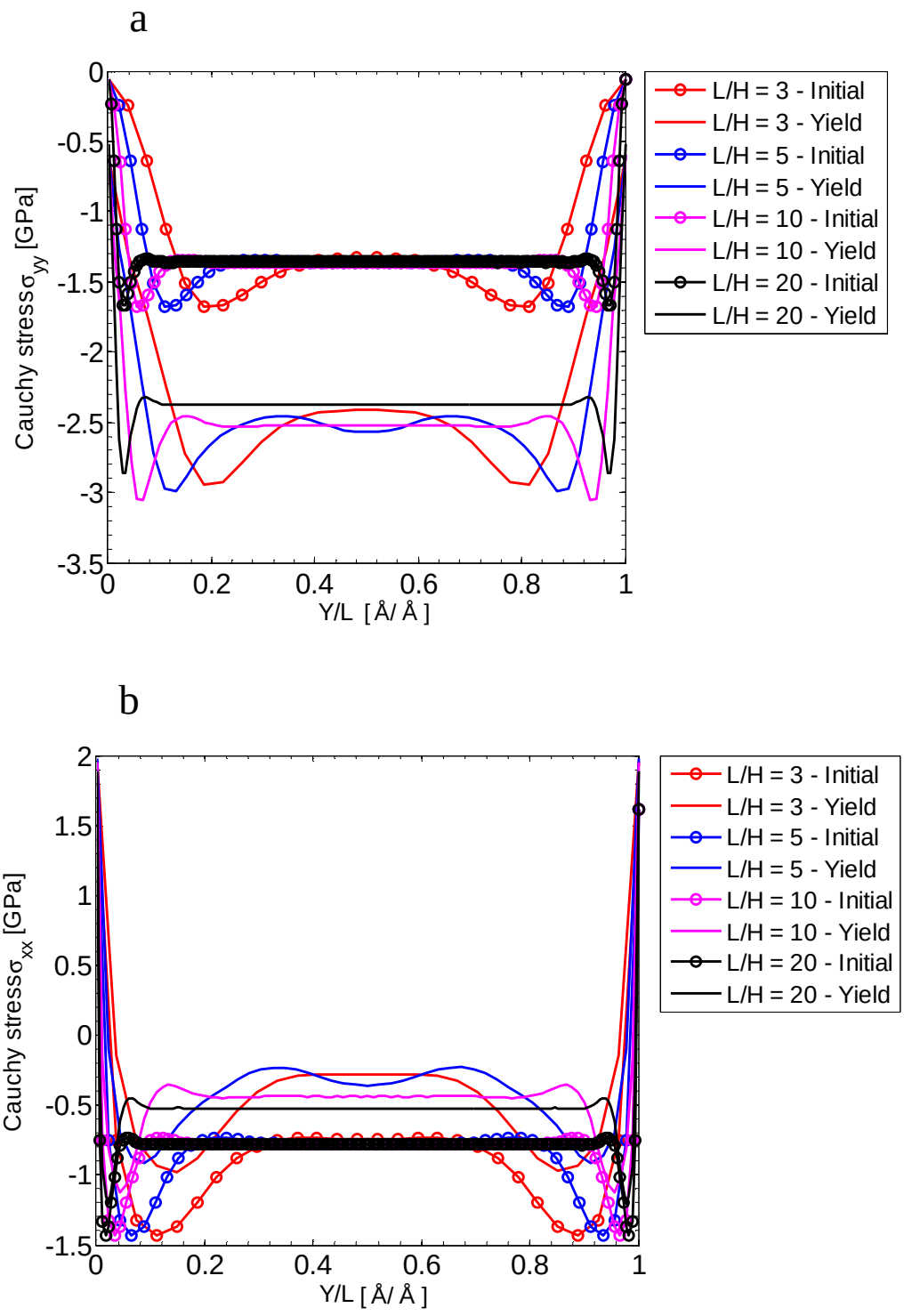

Fig. 5.35. For simple compression deformations at $\varepsilon = 0$ and $\varepsilon = \varepsilon_{yy}^{yield}$, variation of the local Cauchy stresses σ_{yy} and σ_{xx} along the Y-centroidal line; (a) $\sigma_{yy,}$ and (b) σ_{xx}.

5.7 Comparison of equivalent stresses at points where instabilities have initiated

5.7.1 Simple compression

For points where instabilities have initiated just after $\varepsilon = \varepsilon_{yy}^{yield}$, i.e., points identified by negative eigenvalues of $\boldsymbol{H}^{(i)}$, stresses in the configuration for $\varepsilon = \varepsilon_{yy}^{yield}$ have been computed. For L/H = 5, 10 and 20, Figs. 5.36a, b, and c depict, respectively, distributions of $2\tau_{max}$ on unstable points. Large values, ~ 2.5 GPa, of τ_{max} at unstable points are observed on atoms three layers below the lateral free surfaces. These atoms are located near the edges of the specimen (corners of the rhombic shape of unstable atoms) for the three L/H ratios. As the average axial strain increases the number of these atoms increases around the corners of the specimen (see red arrows in Fig.36). The yield point under compression is reached for the lowest value of $|\varepsilon|$ for the specimen with L/H = 20. Even though there are differences among the average axial yield stresses for the three specimens, the maximum shear stress at yield is about the same (see Table 5.4). The maximum value of the average axial yield stress is for the specimen with L/H = 5. It is clear from the results exhibited in Fig. 5.36a that large values of τ_{max} occur at points on the third and the fourth layers of atoms located parallel to the lateral traction free surfaces. Points in the interior experience higher shear stresses as the strain level increases; this is evidenced by the increase in the number of atoms in the orange band surrounding atoms with high values of τ_{max}. It is important to note that atoms with the maximum value of the shear stress are not located on the traction free surfaces but beneath them.

For L/H = 5, 10 and 20, Figs. 5.37a, b, and c depict distributions of σ_{VM} at unstable points. As for the distributions of $2\tau_{max}$ the highest values of the von Mises stress occur at points near the four corners of the specimens that are on the third layer below the traction free surface. The maximum value, ~ 2.23 GPa, of σ_{VM} is almost the same for specimens with L/H = 5 and L/H = 10. The maximum value, ~ 2.1 GPa, for L/H = 20, is slightly less than that for the other two specimens.

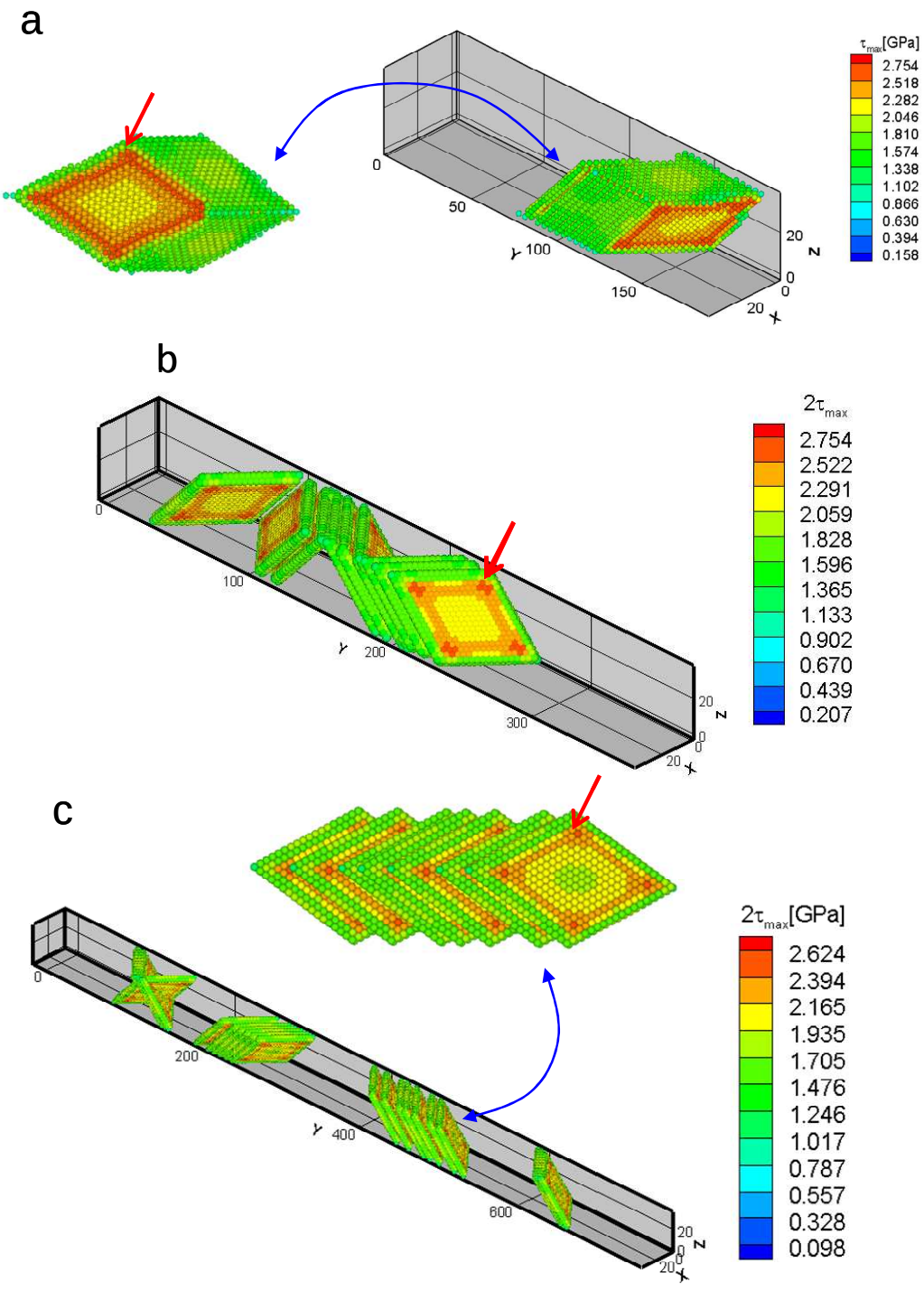

Fig. 5.36. For simulations of the simple compressive deformations, the distribution of $2\tau_{max}$ at the unstable points when $\varepsilon = \varepsilon_{yy}^{yield}$; (a) L/H = 5, (b) L/H = 10, and (c) L/H = 20. Red arrows indicate points with high stress values. Values of σ_{yy}, σ_{VM} and $2\tau_{max}$ at these points are summarized in Table 5.4. The blue arrows indicate sections for which an expanded view is provided.

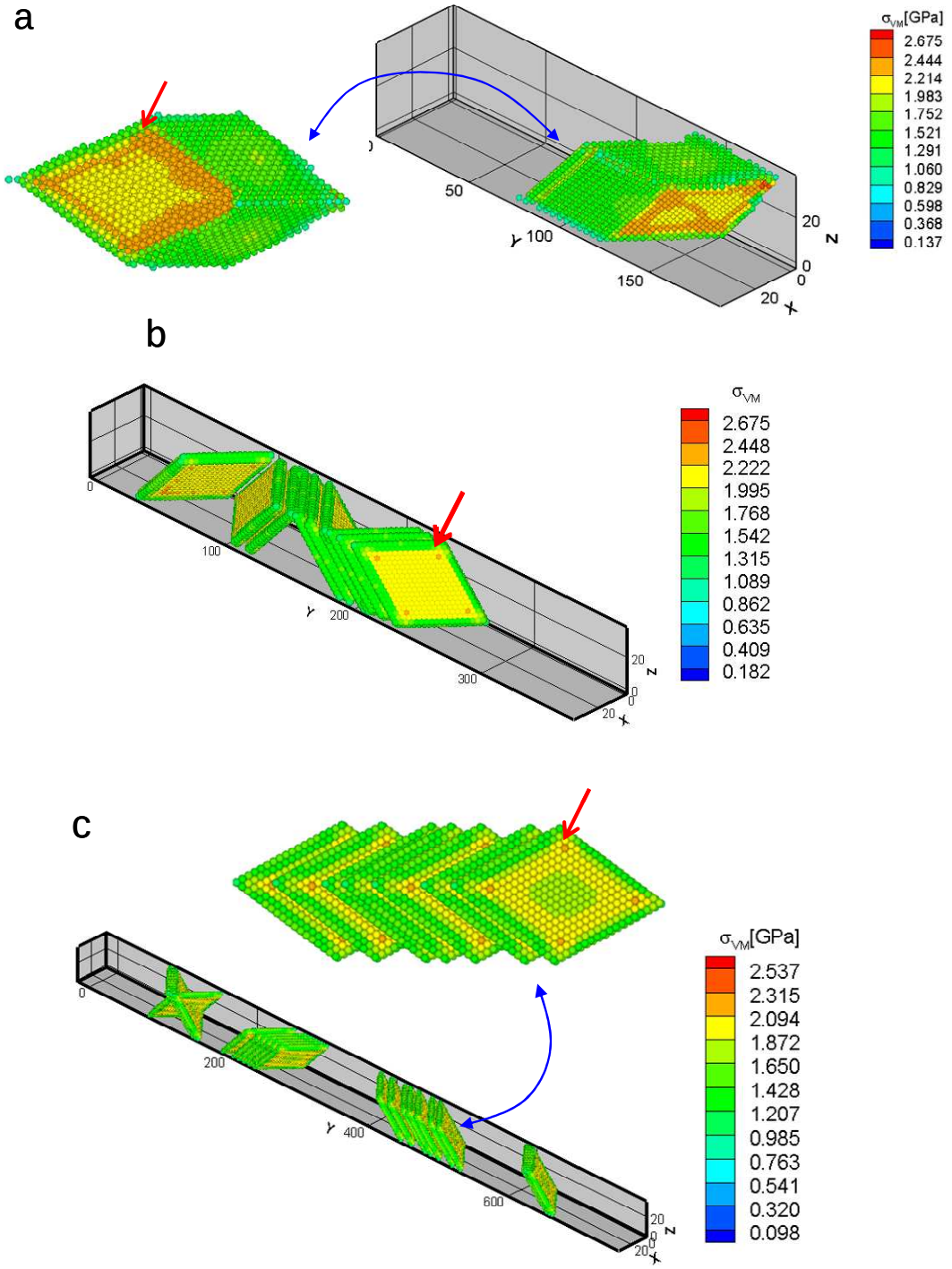

Fig. 5.37. For simulations of the simple compressive deformations, the distribution of σ_{VM} on the unstable points when $\varepsilon = \varepsilon_{yy}^{yield}$; (a) L/H = 5, (b) L/H = 10, and (c) L/H = 20. Red arrows indicate points with high stress values. Values of σ_{yy} ,σ_{VM} and $2\tau_{max}$ at these points are summarized in Table 5.4. The blue arrows indicate sections for which an expanded view is provided.

Table 5.4: For specimens with different L/H ratios deformed in simple compression, maximum values at $\varepsilon = \varepsilon_{yy}^{yield}$ of σ_{yy} , σ_{VM} and $2\tau_{max}$ for unstable atoms and the corresponding values for atoms on the centroidal axis. Points with the maximum values are indicated by red arrows in Figs. 5.36 and 5.37.

	Maximum values			Maximum values at points on the centroidal line			
L/H	σ_{yy} (GPa)	σ_{VM} (GPa)	$2\tau_{max}$ (GPa)	σ_{yy} (GPa)	σ_{VM} (GPa)	$2\tau_{max}$ (GPa)	$(\sigma_{yy})_{average}$ (GPa)
5	-2.772	2.276	2.555	-2.537	2.212	2.341	-1.810
10	-2.789	2.601	2.601	-2.533	2.087	2.131	-1.671
20	-2.584	2.097	2.422	-2.371	1.850	1.862	-1.387

5.7.2 Simple tension

The distributions of $2\tau_{max}$ at $\varepsilon = \varepsilon_{yy}^{yield}$ for simulations of the simple tensile deformations of specimens with L/H = 5, 10 and 20 are depicted in Figs. 5.38a, b, and c. As for simple compressive deformations, atoms with high values of the maximum shear stress are near the edges of the specimen (the corners of the rhombic plane of unstable atoms). Points with high values of τ_{max} are located right beneath the lateral free surfaces. In contrast to results for simple compression, the pattern for the distribution of stresses is the same for the three specimens. The maximum value, ~5.9 GPa, of $2\tau_{max}$ is also the same for the three specimens.

As the average axial stress increases, high values of $2\tau_{max}$ occur at atoms located along the diagonals of the cross section near the center of the specimen. This distribution contrasts with the one observed in simple compression where interior atoms having high stress levels form a closed rectangular band. Values of $2\tau_{max}$ decrease from 5.9 GPa at points on the edges, to 4.5, 4.3 and 3.9 GPa at the centroid of the specimen for L/H = 5, 10 and 20, respectively.

For L/H = 5, 10 and 20 and $\varepsilon = \varepsilon_{yy}^{yield}$, Figs. 5.39a, b, and c depict distributions of σ_{VM} on unstable atoms. The distribution of σ_{VM} is similar to that for $2\tau_{max}$ with large values at atoms localized in clusters near the corners of the rhombic planes of unstable atoms. The minimum value of σ_{VM} among values at unstable points does not occur at the atom at the specimen centroid.

From the distributions of σ_{VM} and $2\tau_{max}$ for simulations of the simple tensile deformations we note that the maximum stress levels are reached at the same locations in the three specimens; these results are summarized in Table 5.5.

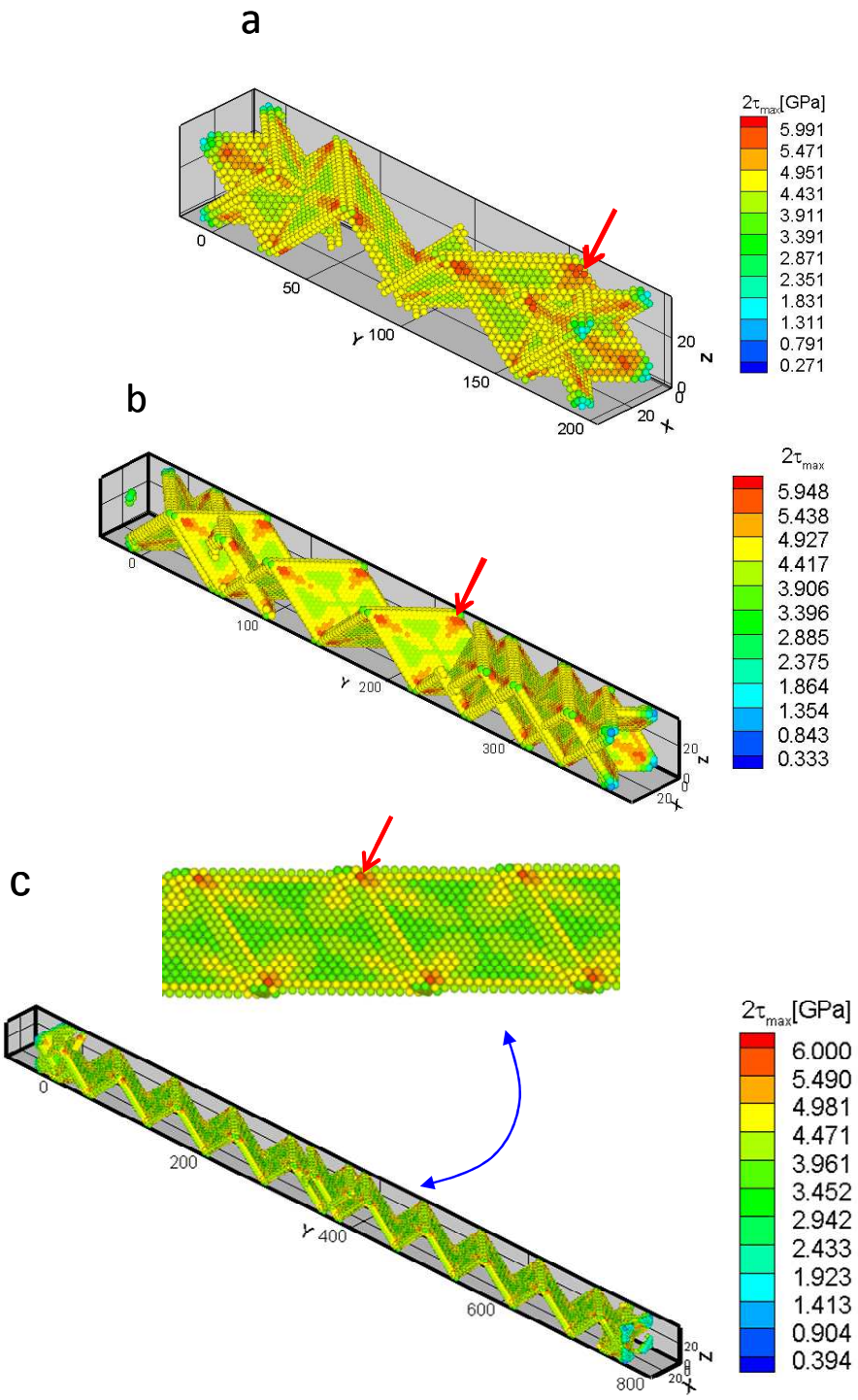

Fig. 5.38. For simulations of the simple tensile deformations, distribution of $2\tau_{max}$ on unstable points when $\varepsilon = \varepsilon_{yy}^{yield}$; (a) L/H = 5, (b) L/H = 10, and (c) L/H = 20. Red arrows indicate points with high stress values. Values of σ_{yy}, σ_{VM} and $2\tau_{max}$ at these points are summarized in Table 5.5. The blue arrows indicate sections for which an expanded view is provided.

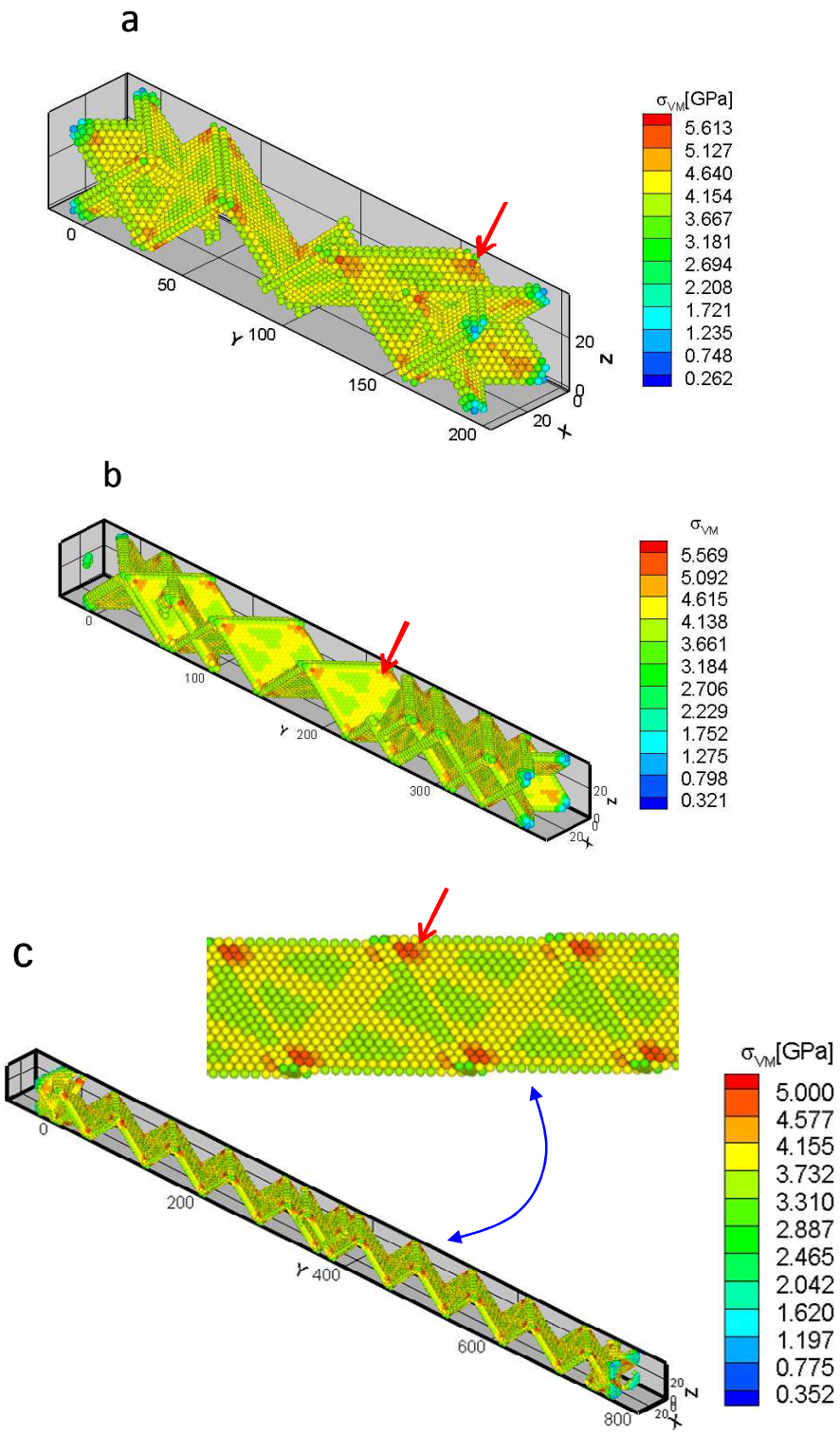

Fig. 5.39. For simulations of the simple tensile deformations, distribution of σ_{VM} on unstable points when $\varepsilon = \varepsilon_{yy}^{yield}$; (a) L/H = 5, (b) L/H = 10, and (c) L/H = 20. Red arrows indicate points with high stress values. Values of σ_{yy} ,σ_{VM} and $2\tau_{max}$ at these points are summarized in Table 5.5. The blue arrows indicate sections for which an expanded view is provided.

Table 5.5: For specimens with different L/H ratios deformed in simple tension, maximum values at $\varepsilon = \varepsilon_{yy}^{yield}$ of σ_{yy} , σ_{VM} and $2\tau_{max}$ for unstable atoms and the corresponding values for atoms on the centroidal axis. Points with the maximum values are indicated by red arrows in Figs. 5.38 and 5.39.

	Maximum values			Maximum values at points on the centroidal line			
L/H	σ_{yy} (GPa)	σ_{VM} (GPa)	$2\tau_{max}$ (GPa)	σ_{yy} (GPa)	σ_{VM} (GPa)	$2\tau_{max}$ (GPa)	$(\sigma_{yy})_{average}$ (GPa)
5	4.627	5.204	5.959	2.930	4.322	4.500	4.996
10	4.579	5.155	5.905	2.839	4.285	4.295	4.990
20	4.281	4.865	5.586	2.436	3.907	3.907	4.618

Chapter 6

Instabilities in tensile and compressive deformations with prescribed essential boundary conditions on bounding surfaces

We now study deformations of rectangular nanorods deformed by prescribing normal displacements on all bounding surfaces. As for the simple shear deformations, we compare results from MM simulations with those of a hyperelastic body whose strain energy density is derived from the TB potential and the Cauchy-Born rule. Recalling that Poisson's ratio for an Au specimen is ~ 0.47, for simplifying the analysis, we consider isochoric deformations of the unconstrained (or compressible) hyperelastic body. For an incompressible hyperelastic body the hydrostatic pressure cannot be determined since tractions are not prescribed anywhere on the boundary.

For a specimen deformed in tension/compression along the y-axis, Figs. 6.1a, 6.1b and 6.2 exhibit the evolution with the average axial strain ε of the average axial stress σ_{yy}, the average axial stress σ_{xx} and the strain energy density obtained from MM simulations of deformations. Corresponding results from the analytical solution of the boundary-value problem with the deformation gradient $\boldsymbol{F} = \text{diag}\{\lambda_1, \lambda_2, \lambda_3\}$ where $\lambda_1 = \lambda_3 = 1/\sqrt{\lambda_2}$ are also exhibited. Here λ_1, λ_2 and λ_3 are stretches along the x-, the y-, and the z-axes, respectively. It is clear that prior to the onset of an instability indicated by a sharp drop with an infinitesimal increase of ε in σ_{yy}, σ_{xx} and the strain energy density, results from MM simulations agree well with those from the analytical solution for each one of the specimens with L/H = 5, 10 and 20. We note that instabilities occurred only when a specimen is deformed in tension but no instabilities ensued when the same specimen is deformed in compression.

Figure 6.3 depicts the variation with the axial strain ε of the minimum eigenvalue of local Hessian $\boldsymbol{H}^{(i)}$. Even though the minimum eigenvalue of $\boldsymbol{H}^{(i)}$ becomes negative in both tensile and compressive deformations at $\varepsilon = 0.1$ and -0.06 no discontinuity in the σ_{yy} vs. ε curve occurs at these values of the average axial strain. Thus the minimum eigenvalue of $\boldsymbol{H}^{(i)}$ becoming negative is not a good criterion for detecting a local instability when essential boundary conditions are prescribed on all bounding surfaces. However, a sharp drop in the minimum eigenvalue of $\boldsymbol{H}^{(i)}$

occurs at ε = ~ 0.14 when the system becomes globally unstable as signified by a noticeable drop in the strain energy density.

Table 6.1: Values of the average axial stress and the average axial strain at the yield point for tension/compression with essential boundary conditions prescribed on all bounding surfaces ($\boldsymbol{F}$ = diag{λ_1, λ_2 , λ_3} where $\lambda_1 = \lambda_3 = 1/\sqrt{\lambda_2}$) for different L/H ratios.

	Tension		Compression	
L/H	σ_{yy}^{yield} (GPa)	ε_{yy}^{yield} (%)	σ_{yy}^{yield} (GPa)	ε_{yy}^{yield} (%)
5	5.005	12.7	-2.449	11.3
10	5.017	12.7	-2.442	11.3
20	5.064	12.7	-2.425	11.3

For the three specimens with L/ H = 5, 10 and 20, we have summarized in Table 6.1 values of the average yield stress and the average yield strain for the triaxial tensile and compressive deformations. It is clear that for each specimen, the yield stress in tension is nearly twice of that in compression even though the average axial strains at yield are not that much different.

For the three cubic specimens whose shear and simple shear deformations were analyzed in Chapter 4, we have studied triaxial tensile/compressive deformations with MM simulations and also analytically of the equivalent hyperelastic material. The stretch in each coordinate direction is assumed to be the same. MM simulation results presented in Figs. 6.4 and 6.5 reveal that systems A, B, and C become globally unstable at average axial strains of 3.8%, 3.7% and 3.5% respectively. However, in the σ_{yy} versus ε and the strain energy density versus ε curves, σ_{yy} and the strain energy density for the equivalent hyperelastic material monotonically increase with ε.

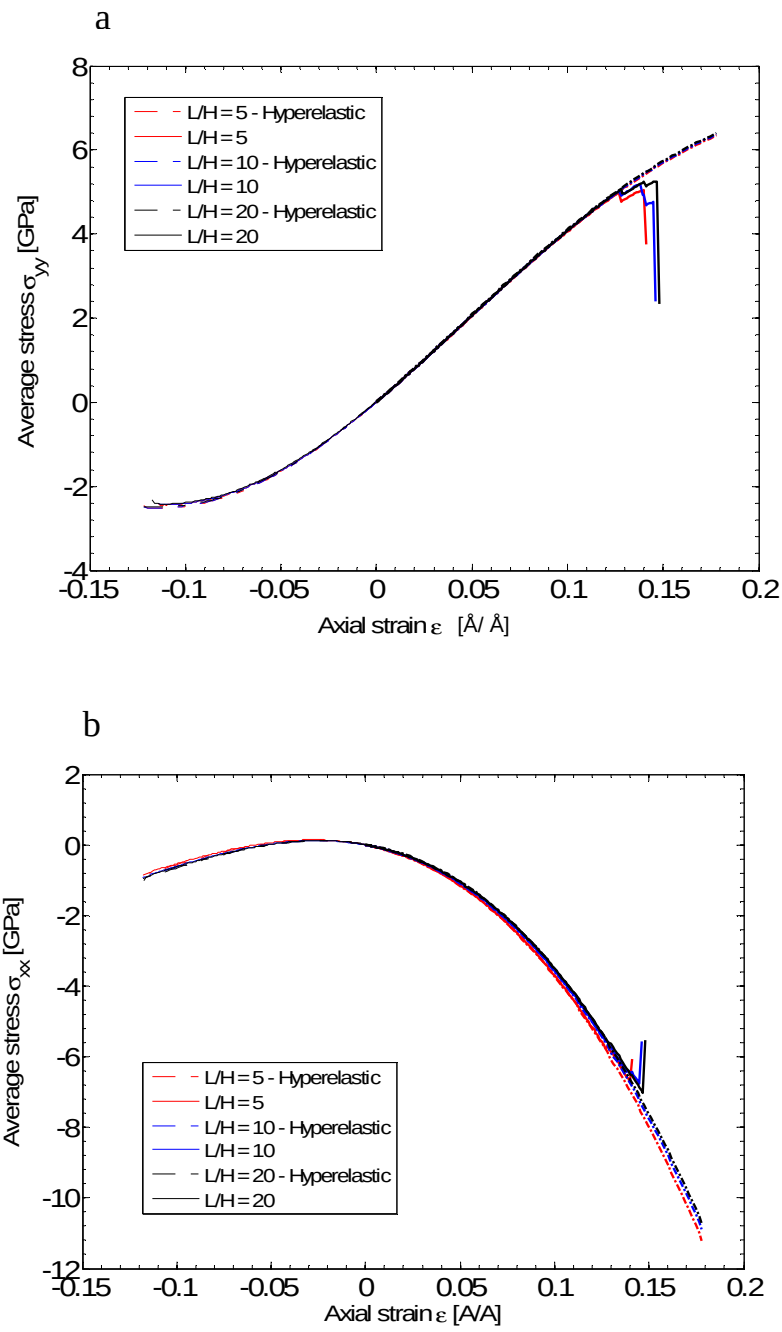

Fig. 6.1. Variation with the axial strain ε of the average components of the Cauchy stress tensor for tension/compression with essential boundary conditions prescribed on all bounding surfaces ($\boldsymbol{F}$ = diag{λ_1, λ_2 , λ_3} where $\lambda_1 = \lambda_3 = 1/\sqrt{\lambda_2}$) for different L/H ratios. (a) σ_{yy}; (b) σ_{xx}.

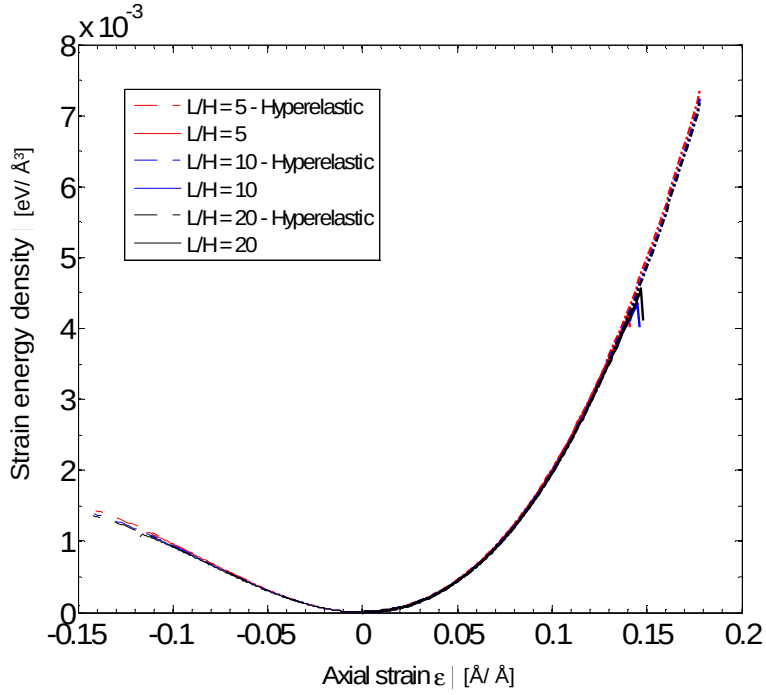

Fig. 6.2. Variation with the axial strain ε of the strain energy density for tension/compression with essential boundary conditions prescribed on all bounding surfaces ($\boldsymbol{F}$ = diag{λ_1, λ_2 , λ_3} where $\lambda_1 = \lambda_3 = 1/\sqrt{\lambda_2}$) for different L/H ratios.

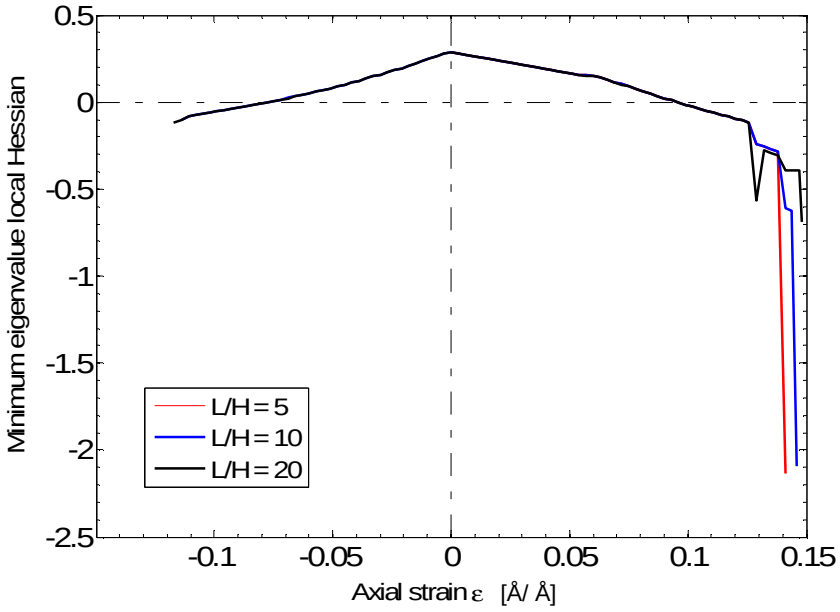

Fig. 6.3. For simulations with different values of L/H, variation with the average axial strain ε of the minimum eigenvalue of the local Hessian $\boldsymbol{H}^{(i)}$ in simple tensile/compressive deformations with essential boundary conditions prescribed on all bounding surfaces ($\boldsymbol{F}$ = *diag*{λ_1, λ_2 , λ_3} where $\lambda_1 = \lambda_3 = 1/\sqrt{\lambda_2}$).

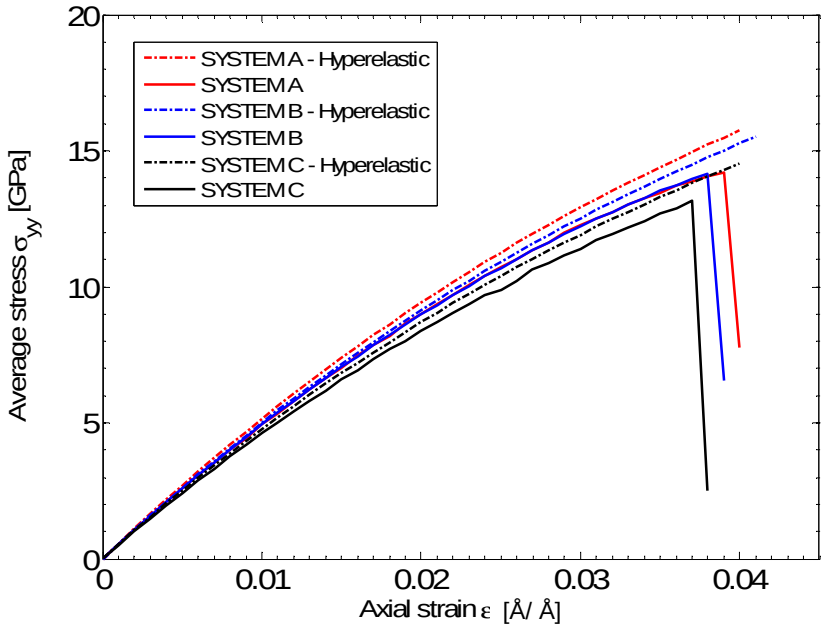

Fig. 6.4. For specimens A, B, and C, evolution with the average axial strain ε of the average value of σ_{yy} component of the Cauchy stress tensor for hydrostatic tension ($\boldsymbol{F} = diag\{\lambda_1, \lambda_2, \lambda_3\}$ where $\lambda_1 = \lambda_2 = \lambda_3$)

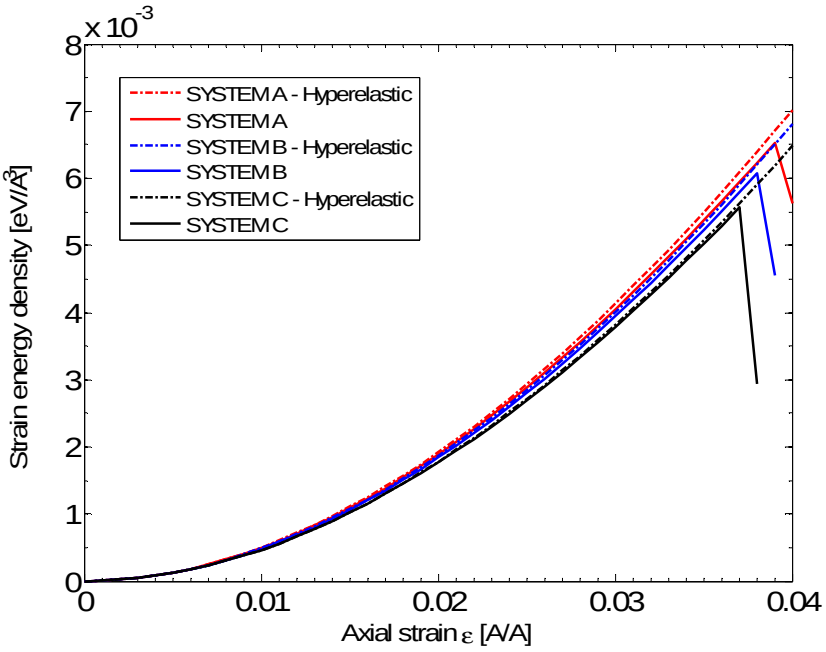

Fig. 6.5. For specimens A, B, and C, variation with the axial strain ε of the strain energy density for hydrostatic tension ($\boldsymbol{F} = diag\{\lambda_1, \lambda_2, \lambda_3\}$ where $\lambda_1 = \lambda_2 = \lambda_3$).

Chapter 7

Conclusions

7.1 General conclusions regarding local and global instabilities in gold crystals

We have used molecular mechanics simulations with the tight-binding potential to study local and global instabilities in initially defect-free nano-specimens of gold deformed in shear, simple shear, tension/compression, simple tension/compression, and triaxial tension/compression. The criteria used to delineate local instabilities include the following: (*i*) a second order spatial derivative of the displacement field having large values relative to its average value in the body, (*ii*) the minimum eigenvalue of the Hessian of the potential energy of an atom becoming nonpositive, and (*iii*) structural changes represented by a high value of the common neighborhood parameter. The system's configuration is said to be globally unstable when its potential energy is smaller than that in another nearby configuration.

For the seven different size specimens studied, Table 7.1 lists changes in the total energy, the volumetric strain, and the axial strain induced during the minimization of the potential energy of their unloaded initial configurations. The volume decreases by ~1.5%, and the axial strain equals ~ -1.5%. Even though the starting configuration has flat bounding surfaces, the unloaded relaxed configuration's bounding surfaces are locally curved, and atoms at the sharp eight corners of the starting configuration are displaced noticeably. Fig. 7.1 depicts the relation between the change in the total potential energy V and the change in the total volume Ω^T upon relaxation. This relation is almost linear regardless of the aspect ratio of the specimen and the number of atoms in it.

For the mechanical tests simulated, namely, the shear (S), the simple shear (SS), the simple tension/compression (ST/SC), the axial tension/compression (AT/AC) with displacements prescribed in all three directions on the end faces, and the triaxial tension/compression with essential boundary conditions prescribed on all six faces, Table 7.2 summarizes at the instantof the specimen yielding values of the von Mises stress σ_{VM}, the maximum shear stress τ_{max}, and the strain energy density $W_{0.}$ It is evident that values of these quantities for different specimens are highly affected by the residual stresses induced during the minimization of the potential energy

of the initial unloaded configuration. A general conclusion is that values of σ_{VM} and τ_{max} are considerably higher when essential boundary conditions are prescribed on all bounding surfaces than when one or more of the bounding surfaces are free of external loads.

Table 7.1: For specimens with different L/H ratios, the relative change in the total potential energy (V), the relative change in the total volume (Ω^T), and the axial strain (ε) induced during the minimization of the potential energy of the initial unloaded configuration.

L/H	L (Å)	No. atoms	$\frac{\Delta V}{V_I}$ (eV/eV)	$\frac{\Delta \Omega^T}{\Omega_I^T}$ (Å^3/Å^3)	ε (Å/Å)
1	~32	3480	3.763E-3	-2.021E-2	-2.081E-2
1	~50	7813	2.549E-3	-1.486E-2	-1.713E-2
1	~100	58825	1.044E-3	-6.923E-3	-1.036E-2
3	~110	9928	2.616E-3	-1.531E-2	-1.589E-2
5	~188	16787	2.369E-3	-1.518E-2	-1.518E-2
10	~367	32671	2.197E-3	-1.361E-2	-1.469E-2
20	~742	65883	2.105E-3	-1.316E-2	-1.430E-2

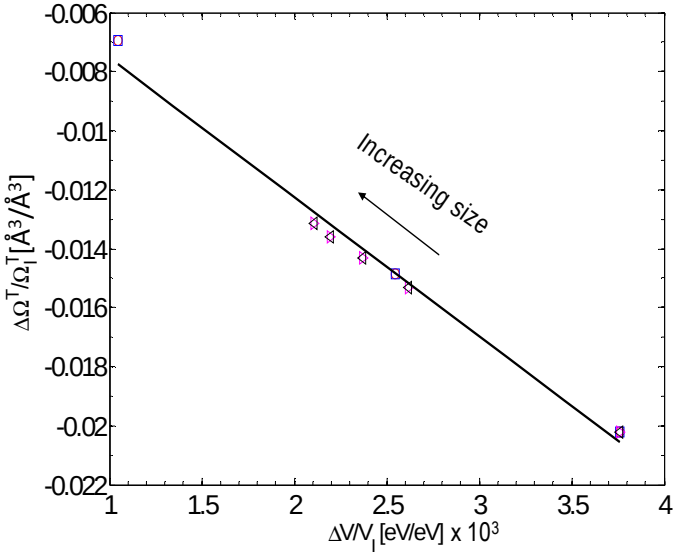

Fig. 7.1. For specimens of different aspect ratios and having different number of atoms, variation of the percentage change in volume with the percentage change in the total potential energy during the relaxation process.

Table 7.2: At the yield point and for specimens with different L/H ratios deformed in shear (S), simple shear (SS), simple tension/compression (ST/SC), axial tension/compression (AT/AC) with prescribed displacements in three-directions at the end faces, and triaxial tension (TT), the average von Mises stress σ_{VM}, the average τ_{max}, and the strain energy density W_0.

L/H	No. atoms	σ_{VM} (GPa)	τ_{max} (GPa)	W_0 (meV/Å^3)	Test
1	3480	6.230(20.22)	3.581(10.932)	3.546(4.477)	S(SS)
1	7813	5.750(18.390)	3.304(9.949)	2.959(3.869)	S(SS)
1	58825	4.030(17.190)	2.322(9.288)	2.028(3.610)	S(SS)
1	3480	4.569(2.498)	2.284(1.247)	1.165(0.879)	ST(SC)
3	9928	5.051(1.784)	2.525(0.894)	1.161(0.498)	ST(SC)
5	16787	4.998(1.809)	2.499(0.905)	1.148(0.540)	ST(SC)
10	32671	4.982(1.671)	2.491(0.836)	1.129(0.335)	ST(SC)
20	65883	4.618(1.387)	2.309(0.536)	0.988(0.220)	ST(SC)
5	16787	10.757(10.757)	5.378(1.711)	4.218(0.855)	AT(AC)
10	32671	10.573(10.573)	5.286(1.629)	4.366(0.814)	AT(AC)
20	65883	10.621(10.621)	5.310(1.590)	4.555(0.795)	AT(AC)
1	3480	0.0	0.0	1.129	TT
1	7813	0.0	0.0	1.093	TT
1	58825	0.0	0.0	1.072	TT

Fig. 7.2 shows the relation between the change in the total potential energy upon relaxation and the strain energy density W_0 at the yield point. Because only three specimens were used to simulate deformations it is hard to draw any general conclusion. However, for seven samples used to study simple tension/compression, one can see that for simple tension the strain energy density at yield is nearly independent of the relative change in the potential energy of the body during the initial relaxation process. For simple compression, the strain energy density at yield seems to approach a constant value with an increase in $\Delta V / V_I$. The value of the strain energy density at yield strongly depends upon the type of deformations induced in the specimen.

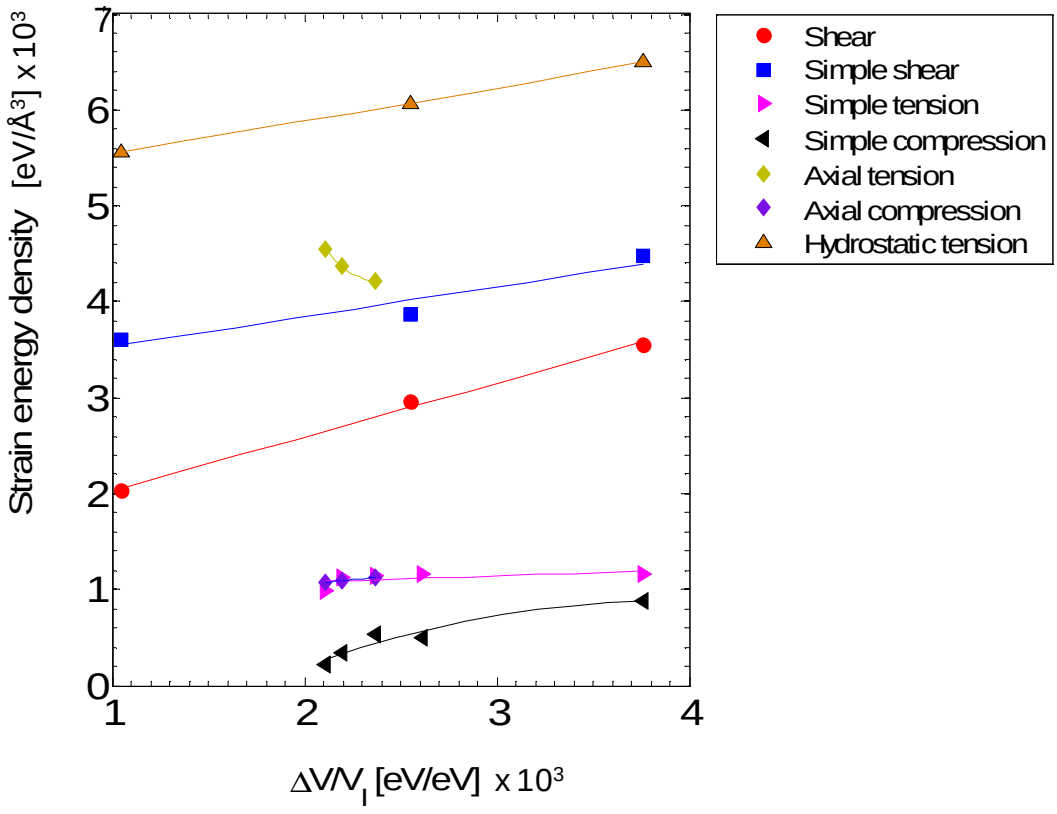

Fig. 7.2. For specimens with different aspect ratios, number of atoms and mechanical tests listed in Table 7.2, the relation between the change in the total potential energy upon relaxation and the strain energy density W_0 at the yield point.

Fig. 7.3 shows the relation between the change in the total potential energy upon relaxation and the average von Mises stress, $\sigma_{VM,,}$ at the yield point. Conclusions similar to those for the strain energy density can be drawn for σ_{VM} .

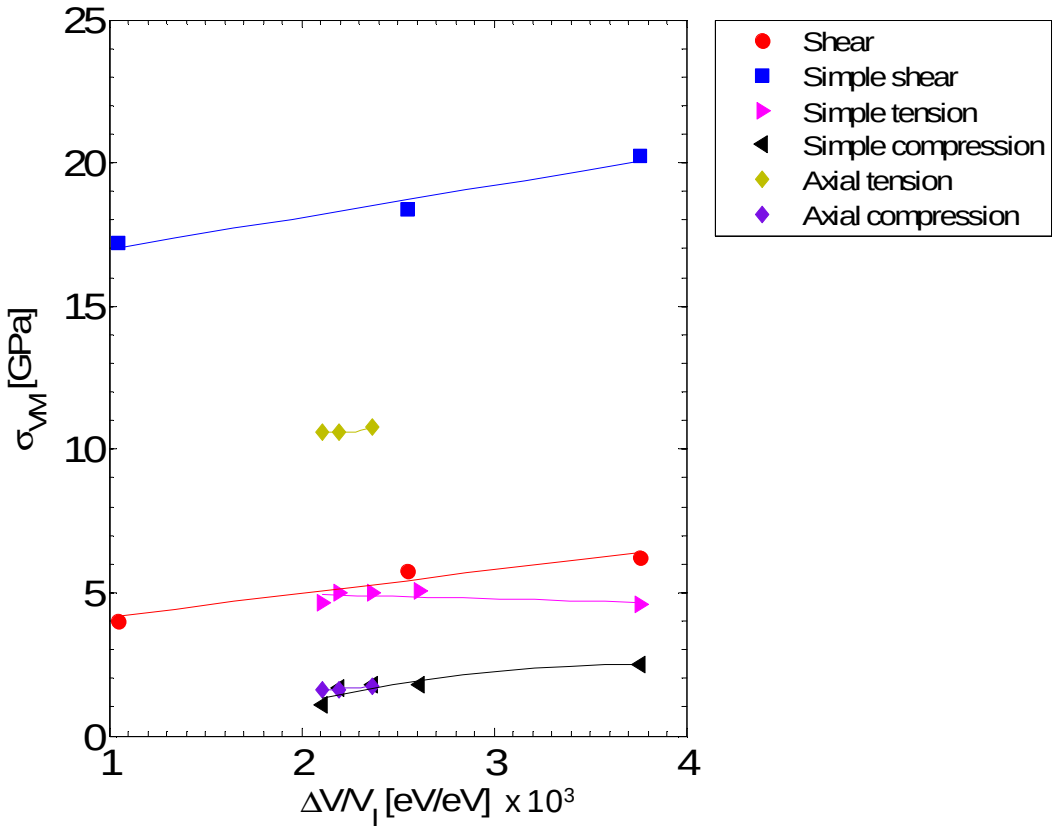

Fig. 7.3. For specimens with different aspect ratios, number of atoms and mechanical tests listed in Table 7.2, the relation between the change in the total potential energy upon relaxation and the average von Mises stress, σ_{VM}, at the yield point.

Conclusions common to all types of deformations studied are summarized below.

- A discontinuity in the average stress - average strain curve does not imply that the system has become globally unstable; however, a sharp drop in the average stress does imply the onset of a global instability.
- The three criteria for the initiation of a local instability are met essentially simultaneously at the same atomic positions.
- The average values of the Cauchy stresses derived from different definitions of the Cauchy stress tensor agree well with each other.

- Large values of σ_{VM} and τ_{max} occur on atoms located beneath the traction free surfaces, and at atoms in the interior that have become unstable.
- For specimens with essential boundary conditions on all bounding surfaces, the local and the global instabilities ensue at nearly the same value of the average axial strain.
- For specimens with some bounding surfaces traction free, the average strain at the occurrence of a local instability is much less than that at the initiation of a global instability.
- Values of the von Mises stress and the maximum shear stress at specimen's yielding depend upon the specimen size and boundary conditions prescribed on the bounding surfaces.
- For essential boundary conditions prescribed on all bounding surfaces of specimens deformed in either simple shear or triaxial tension/compression, the response of the equivalent hyperelastic material matches well with that obtained from MM simulations. However, instabilities seen in the MM simulations are not observed in deformations of the hyperelastic material.
- The response of a specimen in tension and compression is very different. This can be attributed to the presence of nonuniformly distributed stresses in the reference configuration.

Bibliography

Acharya, A., 2003. Driving forces and boundary conditions in continuum dislocations mechanics. Proc. R. Soc. Lond. A 459 (2034), 1343-1363.

Baskes, M. I., Daw M. S., 1984. Embedded atom method: Derivation and application to impurities, surfaces and other defects in metals. Phys. Rev. B 29 (12), 6443-6453.

Baskes, M.I., 1992. Modified embedded-atom potentials for cubic materials and impurities. Phys. Rev. B 46 (5), 2727-2742.

Born, M., Huang K**.,** 1954. Dynamical Theory of Crystal Lattices. Clarendon Press, Oxford.

Clausius, R.J.E., 1870. On a Mechanical Theorem Applicable to Heat. Philos. Mag., Ser. 4 40.

Cleri, F., RosatoV., 1993. Tight-binding potentials for transition metals and alloys. Phys. Rev. B 48 (1), 22-33.

Considère, M., 1888. Die Anwendung von Eisen und Stahl bei Konstruktionen, Gerold-Verlag, Wien.

Cormier, J., Rickman J.M., Delph T.J., 2001. Stress calculation in atomistic simulations of perfect and imperfect solids. J. Appl. Phys. 89 (1), 99-104.

Delph, T.J., 2005. Local stresses and elastic constants at the atomic scale. Proc. R. Soc. London, Ser. A 461 (2058), 1869-1888.

Diao, J., Gall K., Dunn M.L., Zimmerman J.A., 2006. Atomistic simulations of the yielding of gold nanowires. Acta Mater. 54 (3), 643-653.

Diao, J., Gall K., Dunn M.L., 2004. Atomistic simulation of the structure and elastic properties of gold nanowires. J. Mech. Phys. Solids 52 (9), 1935-1962.

Dmitriev, S.V., Kitamura T., Li J., Umeno Y., Yashiro K., Yoshikawa N., 2005. Near-surface lattice instability in 2D fiber and half-space. Acta Mater. 53 (4), 1215-1224.

Djohari, H., Milstein F., Maroudas D., 2006. Analysis of elastic stability and structural response of face-centered cubic crystals subject to [110] loading. Appl. Phys. Lett. 89 (18), 181907.

Ercolessi, F., Parrinello M., Tosatti E., 1988. Simulation of gold in the glue model. Philos. Mag. A 58, 213-226.

Ericksen, J.L., 2008. On the Cauchy-Born rule. Math. Mech. Solids. 13, 199-220.

Falk, M.L., 1999. Molecular dynamics study of ductile and brittle fracture in model noncrystalline solids. Phys. Rev. B 60 (10), 7062-7070.

Finnis, M. W., Sinclair J. E., 1984. A Simple empirical N-body potential for transition-metals. Philos. Mag. A 50 (1), 45-55.

Gall, K., Diao J., Dunn M.L., 2004. The strength of gold nanowires. Nano Lett. 4 (12), 2431-2436.

Gullett, P.M., Horstemeyer M. F., Baskes M. I. , Fang H., 2008. A deformation gradient tensor and strain tensors for atomistic simulations. Modell. Simul. Mater. Sci. Eng. 16 (1), 015001.

Hager, W. W., Zhang H., 2005. A New Conjugate Gradient Method with Guaranteed Descent and an Efficient Line Search. SIAM J. Optim. 16 (1), 170 – 192.

Hardy, R. J. 1981. Formulas for determining local properties in molecular dynamics simulations: Shock waves. J. Chem. Phys. 76 (1), 622-628

Hartley,C.S., Mishin Y., 2005. Representation of dislocation cores using Nye tensor distributions. Mater. Sci. Eng. A 400-401, 18-21.

Heinz, H., 2007.Calculation of local and averaged pressure tensors in molecular simulations. Molecular Simulations, 33 (9), 747-758.

Hill, R., 1962. Acceleration waves in solids. J. Mech. Phys. Solids 10 (1), 1-16.

Irving, J.H., Kirkwood J.G., 1950.The statistical mechanical theory of transport processes. IV. The equations of hydrodynamics. J. Chem. Phys.18 (6), 817–829.

Jacobsen, K.W., Norskov, J.K., Puska, M.J., 1987. Interatomic interactions in the effective-medium theory. Phys. Rev. B 35 (14), 7423-7442.

Ju, S.P., Lin J.S., Lee W.J., 2004. A molecular dynamics study of the tensile behavior of ultrathin gold nanowires. Nanotechnol. 15 (9), 1221-1225.
Kelchner,C. L., Plimpton S. J., Hamilton J. C., 1998. Dislocation nucleation and defect structure during surface indentation. Phys. Rev. B 58 (17), 11085-11088.
Kitamura, T. Umeno Y., Tsuji N., 2004. Analytical evaluation of unstable deformation criterion of atomic structure and its application to nanostructure. Comput. Mater. Sci. 29 (4), 499-510
Kitamura, T., Umeno Y., Fushino R., 2004. Instability criterion of inhomogeneous atomic system. Mater. Sci. Eng. A 379 (1), 229-233.
Kouznetsova, V., Geers M. G. D., Brekelmans W. A. M., 2002. Multi-scale constitutive modeling of heterogeneous materials with a gradient-enhanced computational homogenization scheme. Int. J. Numer. Methods Eng. 54 (8), 1235–1260.
Lee, W.J., Ju S.P., Sun S.J., Weng M.H., 2006. Dynamical behavior of 7-1 gold nanowires under different axial tensile strains. Nanotechnol. 17 (13), 3253-3258.
Li, Q. K., Li M., 2006. Atomic scale characterization of shear bands in an amorphous metal. Appl. Phys. Lett. 88 (24), 241903.
Liang, W., Zhou M., 2004. Response of copper nanowires in dynamic tensile deformation. Proc. Inst. Mech. Eng. Part C J. Mech. Eng. Sci. 218 (6), 599-606.
Lin, J. S., Ju S. P., Lee W. J., 2005. Mechanical behavior of gold nanowires with a multishell helical structure. Phys. Rev. B 72 (8), 085448.
Liu, Y., Van der Giessen E., Needleman A., 2007. An analysis of dislocation nucleation near a free surface. Int. J. Solids Struct. 44 (6), 1719-1732.
Lu, J., Zhang L., 2006. An atomistic instability condition and applications. J. Mech. Mater. Strut. 1 (4), 663-648.
Lusko, J. F., 1988. Stress and elastic constants in anisotropic solids: Molecular dynamics techniques. J. Appl. Pys. 64 (3), 1152–1154.
Ma F., Xu K.W., 2006. Size-dependent theoretical tensile strength and other mechanical properties of [001] oriented Au, Ag, and Cu nanowires. J. Mater. Res. 21 (11), 2810-2816.
Miller, R.E., Acharya A., 2004. A stress-gradient based criterion for dislocation nucleation in crystals. J. Mech. Phys. Solids 52 (7), 1507-1525.
Miller, R.E., Rodney D., 2008. On the nonlocal nature of dislocation nucleation during nanoindentation. J. Mech. Phys. Solids 56 (4), 1203–1223.
Milstein, F., Zhao J., Chantasiriwan S., Maroudas D., 2005. Applicability of Born's stability criterion to face-centered-cubic crystals in [111] loading. Appl. Phys. Lett. 87 (25), 251919.
Mott, P.H., Argon A.S., Suter U.W., 1992. The atomic strain tensor. J. Comput. Phys. 101(1), 140-150.
Ogata, S., Li J., Hirosaki N., Shibutani Y.,Yip S., 2004. Ideal shear strain of metals and ceramics. Phys. Rev. B 70 (10), 104104.
Park, H. S., Gal K., Zimmerman J. A., 2006 .Deformation of FCC nanowires by twinning and slip. J. Mech. Phys. Solids 54 (9), 1862–1881.
Pasianot, R., Xie Z. Y., Farkas D., Savino E. J., 1993. Representation of atomistic dislocation core structures. Scr. Metall. Mater. 28 (3), 319-324.
Potirniche, G. P., Horstemeyer M. F., Wagner G. J., Gullett P. M., 2006.A molecular dynamics study of void growth and coalescence in single crystal nickel. Int. J. Plast. 22 (2), 257-278.
Poynting, J. H., 1909. On pressure perpendicular to the shear planes in finite pure shears, and on the lengthening of loaded wires when twisted. Proc. R. Soc. London, Ser. A 82 (556), 546-549.
Pu, Q., Leng Y., Tsetseris L., Park H. S., Pantelides S. T., Cummings P. T., 2007. Molecular dynamics simulations of stretched gold nanowires: The relative utility of different semiempirical potentials. J. Chem. Phys. 126 (14), 144707.
Rabkin, E., Nam H. S., Srolovitz D. J., 2007.Atomistic simulations of the deformation of gold nanopillars. Acta Mater. 55 (6), 2085-2099.
Rice, J.R., 1976. The Localization of Plastic Deformation. In: W.T. Koiter (Ed), Theoretical and Applied Mechanics, Proceedings of the 14th International Congress on Theoretical and Applied

Mechanics, vol. 1. North-Holland Publishing Co., 207-220.
Root, S., Hardy R. J., Swanson D. R., 2003. Continuum predictions from molecular dynamics simulations: Shock waves. J. Chem. Phys. 118 (7), 3161-3165.
Rubio-Bollinger, G., Bahn S.R., Agrair N., Jacobsen K.W., Vieira S., 2001. Mechanical properties and formation mechanisms of a wire of single gold atoms. Phys. Rev. Lett. 87 (2), 026101.
Shen, S., Atluri S.N., 2004. Atomic-level Stress Calculations and Continuum-Molecular System Equivalence. CMES, 6 (1), 91-104
Stakgold, I., 1950. The Cauchy relations in a molecular theory of elasticity. Quart. Appl. Math. 8, 169-186.
Steinmann, P., Elizondo A. , Zunyk R., 2007. Studies of validity of the Cauchy-Born rule by direct comparison of continuum and atomistic modeling. Modell. Simul. Mater. Sci. Eng. 15 (1), S271-S281.
Sun, Z. H., Wang X. X., Soh A. K., Wu H. A., 2006. On stress calculations in atomistic simulations. Modell. Simul. Mater. Sci. Eng. 14 (3), 423-431.
Szefer, G., 2004. Molecular modelling of stress and deformations in nanostructured materials. Int. J. Appl. Math. Comput. Sci.14, 541-548.
Truesdell,C., Noll W., 1992. The Non-Linear Field Theories of Mechanics, Second edition. Springer-Verlag.
Tsai, D. H., 1979. The virial theorem and stress calculation in molecular dynamics. J. Chem. Phys. 70 (3), 1375-1382.
Tsuzuki, H., Branicio P.S., Rino J.P., 2007. Structural characterization of deformed crystals by analysis of common atomic neighborhood. Comput. Phys. Commun. 177 (6), 518–523
Van Vliet, K.J., Li J., Zhu T., Yip S., Suresh S., 2003. Quantifying the early stages of plasticity through nanoscale experiments and simulations. Phys. Rev. B 67 (10), 104105.
Voter, F., Chen S.P., 1987. Characterization of Defects in Materials. In: Siegel R.W., Weertman J. R., Sinclair R. (Eds.), Mater. Res. Soc. Symp. Proc. 82. Materials Research Society, Pittsburgh, 175.
Wajnryb, E., Altenberger A. R., Dahler J.S., 1995. Uniqueness of the microscopic stress tensor. J. Chem. Phys. 103 (22), 9782-9787.
Wang, J., Li J.,Yip S., Phillpot S.,Wolf D., 1995. Mechanical instabilities of homogeneous crystals. Phys. Rev. B 52 (17), 12627-12635.
Webb, E.B. III , Zimmerman J.A., Seel S.C., 2008. Reconsideration of continuum thermomechanical quantities in atomic scale simulations. Mathematics and Mechanics of Solids 13 (3), 221-266.
Zhang, G.M., Batra R.C., 2004. Modified smoothed particle hydrodynamics method and its application to transient problems. Comput. Mech. 34 (2), 137-146.
Zhang, W., Wang T., Chen X., 2008. Effect of surface stress on the asymmetric yield strength of nanowires. J. Appl. Phys. 103 (12), 123527.
Zhou, M., 2003. A new look at the atomic level virial stress: on continuum-molecular system equivalence. Proc. R. Soc. Lond. A 459, 2347-2392.
Zimmerman, J. A, Bammann D. J., Gao H., 2009. Deformation gradients for continuum mechanical analysis of atomistic simulations. Int. J. Solids Struct. 46 (2), 238-253.
Zimmerman, J. A., Kelchner C. L., Klein P.A., Hamilton J. C., Foiles S.M., 2001. Surface step effects on nanoindentation. Phys. Rev. Lett. 87 (16), 165507.
Zimmerman, J. A., WebbIII E. B., Hoyt J. J., Jones R. E., Klein P. A., Bammann D. J., 2004. Calculation of stress in atomistic simulation. Modell. Simul. Mater. Sci. Eng. 12 (4), S319-S332.